Investigation of Porous Polymer Particle Shells Synthesised by RAFT-PISA with pH- and Thermo- Response

Shaobo Du

July 2023

A thesis submitted to the University of Sheffield in partial fulfilment
to the requirements for degree of Doctor of Philosophy

Content

Authors Declaration

The author of this thesis takes full responsibility for the original work presented, except for the SEM data, which were collected by Jiantgtian Tan. All research presented in this thesis was conducted at the University of Sheffield from March 2019 to March 2023. The opinions expressed in this thesis reflect those of the author and do not necessarily represent the views of the University of Sheffield.

Abstract

Microporous organic polymers (MOPs) with high specific surface areas, low skeletal density, good chemical & thermal stability and ease of functionality are of interest for a range of applications such as gas storage, capture and separations, energy storage, catalysis as well as drug delivery, and chemosensing. However, one of the greatest challenges for the industrial use of MOPs is their lack of solubility limiting their applications to the solid state. This is primarily due to the highly rigid and cross-linked structure required to induce porosity. One class of MOP has however found commercial success due to their solubility in a range of organic solvents - PIMs which achieve the combination of high surface areas and solubility by using rigid and twisted linear polymer chains. There are however a limited number of monomers which can be used to synthesise PIMs. To overcome this limitation, a number of strategies have been used to make network MOPs both highly porous and dispersible. Based on previous research in our group, the metal-free reversible addition fragmentation transfer polymerisation induced self-assembly (RAFT-PISA) was used as a strategy to form core-shell structures to improve the solubility of the MOPs. To date only PEG based solubilising chains have been reported, and this thesis therefore investigates the use of different solubilising shell polymer chains including poly acrylic acid (PAA), poly(diethylaminoethyl methacrylate) (PDEAEMA), poly(4-vinyl pyridine) (P4-VP) and poly(*N*-Isopropylacrylamide).

In Chapter 3, PAA is first investigated as the hydrophilic shell to determine the best reaction conditions to maximise the BET surface area. BET surface areas of up to 322 m^2 g^{-1} and obtained for PAA based particles. Chapter 4 looks at the use of pH- and thermo-responsive PDEAEMA and P(4-VP) based particles with BET surface areas up to 101 m^2 g^{-1} and 133 m^2 g^{-1} respectively. It is shown that these particles exhibit switchable pH-responsive properties. At low pH small particle sizes (~200 nm) are observed while at high pH the particles increase to ~800 nm due to aggregation. Chapter 5 discusses the thermo-response of the particles including above particles and PNIPAm based particles with surface areas of 193 m^2 g^{-1}. At low temperatures the particle sizes are big and form aggregation and precipitated out at high temperatures as water is expelled from the particles. Finally, methods to improve the BET surface areas are investigated in Chapter 6. These include the mixing of chain lengths, the addition of anionic shells to cationic particles and the use of non-ionic higher surface area inducing shells. The surface areas of P4-VP are able to be increased by up to 5 times by the addition of PEG shells while still maintaining both pH and thermo-responsive behaviour.

Abstract

In a summary, the reaction conditions of core-shell structure dispersible porous polymer particles are mapped out, which the particles with a small core and short shell length have a higher BET surface area. Moreover, the stimuli responsive shell chains with pH- and thermos-responsive, which are successfully introduced into the particles, which have small particle sizes at acid condition or low temperature, and large particle size at base condition or high temperature. The adding of anionic shells to cationic particles and the use of non-ionic shells can indeed increase surface area of single shell-chain particles.

Acknowledgements

I would like to express my gratitude to Dr. Robert Dawson, my supervisor, for providing me with the opportunity to undertake this project. I have found him to be exceptionally kind and patient, and it has been a true pleasure to work with him.

I would like to express my gratitude to Dr. Arosha Karunathilake, a postdoctoral researcher in our group, for her invaluable support and guidance throughout the course of my research. Her kindness, expertise, and encouragement have been instrumental in the successful completion of this project.

I am grateful to Dr. Supakorn Tantisriyanurak, Dr. Alex James, Dr. Xuefeng Qi, Jiaqi Zhou, Robert Matthews, as well as all former and current members of the group for their valuable assistance and support throughout my research.

In addition, I would like to express my appreciation to the academic, technical, and administrative staff of the Department of Chemistry and the Department of Biology. I particularly want to thank Dr. Svetomir Tzokov for his assistance and support with TEM analysis, and Prof. Steven Armes for his insights on RAFT-PISA.

I express my sincere gratitude to my family for their unwavering love, encouragement and financial support throughout my PhD journey. Their constant support has been instrumental in enabling me to achieve this significant milestone in my life.

I would also like to acknowledge the valuable contributions of my friends who have been an important part of my support system. I am particularly grateful to Dr. Feifan Lang, Dr. Tao Cheng, Prof. Yin Ning, Dr. Baozhai Han, Dr. Ram Prasad, Mengyuan Qian, Jiangtian Tan, Jialin Chen, and Nandong Yao, for their advice, assistance and encouragement throughout my research. Their insights and support have been invaluable and greatly appreciated.

List of Abbreviation

AA	Acrylic Acid
AIBN	2,2′-Azobis(2-methylpropionitrile)
AIPAAm	2-aminoisopropylacrylamide
ATRP	Atom Transfer Radical Polymerisation
BDBA	1,4-Benzenediboronic acid
BET	Brunauer-Emmett-Teller
BZ	Benzothiadiazole
CIPAAm	2-Carboxylisopropylacrylamide
CMC	Critical Micelle Concentration
CMP	Conjugated Microporous Polymer
COF	Covalent Organic Framework
CPDTC	2-Cyano-2-propyl dodecyl trithiocarbonate
CTA	Chain Transfer Agent
CTF	Covalent Triazine Framework
DCC	N, N'-Dicyclohexylcarbodiimide
DCE	1,2-Dichloroethane
DDMAT	2-(Dodecylthiocarbonothioylthio)-2-methylpropanoic acid
DEAEMA	Diethylaminoethyl methacrylate
DMAP	Dimethylaminopyridine
DLS	Dynamic Light Scattering
DP	Degree of Polymerisation
d-PPPs	Dispersible Porous Polymer Particles
DVB	Divinylbenzene
FN	Fumaronitrile

Abbreviation

FTIR	Fourier-Transform Infrared
GPC	Gel Permeation Chromatography
h	Hours
HCP	Hypercrosslinked Polymer
HHTP	2,3,6,7,10,11-Hexadydroxytriphenylene
HIPAAm	2-Hydroxyisopropylacrylamide
IUPAC	International Union of Pure and Applied Chemistry
K	Kelvin
KAPs	Knitting Aromatic compound Polymers
KPS	Potassium persulfate
LCST	Lower Critical Solution Temperature
mg	Milligram
min	Minutes
mL	Millilitres
nm	Nanometres
M_n	Average number molecular mass
MOF	Metal-Organic Framework
mol	Moles
MOP	Microporous Organic Polymer
M_w	Average weight molecular mass
M_z	Z-average molecular weight
NIPAm	N-Isopropylacrylamide
NMP	Nitroxide-Mediated Polymerisation
NMR	Nuclear Magnetic Resonance

Abbreviation

PAA	Poly(acrylic acid)
PAF	Porous Aromatic Frameworks
PDEMA	Poly(2-(dimethylamino)ethyl methacrylate)
PDI	Polydispersity Index
PDEAEMA	Poly(diethylaminoethyl methacrylate)
PEG	Poly(ethylene glycol)
PIM	Polymers of Intrinsic Microporosity
PISA	Polymerisation-Induced Self-Assembly
pK_a	Acid Dissociation Constant
PMMA	Poly(methyl methacrylate)
PNIPAm	Poly(N-isopropylacrylamide)
POP	Porous Organic Polymers
PS	Polystyrene
PSM	Post-Synthetic Modification
PVP	Poly(vinylpyridine)
P4-VP	Poly(4-vinylpyridine)
RAFT	Reversible Addition Fragmentation Polymerisation
RDRP	Reversible-deactivation radical polymerisation
RT	Room Temperature
SCMPs	Soluble CMPs
SEM	Scanning Electron Microscopy
SI-ATRP	Surface Initiated Atom Transfer Radical Polymerisation
ssNMR	Solid-state Nuclear Magnetic Resonance
TAPB	1,3,5-Tris(4-aminophenyl) benzene

Abbreviation

TB	Tröger’s base
TBDC	Tetraphenyl-5,5-dioctylcyclopentadiene
TBPS	Tetrahedral tetra(4-dihydroxyborylphenyl) silane
TEM	Transmission Electron Microscopy
TFMS	Trifluoromethanesulfonic acid
THF	Tetrahydrofuran
UCST	Upper Critical Solution Temperature
4-VP	4-Vinylpyridine
UV	Ultraviolet
Wt.%	weight percentage

Chapter-1 Introduction

1.1 Porous Materials

Porous materials with various pore dimensions and pore structures have been widely researched over the past few decades. Due to their high surface areas and tuneable pore structures, these materials have been used in a various applications taking advantage of the interactions between the adsorbent and the adsorbate.[1] Porous materials can be classified into 3 categories based on their pore sizes as defined by the International Union of Pure and Applied Chemistry (IUPAC): microporous materials possess diameters less than 2 nm; mesoporous materials have pore diameters between 2 nm and 50 nm; and marcoporous materials have pore diameters larger than 50 nm.[2] Due to the fact that microporous materials have pore sizes in the range of atoms and small molecules, these materials are of particular interest. Microporous materials can also be categorised according their structural composition into 3 further categories; inorganic porous materials (e.g. zeolites), inorganic-organic hybrid porous materials (e.g. MOFs) and organic porous materials which will be the focus of this thesis.[3]

Zeolites are a class of porous aluminosilicate materials with a range of pore cage sizes and channels.[4] Due to the connections of corner-sharing TO_4 tetrahedra (‘T’ means tetrahedrally coordinated Si, Al, or P, etc.), the framework structures of zeolites can be varied to provide numerous zeolite structures.[5] To date, there are 235 different types of zeolite framework which have been identified in nature or synthesised and the International Zeolite Association uses a three-letter code to identify them. In addition, based on their largest pore windows, the zeolites can be categorised into small-pore (≤8-ring), medium-pore (10-ring), large-pore (12-ring), and extra-large-pore zeolites (>12-ring).[6] Due to the negative charges of zeolite framework building blocks, zeolites are usually incorporate additional cations into their pores which can be exchanged for other cations. Thus, the original species in the pores of zeolites can be removed and the selective guest species will occupy the void space due to suitable size, shape, and polarity. Depending on their properties, zeolites can be applied to a variety of applications such as biomass conversion[7–15], fuel cells[16–20], thermal energy storage[21–25], CO_2 capture[26,27] and conversion[28–30], air-pollution remediation[31–35], and water purification[36–40].

Porous materials which consist metal ions or small metal clusters linked together by multitopic organic linkers with one, two, or three-dimensional structures are commonly referred to metal-organic frameworks (MOFs).[41] Depending on the different metals and different shape and size of organic ligands, the structure and pore size can be controlled. Generally, the synthesis method for MOFs is liquid-phase synthesis where the dispersed metal salt and organic ligand are mixed together in a reaction vial.[42] Furthermore, the MOFs can be synthesised by slow evaporation[43,44]; solvothermal synthesis[45]; microwave-assisted synthesis[46,47]; electrochemical synthesis[48]; mechanochemical synthesis[49,50]; and sonochemical synthesis[51,52]. By 2017 69,666 different MOFs had been reported and the underlying topology of a structure is described by a net, assigned by a three-letter symbol.[53] The Reticular Chemistry Structure Resource (RCSR) has a collection of more than 2000 different nets which are available as a searchable database. Due to the properties with controllable pore size and large specific surface area, MOFs are ideal candidates for fuels storage (hydrogen[54–57] and methane[58–61]), carbon dioxide (CO_2) capture[62–66], catalysis[41], magnetic materials[67–71], air-pollution remediation[72–74] and sensors[75–79].

In contrast, porous organic polymers (POPs) or microporous organic polymers (MOPs) cover a wide range of materials comprised of light, non-metallic elements such as carbon, hydrogen, oxygen, nitrogen, and boron. These organic building blocks are connected by covalent bonds to form highly crosslinked networks with good stabilities.[80] Their structures allow MOPs to have high specific surface areas, low skeleton density, good chemical & thermal stability combined with a relative ease of functionality.[81] Depending on their structural characteristics, MOPs have been divided into numerous different subtypes including: covalent organic frameworks (COFs)[82,83], covalent triazine-based frameworks (CTFs)[84,85], conjugated microporous polymers (CMPs)[86–88], porous aromatic frameworks (PAFs)[89–91], hypercrosslinked polymers (HCPs)[92–95], and polymers of intrinsic microporosity (PIMs)[96–99]. MOPs can either be disordered & amorphous or ordered & crystalline depending on the method used to synthesise them. PIMs, HCPs, PAFs and CMPs are amorphous, while COFs and CTFs are crystalline. Crystalline MOPs, in general, are formed using reversible reaction in order to allow the formation of ordered thermodynamic products, while amorphous MOPs are typically synthesised using irreversible reactions under kinetic control.

One of the main advantage of MOPs is their synthetic diversity which can results in a large variety of structures. Thus, the preparation of microporous solids using organic building blocks offers some exciting possibilities in network design to for example to generate new network structures, incorporate functional groups for specific properties, and possibly adjust properties through structural modifications of the system. These modifications can be used to tune the materials for varies of applications.

MOPs exhibit a highly crosslinked network structure, resulting in high specific surface areas, low skeleton density, good chemical & thermal stability and ease of functionality, making them versatile for a wide range of applications. One of the applications is gas storage. Dawson and co-workers designed a series of functionalised CMPs to enhance the CO_2 uptake ability and summarised the CO_2 capture ability in porous materials.[100,101] It is reported that the PPN-4[90] and the PAF-1[89] have a very huge CO_2 uptakes up to 48.2 mmol/g and 29.55 mmol/g at 40 bar and 298 K, respectively. Makhseed et al.[102,103] synthesised a series of MOPs to enhance the hydrogen (H_2) uptake ability and listed different H_2 adsorption capacity in MOPs. The PAF-qtph (PAF-304)[104] exhibits the highest H_2 uptake up to 36.6 mmol/g at 100 bar and 298 K. Wood and co-workers[105] obtained a series of HCPs and summarise the methane (CH_4) adsorption capacity in microporous systems and the found the HCPs which they synthesised has the largest CH_4 uptake up to 5.2 mmol/g at 20 bar and 298 K. Gas separation is one of the applications. Kim and co-workers listed a series of gas separation membranes.[106] Due to the solubility of PIMs, which make it apply to the gas separation membranes more commonly. Adding different functional groups can change the selectivity of different kind of gases, such as N_2, CO_2, O_2, CH_4 and H_2. In addition, MOPs can be used as catalytic materials. The main advantages of MOPs are easily handling and separation the catalyst from the reaction mixture and can be recycled to minimise waste production. Such as, good catalytic activity for hydroquinoneoxidation,[107] high acidity to obtain environmentally friendly biodiesel production from waste cooking oil,[108] and so on. Furthermore, MOPs have potential application for energy storage, especially for supercapacitors which have a higher energy density, compared with traditional batteries such as lithium ion batteries. Xiang and co-workers[109] synthesised a carbonised PAF and compared to other materials such as carbon nanotubes, activated carbon materials, and MOFs, which has a large specific capacitance of 385 F g^{-1} at 0.1 A g^{-1} current density.

Despite MOPs having many advantages, they come with their own set of challenges. Some monomers (especially highly functionalised ones) are relatively expensive, and volatile and toxic organic solvents are often used to synthesise MOPs, which has environmental impacts. Depending on the chemistry used the atom economy can be poor. Furthermore, as most MOPs are highly crosslinked and connected by rigid aromatic rings to maintain their pore structures in the dry state, this results in them having a poor environmental degradability as well as limiting their use to applications in the solid state.[110] This thesis will focus on the synthesis of solution dispersible porous polymer particles made via controlled radical chemistry and will be discussed in more detail in Chapter 1.3

1.2 Background of Different Types of MOPs

1.2.1 Covalent Organic Frameworks (COFs)

COFs are porous polymers with an ordered and crystalline network structures. The rigid units in their structures are arranged to form uniformly sized pores. The properties of crystalline of microporous polymers are precise enough to control their surface chemistry. Moreover, with the addition of specific molecular recognition or catalytic point into the structure, the COFs are conducive to separations or selective adsorption chemistry and heterogeneous catalysis.[111] The synthesis methods of COFs originated from the synthesis of MOFs. The reactions of the building blocks are thermodynamically controlled to form the most stable structure. An ordered network structure is maintained to produce permanent microporous crystalline polymers.[112] Due to the building units, COFs can be designed as either 2D or 3D structures. The first COF was reported in 2005 by Cote and co-workers[113], they used 1,4-benzenediboronic acid (BDBA) in a dioxane/mesitylene solvent mixture to form a layered hexagonal framework based on the molecular dehydration reaction and named it COF-1. The boroxine rings were formed by reversible and strong B-O bonds and they are very similar to the metal centres in the MOFs. Furthermore, their group used different monomers via the same method to form different COFs with different pore diameters (Figure 1.1).

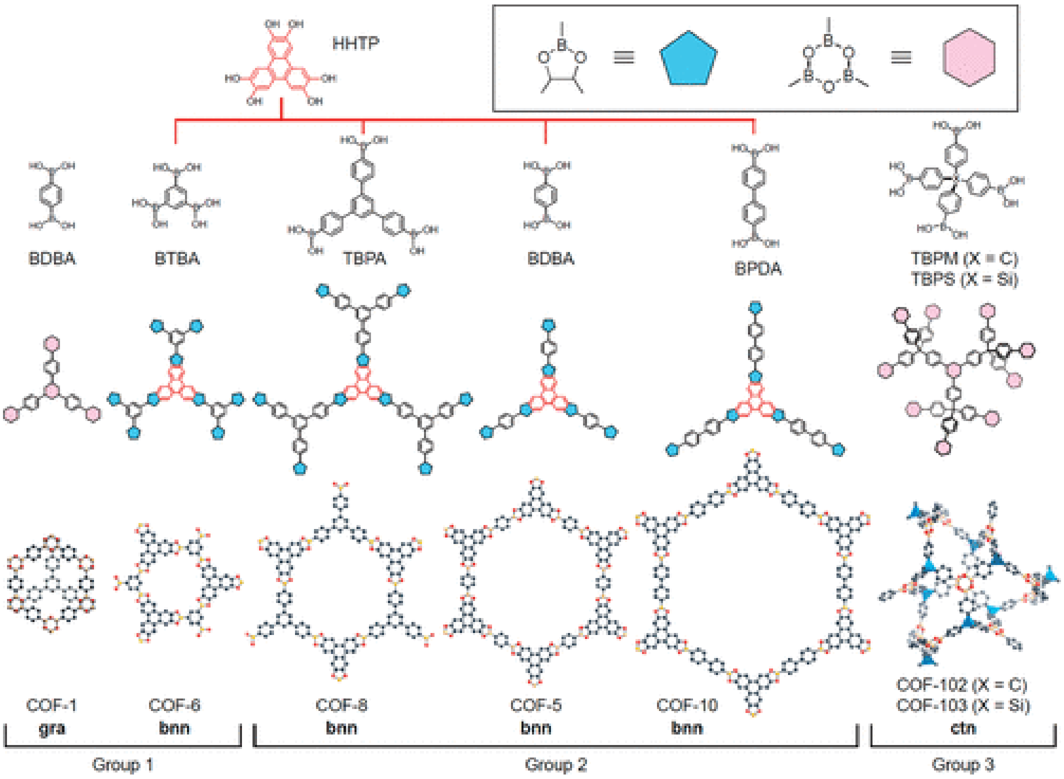

Figure 1.1 Selected COFs synthesised by the Yaghi group[114]

Besides the C-B bond-linked COFs (boroxine and boronic ester), C-N or C=N bond can be used to form COFs, such as reversible imine[115–117], and reversible hydrazine[118,119]. For example, Tian and co-workers[115] used 1,3,5-tris(4-aminophenyl) benzene (TAPB) and 2,5-divinylterephthalaldehyde (DVA) to form COF-V though the condensation reaction between amino groups and aldehyde groups. Moreover, the C-C and C=C bond can also be used to form COFs.[120] The largest BET surface area is reported by El-Kaderi and co-workers[121], they synthesised COF-103 by using 2,3,6,7,10,11-hexadydroxytriphenylene (HHTP) and tetrahedral tetra(4-dihydroxyborylphenyl) silane (TBPS) with BET surface area is about 4210 m^2g^{-1} (Figure 1.1).

COFs offer the advantage of precise pore size control owing to their crystalline structure. However, this advantage is accompanied by a disadvantage stemming from their structural characteristics, which due to the reversible chemistry used for their synthesis often require lengthy reaction periods lasting several days. Furthermore, this reversibility often also leads to less chemically and thermal stable materials.

1.2.2 Covalent Triazine-based Frameworks (CTFs)

CTFs are microporous polymers which are linked though triazine (Figure 1.2). Unlike COFs, which are ordered and crystalline structure, CTFs contain ordered and amorphous structure. This is due to the linkage of triazine is less reversible than the linkage of boroxine, imine and so on which is used to form COFs.[120] This makes CTFs less precise to control their surface chemistry compared to COFs and the amorphous structures come out. One advantage is that monomers of CTFs are cheap and readily available with nitrogen content. Due to the nitrogen content on the structure, CTFs exhibit certain hydrophilicity.[122]

These materials are synthesised by three different methods. Kuhn and co-workers[84] reported the first CTF and named CTF-1 which was obtained by using trimerization of nitriles in a $ZnCl_2$ melt at 400 °C. Strong brønsted acids can also act as catalysis to reduce harsh reaction conditions of trimerization of nitriles. Ren and co-workers[123] synthesised CTFs using trifluoromethanesulfonic acid (TFMS) as the catalyst under both room temperature and microwave-assisted conditions. Puthiaraj et al.[124] and Lim et al.[125] reported a kind of CTFs which were synthesed by Friedel-Crafts ($AlCl_3$) reaction. Puthiaraj and co-workers used 1,3,5-triphenylbenzene or trans-stilbene with cyanuric chloride and anhydrous aluminium chloride in DCM under 70 °C to form MCTP-2 and MCTP-1. Lim and co-workers used benzene or biphenyl or terphenyl with 2,4,6-trichloro-1,3,5-triazine, and aluminum chloride in DCM under

70 °C to form compounds. The largest BET surface area is reported by Kuhn and co-workers[126], they used 1,4-dicyanobenzene and $ZnCl_2$ under an inert atmosphere reacted 20 h at 400 °C and increasing the temperature to 600 °C for 96 h with the BET surface area is about 3270 m^2g^{-1}.

Due to the crystalline structure like COFs, these materials also have a degree of control over their pore sizes. However, there are certain drawbacks associated with their synthesis. Firstly, CTFs require long reaction times and harsh reaction conditions, such as elevated temperatures or the use of strong acids. These conditions are necessary to facilitate the formation of the desired framework but often limits the ability to introduce functionality into the structure.

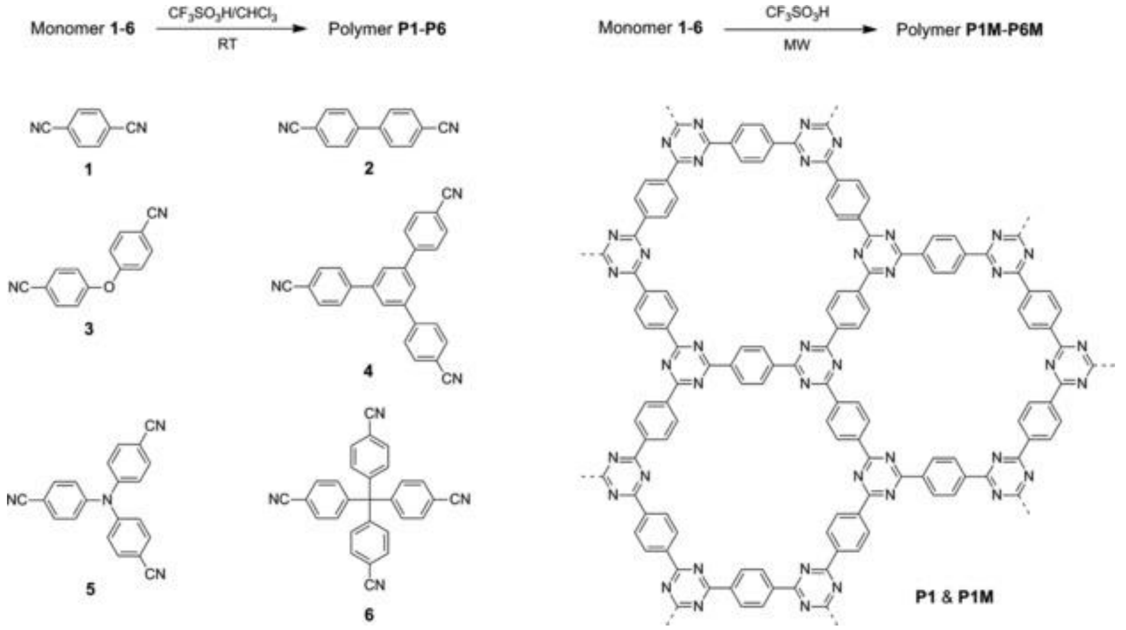

Figure 1.2 Synthesis of the CTF-type polymers P1-P6 and P1M-P6M and representative structure of P1 and P1M[123]

1.2.3 Conjugated Microporous Polymers (CMPs)

CMPs are a class of organic porous polymer that combine extended π-conjugation with a permanent nanoporous network. Due to their structure, these materials are completely disordered and amorphous compared to COFs and CTFs. Meanwhile, PAFs are not π-conjugated over the skeleton and despite the imine linked COF are π-conjugated, it has high crystallinity, which both two porous materials cannot be categorised as CMPs. Furthermore, the identical property of CMPs, π unit can provide a variety of ways for molecular design.[127]

Generally, the building blocks which to form the CMPs networks need at least two reactive groups, and the building blocks are classified into C2, C3, C4 and C6 categories by their functional groups. In addition, the self-condensation reactions (C3+C3 or C4+C4) and cross-coupling reactions (C2+C3, C2+C4, C2+C6, C3+C4, C3+C6, and C4+C6) are main methods to form the CMPs network (Figure 1.3).

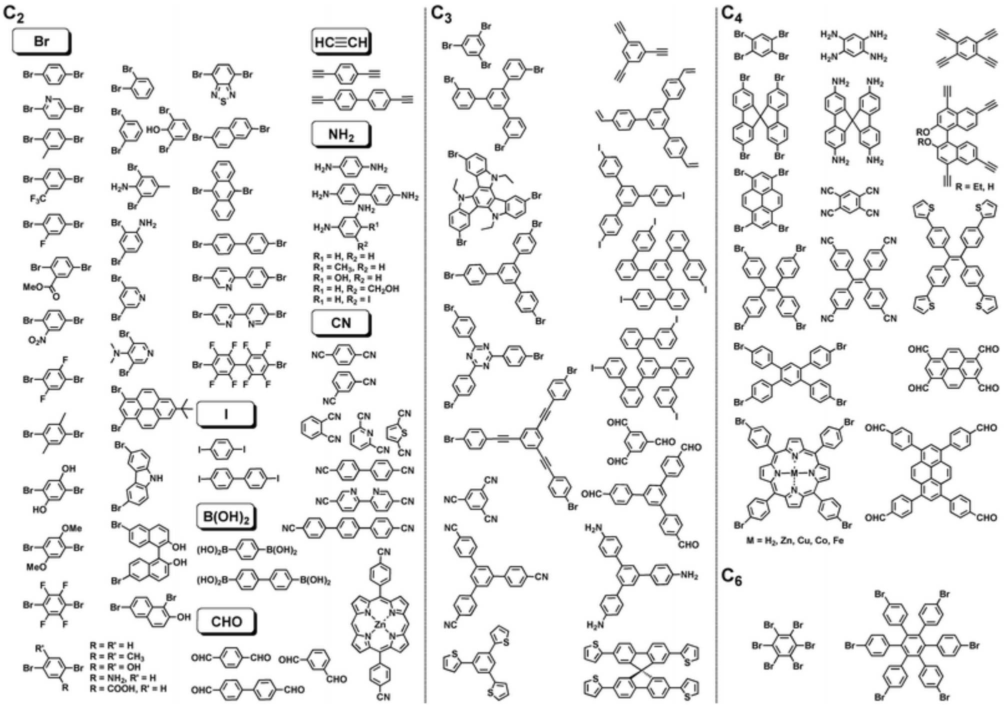

Figure 1.3 Schematic representation of the structures of building blocks with different geometries, sizes and reactive groups for the synthesis of CMPs[127]

There are various methods to prepare the CMPs, including Suzuki cross-coupling[128,129]; Yamamoto reaction[130,131]; Sonogashira-Hagihara reaction[132,133]; oxidative[134,135]; the Schiff-base reaction[136,137]; cyclotrimerization[138]; phenazine ring fusion reaction; and Friedel-Crafts arylation[139,140] (Figure 1.4). The first CMP was reported in 2007 by Jiang and co-workers[141]. They used 1,3,5-triethynylbenzene and 1,4-diiodobenzene with catalysis of tetrakis-(triphenylphosphine)palladium and copper iodide in the mixture of toluene and Et_3N under 80 °C for 24 h to form CMP-1. The largest BET surface area is reported by Kassab and co-workers[142], who used 1,2,4,5-tetrakis(4-bromophenyl)benzene with 1,5-cyclooctadiene (COD), Ni(cod)2, 2,2′-bipyridyl in DMF under 80 °C for 24 h to form NPOF-1 with the BET surface area is about 3127 m^2g^{-1}.

CMPs offer a notable advantage in that the functional groups are inherently present on the monomers, eliminating the need for additional modifications to introduce desired functional groups. Furthermore, CMPs possess an extended conjugated structure that imparts excellent conductivity. However, a key disadvantage is the cost associated with the monomers and catalysts, as they can be expensive or may require preparation from non-commercial sources prior to use.

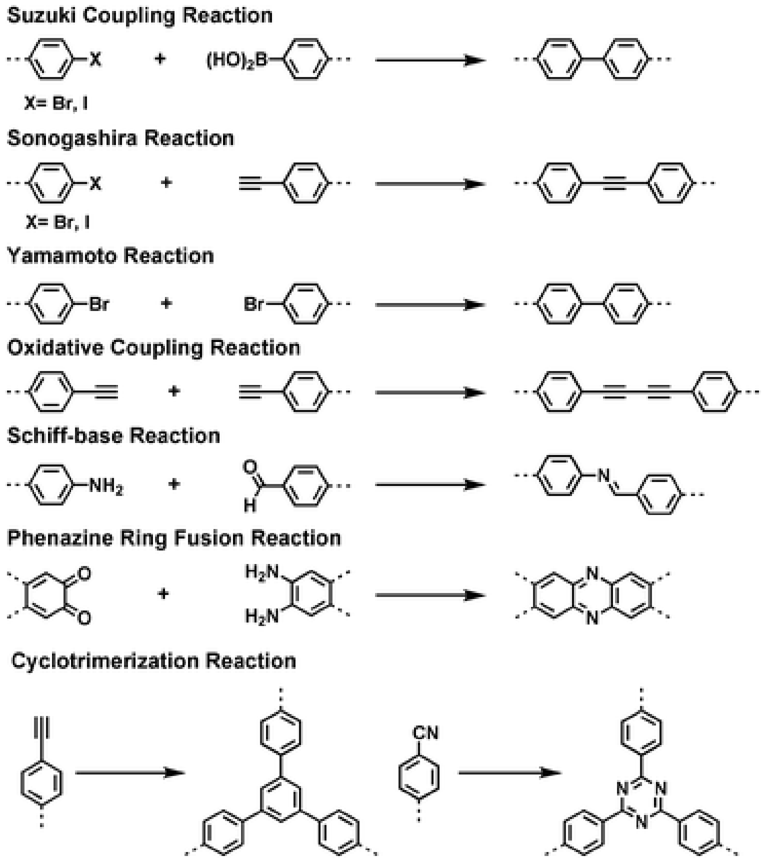

Figure 1.4 Schematic representation of reactions for the synthesis of CMPs[127]

1.2.4 Porous Aromatic Frameworks (PAFs)

PAFs are microporous materials with diverse structures, associated porosity and exceptionally high surface areas which obtained by effective assembly of organic building.[143] PAFs are derived from CMPs, with the key difference being their long-range order. According to the diverse structures, these materials can be designed with various geometries, such as cubic[144], prismatic[145], tetrahedral[146,147], square[148,149], triangular[150,151], and linear. The synthesis methods for PAFs are similar to those for CMPs and include Yamamoto type Ullmann coupling reaction[152,153], cyano cyclotrimerization[154,155], and others (Figure 1.5).

The first PAFs was reported in 2009 by Ben and co-workers[89], they used tetrakis(4-bromophenyl)methane with bis(1,5-cyclooctadiene)nickel(0) ([Ni(cod)$_2$], 1,5-cyclooctadiene (COD) and 2,2′-bipyridyl in dry DMF under 80 °C for 24 h to form PAF-1. The largest BET surface area reported by Yuan and co-workers[90], who used tetrakis(4-bromophenyl)silane with bis(1,5-cyclooctadiene)nickel(0) (Ni(COD)$_2$, 1,5-cyclooctadiene (COD) and 2,2′-bipyridyl in a dry mixture of DMF and THF at room temperature under argon atmosphere overnight to form PPN-4, which exhibited a BET surface area of 6461 m^{2}g^{-1}.

As PAFs are a derivation of CMPs, they possess similar advantages and disadvantages.

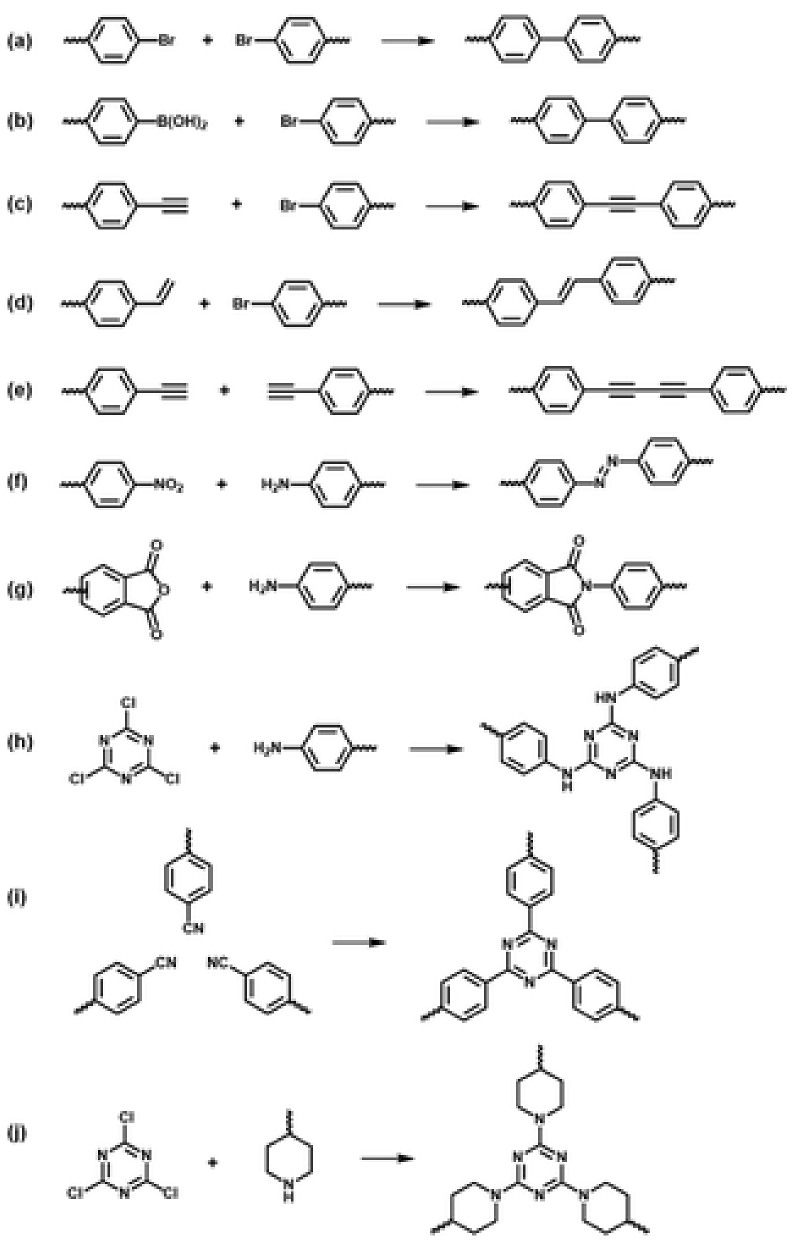

Figure 1.5 Schematic representation of reactions for the synthesis of RAFs: (a) Yamamoto-type Ullmann coupling, (b) Suzuki–Miyaura cross coupling, (c) Sonogashira–Hagihara cross coupling, (d) Mizoroki-Heck cross coupling, (e) oxidative Eglinton coupling, (f) base-mediated azo formation, (g) imidization reaction, (h) nucleophilic substitution reaction, (i) cyano cyclotrimerization, and (j) nucleophilic substitution reaction on piperidine[156]

1.2.5 Hypercrosslinked Polymers (HCPs)

HCPs are microporous materials with diverse synthetic methods, easy functionalization, high surface area, and low cost reagents.[157] HCPs have a long history, the crosslinked polystyrene networks can be traced back to the 1930s.[158] Davankov and co-workers first introduced HCPs in 1970s studied microporous polystyrene gels with more extensive crosslinks than conventional crosslinked polystyrene.[159] Based on the concept of design microporous gels, adding extend the crosslinks resulted in a highly rigid and cross-linked network. Friedel-Crafts reaction can be used to prepare HCPs, which introduce a fast and efficient way to form strong linkages resulted in a highly crosslinked network. HCPs are normal made up by crosslinks and co-monomers in a brief and synthesised by dissolving co-monomers in suitable solvent for separation. Then crosslinks are added to form a network. After the solvent is removed, porous network come out with high surface areas.

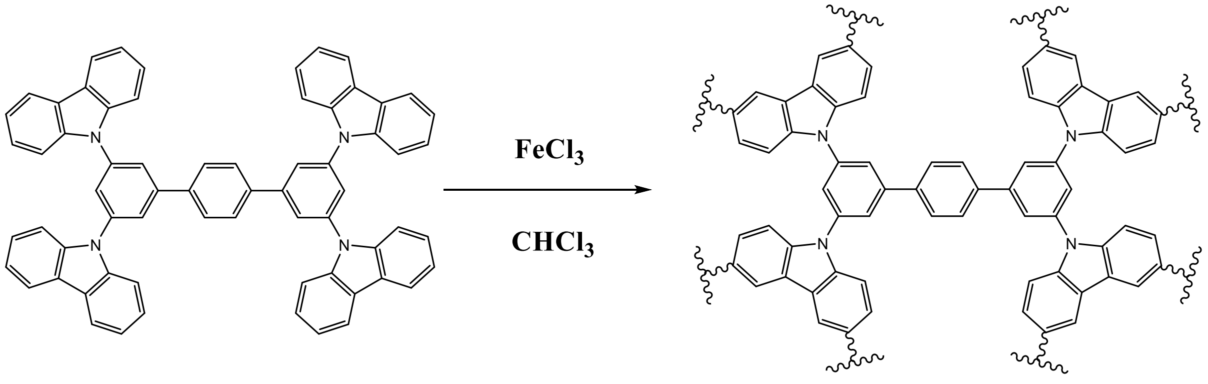

Cz-9 **CPOP-9**

Figure 1.6 Schematic representation of reactions for the synthesis of CPOP-9[160]

HCPs can be prepared by following methods, intermolecular and intramolecular crosslinking of preformed polymer chains[93,161,162], direct step growth polycondensation of suitable monomers[95,105,163], knitting aromatic compound polymers (KAPs) using external crosslinking[164–166]. The highest BET surface area reported by Chen and co-workers[160], they synthesised CPOP-9 by reacting Cz-9 with iron(III) chloride in anhydrous chloroform under nitrogen at room temperature overnight, resulting in a highly porous material with a BET surface area is about 2440 m^2g^{-1} (Figure 1.6).

The primary advantage of HCPs is that the knitting method lies in its versatility, as it allows for the generation of new products with different functional groups by simply varying the choice of monomer, although some functionalities are not compatible with the acid catalysts used. Further disadvantages of HCPs, include the need for stoichiometric amounts of catalyst.

1.2.6 Polymers of Intrinsic Microporosity (PIMs)

PIMs are linear polymer chains with rigid and contorted molecular structures in compared to other MOPs that contain networks of cross-linked covalent bonds. Due to its structure, PIMs have an inefficient packing structure, which introduces the microporosity, whilst maintaining solubility in common solvents.[167] Due to its ability to dissolve in the solvent, these materials have potential to be processed to robust films, coatings or fibres.

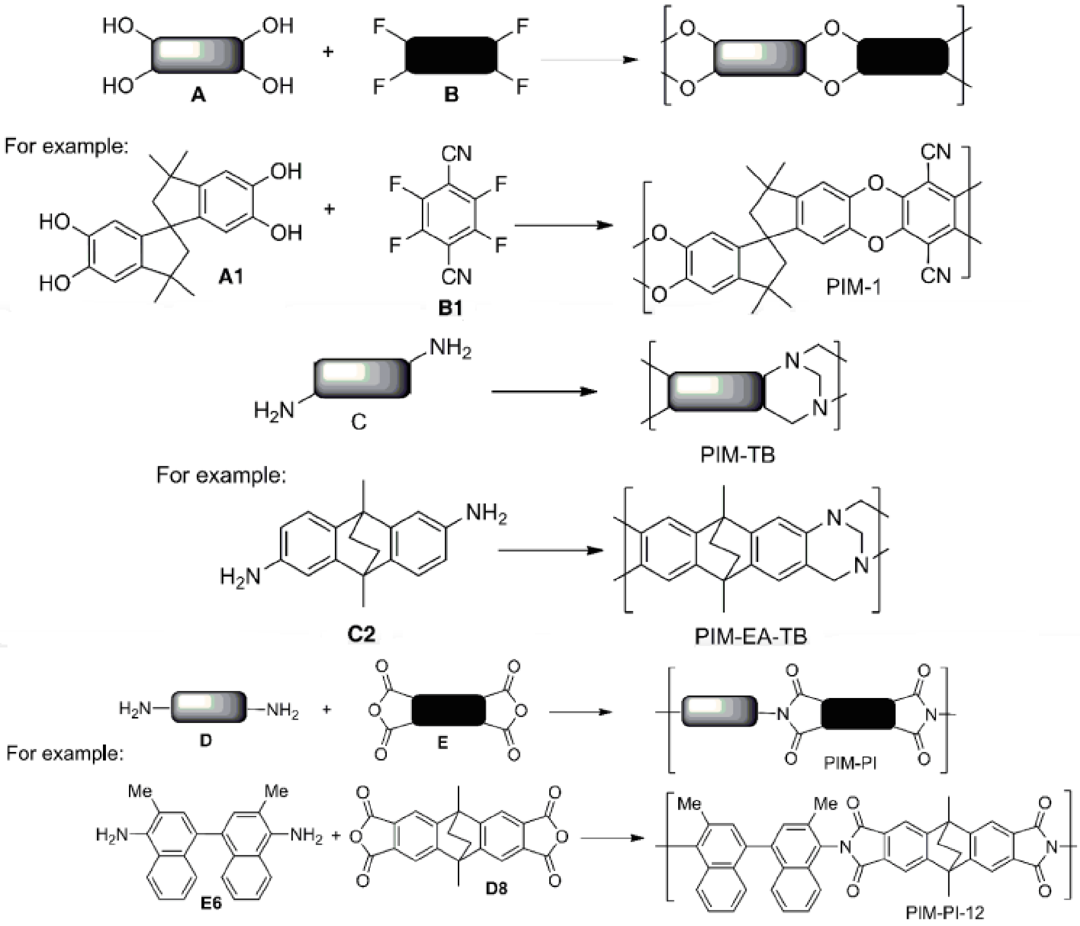

Figure 1.6 Schematic representation of reactions for the synthesis of PIMs: using dibenzodioxane formation, by using Tröger's base (TB) formation, using imide formation[167]

To 2017, these materials have three main types of preparation methods.[168] Kricheldorf et al.[169], Eastmond et al.[170], and Du et al.[171] used biscatechol and tetrahalide-containing monomer to form PIMs by using dibenzodioxane formation based nucleophilic aromatic substitution reaction. Carta and co-workers[172,173] used electrophilic aromatic substitution reaction between aromatic amine and formaldehyde or a formaldehyde proxy to form PIMs by using Tröger's base (TB) formation (Figure 1.7). Ghanem et al.[174,175] used diamine and dianhydride monomers to form PIMs by using imide formation. In addition, PIMs can be obtained by cross-coupling reactions[176], triazine formation[177], palladium-catalysed annulation[178], and stepwise nucleophilic substitution of octafluorocyclopentene[179]. The first PIM was reported in 2004 by Budd and co-workers[180]. They used 3,3,3′,3′-tetra-methyl-1,1″-spirobisindane-5,5′,6,6′-tetrol and 2,3,5,6-tetrafluorophthalonitrile with anhydrous K_2CO_3 in dry DMF under 65 °C for 72 h to form PIM-1. The largest BET surface area is reported by McKeown and co-workers[181], they used dibenzodioxane formation method to form Pc-network-PIM with the BET surface area is about 1000 m^2g^{-1}.

Unlike the network structures of COFs, CTFs, CMPs, PAFs and HCPs, one of the key advantages of PIMs is their solubility in certain organic solvents arising from their linear structures, which distinguishes them from other MOPs However, the use of specific monomers is essential for the successful synthesis of PIMs, limiting their applicability to those specific monomers.

1.3 Soluble Microporous Organic Polymers

One of the greatest challenges for MOPs is that most of them are limited to their applications to the solid state. This is primarily due to the highly rigid and cross-linked structure required to induce porosity. PIMs are one of class of MOP that has however found commercial success due to their solubility in a range of organic solvents which achieve the combination of high surface areas and solubility by using rigid and twisted linear polymer chains. There are however a limited number of these monomers which can be used to synthesise PIMs. To overcome this limitation, a number of strategies have been used to make network MOPs both highly porous and soluble. There are three main strategies to enhance the solution probability of MOPs.

1. The control of linear chains structure;
2. The control of molecular weight and size;
3. The addition of soluble groups.

1.3.1 Soluble Linear Porous Polymers

Linear porous polymer chain structures such as the strategy used in the synthesis of PIMs can lead to soluble porous polymers. As it is known, PIMs with linear and rigid molecular contorted structures can dissolve in organic solvents as discussed in Chapter 1.2.6. Other examples include Fu et al.[182] who reported a kind of soluble CMP, Azo-POP-7 which was synthesised by 9′-bis(4-aminophenyl)fluorene and 9,9-bis(4-hydroxyphenyl)fluorine through azo-coupling polymerisation (Figure 1.8). The Azo-POP-7 with BET surface area about 364 m^2 g^{-1} can dissolve in many solvents. The contorted monomers used in the synthesis of Azo-POP-7 improved the solubility of the resulting polyimide material.

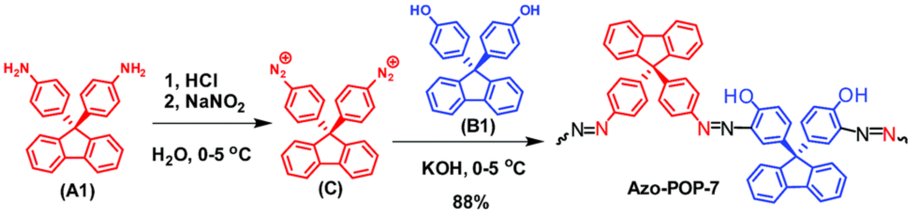

Figure 1.8 Synthesis of Azo-POP-7 by azo-coupling of A1-derived dual diazonium reagent C with bisphenol B1[182]

1.3.2 Solubility by Controlling Size and Shape

The control of molecular weight and size is another strategy to produce soluble particles. Yang and co-workers[183] employed a high dilution method to synthesise solution-processable HCPs. They dissolved the linear polystyrene (PS) in a large quantity of the (toxic) solvent 1,2-dichloroethane (DCE) through intramolecular crosslinking to yield individually crosslinked polymer chains with BET surface areas up to 724 m^2 g^{-1} which can be solution processed (Figure 1.9). The low concentration of PS in the solvent reduces the density of crosslinking units and improves solubility.

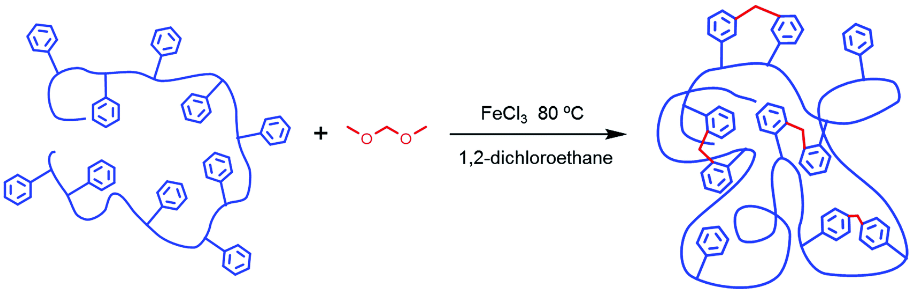

Figure 1.9 Synthesis of soluble HCPs[183]

Cheng et al.[176] reported on a type of soluble CMPs (SCMPs) produced through hyperbranching, which can dissolve in common organic solvents. SCMP-1 was synthesised using a one-pot (A_4+B_2)-type Suzuki coupling reaction with 1,3,6,8-tetrabromopyrene and 1,3-dibromo-7-tert-butylpyrene, resulting in a material with a BET surface area of 505 m^2 g^{-1} (Figure 1.10). The addition of B_2 monomers in the synthesis process appears to limit the growth of the network, while the alkyl parts of the B_2 monomers were found to enhance the solubility of the material.

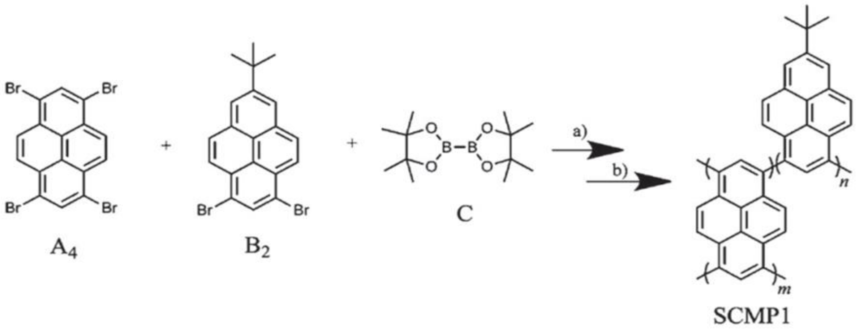

Figure 1.10 Synthesis of soluble SCMP-1[185]

Bandyopadhyay[185] and co-workers reported a series solution processable were produced through the Sonogashira reaction of tetraphenyl-5,5-dioctylcyclopentadiene (TBDC) and 1,4-

diethynylbenzene at varying temperatures and reaction times. P1 was synthesised using conventional Sonogashira reaction and was insoluble, while P2 was prepared with less catalysis and a shorter reaction time than P1, and P3 was synthesised using an emulsion reaction (Figure 1.12). Both P2 and P3 were found to be soluble in common organic solvents, with BET surface areas of 39 $m^2\ g^{-1}$ and 143 $m^2\ g^{-1}$ respectively (Figure 1.11). The emulsion reaction is introduced, which is due to control the polymer size.

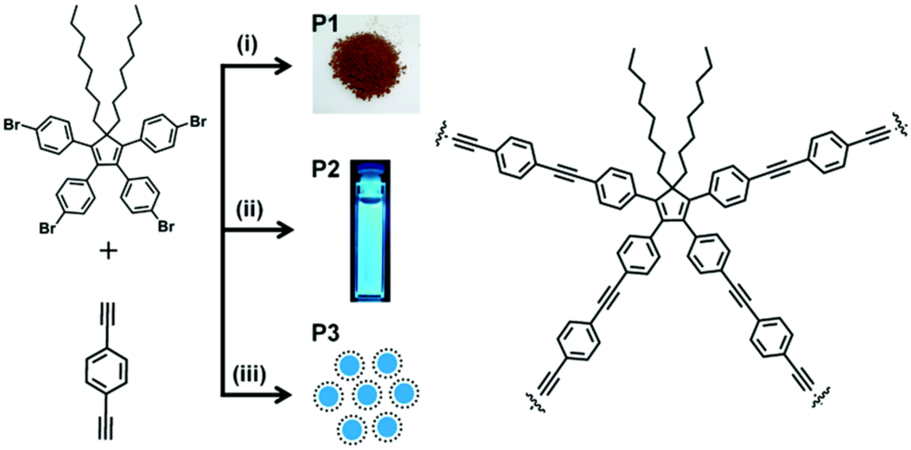

Figure 1.11 Synthesis of soluble SCMP. Reaction conditions: P1 (i) [Pd(PPh$_3$)$_4$], CuI, diisopropylamine, toluene, 80 °C, 48 h, P2 (ii) [Pd(PPh$_3$)$_2$Cl$_2$], CuI, diisopropylamine, toluene, 80 °C, 12 h and P3 (iii) [Pd(PPh$_3$)$_4$], CuI, SDS, water, toluene, 50 °C, 48 h[185]

Nano-reactors have been reported to form SCMPs with well-controlled particle sizes. Deng et al.[186,187] synthesised SCMP-1 by performing a Suzuki coupling reaction of 1,3,5-triiodobenzene and 1,4-phenylenediboronic acid within the channels of ordered mesoporous silica-supported carbon nano-membranes (nanoreactors) (Figure 1.12). The resulting SCMPs had particle sizes of 2.4 nm, 3.8 nm, and 5.4 nm. However, the permanent porosity of these materials was not confirmed.

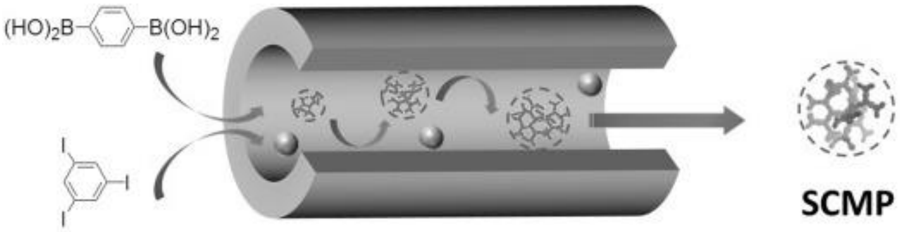

Figure 1.12 Size-controlled synthesis of SCMPs in a nanoreactor[186]

1.3.3 Solubility by Addition of Soluble Chains

The addition of soluble groups is another way to get soluble particles. The adding the long alkane chains to the monomer is the first way. Lim and co-workers[188] synthesised solution-processable PAFs, T-POP, by adding alkane-modified 1,7-dibromo-3,4,9,10-tetracarboxylic acid dianhydride and N-methylpyrrolidone (NMP) through an imidization reaction, resulting in a material with a BET surface area of approximately 25 m^2 g^{-1} (Figure 1.13). Using a similar approach, Pallavi et al.[189] used benzothiadiazole (BZ) instead of 1,4-diethynylbenzene with TBDC to form CzBDP with a BET surface areas about 180 m^2 g^{-1}. Similar to P3, CzBDP can also dissolve in common organic solvents. The alkyl parts of TBDC were found to limit the growth of particle size, while the alkane chains improved the solubility.

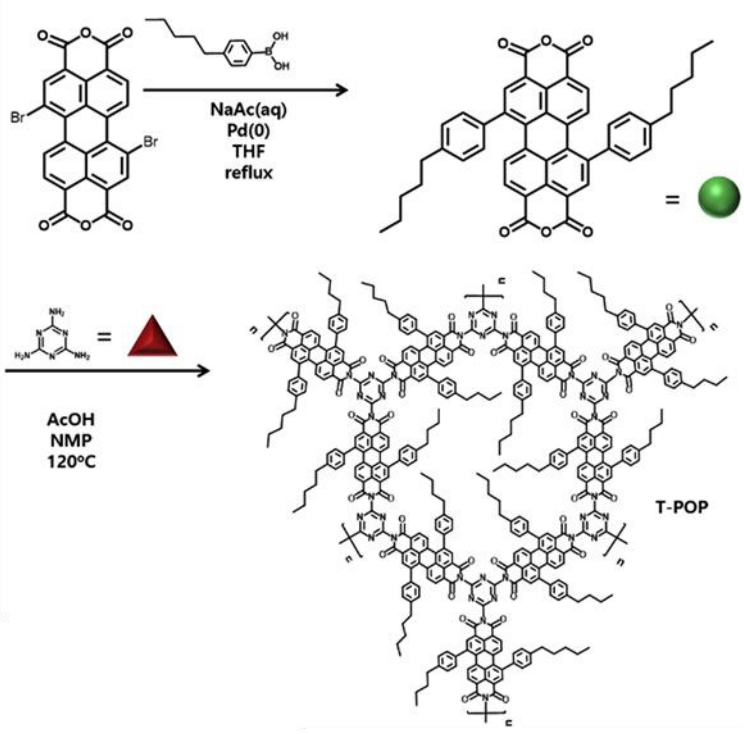

Figure 1.13 Synthesis of soluble PAFs[188]

Gifting the soluble group to the polymer is the second way. Mai and co-workers[190] reported water-dispersible microporous polymeric nanospheres with solubilising polymer chains. The nanoparticles were prepared via a surfactant-free emulsion polymerization process, using 4-chloromethylstyrene monomer and divinylbenzene pre-crosslinker for the first step, followed by normal Friedel-Crafts reaction for the second step. The surface of the nanoparticles was then modified with pH/temperature dual-responsive hydrophilic polymeric blocks via surface-initiated atom transfer radical polymerization (SI-ATRP) (Figure 1.14). This material exhibited good solubility and porosity, with BET surface area up to 562 m^2 g^{-1}. Similarly, Yu et al.[191] prepared pH/temperature dual-responsive hydrophilic nanoparticles using the same approach, and investigated their use as adsorbents for dispersive solid-phase extraction of fluoroquinolones from environmental water and food samples.

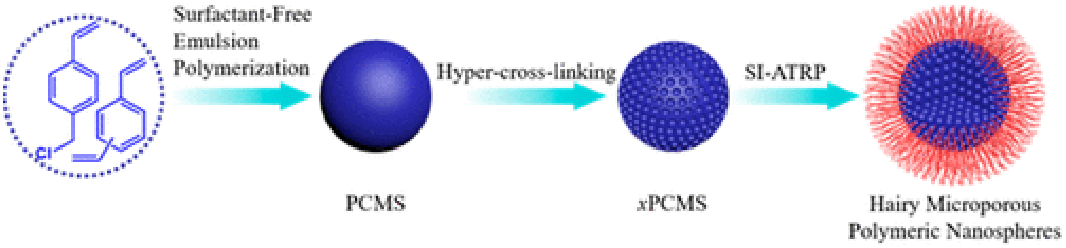

Figure 1.14 Fabrication of water-dispersible, responsive, and carbonizable hairy microporous polymeric nanospheres[192]

1.3.3.1 Porous Polymer Particles via RAFT-PISA

To overcome the use of large quantities of toxic solvents and multi-step syntheses, our group reported a one-pot synthetic approach to syntheses a kind of core-shell dispersible porous polymer particles (d-PPPs) using reversible addition fragmentation transfer polymerization induced self-assembly (RAFT-PISA) in 2019.[193] These particles were prepared by water soluble poly(ethylene glycol) (PEG) based marco-CTA shells with divinylbenzene (DVB) and fumaronitrile (FN) cores. The PEG based marco-CTA shells was prepared in the first step. Then, the white core-shell structure small particles are obtained by dissolving DVB, FN and PEG based marco-CTA with potassium persulfate (KPS) acted as initiator in the water and ethanol mixture solvent under nitrogen atmosphere and 70 °C for 24 hours (Figure 1.15). The particles can disperse in common organic solvent and have a dual morphology with smaller spheres structure of 24-29 nm diameter to aggregate to form larger particles of 204-262 nm diameter. This material have BET surface areas ranging from 274 to 409 $m^2\ g^{-1}$ and the internal pore diameter is around 1.8 nm. Due to the spherical packing of aggregates, this material not only contains microporous structure, but also have mersoporous and macroporous structures. In addition, the polymerisation doesn't contain any toxic solvent and metal catalysis compared to normal HCPs synthesis method which is friendly to the environment. Furthermore, this material undergoes photoluminescence (emission λ_{max} = 326 nm) when exposed to UV light and can be quenched by the addition of nitroaromatic compounds which makes this material used as chemosensor.

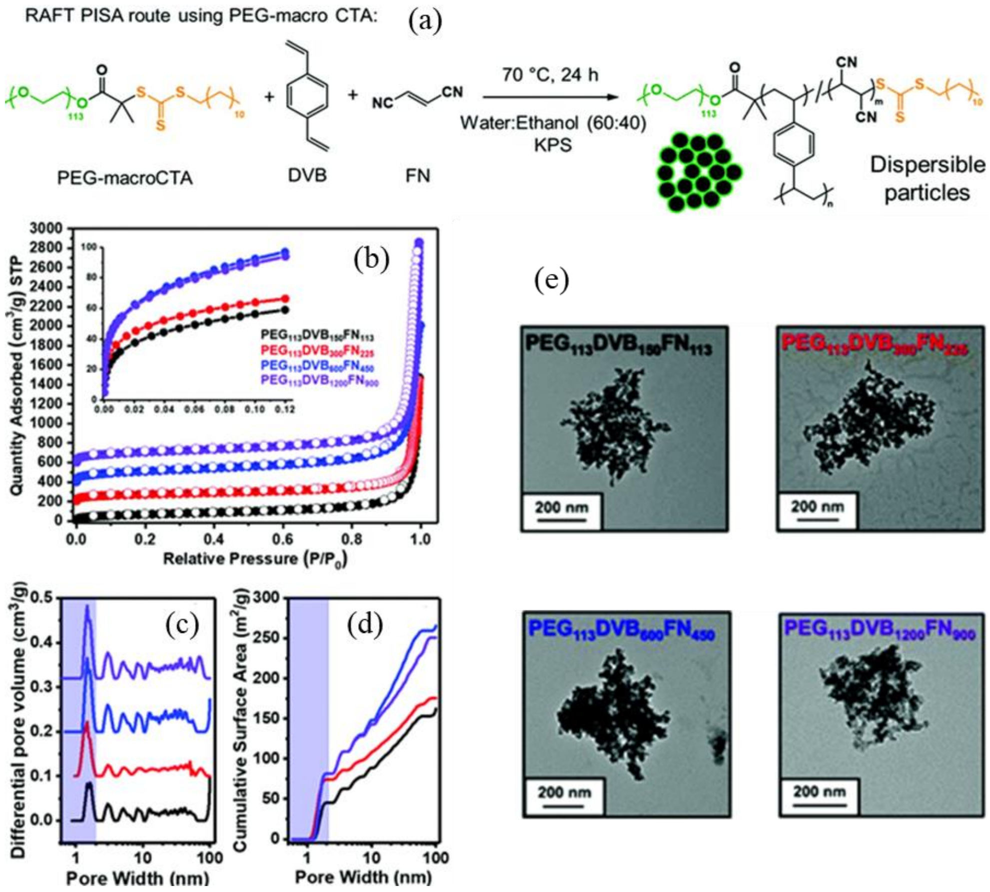

Figure 1.15 (a) Synthesis of porous materials via RAFT mediated PISA; (b) Nitrogen adsorption isotherms; (c)Pore with distributions; (d) Cumulative surface area; (e) TEM images.[193]

Based on this strategy of synthesis of MOPs, Ferguson and co-workers reported a kind of d-PPPs with photocatalytic property for visible light-mediated production of pharmaceutically relevant compounds in multiple solvents in 2020.[194] The particles were prepared using the same approach as in our group's report but with the addition of a photocatalytic divinyl monomer and 4,7-bis(4-vinylphenyl)benzo[c][1,2,5]-thiadiazole (Figure 1.16 a). The resulting core-shell structure particles exhibited a dual morphology similar to our group's report, with smaller spheres that aggregated to form larger aggregates of 375 nm diameter, which can easily disperse in a range of solvents with low to high polarity (Figure 1.16 b). Gas sorption analysis showed the particles to have BET surface area of 288 m^2 g^{-1} with the pore sizes centred around 1.8 nm and further larger pores increasing from the sphere packing of the aggregates. Moreover, the additional photocatalytic functional group introduced the photocatalytic ability to this material. This material was studied of three different photocatalytic conversion in water, acetonitrile and toluene under blue light irradiation ($\lambda = 460$ nm), such as (1) photocatalytic 2-phenylbenzimidazole synthesis though 1,2-benzenediamine and benzyl alcohol; (2) photocatalytic sulfide oxidation of methyl phenyl sulfide or diphenyl sulfide and the selectivity of monoxide or dioxide compound; (3) photocatalytic sulfoxide formation from aniline and sodium p-toluenesulfinate (Figure 1.15 c,d,e).

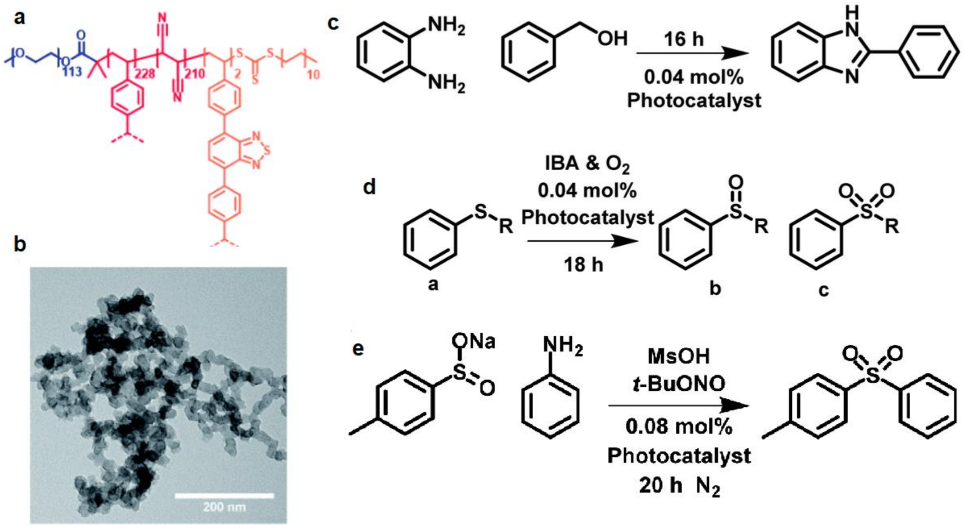

Figure 1.16 (a) Structure; (b) TEM image; (c) Photocatalytic benzimidazole synthesis; (d) Photocatalytic sulfide oxidation; (e) Photocatalytic sulfoxide formation from aniline and sulfonate salts[194]

In 2020, James et al. [194] developed a photocatalytic divinyl monomer that was introduced into the core segments of the particles during polymerisation, our group reported a kind of d-PPPs with efficient and tunable white-light emission in the same year.[195] According to our previous study, FN was used as a comonomer with DVB to produce d-PPPs. Although effective, FN is not easily functionalised, so further applications or post-synthetic modification (PSM) of this material are very limited. The acrylic acid (AA) was investigated as its potential scope for further PSM. The classical d-PPPs was prepared following the same way by adding water soluble PEG based marco-CTA, DVB and AA with KPS in the water and ethanol mixture solvent under nitrogen atmosphere and 80 °C for 24 hours (Figure 1.16 a). Then, the PSM was carried out by dissolving 9-anthracenemethanol, N,N'-dicyclohexylcarbodiimide (DCC), 4-dimethylaminopyridine (DMAP) with classical d-PPPs in THF under room temperature for 24 hours (Figure 1.17 a). The resulting material had a dual morphology, consisting of smaller sphere structures that aggregate to form larger aggregates with a diameter of around 870 nm, which is larger than classical d-PPPs (Figure 1.17 b, c). In addition, it can disperse in most organic solvent. Gas sorption analysis showed that the particles had a BET surface area of 188 $m^2\ g^{-1}$ and a mesoporous structure with the pore sizes centred around 3.0 nm and further larger pores. The postsynthetic modification of the anthracene aromatic groups from AA groups, which resulted in a white-light emitting dispersion with a quantum yield of 38% and commission internationale de l’éclairage coordinates of (X = 0.33, Y = 0.32) which is to the yellow-emitting fluorophore rhodamine B is encapsulated into its core by to the blue-emitting porous polymer (Figure 1.17 d, e, f).

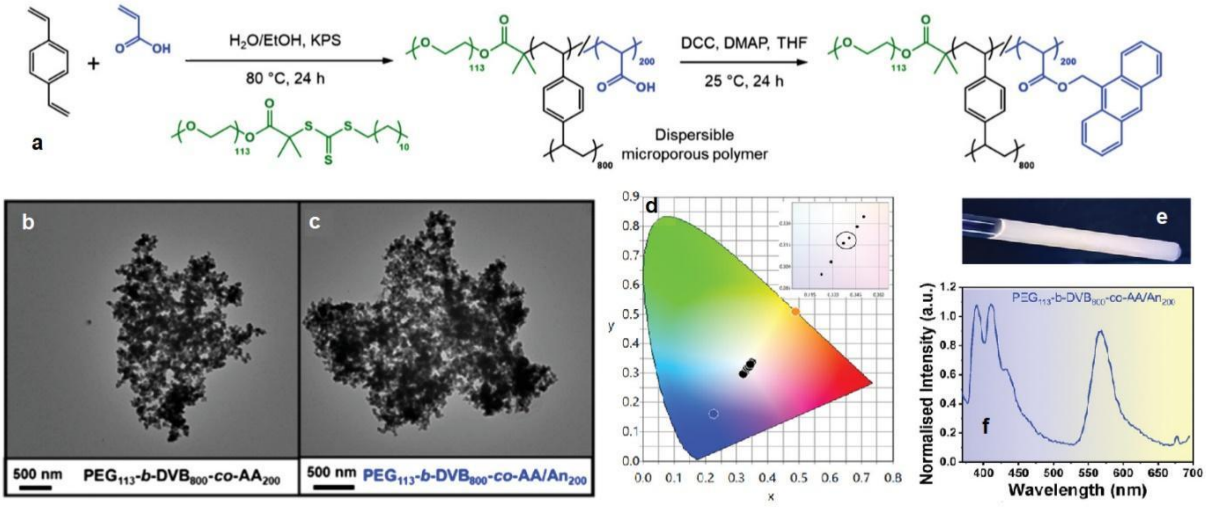

Figure 1.17 (a) Synthetic approach utilised to synthesise porous polymer dispersion and the postsynthetic modification; (b), (c) TEM image; (d) CIE plot showing the change in coordinates as more rhodamine B solution is added to the PEG$_{113}$-b-DVB$_{800}$-co-AA/An$_{200}$ dispersion. (e) Image of the white-light-emitting solution and fluorescence emission spectrum. (f) Normalised fluorescence emission profile of a 1 mg mL^{-1} dispersion of PEG$_{113}$-b-DVB$_{800}$-co-AA/An$_{200}$ and 1.63 ppm of rhodamine B in methanol[195]

Based on the previous work of Ferguson et al. [194] and James et al. [195] to adding photocatalytic functional group to the classical d-PPPs and to do further modification of the classical d-PPPs, respectively. Ivko and co-workers designed a carbonylation catalyst on d-PPPs for catalytic carbonylationin in 2022.[196] Similar to previous research in our group, the 4-vinylpyridine (4-VP) can be PSM by using iodomethane to generate a cationic support which can be used to bind *cis*-[Rh(CO)$_2$I$_2$]$^-$ electrostatically to instead of FN. The classical d-PPPs **1** was prepared following the same way by dissolving water soluble PEG based marco-CTA, DVB and 4-VP with KPS in the water and ethanol mixture solvent under nitrogen atmosphere and 80 °C for 24 hours. Then, the PSM compound **2** was carried out by dissolving iodomethane with compound **1** in chloroform stirring under 80 °C for 72 hours. Then the further PSM compound **3** was obtained by adding [Rh(CO)$_2$I]$_2$ with compound **2** in dry chloroform sonicating under nitrogen gas and room temperature for 16 hours (Figure 1.18 a). The particles can disperse in common organic solvent and have a dual morphology with smaller spheres structure of 25-34 nm diameter to aggregate to form larger aggregates of 190-340 nm diameter (Figure 1.18 d).

Gas sorption analysis showed the particles to have BET surface area of 114 $m^2\ g^{-1}$ and its micropore volume was 0.04 $cm^3\ g^{-1}$. Moreover, the PSM of 4-VP to form a cationic support which is used to bind cis-$[Rh(CO)_2I_2]^-$ electrostatically by adding iodomethane can allow heterogenisation of the anionic carbonylation catalyst via electrostatic interactions.

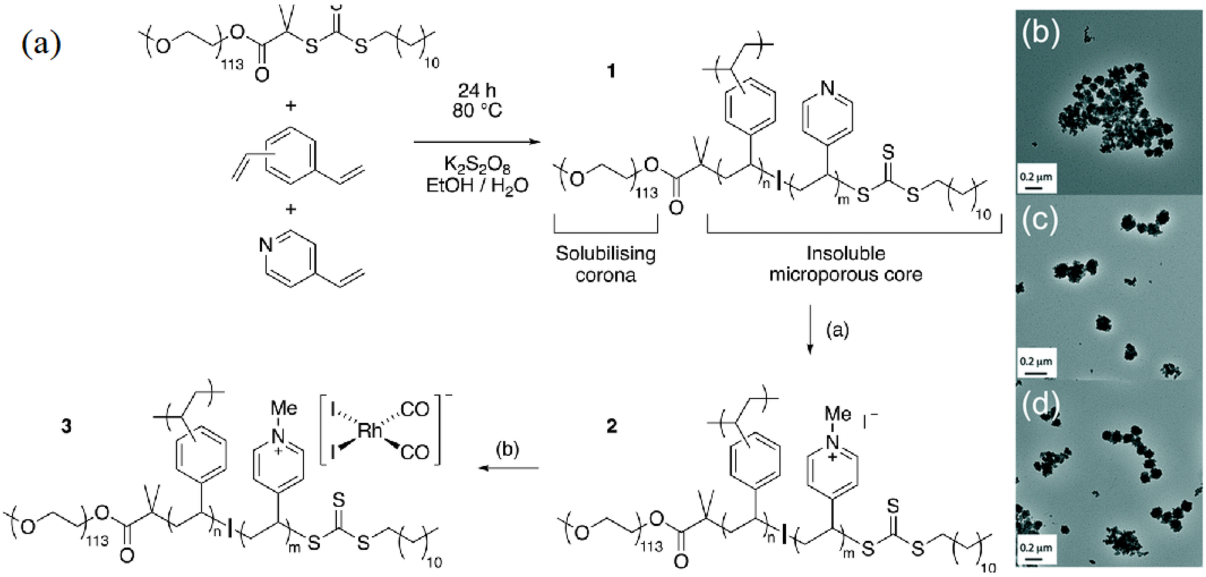

Figure 1.18 (a) Synthesis of pyridine-containing dispersible microporous polymer (**1**), post-synthetic *N*-methylation to form **2** and subsequent reaction with $[Rh(CO)_2I]_2$ to form **3**; (a) MeI in $CHCl_3$, 70 °C, 72 h; (b) $[Rh(CO)_2I]_2$ in $CHCl_3$, RT, 16 h. (b), (c), (d) TEM image of samples **1**, **2**, and **3**[196]

1.4 Background of RAFT-PISA and Stimuli-Responsive Materials

1.4.1 Reversible Addition-Fragmentation Chain-Transfer (RAFT) Polymerisation

Reversible-deactivation radical polymerisation (RDRP) has gained significant attention in recent due to its ability to synthesise a diverse range of polymers with various functionalities, structures, and morphologies. Among the RDRPs, reversible addition-fragmentation chain transfer (RAFT) polymerisation is a popular method that offers greater convenience for synthesizing block structures. Unlike atom transfer radical polymerisation (ATRP) [197], and nitroxide-mediated polymerisation (NMP)[198], RAFT polymerisation controls the polymerisation mechanism by equilibrating propagating species and dormant species through a chain transfer process. This process is facilitated by a thiocarbonylthio chain transfer agent (RAFT agent or CTA) that serves as a mediator for the reversible chain-transfer process. Commonly used RAFT agents include thiocarbonylthio compounds such as dithioesters (Z=C), dithiocarbamates (Z=N), trithiocarbonates (Z=S), and xanthates (Z=O), which enable polymerisation through the addition of monomer units between the S-R bond of the CTA to form polymers. As a result, most polymer chains feature a thiocarbonylthio end-group for RAFT polymerisation, and the overall process resembles the addition of monomer units to form a polymer (Figure 1.19).

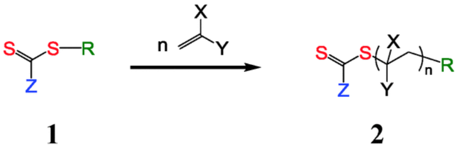

Figure 1.19 Overall outcome of the RAFT process

The structure of CTA is shown above where the C=S double bond is reactive site; the Z is radical retaining group, and the R is a radical leaving group. The selection of Z-group and R-group is crucial for the synthesis of block copolymers by RAFT polymerisation. The Z-group should appropriate for both monomers and exhibit sufficient reactivity of the C=S bond towards the incoming radical, while stabilising the radical. The R-group must act as a good homolytic leaving group that respects the propagating radical of the second monomer and reinitiates polymerisation in a rapid and quantitative manner.[199] The mechanism of RAFT polymerisation is similar to other conventional free radical polymerisations, consisting of initiation, re-initiation, and termination steps. The polymer chains are initiated by the initiator, followed by the addition of a propagating radical (P_n•) to the CTA. The fragmentation of the intermediate radical produces a macro-CTA and a new radical R• at the beginning. The generated radical R• then reacts with the monomer to form a new radical (P_m•). A rapid equilibrium between the active propagating radicals (P_n• and P_m•) and the dormant macro-CTA chains provides an equal probability for all chains to grow with the same length. At the end, most of the chains bear the RAFT end-group and can be isolated and manipulated as stable products (Figure 1.20).[199]

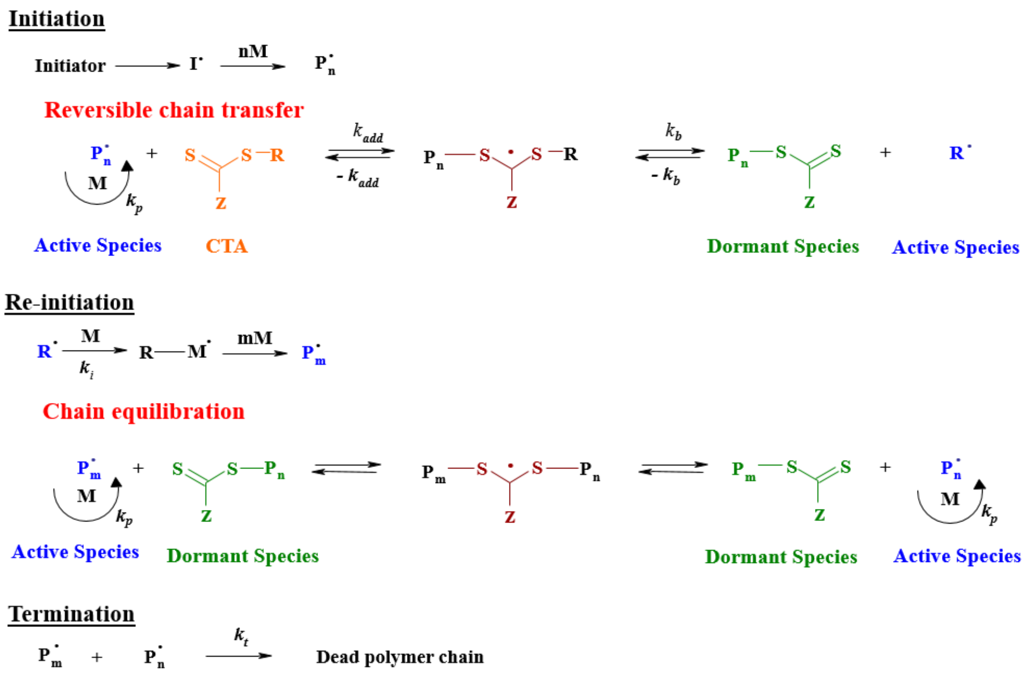

Figure 1.20 Mechanism of RAFT polymerisation[200]

1.4.2 Radical Addition Fragmentation Transfermediated Polymerisation Induced Self-Assembly (RAFT mediated PISA)

Polymerisation-induced self-assembly (PISA) represent an efficient method for the controlled synthesis of block copolymers with specific size and morphology.[201] This process typically involves two steps, a hydrophilic homopolymer (A) is initially synthesised using a suitable CTA via RAFT. Subsequently, a hydrophobic monomer (B) is added using RAFT polymerisation, resulting in the formation of a copolymer. As the block (B) grows, the copolymer gradually becomes insoluble, leading to in situ self-assembly and the formation of AB diblock copolymer nano-objects. This can be explained as follows, as the block (B) increasing, the copolymer becomes hydrophobic. Based on the thermodynamics, the entropy term (ΔS) decreases as due to the water molecules become order status from unordered status. This is due to the fact that the water molecules are distorted by the presence of the hydrophobic segments form the new hydrogen bonds among the hydrophobic segments as an ice-like cage structure called a clathrate cage. Moreover, the temperature is not changed and ΔH is unknown but small. According to Gibbs equation $\Delta G = \Delta H - T\Delta S$, the free energy of the system (ΔG) is positive. As to decrease the ΔG, the hydrophobic segments aggregate together and let the hydrophilic segments face to the water molecules, which can decrease the order status of water molecules around the particle and increase the ΔS of water molecules. Therefore, the self-assembled structure is formed. By adjusting the monomer ratio, different morphologies such as spheres, worms, and vesicles can be obtained (Figure 1.21). The morphology can be also be predicted as the molecular packing parameter (P). Based on the equation $P = V_0 / (a \cdot l_0)$, which the V_0 and l_0 are the hydrophobic segment volume and length, while the a is hydrophilic segment area. Therefore, with the hydrophobic segments growing, the particle morphology changes from sphere, worm and vesicle. Furthermore, as the packing parameter increases, there is a transition in morphology from highly curved assemblies to less curved structures. The use of RAFT-PISA also affords excellent control over molecular weight, particle size and morphology, providing a number of advantages for the synthesis of block copolymers.

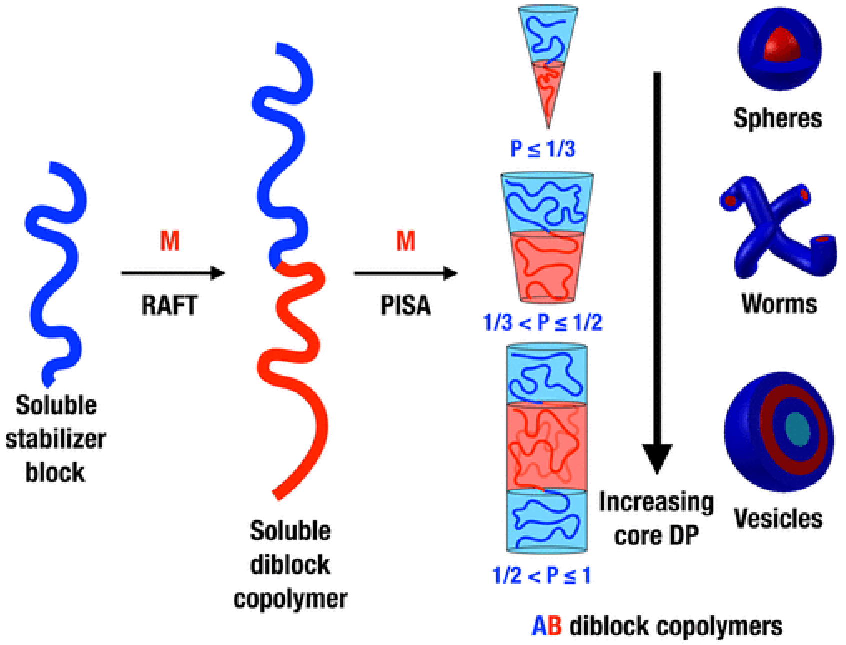

Figure 1.21 Schematic of the Synthesis of Diblock Copolymer Nano-Objects via Polymerisation-Induced Self-Assembly (PISA)[201]

Depending on the chemical composition of the stabiliser block, the surface wettability of particles may vary. Two aqueous polymerisation can be employed to generate particles with different morphologies.[202,203] Such as RAFT aqueous dispersion polymerisation can be used to synthesise spheres, worms, or vesicles with nonionic, zwitterionic, anionic, or cationic character. While, RAFT aqueous emulsion polymerisation can produce spheres with non-ionic, anionic, or cationic character (Figure 1.22).

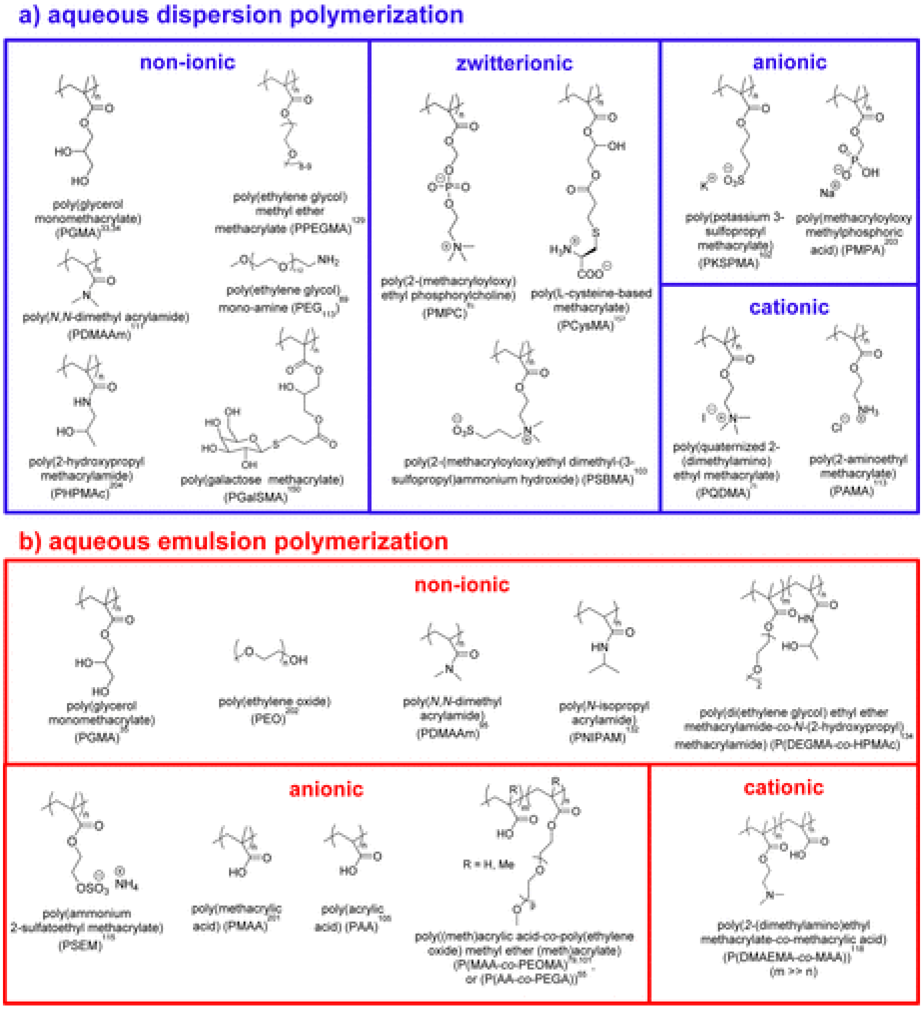

Figure 1.22 Chemical structures of various types of steric stabiliser blocks utilised for (a) RAFT-mediated aqueous dispersion polymerisation and (b) RAFT-mediated aqueous emulsion polymerisation[201]

1.4.3 Stimulus-responsive materials

Stimulus- responsive materials have garnered significant attention from scientists due to their dynamically alterable properties. Among these materials, pH- responsive polymers exhibit reversible changes in solubility, volume, configuration, and conformation in response to variations in pH.[204] This reversible phenomenon is due to alterations in ionic interactions, hydrogen bonding, and hydrophobic interactions upon pH adjustment, leading to microphase separation or self-assembly. These polymers can be classified based on the presence of acidic groups (like poly(carboxylic acid)s), basic groups (which containing tertiary amine groups or pyridine/imidazole groups, etc.) or be made from naturally occurring functional groups (such as aliginic acid, chitosan, etc.).[205] Baines et al.[206] reported a water soluble hydrophilic hydrophobic block copolymers with pH-responsive. The PDMA-b-PMMA which the PMMA block introduces the hydrophobic property and the PDMA block imparts the hydrophilic property with pH-responsive. This material forms micelles in an acidic condition (pH=2.5). However, a basic condition (pH=9.5), the micelle size increases, leading to precipitation.

Thermo-responsive polymers, like pH- responsive polymer, exhibit reversible changes in phase or volume. The thermos-responsive polymers display a temperature-dependent miscibility or solubility gap in aqueous solution, which can be observed in a phase diagram of temperature versus polymer fractional volume. Due to hydrophobic interactions between polymer chains, the phase separation occurs, resulting in the self-assemble and aggregate of polymers in aqueous solutions There are three types of thermo-responsive polymers.

LCST-type polymers display the characteristic of chain aggregation and precipitation above the LCST temperature, whereas below the LCST temperature, the polymer chains become fully hydrated. This temperature at which the polymer solution undergoes a phase transition from a clear to a cloudy state is also known as the cloud point, and is often denoted as LCST.[207] Several examples of LCST-type polymers include those containing isopropyl groups with carboxyl groups (2-carboxylisopropylacrylamide, CIPAAm)[208], amide groups (2-aminoisopropylacrylamide, AIPAAm)[209], or hydroxyl group (2-hydroxyisopropylacrylamide, HIPAAm)[210] are the examples for LCST-type polymers (Figure 1.23). Conversely, UCST-type polymers show the opposite behaviour to LCST-type polymers, in that they are homogeneous and transparent below the LCST and heterogeneous and opaque below the UCST.[211] Examples of UCST-type polymers include polyacrylamide (PAAm)[212] and polyacrylic acid (PAAc)[213] show the same trend (Figure 1.23). In contrast, shape memory polymers (SMPs) are a unique class of thermo-responsive polymers that differ from LCST- or UCST-type polymers. The elasticity of SMPs changes in response to temperature fluctuations above their glass transition temperature (T_g) or their melting temperature (T_m), depending on the mobility of bulk amorphous or crystal, respectively.[214]

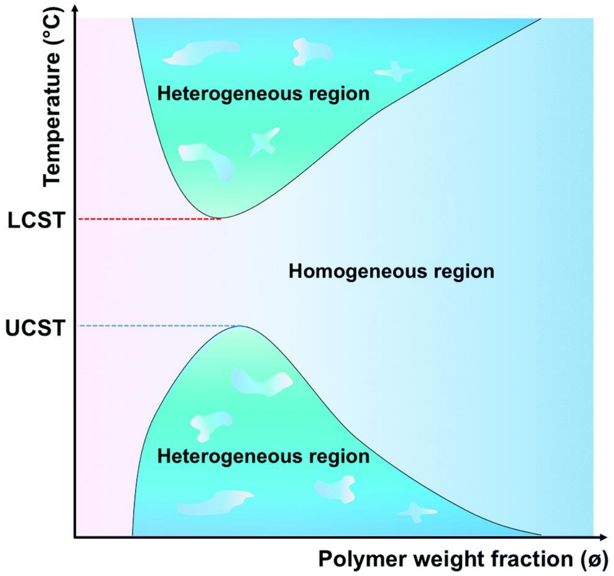

Figure 1.23 Phase diagrams of LCST- and UCST-type polymer aqueous solutions (temperature versus polymer weight fraction)[207]

1.5 Aims

The Dawson group have published a number of papers of RAFT-PISA porous polymer particles, however all of these materials use PEG as the outer solubilising shell. The aim of this thesis is therefore to investigate the use of other solubilising shells to synthesise these materials with stable small particle size (100-600 nm) and good surface area (300~ m^2 g^{-1}). Chapter 3 looks at the use of poly(acrylic acid) shells and maps out the conditions for this water soluble outer shell polymer chain., While simply changing the outer shell is of interest to broaden the scope of usable monomers and polymers, the possibly to radically change the properties of the particles by simply changing the outer shell is of interest, as such chapter 4 looks at pH responsive shells while chapter 5 looks at temperature responsive shells. Chapter 6 looks at the investigation of mixed shells with the aim to increase the surface areas. By introducing responsive outer shells it should be possible produce particles with switch-on/switch-off dispersibility which could be of interest to develop new applications for porous polymers.

1.6 References

(1) Chaisuwan, T. Chapter 26 - Porous Materials from Polybenzoxazine. In *Handbook of Benzoxazine Resins*; Ishida, H., Agag, T., Eds.; Elsevier: Amsterdam, 2011; pp 457–468. https://doi.org/10.1016/B978-0-444-53790-4.00071-0.

(2) Bruce, D. W.; O’Hare, D.; Walton, R. I. *Porous Materials*; John Wiley & Sons, Incorporated: Hoboken, UNITED KINGDOM, 2010.

(3) James, A. M. Microporous Polymers Tailored For Applications in Solution and Sustainability. phd, University of Sheffield, 2019. https://etheses.whiterose.ac.uk/25953/

(4) Alghamdi, N. Zeolites as Sensitizers in Water-Gated Thin Film Transistors Sensors. phd, University of Sheffield, 2021. https://etheses.whiterose.ac.uk/28529/ (accessed 2022-12-16).

(5) Li, Y. and Yu, J. New Stories of Zeolite Structures: Their Descriptions, Determinations, Predictions, and Evaluations. | *Chem. Rev.* **2014**, *114* (14), 7268–7316 https://pubs.acs.org/doi/10.1021/cr500010r.

(6) McCusker, L. B.; Liebau, F.; Engelhardt, G. Nomenclature of Structural and Compositional Characteristics of Ordered Microporous and Mesoporous Materials with Inorganic Hosts(IUPAC Recommendations 2001). *Pure Appl. Chem.* **2001**, *73* (2), 381–394. https://doi.org/10.1351/pac200173020381.

(7) Dapsens, P. Y.; Mondelli, C.; Pérez-Ramírez, J. Design of Lewis-Acid Centres in Zeolitic Matrices for the Conversion of Renewables. *Chem. Soc. Rev.* **2015**, *44* (20), 7025–7043. https://doi.org/10.1039/C5CS00028A.

(8) Li, Y.; Li, L.; Yu, J. Applications of Zeolites in Sustainable Chemistry. *Chem* **2017**, *3* (6), 928–949. https://doi.org/10.1016/j.chempr.2017.10.009.

(9) Dusselier, M.; Van Wouwe, P.; Dewaele, A.; Jacobs, P. A.; Sels, B. F. Shape-Selective Zeolite Catalysis for Bioplastics Production. *Science* **2015**, *349* (6243), 78–80. https://doi.org/10.1126/science.aaa7169.

(10) Gumidyala, A.; Wang, B.; Crossley, S. Direct Carbon-Carbon Coupling of Furanics with Acetic Acid over Brønsted Zeolites. *Sci. Adv.* **2016**, *2* (9), e1601072. https://doi.org/10.1126/sciadv.1601072.

(11) Holm, M. S.; Saravanamurugan, S.; Taarning, E. Conversion of Sugars to Lactic Acid Derivatives Using Heterogeneous Zeotype Catalysts. *Science* **2010**, *328* (5978), 602–605. https://doi.org/10.1126/science.1183990.

(12) Pacheco, J. J.; Davis, M. E. Synthesis of Terephthalic Acid via Diels-Alder Reactions with Ethylene and Oxidized Variants of 5-Hydroxymethylfurfural. *Proc. Natl. Acad. Sci.* **2014**, *111* (23), 8363–8367. https://doi.org/10.1073/pnas.1408345111.

(13) De Clercq, R.; Dusselier, M.; Christiaens, C.; Dijkmans, J.; Iacobescu, R. I.; Pontikes, Y.; Sels, B. F. Confinement Effects in Lewis Acid-Catalyzed Sugar Conversion: Steering Toward Functional Polyester Building Blocks. *ACS Catal.* **2015**, *5* (10), 5803–5811. https://doi.org/10.1021/acscatal.5b01344.

(14) Mielby, J.; Abildstrøm, J. O.; Wang, F.; Kasama, T.; Weidenthaler, C.; Kegnæs, S. Oxidation of Bioethanol Using Zeolite-Encapsulated Gold Nanoparticles. *Angew. Chem.* **2014**, *126* (46), 12721–12724. https://doi.org/10.1002/ange.201406354.

(15) Wang, C.; Wang, L.; Zhang, J.; Wang, H.; Lewis, J. P.; Xiao, F.-S. Product Selectivity Controlled by Zeolite Crystals in Biomass Hydrogenation over a Palladium Catalyst. *J. Am. Chem. Soc.* **2016**, *138* (25), 7880–7883. https://doi.org/10.1021/jacs.6b04951.

(16) Kaur, B.; Srivastava, R.; Satpati, B. Highly Efficient CeO2 Decorated Nano-ZSM-5 Catalyst for Electrochemical Oxidation of Methanol. *ACS Catal.* **2016**, *6* (4), 2654–2663. https://doi.org/10.1021/acscatal.6b00525.

(17) Han, W.; Yeung, K. L. Confined PFSA– Zeolite Composite Membrane for Self-Humidifying Fuel Cell. *Chem. Commun.* **2011**, *47* (28), 8085–8087. https://doi.org/10.1039/C1CC12081F.

(18) Huang, W.; Zhang, S.; Tang, Y.; Li, Y.; Nguyen, L.; Li, Y.; Shan, J.; Xiao, D.; Gagne, R.; Frenkel, A. I.; Tao, F. (Feng). Low-Temperature Transformation of Methane to Methanol on Pd1O4 Single Sites Anchored on the Internal Surface of Microporous Silicate. *Angew. Chem.* **2016**, *128* (43), 13639–13643. https://doi.org/10.1002/ange.201604708.

(19) Grundner, S.; Markovits, M. A. C.; Li, G.; Tromp, M.; Pidko, E. A.; Hensen, E. J. M.; Jentys, A.; Sanchez-Sanchez, M.; Lercher, J. A. Single-Site Trinuclear Copper Oxygen Clusters in Mordenite for Selective Conversion of Methane to Methanol. *Nat. Commun.* **2015**, *6* (1), 7546. https://doi.org/10.1038/ncomms8546.

(20) Wang, N.; Sun, Q.; Bai, R.; Li, X.; Guo, G.; Yu, J. In Situ Confinement of Ultrasmall Pd Clusters within Nanosized Silicalite-1 Zeolite for Highly Efficient Catalysis of Hydrogen Generation. *J. Am. Chem. Soc.* **2016**, *138* (24), 7484–7487. https://doi.org/10.1021/jacs.6b03518.

(21) Krönauer, A.; Lävemann, E.; Brückner, S.; Hauer, A. Mobile Sorption Heat Storage in Industrial Waste Heat Recovery. *Energy Procedia* **2015**, *73*, 272–280. https://doi.org/10.1016/j.egypro.2015.07.688.

(22) Krajnc, A.; Varlec, J.; Mazaj, M.; Ristić, A.; Logar, N. Z.; Mali, G. Superior Performance of Microporous Aluminophosphate with LTA Topology in Solar-Energy Storage and Heat Reallocation. *Adv. Energy Mater.* **2017**, *7* (11), 1601815. https://doi.org/10.1002/aenm.201601815.

(23) Ristić, A.; Logar, N. Z.; Henninger, S. K.; Kaučič, V. The Performance of Small-Pore Microporous Aluminophosphates in Low-Temperature Solar Energy Storage: The Structure–Property Relationship. *Adv. Funct. Mater.* **2012**, *22* (9), 1952–1957. https://doi.org/10.1002/adfm.201102734.

(24) Yu, N.; Wang, R. Z.; Wang, L. W. Sorption Thermal Storage for Solar Energy. *Prog. Energy Combust. Sci.* **2013**, *39* (5), 489–514. https://doi.org/10.1016/j.pecs.2013.05.004.

(25) Lefebvre, D.; Tezel, F. H. A Review of Energy Storage Technologies with a Focus on Adsorption Thermal Energy Storage Processes for Heating Applications. *Renew. Sustain. Energy Rev.* **2017**, *67*, 116–125. https://doi.org/10.1016/j.rser.2016.08.019.

(26) Shang, J.; Li, G.; Singh, R.; Gu, Q.; Nairn, K. M.; Bastow, T. J.; Medhekar, N.; Doherty, C. M.; Hill, A. J.; Liu, J. Z.; Webley, P. A. Discriminative Separation of Gases by a “Molecular Trapdoor” Mechanism in Chabazite Zeolites. *J. Am. Chem. Soc.* **2012**, *134* (46), 19246–19253. https://doi.org/10.1021/ja309274y.

(27) Pera-Titus, M. Porous Inorganic Membranes for CO2 Capture: Present and Prospects. *Chem. Rev.* **2014**, *114* (2), 1413–1492. https://doi.org/10.1021/cr400237k.

(28) Wei, J.; Ge, Q.; Yao, R.; Wen, Z.; Fang, C.; Guo, L.; Xu, H.; Sun, J. Directly Converting CO2 into a Gasoline Fuel. *Nat. Commun.* **2017**, *8* (1), 15174. https://doi.org/10.1038/ncomms15174.

(29) Gao, P.; Li, S.; Bu, X.; Dang, S.; Liu, Z.; Wang, H.; Zhong, L.; Qiu, M.; Yang, C.; Cai, J.; Wei, W.; Sun, Y. Direct Conversion of CO2 into Liquid Fuels with High Selectivity over a Bifunctional Catalyst. *Nat. Chem.* **2017**, *9* (10), 1019–1024. https://doi.org/10.1038/nchem.2794.

(30) Guo, P.; Shin, J.; Greenaway, A. G.; Min, J. G.; Su, J.; Choi, H. J.; Liu, L.; Cox, P. A.; Hong, S. B.; Wright, P. A.; Zou, X. A Zeolite Family with Expanding Structural

Complexity and Embedded Isoreticular Structures. *Nature* **2015**, *524* (7563), 74–78. https://doi.org/10.1038/nature14575.
(31) Meng, Y.; Genuino, H. C.; Kuo, C.-H.; Huang, H.; Chen, S.-Y.; Zhang, L.; Rossi, A.; Suib, S. L. One-Step Hydrothermal Synthesis of Manganese-Containing MFI-Type Zeolite, Mn–ZSM-5, Characterization, and Catalytic Oxidation of Hydrocarbons. *J. Am. Chem. Soc.* **2013**, *135* (23), 8594–8605. https://doi.org/10.1021/ja4013936.
(32) Barakat, T.; Rooke, J. C.; Tidahy, H. L.; Hosseini, M.; Cousin, R.; Lamonier, J.-F.; Giraudon, J.-M.; De Weireld, G.; Su, B.-L.; Siffert, S. Noble-Metal-Based Catalysts Supported on Zeolites and Macro-Mesoporous Metal Oxide Supports for the Total Oxidation of Volatile Organic Compounds. *ChemSusChem* **2011**, *4* (10), 1420–1430. https://doi.org/10.1002/cssc.201100282.
(33) Paolucci, C.; Khurana, I.; Parekh, A. A.; Li, S.; Shih, A. J.; Li, H.; Di Iorio, J. R.; Albarracin-Caballero, J. D.; Yezerets, A.; Miller, J. T.; Delgass, W. N.; Ribeiro, F. H.; Schneider, W. F.; Gounder, R. Dynamic Multinuclear Sites Formed by Mobilized Copper Ions in NOx Selective Catalytic Reduction. *Science* **2017**, *357* (6354), 898–903. https://doi.org/10.1126/science.aan5630.
(34) Kwak, J. H.; Tonkyn, R. G.; Kim, D. H.; Szanyi, J.; Peden, C. H. F. Excellent Activity and Selectivity of Cu-SSZ-13 in the Selective Catalytic Reduction of NOx with NH3. *J. Catal.* **2010**, *275* (2), 187–190. https://doi.org/10.1016/j.jcat.2010.07.031.
(35) Zhang, R.; Liu, N.; Lei, Z.; Chen, B. Selective Transformation of Various Nitrogen-Containing Exhaust Gases toward N2 over Zeolite Catalysts. *Chem. Rev.* **2016**, *116* (6), 3658–3721. https://doi.org/10.1021/acs.chemrev.5b00474.
(36) Thanh Pham, T. C.; Docao, S.; Chul Hwang, I.; Kyung Song, M.; Young Choi, D.; Moon, D.; Oleynikov, P.; Byung Yoon, K. Capture of Iodine and Organic Iodides Using Silica Zeolites and the Semiconductor Behaviour of Iodine in a Silica Zeolite. *Energy Environ. Sci.* **2016**, *9* (3), 1050–1062. https://doi.org/10.1039/C5EE02843D.
(37) Delkash, M.; Ebrazi Bakhshayesh, B.; Kazemian, H. Using Zeolitic Adsorbents to Cleanup Special Wastewater Streams: A Review. *Microporous Mesoporous Mater.* **2015**, *214*, 224–241. https://doi.org/10.1016/j.micromeso.2015.04.039.
(38) Daer, S.; Kharraz, J.; Giwa, A.; Hasan, S. W. Recent Applications of Nanomaterials in Water Desalination: A Critical Review and Future Opportunities. *Desalination* **2015**, *367*, 37–48. https://doi.org/10.1016/j.desal.2015.03.030.
(39) Jamali, S. H.; Vlugt, T. J. H.; Lin, L.-C. Atomistic Understanding of Zeolite Nanosheets for Water Desalination. *J. Phys. Chem. C* **2017**, *121* (21), 11273–11280. https://doi.org/10.1021/acs.jpcc.7b00214.
(40) Yuna, Z. Review of the Natural, Modified, and Synthetic Zeolites for Heavy Metals Removal from Wastewater. *Environ. Eng. Sci.* **2016**, *33* (7), 443–454. https://doi.org/10.1089/ees.2015.0166.
(41) Furukawa, H.; Cordova, K. E.; O'Keeffe, M.; Yaghi, O. M. The Chemistry and Applications of Metal-Organic Frameworks. *Science* **2013**, *341* (6149), 1230444. https://doi.org/10.1126/science.1230444.
(42) Dey, C.; Kundu, T.; Biswal, B. P.; Mallick, A.; Banerjee, R. Crystalline Metal-Organic Frameworks (MOFs): Synthesis, Structure and Function. *Acta Crystallogr. Sect. B Struct. Sci. Cryst. Eng. Mater.* **2014**, *70* (1), 3–10. https://doi.org/10.1107/S2052520613029557.
(43) Du, M.; Li, C.-P.; Zhao, X.-J. Metal-Controlled Assembly of Coordination Polymers with the Flexible Building Block 4-Pyridylacetic Acid (Hpya). *Cryst. Growth Des.* **2006**, *6* (1), 335–341. https://doi.org/10.1021/cg0502542.

(44) Yoo, Y.; Varela-Guerrero, V.; Jeong, H.-K. Isoreticular Metal−Organic Frameworks and Their Membranes with Enhanced Crack Resistance and Moisture Stability by Surfactant-Assisted Drying. *Langmuir* **2011**, *27* (6), 2652–2657. https://doi.org/10.1021/la104775d.

(45) Wang, C.-C.; Ying, J. Y. Sol−Gel Synthesis and Hydrothermal Processing of Anatase and Rutile Titania Nanocrystals. *Chem. Mater.* **1999**, *11* (11), 3113–3120. https://doi.org/10.1021/cm990180f.

(46) Lagashetty, A.; Havanoor, V.; Basavaraja, S.; Balaji, S. D.; Venkataraman, A. Microwave-Assisted Route for Synthesis of Nanosized Metal Oxides. *Sci. Technol. Adv. Mater.* **2007**, *8* (6), 484. https://doi.org/10.1016/j.stam.2007.07.001.

(47) Liang, W.; M. D'Alessandro, D. Microwave-Assisted Solvothermal Synthesis of Zirconium Oxide Based Metal–Organic Frameworks. *Chem. Commun.* **2013**, *49* (35), 3706–3708. https://doi.org/10.1039/C3CC40368H.

(48) Martinez Joaristi, A.; Juan-Alcañiz, J.; Serra-Crespo, P.; Kapteijn, F.; Gascon, J. Electrochemical Synthesis of Some Archetypical Zn2+, Cu2+, and Al3+ Metal Organic Frameworks. *Cryst. Growth Des.* **2012**, *12* (7), 3489–3498. https://doi.org/10.1021/cg300552w.

(49) Beldon, P. J.; Fábián, L.; Stein, R. S.; Thirumurugan, A.; Cheetham, A. K.; Friščić, T. Rapid Room-Temperature Synthesis of Zeolitic Imidazolate Frameworks by Using Mechanochemistry. *Angew. Chem.* **2010**, *122* (50), 9834–9837. https://doi.org/10.1002/ange.201005547.

(50) Friščić, T.; Halasz, I.; Beldon, P. J.; Belenguer, A. M.; Adams, F.; Kimber, S. A. J.; Honkimäki, V.; Dinnebier, R. E. Real-Time and in Situ Monitoring of Mechanochemical Milling Reactions. *Nat. Chem.* **2013**, *5* (1), 66–73. https://doi.org/10.1038/nchem.1505.

(51) Dharmarathna, S.; King'ondu, C. K.; Pedrick, W.; Pahalagedara, L.; Suib, S. L. Direct Sonochemical Synthesis of Manganese Octahedral Molecular Sieve (OMS-2) Nanomaterials Using Cosolvent Systems, Their Characterization, and Catalytic Applications. *Chem. Mater.* **2012**, *24* (4), 705–712. https://doi.org/10.1021/cm203366m.

(52) Kim, J.; Yang, S.-T.; Beom Choi, S.; Sim, J.; Kim, J.; Ahn, W.-S. Control of Catenation in CuTATB- n Metal–Organic Frameworks by Sonochemical Synthesis and Its Effect on CO 2 Adsorption. *J. Mater. Chem.* **2011**, *21* (9), 3070–3076. https://doi.org/10.1039/C0JM03318A.

(53) Moghadam, P. Z.; Li, A.; Wiggin, S. B.; Tao, A.; Maloney, A. G. P.; Wood, P. A.; Ward, S. C.; Fairen-Jimenez, D. Development of a Cambridge Structural Database Subset: A Collection of Metal–Organic Frameworks for Past, Present, and Future. *Chem. Mater.* **2017**, *29* (7), 2618–2625. https://doi.org/10.1021/acs.chemmater.7b00441.

(54) Farha, O. K.; Özgür Yazaydın, A.; Eryazici, I.; Malliakas, C. D.; Hauser, B. G.; Kanatzidis, M. G.; Nguyen, S. T.; Snurr, R. Q.; Hupp, J. T. De Novo Synthesis of a Metal–Organic Framework Material Featuring Ultrahigh Surface Area and Gas Storage Capacities. *Nat. Chem.* **2010**, *2* (11), 944–948. https://doi.org/10.1038/nchem.834.

(55) Lin, X.; Telepeni, I.; Blake, A. J.; Dailly, A.; Brown, C. M.; Simmons, J. M.; Zoppi, M.; Walker, G. S.; Thomas, K. M.; Mays, T. J.; Hubberstey, P.; Champness, N. R.; Schröder, M. High Capacity Hydrogen Adsorption in Cu(II) Tetracarboxylate Framework Materials: The Role of Pore Size, Ligand Functionalization, and Exposed Metal Sites. *J. Am. Chem. Soc.* **2009**, *131* (6), 2159–2171. https://doi.org/10.1021/ja806624j.

(56) Wang, X.-S.; Ma, S.; Forster, P. M.; Yuan, D.; Eckert, J.; López, J. J.; Murphy, B. J.; Parise, J. B.; Zhou, H.-C. Enhancing H2 Uptake by “Close-Packing” Alignment of Open Copper Sites in Metal–Organic Frameworks. *Angew. Chem.* **2008**, *120* (38), 7373–7376. https://doi.org/10.1002/ange.200802087.

(57) Wong-Foy, A. G.; Matzger, A. J.; Yaghi, O. M. Exceptional H2 Saturation Uptake in Microporous Metal−Organic Frameworks. *J. Am. Chem. Soc.* **2006**, *128* (11), 3494–3495. https://doi.org/10.1021/ja058213h.

(58) Konstas, K.; Osl, T.; Yang, Y.; Batten, M.; Burke, N.; J. Hill, A.; R. Hill, M. Methane Storage in Metal Organic Frameworks. *J. Mater. Chem.* **2012**, *22* (33), 16698–16708. https://doi.org/10.1039/C2JM32719H.

(59) Wu, H.; Zhou, W.; Yildirim, T. High-Capacity Methane Storage in Metal−Organic Frameworks M2(Dhtp): The Important Role of Open Metal Sites. *J. Am. Chem. Soc.* **2009**, *131* (13), 4995–5000. https://doi.org/10.1021/ja900258t.

(60) Noro, S.; Kitagawa, S.; Kondo, M.; Seki, K. A New, Methane Adsorbent, Porous Coordination Polymer [CuSiF6(4,4′-Bipyridine)2n]. *Angew. Chem. Int. Ed.* **2000**, *39* (12), 2081–2084. https://doi.org/10.1002/1521-3773(20000616)39:12<2081::AID-ANIE2081>3.0.CO;2-A.

(61) Perry; Kravtsov, V. Ch.; McManus, G. J.; Zaworotko, M. J. Bottom up Synthesis That Does Not Start at the Bottom: Quadruple Covalent Cross-Linking of Nanoscale Faceted Polyhedra. *J. Am. Chem. Soc.* **2007**, *129* (33), 10076–10077. https://doi.org/10.1021/ja0734952.

(62) Panda, T.; Pachfule, P.; Chen, Y.; Jiang, J.; Banerjee, R. Amino Functionalized Zeolitic Tetrazolate Framework (ZTF) with High Capacity for Storage of Carbon Dioxide. *Chem. Commun.* **2011**, *47* (7), 2011–2013. https://doi.org/10.1039/C0CC04169F.

(63) Furukawa, H.; Ko, N.; Go, Y. B.; Aratani, N.; Choi, S. B.; Choi, E.; Yazaydin, A. Ö.; Snurr, R. Q.; O’Keeffe, M.; Kim, J.; Yaghi, O. M. Ultrahigh Porosity in Metal-Organic Frameworks. *Science* **2010**, *329* (5990), 424–428. https://doi.org/10.1126/science.1192160.

(64) O’Keeffe, M.; Yaghi, O. M. Deconstructing the Crystal Structures of Metal–Organic Frameworks and Related Materials into Their Underlying Nets. *Chem. Rev.* **2012**, *112* (2), 675–702. https://doi.org/10.1021/cr200205j.

(65) Sakakura, T.; Choi, J.-C.; Yasuda, H. Transformation of Carbon Dioxide. *Chem. Rev.* **2007**, *107* (6), 2365–2387. https://doi.org/10.1021/cr068357u.

(66) Sumida, K.; Rogow, D. L.; Mason, J. A.; McDonald, T. M.; Bloch, E. D.; Herm, Z. R.; Bae, T.-H.; Long, J. R. Carbon Dioxide Capture in Metal–Organic Frameworks. *Chem. Rev.* **2012**, *112* (2), 724–781. https://doi.org/10.1021/cr2003272.

(67) Cheetham, K. A.; Rao, C. N. R.; Feller, K. R. Structural Diversity and Chemical Trends in Hybrid Inorganic–Organic Framework Materials. *Chem. Commun.* **2006**, *0* (46), 4780–4795. https://doi.org/10.1039/B610264F.

(68) Espallargas, G. M.; Coronado, E. Magnetic Functionalities in MOFs: From the Framework to the Pore. *Chem. Soc. Rev.* **2018**, *47* (2), 533–557. https://doi.org/10.1039/C7CS00653E.

(69) Kurmoo, M. Magnetic Metal–Organic Frameworks. *Chem. Soc. Rev.* **2009**, *38* (5), 1353–1379. https://doi.org/10.1039/B804757J.

(70) Ōkawa, H.; Shigematsu, A.; Sadakiyo, M.; Miyagawa, T.; Yoneda, K.; Ohba, M.; Kitagawa, H. Oxalate-Bridged Bimetallic Complexes {NH(Prol)3}[MCr(Ox)3] (M = MnII, FeII, CoII; NH(Prol)3+ = Tri(3-Hydroxypropyl)Ammonium) Exhibiting Coexistent Ferromagnetism and Proton Conduction. *J. Am. Chem. Soc.* **2009**, *131* (37), 13516–13522. https://doi.org/10.1021/ja905368d.

(71) Roques, N.; Maspoch, D.; Imaz, I.; Datcu, A.; Sutter, J.-P.; Rovira, C.; Veciana, J. A Three-Dimensional Lanthanide- Organic Radical Open-Framework. *Chem. Commun.* **2008**, *0* (27), 3160–3162. https://doi.org/10.1039/B802196A.

(72) Shimomura, S.; Higuchi, M.; Matsuda, R.; Yoneda, K.; Hijikata, Y.; Kubota, Y.; Mita, Y.; Kim, J.; Takata, M.; Kitagawa, S. Selective Sorption of Oxygen and Nitric Oxide by an Electron-Donating Flexible Porous Coordination Polymer. *Nat. Chem.* **2010**, *2* (8), 633–637. https://doi.org/10.1038/nchem.684.

(73) Allan, P. K.; Xiao, B.; Teat, S. J.; Knight, J. W.; Morris, R. E. In Situ Single-Crystal Diffraction Studies of the Structural Transition of Metal−Organic Framework Copper 5-Sulfoisophthalate, Cu-SIP-3. *J. Am. Chem. Soc.* **2010**, *132* (10), 3605–3611. https://doi.org/10.1021/ja910600b.

(74) McKinlay, A. C.; Xiao, B.; Wragg, D. S.; Wheatley, P. S.; Megson, I. L.; Morris, R. E. Exceptional Behavior over the Whole Adsorption−Storage−Delivery Cycle for NO in Porous Metal Organic Frameworks. *J. Am. Chem. Soc.* **2008**, *130* (31), 10440–10444. https://doi.org/10.1021/ja801997r.

(75) Cui, Y.; Xu, H.; Yue, Y.; Guo, Z.; Yu, J.; Chen, Z.; Gao, J.; Yang, Y.; Qian, G.; Chen, B. A Luminescent Mixed-Lanthanide Metal–Organic Framework Thermometer. *J. Am. Chem. Soc.* **2012**, *134* (9), 3979–3982. https://doi.org/10.1021/ja2108036.

(76) Sun, C.-Y.; Wang, X.-L.; Qin, C.; Jin, J.-L.; Su, Z.-M.; Huang, P.; Shao, K.-Z. Solvatochromic Behavior of Chiral Mesoporous Metal–Organic Frameworks and Their Applications for Sensing Small Molecules and Separating Cationic Dyes. *Chem. – Eur. J.* **2013**, *19* (11), 3639–3645. https://doi.org/10.1002/chem.201203080.

(77) Lu, Z.-Z.; Zhang, R.; Li, Y.-Z.; Guo, Z.-J.; Zheng, H.-G. Solvatochromic Behavior of a Nanotubular Metal−Organic Framework for Sensing Small Molecules. *J. Am. Chem. Soc.* **2011**, *133* (12), 4172–4174. https://doi.org/10.1021/ja109437d.

(78) Reddy, M. L. P.; Sivakumar, S. Lanthanide Benzoates : A Versatile Building Block for the Construction of Efficient Light Emitting Materials. *Dalton Trans.* **2013**, *42* (8), 2663–2678. https://doi.org/10.1039/C2DT32470A.

(79) Zhan, S.-Z.; Li, M.; Ng, S. W.; Li, D. Luminescent Metal–Organic Frameworks (MOFs) as a Chemopalette: Tuning the Thermochromic Behavior of Dual-Emissive Phosphorescence by Adjusting the Supramolecular Microenvironments. *Chem. – Eur. J.* **2013**, *19* (31), 10217–10225. https://doi.org/10.1002/chem.201204632.

(80) Uoyama, H.; Goushi, K.; Shizu, K.; Nomura, H.; Adachi, C. Highly Efficient Organic Light-Emitting Diodes from Delayed Fluorescence. *Nature* **2012**, *492* (7428), 234–238. https://doi.org/10.1038/nature11687.

(81) Chaoui, N.; Trunk, M.; Dawson, R.; Schmidt, J.; Thomas, A. Trends and Challenges for Microporous Polymers. *Chem. Soc. Rev.* **2017**, *46* (11), 3302–3321. https://doi.org/10.1039/C7CS00071E.

(82) Cote, A. P., Benin, A. I., Ockwig, N. W., O'Keeffe, M., Matzger, A. J. and Yaghi, O. M., Porous, Crystalline, Covalent Organic Frameworks. *Sci.* **2005**, *310*(5751), 1166-1170. https://doi.org/10.1126/science.1120411.

(83) El-Kaderi, H. M., Hunt, J. R., Mendoza-Cortés, J. L., Côté, A. P., Taylor, R. E., O'Keeffe, M. and Yaghi, O. M., Designed Synthesis of 3D Covalent Organic Frameworks. *Sci.* **2007**, *316*(5822), 268-272. https://doi.org/10.1126/science.1139915.

(84) Kuhn, P.; Antonietti, M.; Thomas, A. Porous, Covalent Triazine-Based Frameworks Prepared by Ionothermal Synthesis. *Angew. Chem. Int. Ed.* **2008**, *47* (18), 3450–3453. https://doi.org/10.1002/anie.200705710.

(85) Kuhn, P.; Thomas, A.; Antonietti, M. Toward Tailorable Porous Organic Polymer Networks: A High-Temperature Dynamic Polymerization Scheme Based on Aromatic Nitriles. *Macromolecules* **2009**, *42* (1), 319–326. https://doi.org/10.1021/ma802322j.

(86) Dawson, R.; Adams, D. J.; Cooper, A. I. Chemical Tuning of CO2 Sorption in Robust Nanoporous Organic Polymers. *Chem. Sci.* **2011**, *2* (6), 1173–1177. https://doi.org/10.1039/C1SC00100K.

(87) Wang, X.; Zhao, Y.; Wei, L.; Zhang, C.; Jiang, J.-X. Nitrogen-Rich Conjugated Microporous Polymers: Impact of Building Blocks on Porosity and Gas Adsorption. *J. Mater. Chem. A* **2015**, *3* (42), 21185–21193. https://doi.org/10.1039/C5TA05230K.

(88) Ren, S.; Dawson, R.; Laybourn, A.; Jiang, J.; Khimyak, Y.; Adams, D. J.; Cooper, A. I. Functional Conjugated Microporous Polymers: From 1,3,5-Benzene to 1,3,5-Triazine. *Polym. Chem.* **2012**, *3* (4), 928–934. https://doi.org/10.1039/C2PY00585A.

(89) Ben, T.; Ren, H.; Ma, S.; Cao, D.; Lan, J.; Jing, X.; Wang, W.; Xu, J.; Deng, F.; Simmons, J. M.; Qiu, S.; Zhu, G. Targeted Synthesis of a Porous Aromatic Framework with High Stability and Exceptionally High Surface Area. *Angew. Chem. Int. Ed.* **2009**, *48* (50), 9457–9460. https://doi.org/10.1002/anie.200904637.

(90) Yuan, D.; Lu, W.; Zhao, D.; Zhou, H.-C. Highly Stable Porous Polymer Networks with Exceptionally High Gas-Uptake Capacities. *Adv. Mater.* **2011**, *23* (32), 3723–3725. https://doi.org/10.1002/adma.201101759.

(91) Lu, W.; Bosch, M.; Yuan, D.; Zhou, H.-C. Cost-Effective Synthesis of Amine-Tethered Porous Materials for Carbon Capture. *ChemSusChem* **2015**, *8* (3), 433–438. https://doi.org/10.1002/cssc.201402622.

(92) Schwab, M. G.; Lennert, A.; Pahnke, J.; Jonschker, G.; Koch, M.; Senkovska, I.; Rehahn, M.; Kaskel, S. Nanoporous Copolymer Networks through Multiple Friedel–Crafts-Alkylation—Studies on Hydrogen and Methane Storage. *J. Mater. Chem.* **2011**, *21* (7), 2131–2135. https://doi.org/10.1039/C0JM03017A.

(93) Lee, J.-Y.; Wood, C. D.; Bradshaw, D.; Rosseinsky, M. J.; Cooper, A. I. Hydrogen Adsorption in Microporous Hypercrosslinked Polymers. *Chem. Commun.* **2006**, No. 25, 2670–2672. https://doi.org/10.1039/B604625H.

(94) Germain, J.; Hradil, J.; Fréchet, J. M. J.; Svec, F. High Surface Area Nanoporous Polymers for Reversible Hydrogen Storage. *Chem. Mater.* **2006**, *18* (18), 4430–4435. https://doi.org/10.1021/cm061186p.

(95) Wood, C. D.; Tan, B.; Trewin, A.; Niu, H.; Bradshaw, D.; Rosseinsky, M. J.; Khimyak, Y. Z.; Campbell, N. L.; Kirk, R.; Stöckel, E.; Cooper, A. I. Hydrogen Storage in Microporous Hypercrosslinked Organic Polymer Networks. *Chem. Mater.* **2007**, *19* (8), 2034–2048. https://doi.org/10.1021/cm070356a.

(96) McKeown, N. B.; Makhseed, S.; Budd, P. M. Phthalocyanine-Based Nanoporous Network Polymers. *Chem. Commun.* **2002**, No. 23, 2780–2781. https://doi.org/10.1039/B207642J.

(97) McKeown, N. B.; Gahnem, B.; Msayib, K. J.; Budd, P. M.; Tattershall, C. E.; Mahmood, K.; Tan, S.; Book, D.; Langmi, H. W.; Walton, A. Towards Polymer-Based Hydrogen Storage Materials: Engineering Ultramicroporous Cavities within Polymers of Intrinsic Microporosity. *Angew. Chem. Int. Ed.* **2006**, *45* (11), 1804–1807. https://doi.org/10.1002/anie.200504241.

(98) Budd, P. M.; Butler, A.; Selbie, J.; Mahmood, K.; McKeown, N. B.; Ghanem, B.; Msayib, K.; Book, D.; Walton, A. The Potential of Organic Polymer-Based Hydrogen Storage Materials. *Phys. Chem. Chem. Phys.* **2007**, *9* (15), 1802–1808. https://doi.org/10.1039/B618053A.

(99) Mason, C. R., Maynard-Atem, L., Al-Harbi, N. M., Budd, P. M., Bernardo, P., Bazzarelli, F., Clarizia, G. and Jansen, J. C., Polymer of Intrinsic Microporosity Incorporating Thioamide Functionality: Preparation and Gas Transport Properties. *Macromol.* **2011**, *44* (16), 6471–6479. https://pubs.acs.org/doi/10.1021/ma200918h.

(100) Dawson, R.; Stöckel, E.; Holst, J. R.; Adams, D. J.; Cooper, A. I. Microporous Organic Polymers for Carbon Dioxide Capture. *Energy Environ. Sci.* **2011**, *4* (10), 4239–4245. https://doi.org/10.1039/C1EE01971F.

(101) Dawson, R.; Cooper, A. I.; Adams, D. J. Chemical Functionalization Strategies for Carbon Dioxide Capture in Microporous Organic Polymers. *Polym. Int.* **2013**, *62* (3), 345–352. https://doi.org/10.1002/pi.4407.

(102) Makhseed, S.; Samuel, J. Hydrogen Adsorption in Microporous Organic Framework Polymer. *Chem. Commun.* **2008**, *0* (36), 4342–4344. https://doi.org/10.1039/B805656K.

(103) Makhseed, S.; Samuel, J. Microporous Organic Polymers Incorporating Dicarboximide Units for H 2 Storage and Remarkable CO 2 Capture. *J. Mater. Chem. A* **2013**, *1* (41), 13004–13010. https://doi.org/10.1039/C3TA12233F.

(104) Lukose, B.; Wahiduzzaman, M.; Kuc, A.; Heine, T. Mechanical, Electronic, and Adsorption Properties of Porous Aromatic Frameworks. *J. Phys. Chem. C* **2012**, *116* (43), 22878–22884. https://doi.org/10.1021/jp3067102.

(105) Wood, C. D.; Tan, B.; Trewin, A.; Su, F.; Rosseinsky, M. J.; Bradshaw, D.; Sun, Y.; Zhou, L.; Cooper, A. I. Microporous Organic Polymers for Methane Storage. *Adv. Mater.* **2008**, *20* (10), 1916–1921. https://doi.org/10.1002/adma.200702397.

(106) Kim, S.; Lee, Y. M. Rigid and Microporous Polymers for Gas Separation Membranes. *Prog. Polym. Sci.* **2015**, *43*, 1–32. https://doi.org/10.1016/j.progpolymsci.2014.10.005.

(107) Mackintosh, H. J.; Budd, P. M.; McKeown, N. B. Catalysis by Microporous Phthalocyanine and Porphyrin Network Polymers. *J. Mater. Chem.* **2008**, *18* (5), 573–578. https://doi.org/10.1039/B715660J.

(108) Tantisriyanurak, S.; Duguid, H. N.; Peattie, L.; Dawson, R. Acid Functionalized Conjugated Microporous Polymers as a Reusable Catalyst for Biodiesel Production. *ACS Appl. Polym. Mater.* **2020**, *2* (9), 3908–3915. https://doi.org/10.1021/acsapm.0c00595.

(109) Xiang, Z.; Wang, D.; Xue, Y.; Dai, L.; Chen, J.-F.; Cao, D. PAF-Derived Nitrogen-Doped 3D Carbon Materials for Efficient Energy Conversion and Storage. *Sci. Rep.* **2015**, *5* (1), 8307. https://doi.org/10.1038/srep08307.

(110) Parthiban, A. *Synthesis and Applications of Copolymers*; John Wiley & Sons, Incorporated: Somerset, UNITED STATES, 2014.

(111) Kitagawa, S.; Kitaura, R.; Noro, S. Functional Porous Coordination Polymers. *Angew. Chem. Int. Ed.* **2004**, *43* (18), 2334–2375. https://doi.org/10.1002/anie.200300610.

(112) Li, H.; Eddaoudi, M.; O'Keeffe, M.; Yaghi, O. M. Design and Synthesis of an Exceptionally Stable and Highly Porous Metal-Organic Framework. *Nature* **1999**, *402* (6759), 276–279. https://doi.org/10.1038/46248.

(113) Côté, A. P.; Benin, A. I.; Ockwig, N. W.; O'Keeffe, M.; Matzger, A. J.; Yaghi, O. M. Porous, Crystalline, Covalent Organic Frameworks. *Science* **2005**, *310* (5751), 1166–1170. https://doi.org/10.1126/science.1120411.

(114) Furukawa, H.; Yaghi, O. M. Storage of Hydrogen, Methane, and Carbon Dioxide in Highly Porous Covalent Organic Frameworks for Clean Energy Applications. *J. Am. Chem. Soc.* **2009**, *131* (25), 8875–8883. https://doi.org/10.1021/ja9015765.

(115) Tian, X.; Zhou, G.; Xi, J.; Sun, R.; Zhang, X.; Wang, G.; Mei, L.; Hou, C.; Jiang, L.; Qiu, J. Vinyl-Functionalized Covalent Organic Frameworks for Effective Radioactive

Iodine Capture in Aqueous Solution. *Sep. Purif. Technol.* **2023**, *310*, 123160. https://doi.org/10.1016/j.seppur.2023.123160.

(116) Xu, G.; Dong, X.; Hou, L.; Wang, X.; Liu, L.; Ma, H.; Zhao, R.-S. Room-Temperature Synthesis of Flower-Shaped Covalent Organic Frameworks for Solid-Phase Extraction of Quinolone Antibiotics. *Anal. Chim. Acta* **2020**, *1126*, 82–90. https://doi.org/10.1016/j.aca.2020.05.071.

(117) Jiang, W.; Cui, W.-R.; Liang, R.-P.; Qiu, J.-D. Difunctional Covalent Organic Framework Hybrid Material for Synergistic Adsorption and Selective Removal of Fluoroquinolone Antibiotics. *J. Hazard. Mater.* **2021**, *413*, 125302. https://doi.org/10.1016/j.jhazmat.2021.125302.

(118) Liu, W.; Su, Q.; Ju, P.; Guo, B.; Zhou, H.; Li, G.; Wu, Q. A Hydrazone-Based Covalent Organic Framework as an Efficient and Reusable Photocatalyst for the Cross-Dehydrogenative Coupling Reaction of N-Aryltetrahydroisoquinolines. *ChemSusChem* **2017**, *10* (4), 664–669. https://doi.org/10.1002/cssc.201601702.

(119) Zhang, K.; Cai, S.-L.; Yan, Y.-L.; He, Z.-H.; Lin, H.-M.; Huang, X.-L.; Zheng, S.-R.; Fan, J.; Zhang, W.-G. Construction of a Hydrazone-Linked Chiral Covalent Organic Framework–Silica Composite as the Stationary Phase for High Performance Liquid Chromatography. *J. Chromatogr. A* **2017**, *1519*, 100–109. https://doi.org/10.1016/j.chroma.2017.09.007.

(120) Yuan, C.; Fu, S.; Yang, K.; Hou, B.; Liu, Y.; Jiang, J.; Cui, Y. Crystalline C—C and C═C Bond-Linked Chiral Covalent Organic Frameworks. *J. Am. Chem. Soc.* **2021**, *143* (1), 369–381. https://doi.org/10.1021/jacs.0c11050.

(121) El-Kaderi, H. M.; Hunt, J. R.; Mendoza-Cortés, J. L.; Côté, A. P.; Taylor, R. E.; O'Keeffe, M.; Yaghi, O. M. Designed Synthesis of 3D Covalent Organic Frameworks. *Science* **2007**, *316* (5822), 268–272. https://doi.org/10.1126/science.1139915.

(122) Dey, S.; Bhunia, A.; Esquivel, D.; Janiak, C. Covalent Triazine-Based Frameworks (CTFs) from Triptycene and Fluorene Motifs for CO2 Adsorption. *J. Mater. Chem. A* **2016**, *4* (17), 6259–6263. https://doi.org/10.1039/C6TA00638H.

(123) Ren, S.; Bojdys, M. J.; Dawson, R.; Laybourn, A.; Khimyak, Y. Z.; Adams, D. J.; Cooper, A. I. Porous, Fluorescent, Covalent Triazine-Based Frameworks Via Room-Temperature and Microwave-Assisted Synthesis. *Adv. Mater.* **2012**, *24* (17), 2357–2361. https://doi.org/10.1002/adma.201200751.

(124) Puthiaraj, P.; Cho, S.-M.; Lee, Y.-R.; Ahn, W.-S. Microporous Covalent Triazine Polymers: Efficient Friedel–Crafts Synthesis and Adsorption/Storage of CO 2 and CH 4. *J. Mater. Chem. A* **2015**, *3* (13), 6792–6797. https://doi.org/10.1039/C5TA00665A.

(125) Lim, H.; Cha, M. C.; Chang, J. Y. Preparation of Microporous Polymers Based on 1,3,5-Triazine Units Showing High CO2 Adsorption Capacity. *Macromol. Chem. Phys.* **2012**, *213* (13), 1385–1390. https://doi.org/10.1002/macp.201200195.

(126) Kuhn, P.; Forget, A.; Su, D.; Thomas, A.; Antonietti, M. From Microporous Regular Frameworks to Mesoporous Materials with Ultrahigh Surface Area: Dynamic Reorganization of Porous Polymer Networks. *J. Am. Chem. Soc.* **2008**, *130* (40), 13333–13337. https://doi.org/10.1021/ja803708s.

(127) Xu, Y.; Jin, S.; Xu, H.; Nagai, A.; Jiang, D. Conjugated Microporous Polymers : Design, Synthesis and Application. *Chem. Soc. Rev.* **2013**, *42* (20), 8012–8031. https://doi.org/10.1039/C3CS60160A.

(128) Saber, A. F.; Sharma, S. U.; Lee, J.-T.; EL-Mahdy, A. F. M.; Kuo, S.-W. Carbazole-Conjugated Microporous Polymers from Suzuki–Miyaura Coupling for Supercapacitors. *Polymer* **2022**, *254*, 125070. https://doi.org/10.1016/j.polymer.2022.125070.

(129) Wang, C.-A.; Zhao, W.; Li, Y.-W.; Han, Y.-F.; Zhang, J.-P.; Li, Q.; Nie, K.; Chang, J.-G.; Liu, F.-S. The Bulky Pd-PEPPSI-Embedded Conjugated Microporous Polymer-Catalyzed Suzuki–Miyaura Cross-Coupling of Aryl Chlorides and Arylboronic Acids. *Polym. Chem.* **2022**, *13* (11), 1547–1558. https://doi.org/10.1039/D1PY01616D.

(130) Zhang, Q.; Yu, S.; Wang, Q.; Xiao, Q.; Yue, Y.; Ren, S. Fluorene-Based Conjugated Microporous Polymers: Preparation and Chemical Sensing Application. *Macromol. Rapid Commun.* **2017**, *38* (23), 1700445. https://doi.org/10.1002/marc.201700445.

(131) Schmidt, J.; Werner, M.; Thomas, A. Conjugated Microporous Polymer Networks via Yamamoto Polymerization. *Macromolecules* **2009**, *42* (13), 4426–4429. https://doi.org/10.1021/ma9005473.

(132) Samy, M. M.; Mohamed, M. G.; Mansoure, T. H.; Meng, T. S.; Khan, M. A. R.; Liaw, C.-C.; Kuo, S.-W. Solid State Chemical Transformations through Ring-Opening Polymerization of Ferrocene-Based Conjugated Microporous Polymers in Host–Guest Complexes with Benzoxazine-Linked Cyclodextrin. *J. Taiwan Inst. Chem. Eng.* **2022**, *132*, 104110. https://doi.org/10.1016/j.jtice.2021.10.010.

(133) Sheng, X.; Ding, X.; You, D.; Peng, M.; Dai, Z.; Hu, X.; Shi, H.; Yang, L.; Shao, P.; Luo, X. Perfluorinated Conjugated Microporous Polymer for Targeted Capture of Ag(I) from Contaminated Water. *Environ. Res.* **2022**, *211*, 113007. https://doi.org/10.1016/j.envres.2022.113007.

(134) Guo, X.-X.; Jiang, J.; Han, Q.; Liu, X.-H.; Zhou, X.-T.; Ji, H.-B. Zinc Porphyrin-Based Electron Donor–Acceptor-Conjugated Microporous Polymer for the Efficient Photocatalytic Oxidative Coupling of Amines under Visible Light. *Appl. Catal. Gen.* **2020**, *590*, 117352. https://doi.org/10.1016/j.apcata.2019.117352.

(135) Chen, Q.; Liu, D.-P.; Luo, M.; Feng, L.-J.; Zhao, Y.-C.; Han, B.-H. Nitrogen-Containing Microporous Conjugated Polymers via Carbazole-Based Oxidative Coupling Polymerization: Preparation, Porosity, and Gas Uptake. *Small* **2014**, *10* (2), 308–315. https://doi.org/10.1002/smll.201301618.

(136) Shuangzhi, C.; Liu, H.; Zhang, X.; Han, Y.; Hu, N.; Wei, L.; Cong, F.; Wei, H.; Wang, L. Synthesis of a Novel β-Ketoenamine-Linked Conjugated Microporous Polymer with NH Functionalized Pore Surface for Carbon Dioxide Capture. *Appl. Surf. Sci.* **2016**, *384*, 539–543. https://doi.org/10.1016/j.apsusc.2016.05.068.

(137) Jiang, J.; Xiangying, L.; Rongchang, L.; Link to external site, this link will open in a new window. Donor–Acceptor Type Conjugated Microporous Polymer as a Metal-Free Photocatalyst for Visible-Light-Driven Aerobic Oxidative Coupling of Amines. *Catal. Lett.* **2021**, *151* (11), 3145–3153. https://doi.org/10.1007/s10562-021-03574-z.

(138) Kim, J.; Moisanu, C. M.; Gannett, C. N.; Halder, A.; Fuentes-Rivera, J. J.; Majer, S. H.; Lancaster, K. M.; Forse, A. C.; Abruña, H. D.; Milner, P. J. Conjugated Microporous Polymers via Solvent-Free Ionothermal Cyclotrimerization of Methyl Ketones. *Chem. Mater.* **2021**, *33* (21), 8334–8342. https://doi.org/10.1021/acs.chemmater.1c02622.

(139) Fang, X.-C.; Geng, T.-M.; Wang, F.-Q.; Xu, W.-H. The Synthesis of Conjugated Microporous Polymers via Friedel–Crafts Reaction of 2,4,6-Trichloro-1,3,5-Triazine with Thienyl Derivatives for Fluorescence Sensing to 2,4-Dinitrophenol and Capturing Iodine. *J. Solid State Chem.* **2022**, *307*, 122818. https://doi.org/10.1016/j.jssc.2021.122818.

(140) Geng, T.; Ye, S.; Zhu, Z.; Zhang, W. Triazine-Based Conjugated Microporous Polymers with N,N,N′,N′-Tetraphenyl-1,4-Phenylenediamine, 1,3,5-Tris(Diphenylamino)Benzene and 1,3,5-Tris[(3-Methylphenyl)-Phenylamino]Benzene

as the Core for High Iodine Capture and Fluorescence Sensing of o-Nitrophenol. *J. Mater. Chem. A* **2018**, *6* (6), 2808–2816. https://doi.org/10.1039/C7TA08251G.

(141) Jiang, J.-X.; Su, F.; Trewin, A.; Wood, C. D.; Campbell, N. L.; Niu, H.; Dickinson, C.; Ganin, A. Y.; Rosseinsky, M. J.; Khimyak, Y. Z.; Cooper, A. I. Conjugated Microporous Poly(Aryleneethynylene) Networks. *Angew. Chem.* **2007**, *119* (45), 8728–8732. https://doi.org/10.1002/ange.200701595.

(142) Kassab, R. M.; Jackson, K. T.; El-Kadri, O. M.; El-Kaderi, H. M. Nickel-Catalyzed Synthesis of Nanoporous Organic Frameworks and Their Potential Use in Gas Storage Applications. *Res. Chem. Intermed.* **2011**, *37* (7), 747. https://doi.org/10.1007/s11164-011-0321-z.

(143) Yuan, Y.; Zhu, G. Porous Aromatic Frameworks as a Platform for Multifunctional Applications. *ACS Cent. Sci.* **2019**, *5* (3), 409–418. https://doi.org/10.1021/acscentsci.9b00047.

(144) Li, M.; Ren, H.; Sun, F.; Tian, Y.; Zhu, Y.; Li, J.; Mu, X.; Xu, J.; Deng, F.; Zhu, G. Construction of Porous Aromatic Frameworks with Exceptional Porosity via Building Unit Engineering. *Adv. Mater.* **2018**, *30* (43), 1804169. https://doi.org/10.1002/adma.201804169.

(145) Li, M.; Ren, H.; Sun, F.; Tian, Y.; Zhu, Y.; Li, J.; Mu, X.; Xu, J.; Deng, F.; Zhu, G. Construction of Porous Aromatic Frameworks with Exceptional Porosity via Building Unit Engineering. *Adv. Mater.* **2018**, *30* (43), 1804169. https://doi.org/10.1002/adma.201804169.

(146) Yuan, Y.; Sun, F.; Ren, H.; Jing, X.; Wang, W.; Ma, H.; Zhao, H.; Zhu, G. Targeted Synthesis of a Porous Aromatic Framework with a High Adsorption Capacity for Organic Molecules. *J. Mater. Chem.* **2011**, *21* (35), 13498–13502. https://doi.org/10.1039/C1JM11998B.

(147) Rose, M.; Klein, N.; Böhlmann, W.; Böhringer, B.; Fichtner, S.; Kaskel, S. New Element Organic Frameworks via Suzuki Coupling with High Adsorption Capacity for Hydrophobic Molecules. *Soft Matter* **2010**, *6* (16), 3918–3923. https://doi.org/10.1039/C003130E.

(148) Yan, Z.; Ren, H.; Ma, H.; Yuan, R.; Yuan, Y.; Zou, X.; Sun, F.; Zhu, G. Construction and Sorption Properties of Pyrene-Based Porous Aromatic Frameworks. *Microporous Mesoporous Mater.* **2013**, *173*, 92–98. https://doi.org/10.1016/j.micromeso.2013.02.006.

(149) Xu, Y.; Chen, L.; Guo, Z.; Nagai, A.; Jiang, D. Light-Emitting Conjugated Polymers with Microporous Network Architecture: Interweaving Scaffold Promotes Electronic Conjugation, Facilitates Exciton Migration, and Improves Luminescence. *J. Am. Chem. Soc.* **2011**, *133* (44), 17622–17625. https://doi.org/10.1021/ja208284t.

(150) Zhang, L.; Sun, J.-S.; Sun, F.; Chen, P.; Liu, J.; Zhu, G. Facile Synthesis of Ultrastable Porous Aromatic Frameworks by Suzuki–Miyaura Coupling Reaction for Adsorption Removal of Organic Dyes. *Chem. – Eur. J.* **2019**, *25* (15), 3903–3908. https://doi.org/10.1002/chem.201805713.

(151) Gu, C.; Liu, D.; Huang, W.; Liu, J.; Yang, R. Synthesis of Covalent Triazine-Based Frameworks with High CO 2 Adsorption and Selectivity. *Polym. Chem.* **2015**, *6* (42), 7410–7417. https://doi.org/10.1039/C5PY01090J.

(152) Trewin, A.; Cooper, A. I. Porous Organic Polymers: Distinction from Disorder? *Angew. Chem. Int. Ed.* **2010**, *49* (9), 1533–1535. https://doi.org/10.1002/anie.200906827.

(153) Jia, J.; Chen, Z.; Jiang, H.; Belmabkhout, Y.; Mouchaham, G.; Aggarwal, H.; Adil, K.; Abou-Hamad, E.; Czaban-Jóźwiak, J.; Tchalala, M. R.; Eddaoudi, M. Extremely

Hydrophobic POPs to Access Highly Porous Storage Media and Capturing Agent for Organic Vapors. *Chem* **2019**, *5* (1), 180–191. https://doi.org/10.1016/j.chempr.2018.10.005.

(154) Ren, H.; Ben, T.; Wang, E.; Jing, X.; Xue, M.; Liu, B.; Cui, Y.; Qiu, S.; Zhu, G. Targeted Synthesis of a 3D Porous Aromatic Framework for Selective Sorption of Benzene. *Chem. Commun.* **2010**, *46* (2), 291–293. https://doi.org/10.1039/B914761F.

(155) Wang, W.; Ren, H.; Sun, F.; Cai, K.; Ma, H.; Du, J.; Zhao, H.; Zhu, G. Synthesis of Porous Aromatic Framework with Tuning Porosity via Ionothermal Reaction. *Dalton Trans.* **2012**, *41* (14), 3933–3936. https://doi.org/10.1039/C2DT11996J.

(156) Tian, Y.; Zhu, G. Porous Aromatic Frameworks (PAFs). *Chem. Rev.* **2020**, *120* (16), 8934–8986. https://doi.org/10.1021/acs.chemrev.9b00687.

(157) Tan, L.; Tan, B. Hypercrosslinked Porous Polymer Materials: Design, Synthesis, and Applications. *Chem. Soc. Rev.* **2017**, *46* (11), 3322–3356. https://doi.org/10.1039/C6CS00851H.

(158) Staudinger, H.; Heuer, W. Über Hochpolymere Verbindungen, 93. Mitteil.: Über Das Zerreißen Der Faden-Moleküle Des Poly-Styrols. *Berichte Dtsch. Chem. Ges. B Ser.* **1934**, *67* (7), 1159–1164. https://doi.org/10.1002/cber.19340670708.

(159) Davankov, V. A.; Rogoshin, S. V.; Tsyurupa, M. P. Macronet Isoporous Gels through Crosslinking of Dissolved Polystyrene. *J. Polym. Sci. Polym. Symp.* **1974**, *47* (1), 95–101. https://doi.org/10.1002/polc.5070470113.

(160) Chen, Q.; Liu, D.-P.; Zhu, J.-H.; Han, B.-H. Mesoporous Conjugated Polycarbazole with High Porosity via Structure Tuning. *Macromolecules* **2014**, *47* (17), 5926–5931. https://doi.org/10.1021/ma501330v.

(161) Davankov, V. A.; Pastukhov, A. V.; Tsyurupa, M. P. Unusual Mobility of Hypercrosslinked Polystyrene Networks: Swelling and Dilatometric Studies. *J. Polym. Sci. Part B Polym. Phys.* **2000**, *38* (11), 1553–1563. https://doi.org/10.1002/(SICI)1099-0488(20000601)38:11<1553::AID-POLB160>3.0.CO;2-L.

(162) Ahn, J.-H.; Jang, J.-E.; Oh, C.-G.; Ihm, S.-K.; Cortez, J.; Sherrington, D. C. Rapid Generation and Control of Microporosity, Bimodal Pore Size Distribution, and Surface Area in Davankov-Type Hyper-Cross-Linked Resins. *Macromolecules* **2006**, *39* (2), 627–632. https://doi.org/10.1021/ma051152n.

(163) Tsyurupa, M. P.; Davankov, V. A. Hypercrosslinked Polymers: Basic Principle of Preparing the New Class of Polymeric Materials. *React. Funct. Polym.* **2002**, *53* (2), 193–203. https://doi.org/10.1016/S1381-5148(02)00173-6.

(164) Li, B.; Gong, R.; Wang, W.; Huang, X.; Zhang, W.; Li, H.; Hu, C.; Tan, B. A New Strategy to Microporous Polymers: Knitting Rigid Aromatic Building Blocks by External Cross-Linker. *Macromolecules* **2011**, *44* (8), 2410–2414. https://doi.org/10.1021/ma200630s.

(165) Errahali, M.; Gatti, G.; Tei, L.; Paul, G.; Rolla, G. A.; Canti, L.; Fraccarollo, A.; Cossi, M.; Comotti, A.; Sozzani, P.; Marchese, L. Microporous Hyper-Cross-Linked Aromatic Polymers Designed for Methane and Carbon Dioxide Adsorption. *J. Phys. Chem. C* **2014**, *118* (49), 28699–28710. https://doi.org/10.1021/jp5096695.

(166) Saleh, M.; Lee, H. M.; Kemp, K. C.; Kim, K. S. Highly Stable CO2/N2 and CO2/CH4 Selectivity in Hyper-Cross-Linked Heterocyclic Porous Polymers. *ACS Appl. Mater. Interfaces* **2014**, *6* (10), 7325–7333. https://doi.org/10.1021/am500728q.

(167) McKeown, N. B. Polymers of Intrinsic Microporosity. *ISRN Mater. Sci.* **2012**, *2012*, 1–16. https://doi.org/10.5402/2012/513986.

(168) McKeown, N. B. The Synthesis of Polymers of Intrinsic Microporosity (PIMs). *Sci. China Chem.* **2017**, *60* (8), 1023–1032. https://doi.org/10.1007/s11426-017-9058-x.

(169) Kricheldorf, H. R.; Fritsch, D.; Vakhtangishvili, L.; Schwarz, G. Cyclic Ladder Polymers by Polycondensation of Silylated Tetrahydroxy-Tetramethylspirobisindane with 1,4-Dicyanotetrafluorobenzene. *Macromol. Chem. Phys.* **2005**, *206* (22), 2239–2247. https://doi.org/10.1002/macp.200500280.
(170) Eastmond, G. C.; Paprotny, J.; Steiner, A.; Swanson, L. Synthesis of Cyanodibenzo[1,4]Dioxines and Their Derivatives by Cyano-Activated Fluoro Displacement Reactions. *New J. Chem.* **2001**, *25* (3), 379–384. https://doi.org/10.1039/B008508L.
(171) Du, N.; Song, J.; Robertson, G. P.; Pinnau, I.; Guiver, M. D. Linear High Molecular Weight Ladder Polymer via Fast Polycondensation of 5,5′,6,6′-Tetrahydroxy-3,3,3′,3′-Tetramethylspirobisindane with 1,4-Dicyanotetrafluorobenzene. *Macromol. Rapid Commun.* **2008**, *29* (10), 783–788. https://doi.org/10.1002/marc.200800038.
(172) Carta, M.; Malpass-Evans, R.; Croad, M.; Rogan, Y.; Jansen, J. C.; Bernardo, P.; Bazzarelli, F.; McKeown, N. B. An Efficient Polymer Molecular Sieve for Membrane Gas Separations. *Science* **2013**, *339* (6117), 303–307. https://doi.org/10.1126/science.1228032.
(173) Carta, M.; Malpass-Evans, R.; Croad, M.; Rogan, Y.; Lee, M.; Rose, I.; B. McKeown, N. The Synthesis of Microporous Polymers Using Tröger's Base Formation. *Polym. Chem.* **2014**, *5* (18), 5267–5272. https://doi.org/10.1039/C4PY00609G.
(174) Ghanem, B. S.; McKeown, N. B.; Budd, P. M.; Selbie, J. D.; Fritsch, D. High-Performance Membranes from Polyimides with Intrinsic Microporosity. *Adv. Mater.* **2008**, *20* (14), 2766–2771. https://doi.org/10.1002/adma.200702400.
(175) Ghanem, B. S.; McKeown, N. B.; Budd, P. M.; Al-Harbi, N. M.; Fritsch, D.; Heinrich, K.; Starannikova, L.; Tokarev, A.; Yampolskii, Y. Synthesis, Characterization, and Gas Permeation Properties of a Novel Group of Polymers with Intrinsic Microporosity: PIM-Polyimides. *Macromolecules* **2009**, *42* (20), 7881–7888. https://doi.org/10.1021/ma901430q.
(176) Cheng, G.; Hasell, T.; Trewin, A.; Adams, D. J.; Cooper, A. I. Soluble Conjugated Microporous Polymers. *Angew. Chem. Int. Ed.* **2012**, *51* (51), 12727–12731. https://doi.org/10.1002/anie.201205521.
(177) Zhu, X.; Tian, C.; Mahurin, S. M.; Chai, S.-H.; Wang, C.; Brown, S.; Veith, G. M.; Luo, H.; Liu, H.; Dai, S. A Superacid-Catalyzed Synthesis of Porous Membranes Based on Triazine Frameworks for CO2 Separation. *J. Am. Chem. Soc.* **2012**, *134* (25), 10478–10484. https://doi.org/10.1021/ja304879c.
(178) Liu, S.; Jin, Z.; Teo, Y. C.; Xia, Y. Efficient Synthesis of Rigid Ladder Polymers via Palladium Catalyzed Annulation. *J. Am. Chem. Soc.* **2014**, *136* (50), 17434–17437. https://doi.org/10.1021/ja5110415.
(179) Ranganathan, K.; Anbanandam, P. Soluble, Microporous Ladder Polymers Formed by Stepwise Nucleophilic Substitution of Octafluorocyclopentene. *Polym. Chem.* **2015**, *6* (25), 4560–4564. https://doi.org/10.1039/C5PY00359H.
(180) Budd, P. M.; Elabas, E. S.; Ghanem, B. S.; Makhseed, S.; McKeown, N. B.; Msayib, K. J.; Tattershall, C. E.; Wang, D. Solution-Processed, Organophilic Membrane Derived from a Polymer of Intrinsic Microporosity. *Adv. Mater.* **2004**, *16* (5), 456–459. https://doi.org/10.1002/adma.200306053.
(181) McKeown, N. B.; Hanif, S.; Msayib, K.; Tattershall, C. E.; Budd, P. M. Porphyrin-Based Nanoporous Network Polymers. *Chem. Commun.* **2002**, No. 23, 2782–2783. https://doi.org/10.1039/B208702M.
(182) Fu, H.-X.; Zhang, Z.-H.; Fan, W.; Wang, S.; Liu, Y.; Huang, M.-H. A Soluble Porous Organic Polymer for Highly Efficient Organic-Aqueous Biphasic Catalysis and

Convenient Reuse of Catalysts. *J. Mater. Chem. A* **2019**, *7* (25), 15048–15053. https://doi.org/10.1039/C9TA04594E.
(183) Yang, Y.; Tan, B.; D. Wood, C. Solution-Processable Hypercrosslinked Polymers by Low Cost Strategies: A Promising Platform for Gas Storage and Separation. *J. Mater. Chem. A* **2016**, *4* (39), 15072–15080. https://doi.org/10.1039/C6TA05226F.
(184) Cheng, G.; Hasell, T.; Trewin, A.; Adams, D. J.; Cooper, A. I. Soluble Conjugated Microporous Polymers. *Angew. Chem. Int. Ed.* **2012**, *51* (51), 12727–12731. https://doi.org/10.1002/anie.201205521.
(185) Bandyopadhyay, S.; Pallavi, P.; G. Anil, A.; Patra, A. Fabrication of Porous Organic Polymers in the Form of Powder, Soluble in Organic Solvents and Nanoparticles: A Unique Platform for Gas Adsorption and Efficient Chemosensing. *Polym. Chem.* **2015**, *6* (20), 3775–3780. https://doi.org/10.1039/C5PY00235D.
(186) Deng, S.; Zhi, J.; Zhang, X.; Wu, Q.; Ding, Y.; Hu, A. Size-Controlled Synthesis of Conjugated Polymer Nanoparticles in Confined Nanoreactors. *Angew. Chem.* **2014**, *126* (51), 14368–14372. https://doi.org/10.1002/ange.201407387.
(187) Deng, S.; Zhao, P.; Dai, Y.; Huang, B.; Hu, A. Synthesis of Soluble Conjugated Polymeric Nanoparticles through Heterogeneous Suzuki Coupling Reaction. *Polymer* **2015**, *64*, 216–220. https://doi.org/10.1016/j.polymer.2015.02.006.
(188) Lim, J.; Kim, M.-S.; Jang, W.; Wang, D. H.; Park, J. K. Solution-Processable Porous Organic Polymer for Tailoring the Charge Transport Property of Planar Perovskite Solar Cells. *Dyes Pigments* **2020**, *178*, 108332. https://doi.org/10.1016/j.dyepig.2020.108332.
(189) Pallavi, P.; Bandyopadhyay, S.; Louis, J.; Deshmukh, A.; Patra, A. A Soluble Conjugated Porous Organic Polymer: Efficient White Light Emission in Solution, Nanoparticles, Gel and Transparent Thin Film. *Chem. Commun.* **2017**, *53* (7), 1257–1260. https://doi.org/10.1039/C6CC08903H.
(190) Mai, W.; Sun, B.; Chen, L.; Xu, F.; Liu, H.; Liang, Y.; Fu, R.; Wu, D.; Matyjaszewski, K. Water-Dispersible, Responsive, and Carbonizable Hairy Microporous Polymeric Nanospheres. *J. Am. Chem. Soc.* **2015**, *137* (41), 13256–13259. https://doi.org/10.1021/jacs.5b08978.
(191) Yu, H.; Wang, Z.; Wu, R.; Chen, X.; Chan, T.-W. D. Water-Dispersible PH/Thermo Dual-Responsive Microporous Polymeric Microspheres as Adsorbent for Dispersive Solid-Phase Extraction of Fluoroquinolones from Environmental Water Samples and Food Samples. *J. Chromatogr. A* **2019**, *1601*, 27–34. https://doi.org/10.1016/j.chroma.2019.05.004.
(192) Mai, W.; Sun, B.; Chen, L.; Xu, F.; Liu, H.; Liang, Y.; Fu, R.; Wu, D.; Matyjaszewski, K. Water-Dispersible, Responsive, and Carbonizable Hairy Microporous Polymeric Nanospheres. *J. Am. Chem. Soc.* **2015**, *137* (41), 13256–13259. https://doi.org/10.1021/jacs.5b08978.
(193) James, A. M.; Derry, M. J.; Train, J. S.; Dawson, R. Dispersible Microporous Diblock Copolymer Nanoparticles via Polymerisation-Induced Self-Assembly. *Polym. Chem.* **2019**, *10* (28), 3879–3886. https://doi.org/10.1039/C9PY00596J.
(194) Ferguson, C. T. J.; Huber, N.; Kuckhoff, T.; Zhang, K. A. I.; Landfester, K. Dispersible Porous Classical Polymer Photocatalysts for Visible Light-Mediated Production of Pharmaceutically Relevant Compounds in Multiple Solvents. *J. Mater. Chem. A* **2020**, *8* (3), 1072–1076. https://doi.org/10.1039/C9TA11242A.
(195) James, A. M.; Dawson, R. Efficient and Tunable White-Light Emission Using a Dispersible Porous Polymer. *Macromol. Rapid Commun.* **2020**, *41* (12), 2000176. https://doi.org/10.1002/marc.202000176.

(196) Ivko, S. A.; James, A. M.; Derry, M. J.; Dawson, R.; Haynes, A. Heterogenisation of a Carbonylation Catalyst on Dispersible Microporous Polymer Nanoparticles. *Catal. Sci. Technol.* **2022**, *12* (2), 664–673. https://doi.org/10.1039/D1CY01989A.

(197) Matyjaszewski, K.; Xia, J. Atom Transfer Radical Polymerization. *Chem. Rev.* **2001**, *101* (9), 2921–2990. https://doi.org/10.1021/cr940534g.

(198) Hawker, C. J.; Bosman, A. W.; Harth, E. New Polymer Synthesis by Nitroxide Mediated Living Radical Polymerizations. *Chem. Rev.* **2001**, *101* (12), 3661–3688. https://doi.org/10.1021/cr990119u.

(199) Keddie, D. J. A Guide to the Synthesis of Block Copolymers Using Reversible-Addition Fragmentation Chain Transfer (RAFT) Polymerization. *Chem. Soc. Rev.* **2014**, *43* (2), 496–505. https://doi.org/10.1039/C3CS60290G.

(200) Stenzel, M. H.; Cummins, L.; Roberts, G. E.; Davis, T. P.; Vana, P.; Barner-Kowollik, C. Xanthate Mediated Living Polymerization of Vinyl Acetate: A Systematic Variation in MADIX/RAFT Agent Structure. *Macromol. Chem. Phys.* **2003**, *204* (9), 1160–1168. https://doi.org/10.1002/macp.200390089.

(201) Canning, S. L.; Smith, G. N.; Armes, S. P. A Critical Appraisal of RAFT-Mediated Polymerization-Induced Self-Assembly. *Macromolecules* **2016**, *49* (6), 1985–2001. https://doi.org/10.1021/acs.macromol.5b02602.

(202) Hoffman, A. S. Stimuli-Responsive Polymers: Biomedical Applications and Challenges for Clinical Translation. *Adv. Drug Deliv. Rev.* **2013**, *65* (1), 10–16. https://doi.org/10.1016/j.addr.2012.11.004.

(203) Yin, X.; Hoffman, A. S.; Stayton, P. S. Poly(N-Isopropylacrylamide-Co-Propylacrylic Acid) Copolymers That Respond Sharply to Temperature and PH. *Biomacromolecules* **2006**, *7* (5), 1381–1385. https://doi.org/10.1021/bm0507812.

(204) Roy, I.; Gupta, M. N. Smart Polymeric Materials: Emerging Biochemical Applications. *Chem. Biol.* **2003**, *10* (12), 1161–1171. https://doi.org/10.1016/j.chembiol.2003.12.004.

(205) Dai, S.; Ravi, P.; Chiu Tam, K. PH-Responsive Polymers : Synthesis, Properties and Applications. *Soft Matter* **2008**, *4* (3), 435–449. https://doi.org/10.1039/B714741D.

(206) Baines, F. L.; Billingham, N. C.; Armes, S. P. Synthesis and Solution Properties of Water-Soluble Hydrophilic−Hydrophobic Block Copolymers. *Macromolecules* **1996**, *29* (10), 3416–3420. https://doi.org/10.1021/ma951699+.

(207) Kim, Y.-J.; Matsunaga, Y. T. Thermo-Responsive Polymers and Their Application as Smart Biomaterials. *J. Mater. Chem. B* **2017**, *5* (23), 4307–4321. https://doi.org/10.1039/C7TB00157F.

(208) Aoyagi, T.; Ebara, M.; Sakai, K.; Sakurai, Y.; Okano, T. Novel Bifunctional Polymer with Reactivity and Temperature Sensitivity. *J. Biomater. Sci. Polym. Ed.* **2000**, *11* (1), 101–110. https://doi.org/10.1163/156856200743526.

(209) Yoshida, T.; Aoyagi, T.; Kokufuta, E.; Okano, T. Newly Designed Hydrogel with Both Sensitive Thermoresponse and Biodegradability. *J. Polym. Sci. Part Polym. Chem.* **2003**, *41* (6), 779–787. https://doi.org/10.1002/pola.10595.

(210) Maeda, T.; Yamamoto, K.; Aoyagi, T. Importance of Bound Water in Hydration–Dehydration Behavior of Hydroxylated Poly(N-Isopropylacrylamide). *J. Colloid Interface Sci.* **2006**, *302* (2), 467–474. https://doi.org/10.1016/j.jcis.2006.06.047.

(211) Glatzel, S.; Laschewsky, A.; Lutz, J.-F. Well-Defined Uncharged Polymers with a Sharp UCST in Water and in Physiological Milieu. *Macromolecules* **2011**, *44* (2), 413–415. https://doi.org/10.1021/ma102677k.

(212) Owens, D. E.; Jian, Y.; Fang, J. E.; Slaughter, B. V.; Chen, Y.-H.; Peppas, N. A. Thermally Responsive Swelling Properties of Polyacrylamide/Poly(Acrylic Acid)

Interpenetrating Polymer Network Nanoparticles. *Macromolecules* **2007**, *40* (20), 7306–7310. https://doi.org/10.1021/ma071089x.

(213) Chu, L.-Y.; Li, Y.; Zhu, J.-H.; Chen, W.-M. Negatively Thermoresponsive Membranes with Functional Gates Driven by Zipper-Type Hydrogen-Bonding Interactions. *Angew. Chem.* **2005**, *117* (14), 2162–2165. https://doi.org/10.1002/ange.200462687.

(214) Xie, T. Recent Advances in Polymer Shape Memory. *Polymer* **2011**, *52* (22), 4985–5000. https://doi.org/10.1016/j.polymer.2011.08.003.

Chapter-2 Methods

2.1 Characterisation Techniques

2.1.1 ^{1}H NMR and ^{13}C nuclear magnetic resonance (NMR) spectroscopy

The solution state NMR spectra were recorded by using a Bruker Avance III HD spectrometer at 400MHz. Each Sample was dissolved in an suitable deuterated solvent and filtered with cotton wool before analysis at room temperature. ^{1}H NMR was conducted with 128 scans per spectrum. The ^{13}C NMR was performed on the same instrument with 1024 scans on average per spectrum.

2.1.2 Mass spectroscopy (Matrix-assisted laser desorption/ionization)

MS spectra was obtained using an Agilent Technologies 6530 Accurate-Mass Q-TOF LC/MS. Each sample is prepared in a suitable solvent and the results was recorder directly from the instrument.

2.1.3 Elemental analysis (EA)

EA result was carried out by using an Elementar Vario MICRO Cube CHN/S analyser. Approximately 10 mg of sample was burned in a stream of oxygen, with excess oxygen and NO_x reduced to N_2 by passing the sample through a copper tube prior to combustion. Thermal Programmed Desorption column was used to separate the resulting gases, which were then detected using a Thermal Conductivity Detector.

2.1.4 Gel Permeation Chromatography (GPC)

Molecular weights (M_n, M_w, M_z) and polydispersity indices (PDI) results were obtained using a PL-GPC 50 integrated GPC System with PLgel MIXED-C columns and a Refractive Index detector. The eluent, THF was used at a flow rate of 1 mL min^{-1} and the analysis was preformed at 25 °C. Polystyrene was used as the standard calibration. Each injection sample was prepared by dissolving 1 mg of sample in 1 mL THF solvent after PTFE syringe filtration.

2.1.5 Nitrogen gas adsorption and desorption isotherms

Nitrogen adsorption/desorption isotherms were conducted on an ASAP 2020 Plus Micromeritics volumetric adsorption analyser using high purity gases at 77 K. Each sample was precisely weighted (around 100 mg) in a tube before degassed at 80 °C under dynamic vacuum of at least 10^{-5} bar about 16 hours. The sample was accurately weighted again in the tube after degassing and the analysis started. The BET surface areas were calculated over a relative pressure range of 0.01-0.15 P/P_0 and the pore size distributions and pore volumes were calculated by nonlocal density functional theory model (NL-DFT). The data were automatically recorded by the software.

2.1.6 Dynamic Light Scattering (DLS)

The particle size and derived count rate (kcps) results were recorded using a Malvern Zetasizer nanoZS instrument. The samples were prepared in quartz or polystyrene cuvettes with a concentration of 0.1 wt. / vol % water or methanol solution. DLS was employed to determine particle size, which is based on the principle of relating particle velocity in a solution (known as the translational diffusion coefficient) to its size through Brownian motion which the small particles move faster while the large one move slower. A laser was used to illuminate the sample, and the scattering light was recorded at a fixed angle. The observed fluctuations in the scattered light are a consequence of the relative motion between the particles, which leads to constantly changing interferences within the overall scattered light. This movement of the particles results in slight frequency shifts in the scattered light due to the time-dependent positions or velocities of the particles. Over time, this motion generates a distribution of frequency shifts when measured. The correlator is used as a signal comparator, which can measure the degree of similarity one signal with itself at varying time intervals. The correlation of a signal arriving from a random source will decrease with time goes on. However, when the particles are large in size, the resulting signal changes at a slower rate, and the correlation between measurements persists for a longer duration. Conversely, when the particles are small and exhibit rapid movement, the correlation between measurements decreases more quickly (Figure 2.1).

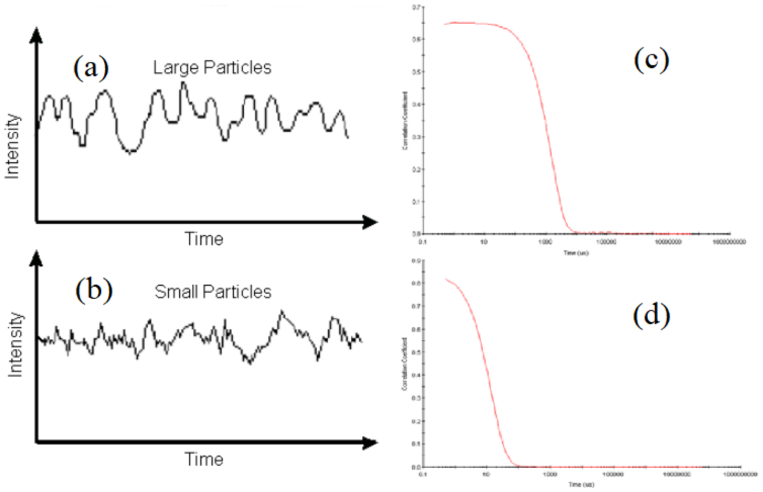

Figure 2.1 Typical intensity fluctuations for large (a) and small (b) particles; and Typical correlogram from a sample containing large particles (c) and small particles (d)

Based on the above plots, the translational diffusion coefficient (D) can be obtained and allowed particle size to be calculated using the Stokes-Einstein equation.[1] The Stokes-Einstein equation is shown below.

$$D = \frac{k_B T}{6\pi\eta R_H} \qquad 2.1$$

Where D is the translational diffusion coefficient (m^2 s^{-1}), k_B is the Boltzmann constant (m^2 kg^{-1} Ks^{-2}), T is the temperature (K), η is the sample viscosity (Pa s^{-1}) and R_H is the hydrodynamic radius (m), respectively.

2.1.7 UV-Vis Spectroscopy

The UV-Vis absorption spectra were obtained by using a Cary 60 UV-Vis. Samples were prepared in a quartz cuvette with a concentration of 0.001 wt. / vol % spectroscopic grade solvent.

2.1.8 Scanning Electron Microscopy (SEM)

SEM images were carried out by using a Fei Inspect F50 Field Emission Gun SEM with running in secondary electron mode. Each sample was prepared by mounting onto carbon tape, which is supported on aluminium stubs. The SEM images were collected by Jiangtian Tan.

2.1.9 Transmission Electron Microscopy (TEM)

TEM images were recorded by using a Philips CM-100 instrument operating at 100 kV with a Gatan 1k CCD camera. The sample was dissolved in a 0.1 wt / vol %[2,3] water or 0.5 M hydrochloric acid (HCl) or 0.5 M sodium hydroxide (NaOH) solution and was sonicated for 3 hours. The tiny sample was transformed to a carbon-coated copper grid at request temperature and was allowed to dry for 1 minute. Then, the 0.75% uranyl formate stain was covered on the grid of the sample and was allowed to dry for 1 minute. The 0.75% uranyl formate stain was prepared by Dr. Christopher Hill.

2.2 Gas sorption theory

The gas physisorption phenomenon is crucial to the gas-mixture separation industry.[4] The design of gas separation and purification equipment require the data of adsorption equilibria. Therefore, the proper understanding of gas sorption theory is very imperative. Sorption can be categorized into absorption and adsorption, where absorption refers to the permeation of liquid or gas into bulk, while adsorption involves the selective concentration of certain molecules, atoms, or ions on surfaces. Adsorption can further be divided into chemisorption and physisorption, with chemisorption involving the formation of chemical bonds during adsorption, while physisorption involves only weak forces between the surface and molecule, such as charges, hydrogen bonds, and van der Waals repulsion. Nitrogen gas physisorption is often used to determine the surface area, pore size, and volume of porous materials at 77 K, where gas molecules start to adsorb on the isolated sites of the solid surface at low pressure, and as pressure increases, more gas molecules are adsorbed to form a monolayer to multi-layer. Moreover, the smaller pores of the sample are filled first until all the pores are filled by the gas molecules. Several theories and models, such as the Langmuir and Brunauer-Emmett-Teller (BET) models, have been developed to explain the pure-gas adsorption equilibria in porous materials and are commonly used in related research.

2.2.1 Langmuir isotherm model

Langmuir's approach remains the most useful method for separating data dependencies, and it is the basis for the development of other models.[5] The basic assumptions of Langmuir are, the surface is homogeneous; the adsorption energy is constant over all adsorption sites; the adsorption on surface is localised; and each site can accommodate only one molecule or atom.[6] A state of dynamic equilibrium is achieved, where the rate of adsorption is balanced by the rate of desorption from the surface. The format can be expressed in equation 2.2.

$$A(g) + B(s) \underset{k_a/k_d}{\longleftrightarrow} AB \tag{2.2}$$

Where, A(g) means the gas molecule; B(s) means the solid surface; A-B means the adsorption state of the gas molecules on the solid surface; k_a means the rate constant of adsorption; and k_d means rate constant of desorption, respectively.

The kinetic theory can be used to determine the rate of the two processes. The equilibrium constant can be expressed in equation 2.3.

$$K_{eq} = {}^{k_a}\!/_{k_d} = {}^{k_a(N-n)}\!/_{k_d n} \tag{2.3}$$

Where, $k_aP(N\text{-}n)$ means the rate of adsorption; k_dn means the rate of desorption; P means the pressure of the adsorption; N means the total number of adsorption sites; n means the number of occupied sites; and K_{eq} means the equilibrium constant.

At a specific pressure, when a system is at equilibrium, the rate of desorption from occupied sites is equal to the rate of adsorption to the occupied sites. This can be expressed in equation 2.4.

$$k_aP(1-\theta) = k_d\theta \tag{2.4}$$

Where, θ means the fractional surface coverage. And the equation 2.4 can be rearranged and expressed in equation 2.5.

$$\theta = {}^{k_a P}\!/_{k_d + k_a P} \tag{2.5}$$

According to the equation 2.3 and 2.5, the θ can be expressed in another way and shown in equation 2.6.

$$\theta = {}^{K_{eq} P}\!/_{1 + K_{eq} P} \tag{2.6}$$

This is equation is well known as the Langmuir adsorption equation. The equation can be expressed by volume of gas adsorbed by a sorbent and shown in the equation 2.7.

$$\theta = {}^{V_{ads}}\!/_{V_{mono}} \tag{2.7}$$

Where, V_{ads} means the volume of gas adsorbed; and V_{mono} means the amount of gas adsorbed corresponding to monolayer coverage.

According to the equation 2.6 and equation 2.7, the Langmuir equation can be rearranged in linear form and expressed in equation 2.8.

$${}^{P}\!/_{V_{ads}} = {}^{P}\!/_{V_{mono}} + {}^{1}\!/_{(K_{eq} V_{mono})} \tag{2.8}$$

If a graph of P/V_{ads} vs P is plotted, a linear relationship can be observed, where the slope is equivalent to $1/V_{mono}$ and the intercept is equal to $1/K_{eq}V_{mono}$.

The Langmuir surface area (SA_{lang}) can be determined by the equation 2.9.

$$SA_{lang} = V_{mono} A \tag{2.9}$$

Where, A means the area of one molecule.

The disadvantage of Langmuir model for gas adsorption only considered the monolayer. Thus, it can only be really effective under low pressure conditions, and other than that, different gas adsorption models need to be applied.

2.2.2 BET Theory

Langmuir's model is widely used to analyse surface area data, but it has limitations at high pressures. Brunauer and co-workers[7] proposed a theory that accounts for both monolayer and multilayer adsorption. The following hypotheses are made for multi-layer adsorption, gas molecules are physically attached to the solids in infinite layers; gas molecules only interact with neighbouring layers and Langmuir theory can be applied to every layer; the adsorption enthalpy of the first layer is constant and greater than that of the second layer (and higher); and the enthalpy of adsorption in the second (and higher) layer is the same as the enthalpy of liquefaction.

The overall equation for BET theory can be expressed by equation 2.10.

$${}^{P}\!/_{V(P_0 - P)} = {}^{1}\!/_{V_m C} + {}^{(C-1)P}\!/_{V_m C P_0} \tag{2.10}$$

Where, P means the partial pressure of the adsorbate; P_0 means the saturation vapor pressure of the adsorbate; V means the volume of the adsorbed gas at the adsorption equilibrium; V_m means volume of the adsorbed gas when monolayer adsorption is completed; C means the constant related with the heat of the adsorption and it is shown in equation 2.11.

$$C = e^{{}^{E_1 - E_l}\!/_{RT}} \tag{2.11}$$

Where, E_1 means the heat of adsorption for the first layer; E_L means the adsorption heat of the second and higher layers, equals to the heat of liquefaction or the heat of vaporization; R means the ideal gas constant; and T means the temperature.

Equation 2.10 is an adsorption isotherm and if we were then to plot a graph of $1/(V(P_0/P)-1)$ vs P/P_0, the linear line can be shown, where the slope (S) is equal to $(C-1)/V_mC$ and the intercept (I) $1/V_mC$. This plot is called a BET plot and it is a straight line between 0.05 and 0.35. Based on the slop and intercept, C and V_m ban be expressed by equation 2.12 and 2.13.

$$C = 1 + {}^{S}\!/_{I} \tag{2.12}$$

$$V_m = {}^{1}\!/_{S + 1} \tag{2.13}$$

Where, S means the slope; and I means the intercept.

Thus, BET surface can be expressed by equation 2.14.

$$SA_{BET} = {}^{V_m N_A \sigma}\!/_{V_{MV} m} \tag{2.14}$$

Where, V_m means the volume of the adsorbed gas when monolayer adsorption is completed at STP; V_{MV} means the molar volume of the adsorbed gas at STP; N_A means the Avogadro constant; and σ means the adsorption cross section of the adsorbed gas and m is the mass of the adsorbent.

2.2.3 Isotherm Shapes

There are six shapes of gas sorption isotherms which are divided by the IUPAC in 1985[8], and the IUPA divided the Type I and Type IV into two subtypes in 2015[9] (Figure 2.2).

Reversible Type I isotherm is indicative of materials that possess relatively small outer surfaces. The curve of the isotherm demonstrates a concavity towards the p/p_0 axis, with adsorption capacity close to a limit value. The adsorption is limited by the volume of accessible micropores rather than by the internal surface area. The steep increase in adsorption at very low p/p_0 indicates that the micropores are filled at low p/p_0 due to the improved adsorbent-adsorption interaction in the narrow micropore. The updated classifications provide further distinction. Type I (a) isotherm demonstrates an even steeper absorption at very low p/p_0, implying that the material has mainly narrow micropores (width <1 nm). However, the Type I (b) isotherm is similar to the original Type I isotherm, exhibiting steep absorption at very low p/p_0, suggesting that the material has a wider pore size distribution with micropores and possibly mesopores (width< 2.5 nm).

Reversible Type II isotherm illustrates that the material is nonporous or marcoporous. The curve exhibits unrestricted single-multilayer adsorption from low p/p_0 to high p/p_0. The inflection point B represents the complete of the monolayer adsorption stage with the sharp absorption, followed by the start of the multi-layer adsorption stage with the gentler curvature. Furthermore, the increasing of adsorption at $p/p_0=1$, indicates that the thickness of the adsorbed multilayer film typically increases without limit.

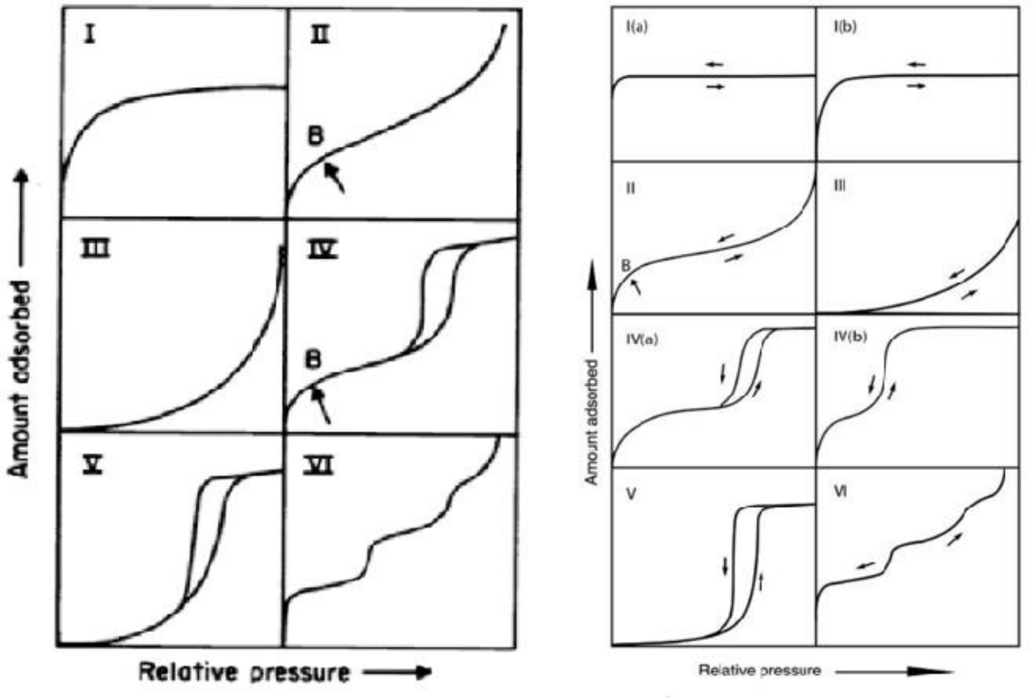

Figure 2.2 IUPAC isotherm classifications in 1985 (left)[8] and in 2015 (right)[9]

Type III isotherm illustrates that these materials are nonporous or marcoporous. The isotherm shows identifiable monolayer formation, which is due to the no clearly inflection point B. The adsorbate-adsorbent interaction is much weaker than the interactions between adsorbate molecules. It is different to compared with Type II isotherm, which a finite adsorption at $p/p_0=1$.

Type IV isotherm depicts the adsorption behaviour of mesoporous material, where the interaction between adsorbate molecules and adsorbent adsorbate plays a critical role. This isotherm is similar to the Type II isotherm. However, the hysteresis loops are caused by pore condensation which is due to the pressure p is less than the saturation pressure p_0. In addition it has a saturation platform compared to Type II isotherm. The updated the Type IV (a) isotherm is similar to the original Type IV isotherm. Whereas the Type IV (b) isotherm has no hysteresis loops and it is reversible isotherm.

Type V isotherm showcases materials that both are microporous and mesoporous. The shape of adsorption is quite similar to that of Type III isotherm except the hysteresis loops, which is due to the relatively weak adsorbent-adsorbate interactions.

Reversible stepwise Type VI isotherm illustrates that this kind of materials nonporous. The image exhibits the layer-by-layer adsorption on a highly uniform nonporous surface. The step height represents the monolayer capacity for each adsorbed layer.

2.2.4 Adsorption Hysteresis

Hysteresis loops observed in multilayer physisorption are typically linked to capillary condensation, and their shapes can vary due to differences in pore structures (Figure 2.3).

Type H1 loop type is commonly found in mesoporous materials with a narrow pore size distribution. The effects of network interactions are typically minimal, resulting in steep and narrow loops that indicate delayed condensation during adsorption.

The more complex pore structures associated with Type H2 loops result in significant network effects. Type H2 loops can be further divided into two subtypes: Type H2(a) loops exhibit a very steep desorption branch due to pore-blocking or percolation resulting from a narrow range of pore necks; Type H2(b) loops are also related to pore blocking but have a wider range of pore necks.

Type H3 loops have a similar adsorption branch to a Type II isotherm and typically exhibit a lower limit on the desorption branch located at the cavity-induced p/p_0.

Type H4 loops have an adsorption branch that is similar to the combination of Types I and II, and uptake at low p/p0 is related to filling of micropores.

Type H5 loops are unusual and are associated with pore structures containing open and partially blocked mesoporous holes.

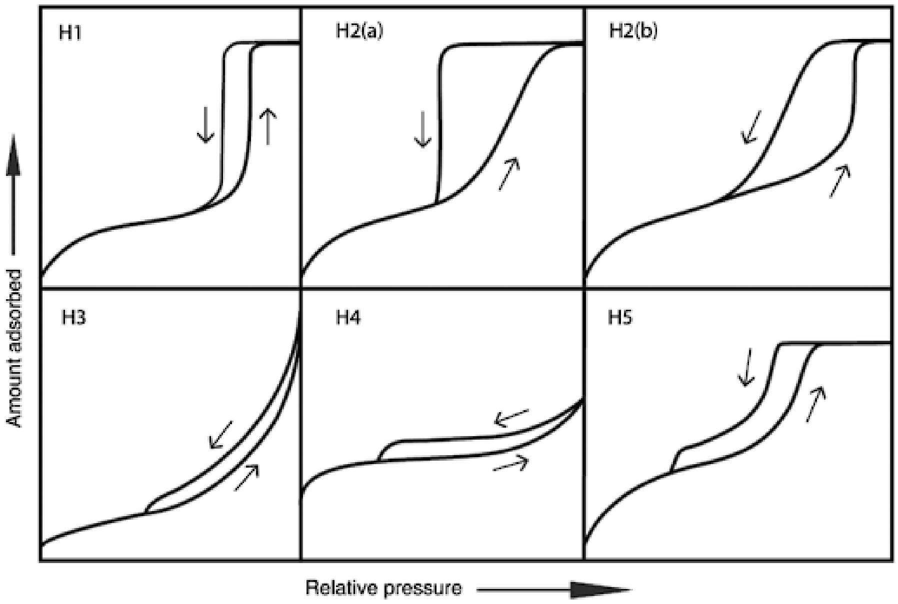

Figure 2.3 IUPAC classification of hysteresis loops[9]

2.3 References

(1) Parker, E. T.; Lollar, P. Measurement of the Translational Diffusion Coefficient and Hydrodynamic Radius of Proteins by Dynamic Light Scattering. *Bio-Protoc.* **2021**, *11* (20), e4195. https://doi.org/10.21769/BioProtoc.4195.

(2) Hunter, S. J.; Penfold, N. J. W.; Jones, E. R.; Zinn, T.; Mykhaylyk, O. O.; Armes, S. P. Synthesis of Thermoresponsive Diblock Copolymer Nano-Objects via RAFT Aqueous Emulsion Polymerisation of Hydroxybutyl Methacrylate. *Macromolecules* **2022**, *55* (8), 3051–3062. https://doi.org/10.1021/acs.macromol.2c00379.

(3) Varlas, S.; J. Neal, T.; P. Armes, S. Polymerisation-Induced Self-Assembly and Disassembly during the Synthesis of Thermoresponsive ABC Triblock Copolymer Nano-Objects in Aqueous Solution. *Chem. Sci.* **2022**, *13* (24), 7295–7303. https://doi.org/10.1039/D2SC01611G.

(4) Yue, B.; Liu, S.; Chai, Y.; Wu, G.; Guan, N.; Li, L. Zeolites for Separation: Fundamental and Application. *J. Energy Chem.* **2022**, *71*, 288–303. https://doi.org/10.1016/j.jechem.2022.03.035.

(5) Langmuir, I. The Adsorption of Gases on Plane Surfaces of Glass, Mica and Platinum. *J. Am. Chem. Soc.* **1918**, *40* (9), 1361–1403.

(6) Chilev, C.; Dicko, M.; Langlois, P.; Lamari, F. Modelling of Single-Gas Adsorption Isotherms. *Metals* **2022**, *12* (10), 1698. https://doi.org/10.3390/met12101698.

(7) Brunauer, S.; Emmett, P. H.; Teller, E. Adsorption of Gases in Multimolecular Layers. *J. Am. Chem. Soc.* **1938**, *60* (2), 309–319. https://doi.org/10.1021/ja01269a023.

(8) Sing, K. S. W.; Everett, H. D.; Haul, W. A. R.; Moscou, L.; Pierotti, A. R.; Rouquerol, J.; Siemieniewska, T. Pure & Appl. Chem 57, 603–619 (1985).

(9) Thommes, M.; Kaneko, K.; Neimark, A. V.; Olivier, J. P.; Rodriguez-Reinoso, F.; Rouquerol, J.; Sing, K. S. W. Physisorption of Gases, with Special Reference to the Evaluation of Surface Area and Pore Size Distribution (IUPAC Technical Report). *Pure Appl. Chem.* **2015**, *87* (9–10), 1051–1069. https://doi.org/10.1515/pac-2014-1117.

Chapter-3 Core-Shell Ratios

3.1 Aims

Previous research in our group into poly(ethylene glycol)-block-(divinylbenzene-co-fumaronitrile) (PEG_{113}-DVB_x/FN_y) particles using a metal-free radical addition fragmentation transfer mediated polymerisation induced self-assembly (RAFT mediated PISA) approach introduced both porosity and dispersibility into the porous polymer particles. We believe the strategy of using block copolymers to synthesise porous polymers has much promise due to wide range of available monomers and the use of non-toxic solvents. However, more research is required to understand the reaction conditions and how to form consistently soluble and highly porous MOPs. Until now all of these materials have been synthesised using a PEG based macro-CTA as the outer shell solubilising chain.[1–4] One of the main advantages of this strategy is the wide range of vinyl containing building blocks containing functionalities available to synthesise these materials.

This chapter looks at poly(acrylic acid) (PAA) (Figure 3.1) as an outer solubilising chain and aims delineate the requirements for these materials, such as the selection of reaction conditions, the required ratios of the different components such as the crosslinker (DVB) to spacer (FN) ratio as well as the core-shell ratio. PAA was chosen as a new monomer used for these investigations as it has not yet been used, has good solubility in both water and organic solvents, and is biocompatible which could lead to interesting applications.

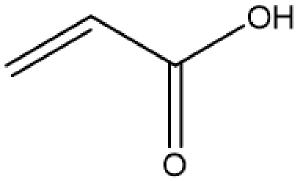

Figure 3.1 Molecular structure of acrylic acid (AA)

3.2 Experimental

3.2.1 Materials

Acrylic acid (AA) and divinylbenzene (DVB, technical grade 80 %) was passed through an alumina column in order to remove the inhibitor before use. 2-bromoisobutyryl bromide, dodecane thiol, potassium phosphate tribasic (K_3PO_4), Fumaronitrile (FN, 98 %) and potassium persulfate (KPS) were all purchased from Sigma-Aldrich and used as received. Dry THF was obtained in a method of Grubbs.[5] Magnesium sulfate ($MgSO_4$) and carbon disulphide (CS_2) were purchased from Fischer and used as received. Fumaronitrile (FN, 98 %), and 2,2′-azobis(2- methylpropionitrile) (AIBN, 98 %) were purchased from Sigma-Aldrich and used without further purification. All other chemicals were purchased from Sigma-Aldrich and used without any further purification.

3.2.2 Synthesis (The preparations were used a method adapted from James et al.[1])

3.2.2.1 Synthesis of 2-(dodecylthiocarbonothioylthio)-2-methylpropanoic acid (DDMAT) (chain transfer agent (CTA))

The synthesis of 2-(dodecylthiocarbonothioylthio)-2-methylpropanoic acid (DDMAT) was conducted using a modified method from O'Reilly et al.[6] Initially, dodecane thiol (3.61 mL, 15.07 mmol) was added to a stirred mixture of K_3PO_4 (3.199 g, 15.07 mmol) in acetone (20 ml) and stirred for 30 minutes. The mixture was then treated with CS_2 (3.129 g, 41.10 mmol) and stirred for an additional 60 minutes. Next, 2-bromoisobutyric acid (2.288 g, 13.70 mmol) was added to the reaction mixture, which was stirred overnight at room temperature. The solvent was extracted twice with CH_2Cl_2 (100 mL each) from 1 M HCl (100 mL). The organic extracts were washed with brine (150 mL) and $MgSO_4$ powder, followed by solvent removal using rotary evaporation. The obtained product was purified by precipitation in excess cold n-hexane twice to ensure purity and then dried in a vacuum oven overnight at 40 °C to yield the RAFT CTA (Yield = 49%. Found C: 57.04 %, H: 8.78 %, S: 26.47 %, Expected C: 56.04 %, H: 8.79 %, S: 26.37 %. δH (400 MHz, $CDCl_3$) = 3.31 (2H, t, S-CH_2-$(CH_2)_{10}$-CH_3), 1.75 (6H, s, C-$(CH_3)_2$), 1.76-1.20 (20H, t, S-CH_2-$(CH_2)_{10}$-CH_3), 0.90 (3H, t, SCH_2-$(CH_2)_{10}$-CH_3); δC (400 MHz, $CDCl_3$) = 220.85, 178.08, 55.53, 37.09, 31.93, 29.64, 29.57, 29.46, 29.36, 29.12, 28.98, 27.82, 25.24, 25.23, 22.70, 14.14; m/z (EI) 363.3, 303.3, 277.2, 201.3) (Figure 3.1 in appendix).

3.2.2.2 Synthesis of Poly(acrylic acid) (PAA) Based Macro-Chain Transfer Agent (CTA) (Macro-CTA (DDMAT-PAA)) via RAFT

The macro-CTA (DDMAT-PAA_x) (x=35, 50, 95) was prepared in a method similar to that reported by Chaduc and coworkers.[7] In brief, 2-(dodecylthiocarbonothioylthio)-2-methylpropanoic acid (DDMAT) and 1, 3, 5-trioxane were combined in a 2-necked round bottom flask, which was then subjected to evacuation and nitrogen backfilling procedures three times. A solution of dry THF and acrylic acid (AA) was added to the flask, followed by bubbling with nitrogen gas to remove any residual air. The mixture was then heated to 75 °C, and polymerisation was initiated by adding 2,2′-azobis(2- methylpropionitrile) (AIBN) with THF (1 mL), which was allowed to react for 3.5 h at 75 °C. The resulting product was purified by recrystallisation with cold n-hexane and THF for three cycles, and subsequently dried overnight in a vacuum oven at 60 °C to yield the desired product (Table 3.1).

Table 3.1 Different components for synthesis of PAA_x based Macro-CTA

Sample Name	AA	CTA	Trioxane	AIBN	THF	Yield
	mL/mmol	mg/mmol	mg/mmol	mg/mmol	mL	
PAA_{35} based Macro-CTA	3.5/51.00	364.0/1.00	656.3/7.29	16.5/0.10	31.0	67%
PAA_{50} based Macro-CTA	7.4/107.9	364.0/1.00	669.0/7.43	16.4/0.10	62.0	47%
PAA_{95} based Macro-CTA	3.5/51.00	91.3/0.25	171.3/1.90	4.2/0.025	31.0	48%

3.2.2.3 Synthesis of Poly(acrylic acid) (PAA) Based Particles via RAFT Mediated Polymerisation Induced Self-Assembly in different ratios of water to ethanol

The $PAA_{35}DVB_{94}FN_{70}$ was prepared using a method adapted from James et al.[1] In a 2-necked round bottom flask, a PAA-based macro-CTA (Macro-CTA (DDMAT-PAA_{35}), and FN were combined. The flask was then subjected to three rounds of evacuation and backfilling with nitrogen. A 1.0 wt.% solution was created by adding water and ethanol in a certain ratio (100:00, 80:20, 60:40, 40:60, 20:80, 00:100) (wt.%), along with DVB, to the flask. The solution was bubbled with nitrogen gas to remove any air before being heated to 70 °C. Polymerisation was initiated by adding potassium persulfate (KPS) and held at 70 °C for 24 hours. The product was isolated as a white solid through reprecipitation into diethyl ether, then dried under vacuum at 40 °C for 16 hours (Table 3.2).

Table 3.2 Different solution components for synthesis of $PAA_{35}DVB_{94}FN_{70}$

Monomer Composition				Solution Composition		Ratio of water to ethanol
PAA_{35}	DVB	FN	KPS	Water	Ethanol	
mg/mmol	mL/mmol	mg/mmol	mg/mmol	mL	mL	
57.7/0.02	0.27/1.88	109.2/1.40	1.1/0.004	43.1	0.0	100:00
57.7/0.02	0.27/1.88	109.2/1.40	1.1/0.004	34.5	8.6	80:20
57.7/0.02	0.27/1.88	109.2/1.40	1.1/0.004	25.9	17.2	60:40
57.7/0.02	0.27/1.88	109.2/1.40	1.1/0.004	17.2	25.9	40:60
57.7/0.02	0.27/1.88	109.2/1.40	1.1/0.004	8.6	34.5	20:80
57.7/0.02	0.27/1.88	109.2/1.40	1.1/0.004	0.0	43.1	00:100

3.2.2.4 Synthesis of Poly(acrylic acid) (PAA) Based Particles via RAFT Mediated Polymerisation Induced Self-Assembly with different ratios of DVB to FN

In a 2-necked round bottom flask, a PAA-based macro-CTA (Macro-CTA (DDMAT-PAA_{35})), and FN were combined. The flask was then subjected to three rounds of evacuation and backfilling with nitrogen. A 1.0 wt.% solution was created by adding water and ethanol in a 60:40 (wt.%) ratio, along with DVB, to the flask. The solution was bubbled with nitrogen gas to remove any air before being heated to 70 °C. Polymerisation was initiated by adding 2 potassium persulfate (KPS) and held at 70 °C for 24 hours. The product was isolated as a white solid through reprecipitation into diethyl ether, then dried under vacuum at 40 °C for 16 hours (Table 3.3).

Table 3.3 Different monomer components for synthesis of PAA_{35} based particles

Sample Name	Monomer Composition				Solution Composition	
	PAA_{35}	DVB	FN	KPS	Water	Ethanol
	mg/mmol	mL/mmol	mg/mmol	mg/mmol	mL	mL
$PAA_{35}DVB_{210}FN_{70}$	28.8/0.01	0.30/2.10	54.6/0.70	0.6/0.002	22.5	15.0
$PAA_{35}DVB_{140}FN_{70}$	57.7/0.02	0.40/2.80	109.2/1.40	1.1/0.004	33.0	22.0
$PAA_{35}DVB_{105}FN_{70}$	57.7/0.02	0.30/2.10	109.2/1.40	1.1/0.004	27.6	18.4
$PAA_{35}DVB_{94}FN_{70}$	57.7/0.02	0.27/1.88	109.2/1.40	1.1/0.004	17.2	25.9
$PAA_{35}DVB_{70}FN_{70}$	57.7/0.02	0.20/1.40	109.2/1.40	1.1/0.004	22.1	14.8
$PAA_{35}DVB_{35}FN_{70}$	28.8/0.01	0.05/0.35	54.6/0.70	0.6/0.002	8.9	5.9

3.2.2.5 Synthesis of Poly(acrylic acid) (PAA) Based Particles via RAFT Mediated Polymerisation Induced Self-Assembly with Different Core-Shell Ratios

Synthesis of $PAA_{35}DVB_{47}FN_{35}$

In a 2-necked round bottom flask, a PAA-based macro-CTA (Macro-CTA (DDMAT-PAA_x), (x=35, 50, 95) and FN were combined. The flask was then subjected to three rounds of evacuation and backfilling with nitrogen. A 1.0 wt.% solution was created by adding water and ethanol in a 60:40 (wt.%) ratio, along with DVB, to the flask. The solution was bubbled with nitrogen gas to remove any air before being heated to 70 °C. Polymerisation was initiated by adding 2 potassium persulfate (KPS) and held at 70 °C for 24 hours. The product was isolated as a white solid through reprecipitation into diethyl ether, then dried under vacuum at 40 °C for 16 hours (Table 3.4).

Table 3.4 Different monomer components for synthesis of different PAA based particles

Sample Name	Monomer Composition				Solution Composition	
	PAA_x	DVB	FN	KPS	Water	Ethanol
	mg/mmol	mL/mmol	mg/mmol	mg/mmol	mL	mL
$PAA_{35}DVB_{47}FN_{35}$	115.4/0.04	0.26/1.88	109.2/1.40	2.2/0.008	29.4	19.6
$PAA_{35}DVB_{94}FN_{70}$	57.7/0.02	0.26/1.88	109.2/1.40	1.1/0.004	25.9	17.2
$PAA_{35}DVB_{188}FN_{140}$	28.8/0.01	0.26/1.88	109.2/1.40	0.6/0.002	24.1	16.1
$PAA_{35}DVB_{300}FN_{225}$	57.7/0.02	0.87/6.00	351.0/4.50	0.6/0.002	72.5	48.3
$PAA_{50}DVB_{47}FN_{35}$	158.6/0.04	0.26/1.88	109.2/1.40	2.2/0.008	32.0	21.3
$PAA_{50}DVB_{94}FN_{70}$	79.3/0.02	0.26/1.88	109.2/1.40	1.1/0.004	27.2	18.1
$PAA_{50}DVB_{188}FN_{140}$	39.6/0.01	0.26/1.88	109.2/1.40	0.6/0.002	24.8	16.5
$PAA_{50}DVB_{300}FN_{225}$	39.6/0.01	0.42/3.00	175.5/2.25	0.6/0.002	36.5	24.3
$PAA_{95}DVB_{47}FN_{35}$	144.1/0.02	0.13/0.94	54.6/0.70	1.1/0.004	20.4	13.6
$PAA_{95}DVB_{94}FN_{70}$	144.1/0.02	0.26/1.88	109.2/1.40	1.1/0.004	31.1	20.7
$PAA_{95}DVB_{188}FN_{140}$	72.0/0.01	0.26/1.88	109.2/1.40	0.6/0.002	26.7	17.8
$PAA_{95}DVB_{300}FN_{225}$	72.0/0.01	0.42/3.00	175.5/2.25	0.6/0.002	38.5	25.6

3.3 Results and discussion

3.3.1 Reaction kinetics of PAA based macro-CTAs and molecular weight

To begin, several different sizes (or degree of polymerisation (DP)) of PAA based shells need to be prepared. Acrylic acid (AA) was polymerised using 2-(dodecylthiocarbonothioylthio)-2-methylpropanoic acid (DDMAT) as a chain transfer agent (CTA) targeting chain lengths of 35, 50 and 100. As the RAFT polymerisation is well controlled and exhibits a linear relationship between conversion and time until high conversion is reached, after which the conversion becomes non-linear due to the low concentration of monomers in the solvent. As the reaction nears completion, it becomes difficult to precisely attain the target DP based solely on the reaction time. Therefore, extra monomer is added, and the reaction is stopped at a lower conversion to allow for the target DP to be obtained. Here, target DP of 50, 100 and 200 were used to synthesise polymers with DPs of 35, 50, and 100 while maintaining good control. 1,3,5-trioxane was used as an NMR reference according to the synthesis method of macro-CTA (DDMAT-PAA$_{35}$) at 75 °C, (during the reaction, the area of reference peak area remained constant). The conversion can be obtained by calculating the area of the residual AA by ^{1}H NMR spectroscopy and the time vs conversion can be plotted (Figure 3.2). As expected a linear relationship between time vs conversion of different samples was obtained. In addition, the mean squared error is 0.99 and is very close to 1, which means the RAFT polymerisation of acrylic acid is controllable.

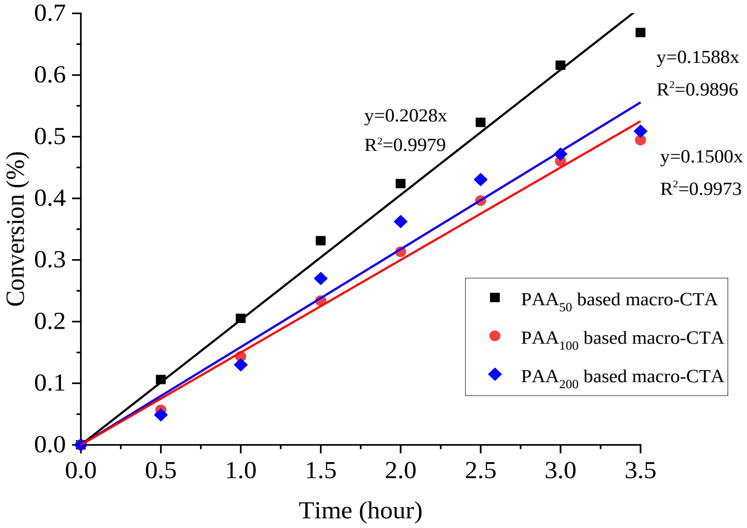

Figure 3.2 The time vs conversion of PAA based macro-CTA (DP=35, 50, 95) at 75°C

The three PAA samples synthesised had target DPs of 35, 50, and 100, but the actual DPs were determined to be 35, 50, and 95, respectively. Each DP was obtained from the time vs conversion plot, which was calculated using the ratios of ^{1}H NMR spectrum of the peaks belong to AA and the reference (1,3,5-trioxane). This is due to the concentration of the AA decreases over time while the reference peak remains constant. Here, the conversion is calculated by using this equation shown below.

$$Con\% = 1 - {}^{m_t}\!/_{m_0} = 1 - {}^{A_t}\!/_{A_0} \tag{1}$$

Here, the m_0 means the mole of AA at beginning, just adding the initiator to the system, which has the linear relationship to the integral of AA (area of AA (A_0)), m_t means the mole of AA at a certain time which equals to the integral of AA (area of AA (A_t)). The A_t can be confirmed by using the area of 1,3,5-trioxane as the standard parameter which is not changing during the whole reaction. Therefore, the conversion is about 67 % at 3.5 h and the DP is 35, for a sample of PAA_{35}. Based on the general molecular structure of macro-CTA (Figure 1.18), the DP can be determined by the ratio of monomer to CTA, which due to the repeat units of monomer of each polymer chain contain the CTA ending groups on the both sides of the polymer chain. Therefore, the DP can also be confirmed by the ^{1}H NMR spectrum of the final sample, which is after methylation (Figure 3.2 in appendix), here the DP is calculated by comparing the area of methyl (CH_3-O-) peak on the AA and the area of methylene (-S-CH_2-) peak on the DDMAT. This is based on the equation below.

$$DP = {}^{m_{mono}}\!/_{m_{CTA}} \tag{2}$$

Here, m_{mono} means the mole of AA monomer on to the macro-CTA polymer chains, and m_{CTA} means the mole of CTA on to the macro-CTA polymer chain ending groups. Moreover, the molecular weight determined by GPC analysis was 3282, which corresponds to a DP of 35 (Table 3.1 in appendix). The polydispersity index is about 1.457, which is not good enough. This may due to the higher reaction conversion, which makes the less control of the polymerisation. Using the same methods, the DPs were confirmed to be 50 and 95 with the addition of 100 and 200 monomer units, respectively.

3.3.2 Investigation of synthesis of PAA based particle in different water to ethanol ratios

To synthesise the porous polymer particles, the PAA shells need to be polymerised with a porous core forming co-polymer mixture. Divinylbenzene (DVB) and fumaronitrile (FN) are used based on the research of Li and co-workers, who synthesised a series of MOPs by using the widely available vinyl precursors DVB and FN via conventional radical polymerisation.[8] This conventional free radical polymerisation can be converted into a RAFT-PISA reaction to form porous polymer particles. The DVB acted as crosslinker while the FN acted as co-monomer in this system. Furthermore, this work can avoid some issues toward to the synthesis of conversional HCPs, such as toxic solvent, metal catalysis and by-products. This material has good BET surface area up to 805 m^2 g^{-1} and is cheap to synthesise. Moreover, James et al.[1] and Ferguson et al.[4] also used DVB and FN as the core segment to form the dispersible porous polymer particles (d-PPPs) via RAFT-PISA and confirmed that it was efficient to form the particles.

Different monomers have different reaction conditions when polymerised via RAFT-PISA depending on their reactivity and the CTA used. According to our previous research, James et al.[1] synthesised PEG based particles in a water and ethanol mixture system, which the PEG based shell can dissolve in the water and ethanol can help DVB and FN miscible in the solvent. Moreover, ethanol is friendly to the environment. Here, the water-ethanol mixture system was used to synthesise PAA based particles and the different combinations of the water to ethanol was investigated to find the best BET surface area. The BET surface area was calculated from the nitrogen adsorption isotherms at 77.3 K using the BET equation. The hydrodynamic diameter was measured by using DLS and the sample was prepared following James et al.'[1] method. 1 mg mL^{-1} water solution sample was prepared first and the water mixture was sonicated 3.0 h before the DLS analysis.

Table 3.5 Solution composition, BET surface area and size of $P(AA_{35}\text{-}DVB_{94}FN_{70})$ particles

Solution Composition (wt.%)		BET Surface Area (m^2 g^{-1})	Hydrodynamic Diameter (After 3 hours Sonication nm)
Water	Ethanol		
100	00	180	76.6
80	20	206	135.2
60	40	275	157.4
40	60	258	165.3
20	80	252	182.5
00	100	224	251.8

From the table above, the column charts can be plotted to display the relationship between the water to ethanol ratios (wt.%) and the BET surface area (Figure 3.3) and particle size (Figure 3.4). The x-axis of each chart represents the different water to ethanol ratios, while the y-axis of Figure 3.2 represents the BET surface area and the y-axis of Figure 3.3 represents the particle size.

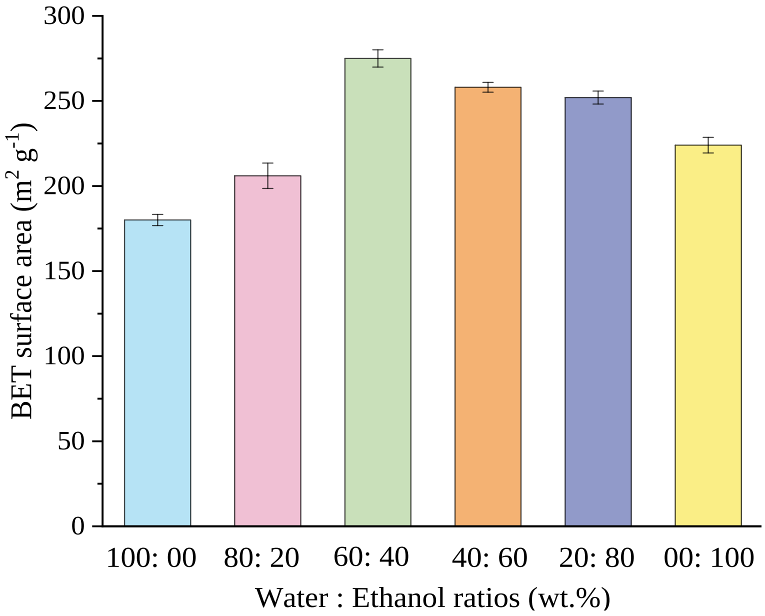

Figure 3.3 BET surface area of P(AA_{35}-$DVB_{94}FN_{70}$) particles synthesised using different water to ethanol ratios vs the BET surface area

It is very clear to see that the BET surface area initially increases as the proportion of ethanol in the water and ethanol mixture increases. The highest BET surface area is achieved at a ratio of 60:40 (wt.%) of water to ethanol. Subsequently, as the proportion of ethanol in the mixture continues to increase, the BET surface area decreases.

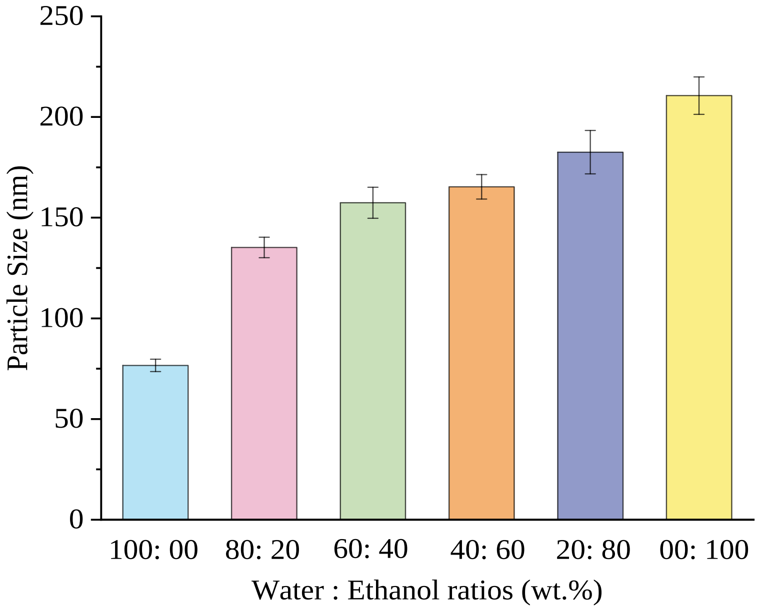

Figure 3.4 Particle size of P(AA_{35}-$DVB_{94}FN_{70}$) particles when using different water to ethanol ratios

The particle size exhibits an increasing trend with the increase of ethanol concentration in the water and ethanol mixture. This can be attributed to the solubility of DVB and FN in the mixture. When it is in an all-water condition, the solubility of DVB and FN in water is limited, resulting in fewer monomers in the system. As a result, the PAA based micelles have less these monomers inside, resulting in smaller particles with less core inside. As the concentration of ethanol increases, the ethanol monomers aid the proper dissolution of DVB and FN in the solution, resulting in an increased number of monomers in the system. Consequently, the PAA based micelles have more these monomers inside, resulting in larger particles with more core inside. When there is no water in the synthesis system, it is not a RAFT-PISA polymerisation anymore; it is becoming a conventional RAFT solution route polymerisation and the resulting particles are not dispersible in the solvent.[1]

Here the BET surface area of the particles is influenced by both their internal and external porosity. The internal porosity is created by the rigid network structure of the core part formed by DVB and FN synthesis. On the other hand, the external porosity is introduced by the voids created from the aggregation of small particles. For the sample synthesised in water, which has less internal porosity due to the less solubility of DVB and FN. For the sample synthesised in water, the internal porosity is limited due to the poor solubility of DVB and FN. However, as the concentration of ethanol in the water-ethanol mixture increases, the DVB and FN can dissolve more effectively, leading to an increase in both internal and external porosity. The largest BET surface area is achieved at a ratio of 60:40 (wt.%) of water to ethanol as the concentration of ethanol continues to increase, the polymerisation becomes more conventional, leading to a change in morphology and a decrease in BET surface area.

3.3.3 Investigation of synthesis of PAA based particle with different DVB to FN ratios

The ratio of co-monomers and crosslinks may affect the BET surface area. According to our previous research, James et al.[1] synthesised PEG based particles with the DVB and FN, and the optimal ratio of DVB and FN was found to be 4:3, which resulted in the highest BET surface area. Here, the different shell part was investigated to check if it influenced the ratio of DVB and FN. The BET surface area and particle size were measured following the above methods as described earlier.

Table 3.6 Monomer composition, BET surface area and size of particles using a water-ethanol mixture of 60:40 (wt.%)

Monomer Composition			Ratios	BET Surface	Hydrodynamic Diameter (After 3
PAA	DVB	FN	DVB:FN	Area (m^2 g^{-1})	hours Sonication nm)
35	210	70	3:1	86	242.4
35	140	70	2:1	152	236.7
35	105	70	3:2	223	175.9
35	94	70	4:3	283	157.4
35	70	70	1:1	250	171.1
35	35	70	1:2	179	176.2

From the table above, the column charts can be plotted with x-axis representing the different ratios of DVB to FN, and y-axis representing the BET surface area (Figure 3.5) and particle size (Figure 3.8).

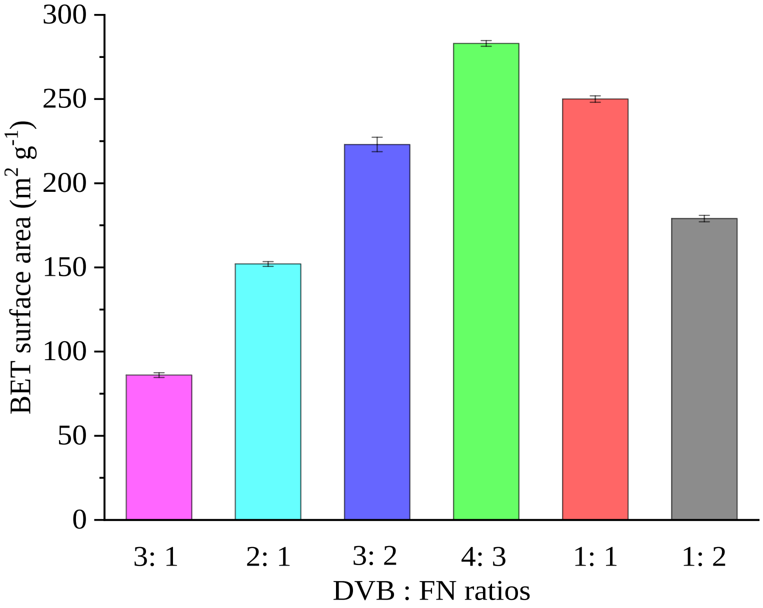

Figure 3.5 BET surface area of particles synthesised when using different DVB to FN ratios

It is very clear to see that as the proportion of FN increases, the BET surface area initially increases starting from the ratio of DVB to FN of 3:1 and reaches maximum at the ratio of 4:3. However, as the proportion of FN further increases, the BET surface area starts decreasing and reaches the minimum value at the ratio of DVB to FN of 1:2.

It has been verified that PAA_{35} based particles with different DVB to FN ratios contain a dual morphology with smaller spheres structure to aggregate to form larger particles as well compared to the PEG based particles[1] (Figure 3.6).

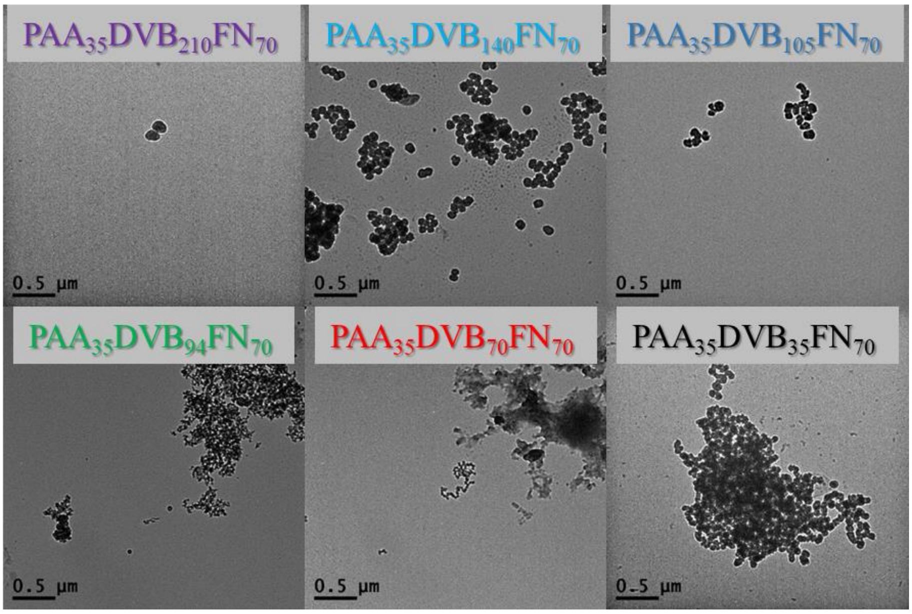

Figure 3.6 TEM images of PAA_{35} based particles with different DVB to FN ratios

The nitrogen adsorption isotherms (Figure 3.7 a) exhibit a slight increase for all particles at a very low pressure ($P/P_0 < 0.1$), indicating a limited presence of microporous structures. This is different from the PEG based particles[1–4] which were synthesised by DVB and FN and show more microporous structures, which may be due to the PAA based shells is branched and larger than the PEG based shell. Additionally, no hysteresis loop is observed in the relative pressure region of $0.2 < P/P_0 < 0.8$, which is the same as the PEG based particles. The significant increase of gas uptake at a high pressure ($P/P_0 > 0.9$) corresponds to nitrogen condensation in large pores. This is due to the condensation of nitrogen between the smaller particles in the larger particle agglomeration, as observed in PEG based particles. The pore size distributions (PSDs) of the PAA_{35} based particles with different combination of DVB and FN (Figure 3.7 b) demonstrate a range of pore sizes for particles with varying DVB to FN ratios. However it should be noted that no measurements were taken for very low-pressure points in these samples, which precludes an accurate estimation of micropore sizes. All samples exhibit similar pore diameters, except for the $P(AA_{35}\text{-}DVB_{210}FN_{70})$ particles, contain a small amount of mesopores and larger pores and voids. For other particles, larger peaks appear at pore widths of approximately 3.1 nm, 5.2 nm, and 9.1 nm, along with further larger pores and voids resulting from the aggregation of small sphere particles.

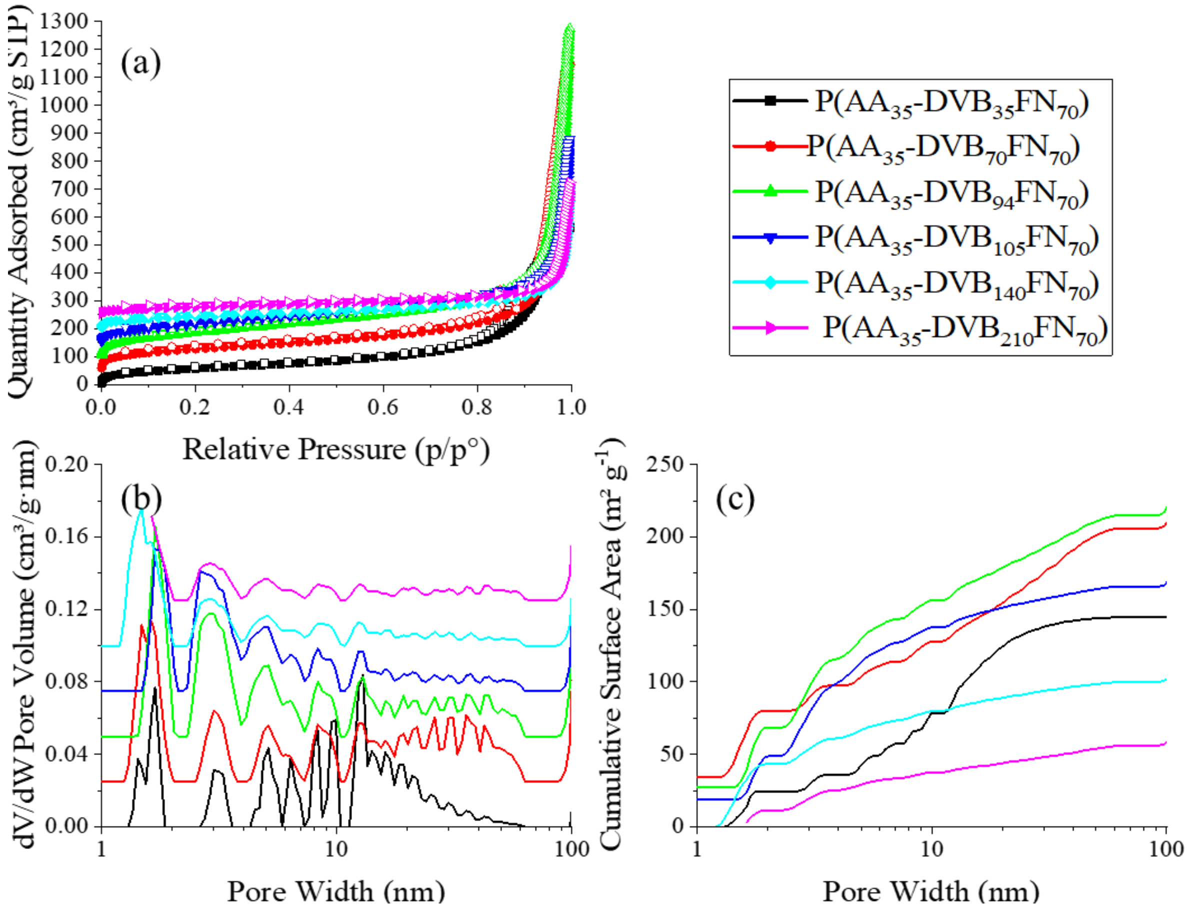

Figure 3.7 (a) Nitrogen adsorption isotherms of PAA_{35} based particles with different combination of DVB and FN at 77.3 K (Isotherms each offset by 50 $cm^3\ g^{-1}$); (b) Pore size distributions calculated using NLDFT method (slit pore models, differential pore volume vs pore width); and (c) Cumulative surface areas

The cumulative surface area plots (Figure 3.7 c) also show that most of the pore volume is the larger meso- and macropore region, while the particles have less microporous region, especially for $P(AA_{35}\text{-}DVB_{35}FN_{70})$, $P(AA_{35}\text{-}DVB_{140}FN_{70})$, and $P(AA_{35}\text{-}DVB_{210}FN_{70})$ particles which nearly no-micropores. Among particles with varying DVB to FN ratios, those with a ratio of 4:3 exhibit higher cumulative surface area compared to others. Moreover, the amount of cumulative surface area decreases with the ratio of DVB to FN further increasing or decreasing. For the $P(AA_{35}\text{-}DVB_{35}FN_{70})$, $P(AA_{35}\text{-}DVB_{140}FN_{70})$, and $P(AA_{35}\text{-}DVB_{210}FN_{70})$ particles which have the smaller amounts of small voids and large voids compared to the $P(AA_{35}\text{-}DVB_{70}FN_{70})$, $P(AA_{35}\text{-}DVB_{94}FN_{70})$, and $P(AA_{35}\text{-}DVB_{105}FN_{70})$ particles. This observation may arise from the fact that the latter group contains smaller sphere particles that aggregate to form larger aggregates with more voids, while the former group contains larger sphere particles.

The particle size varies when using the PAA_{35} based particles with different combinations of DVB and FN. These particles exhibit a dual morphology with smaller spheres structure to aggregate to form larger particles of 171-243 nm diameter. Additionally, particle size is inversely proportional to BET surface area and TEM images show the same trends (Figure 3.3, Figure 3.4, Figure 3.5, Figure 3.6, Figure 3.7 and Figure 3.8 in appendix). Moreover, the particle size from TEM images are 250 nm, 240 nm, 200 nm, 150 nm, 180 nm and 200 nm, respectively, which are very close to the DLS results.

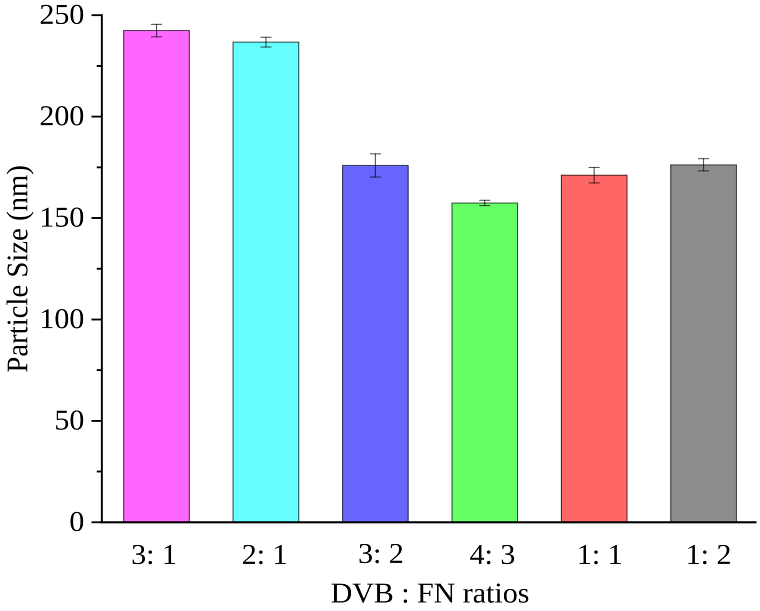

Figure 3.8 Particle size of particles synthesised when using different DVB to FN ratios

The results we obtained matched the principles which Xie et al.[8] found. They found that the concentration of nitrogen had an influence on the BET surface area in the FN/St system. They thought the low concentration of FN would prevent the FN units joining in the polymerisation and it would be a tendency toward the other periodic copolymers (DVB-DVB-FN) exists.[9,10] When the concentration increased, FN not only increased the content of DVB units with both double bonds polymerisation, but also increased the concentration of nitrogen in the system leading to higher crosslinking density and thus a higher surface area. When the concentration of FN was very high, steric hindrance prevents FN units from participating in the polymerisation, resulting in a low surface area.[11,12] Mole ratio of 0.75 of FN to DVB (equivalent to DVB to FN in a 4:3 ratio) had the highest BET surface area. Moreover, the different ratios of DVB to FN can affect the particle size. According to the study of Xie and co-workers[8], the formation of copolymers may increase the core particle size at low FN concentrations, while at high concentrations, the electrostatic repulsion between nitrile groups may also contribute to an increase in particle size.

3.3.4 Investigation of synthesis of PAA based particle with different core-shell ratios

The ratios of core to shell may influence the BET surface area as well. According to our previous research, James et al.[1] synthesised PEG based particles with varying ratios of PEG part to the DVB and FN part have different BET surface area. Here, the different core-shell ratios were investigated to check if it influences the BET surface area. The BET surface area and particle size were measured following the same methods.

Table 3.7 Monomer composition, BET surface area and size of PAA based particles with different ratios of core-shell

Monomer Composition			BET Surface	Hydrodynamic Diameter (After 3
PAA	DVB	FN	Area (m^2 g^{-1})	hours Sonication nm)
35	47	35	322	195.4
35	94	70	283	157.4
35	188	140	261	261.3
35	300	225	150	197.6
50	47	35	219	121.1
50	94	70	257	128.8
50	188	140	170	111.8
50	300	225	147	174.0
95	47	35	188	174.0
95	94	70	227	123.0
95	188	140	145	225.8
95	300	225	60	298.4

From the table above, the column charts can be plotted that x-axis means the different core-shell ratios, y-axis means the BET surface area (Figure 3.9) and particle size (Figure 3.13).

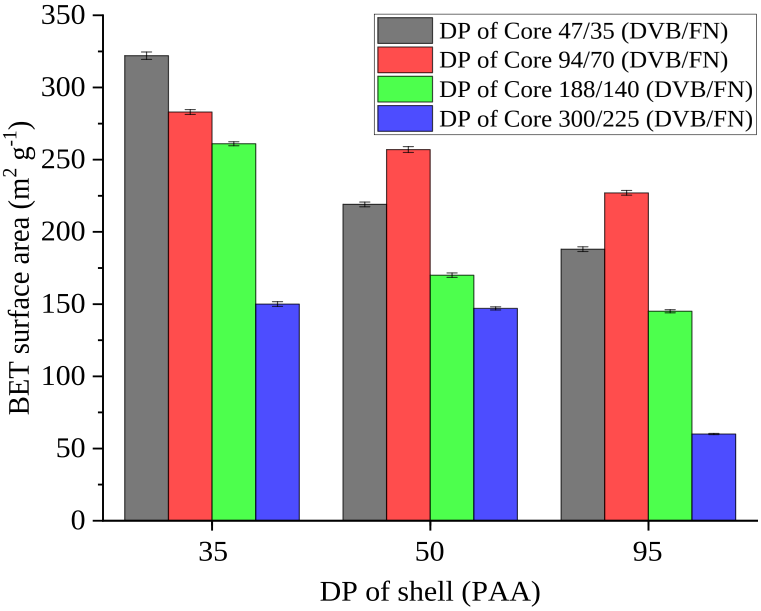

Figure 3.9 BET surface area of particles synthesised when using different core-shell ratios

For the particles with same shell chain length (together), changes in core-shell ratios can impact the BET surface. For PAA_{35} based shells, increasing core size results in a decrease in BET surface area. For the other two shells, the BET surface area slightly increases as core size grows from 47 to 94 (DP of DVB), but then decreases as core size increases from 94 to 300, gradually. It seems there appears to be a fixed ratio of shell-to-core weight percentage that maximizes the BET surface area, as observed in PEG based particles where the BET surface area initially increases with core size before decreasing after reaching $P(EG_{113}\text{-}DVB_{600}FN_{450})$.[1] However, the core size at which the BET surface reaches a maximum is lower compared to that for the PEG based particles. For the particles with same core size (same colour), the BET surface decreases with the growing of the shell chain length. In brief, the particles with smaller shells have larger BET surface area than the particles with the long shell chains.

PAA_{35}, PAA_{50} and PAA_{95} based particles with different core-shell ratios display a similar morphology to the PAA_{35} based particles with different DVB to FN ratios with a dual morphology with smaller spheres structure to aggregate to form larger (Figure 3.9-19 in appendix).

The nitrogen adsorption isotherms of PAA_{35} based particles with different core-shell ratios (Figure 3.10 a) show a similar pattern to those with varying DVB to FN ratios. They all exhibit large peaks at a pore width of around 1.8 nm, 3.0 nm, 5.1 nm and along with further larger pores and voids from the pore size distributions (Figure 3.10 b). These materials exhibit microporosity in the cumulative surface area plots (Figure 3.10 c). However, for $\mathrm{P(AA_{35}DVB_{300}FN_{220})}$ particles, which have little microporous structures.

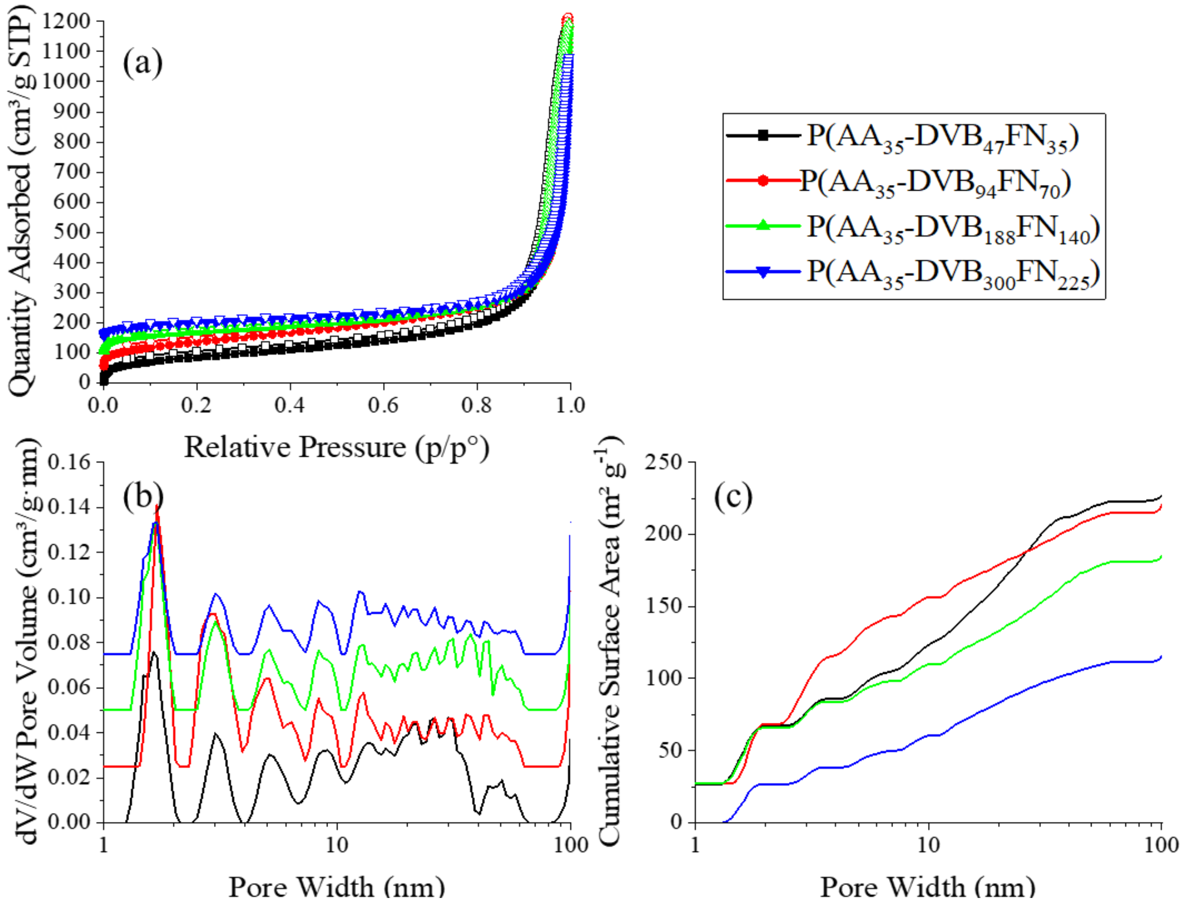

Figure 3.10 Nitrogen adsorption isotherms of (a) the $\mathrm{PAA_{35}}$ based particles (b) Pore size distributions calculated using NLDFT method (slit pore models, differential pore volume vs pore width); and (c) Cumulative surface areas

It seems that the $\mathrm{PAA_{50}}$ based particles have a similar nitrogen uptake curves (Figure 3.11 a) to the $\mathrm{PAA_{35}}$ based particles. The pore size distributions of $\mathrm{PAA_{50}}$ based particles (Figure 3.11 b) show the similar results compared to $\mathrm{PAA_{35}}$ based particles, that all have small pores at a pore width of about 1.8 nm, 3.0 nm, 5.1 nm, 8.4 nm and along with further larger pores.

The difference is that the ratios of amounts of different pores decreased. These materials have little micropores except for $\mathrm{P(AA_{50}DVB_{94}FN_{70})}$ particles which contain more microporous region in the cumulative surface area plots (Figure 3.11 c).

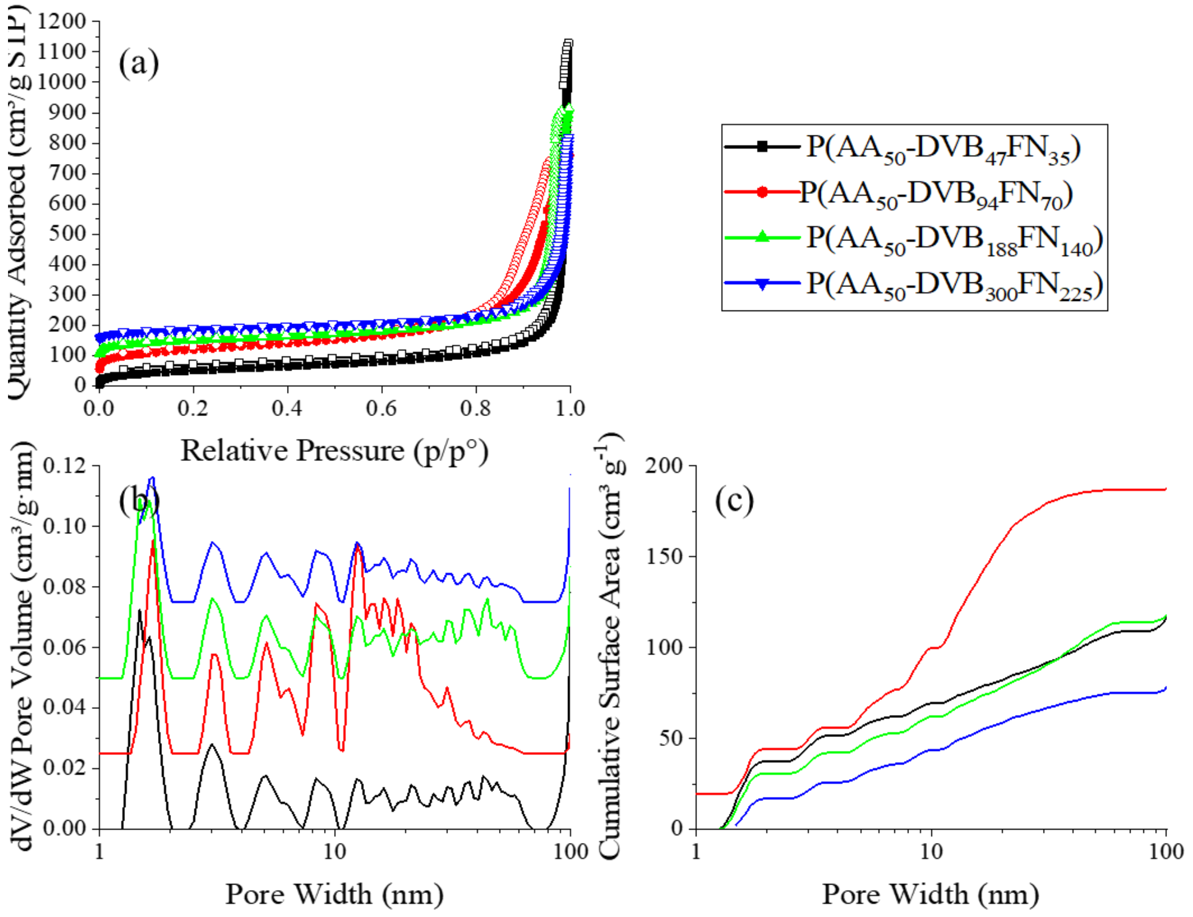

Figure 3.11 Nitrogen adsorption isotherms of (a) the PAA_{50} based particles (b) Pore size distributions calculated using NLDFT method (slit pore models, differential pore volume vs pore width); and (c) Cumulative surface areas

There are similar adsorption isotherms of PAA_{95} based particles (Figure 3.12 a) were as seen for all PAA based particles. They all reveal the similar pore size to other PAA based particles with main peaks at a pore width about 1.8 nm, 3.0 nm, 5.2 nm, 7.1 nm and along with further larger pores and voids (Figure 3.12 b). The cumulative surface area plots (Figure 3.12 c) illustrate the structures of the particles as well, which most of the pore volume is the larger meso- and macropore region. This means that these materials are all less microporous except for $P(AA_{95}DVB_{300}FN_{220})$ particles like previous shells with the largest core have nearly no-porous structure.

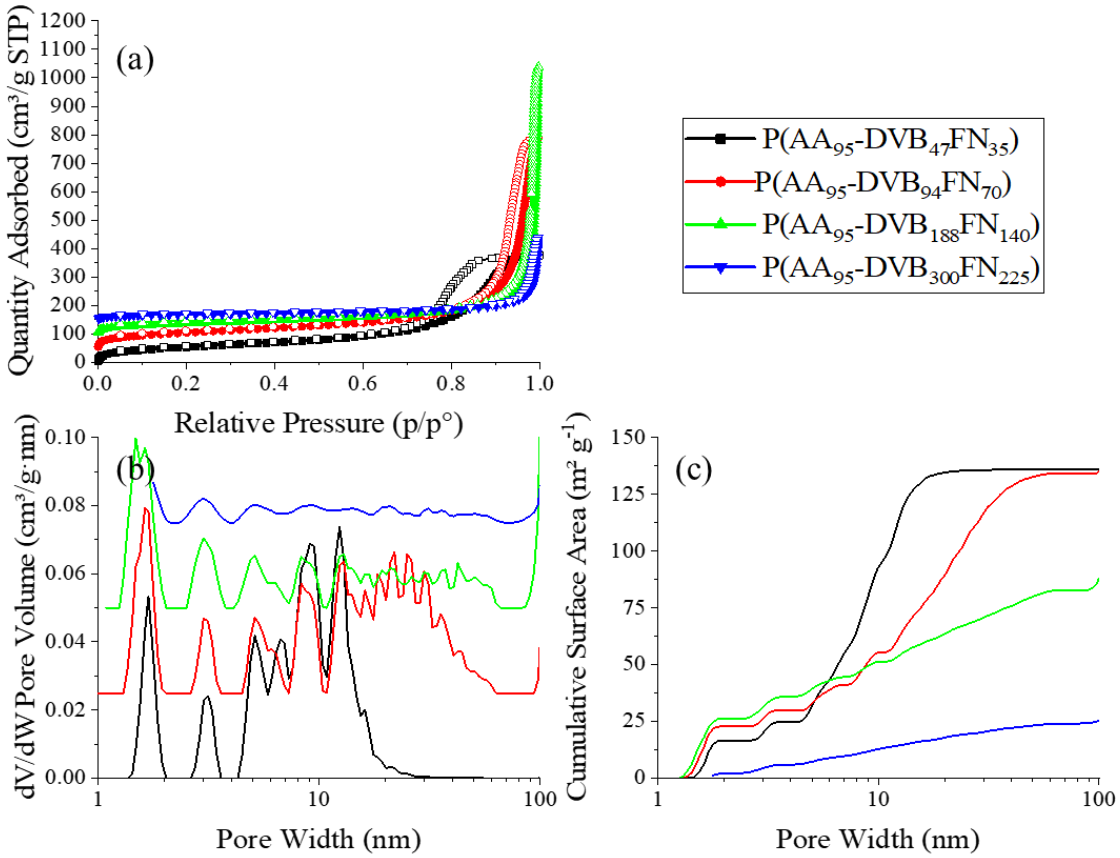

Figure 3.12 Nitrogen adsorption isotherms of (a) the PAA_{95} based particles (b) Pore size distributions calculated using NLDFT method (slit pore models, differential pore volume vs pore width); and (c) Cumulative surface areas

For the plot of core vs shell vs particle size, it seems that there is no obvious tendency among core size, shell chain length and particle size. However, the particle with a large BET surface area tend to have a small particle size (Figure 3.13). This trend is also observed in TEM images (Figure 3.6, Figure 3.9-19 in appendix). The particle sizes measured from TEM images are consistent with those from DLS, with values ranging from 120 to 300 nm. In addition, after sonication 3 hours, the particles are quite stable in the solvent. It is stable and disperses very well in the organic solvent, such as methanol (Figure 3.20-22 in appendix). It can also last 1 week in the water (Figure 3.23-25 in appendix).

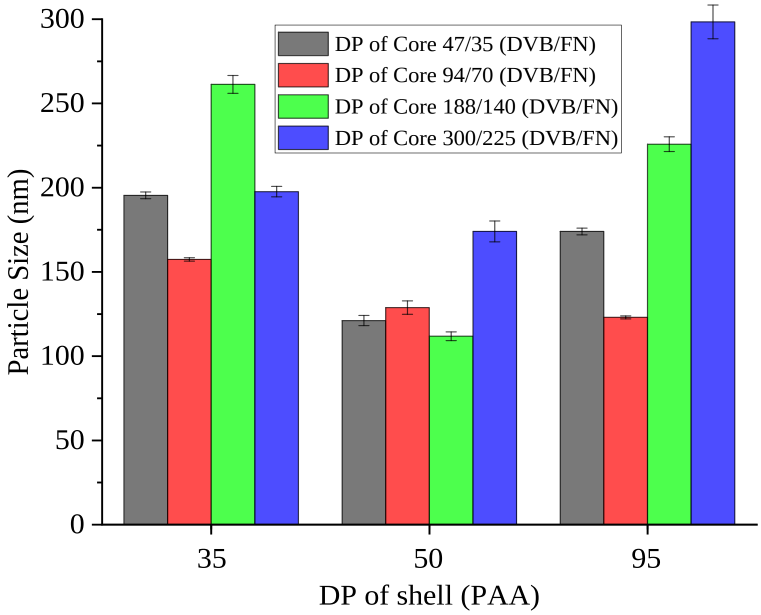

Figure 3.13 Particle size of particles synthesised when using different core-shell ratios

3.4 Conclusion

To conclude, RAFT can be used to synthesise the diblock copolymer with hydrophobic parts and hydrophilic parts. 2-(dodecylthiocarbonothioylthio)-2-methylpropanoic acid used as CTA was well synthesised via one pot step, firstly. It is determined to be a good choice to synthesise the monomer, which has a carboxylic group.

The hydrophilic block (PAA) was synthesised to obtain the macro-CTA via RAFT. The synthesis of PAA can be well controlled through the study of the reaction kinetics. It is a linear relationship between reaction time and conversion at the beginning; this is due to the side reaction that will lead to a big DPI at high conversion. Furthermore, the temperature and the concentration are important which will have effects on the polymerisation. The molecular weight of different macro-CTAs were determined by 35, 50, 95 via the conversion data by ^{1}H NMR spectrum, the ^{1}H NMR spectrum after methylation, and GPC analysis after methylation.

Poly(acrylic acid-b-divinylbenzene/fumaronitrile) (PAA-DVB/FN) was synthesised via RAFT mediated polymerisation induced self-assembly. This makes the PAA-DVB/FN to be a core-shell structure where the PAA is the hydrophilic part of the shell structure and the DVB/FN is the hydrophobic part of the core structure, which contains both porosity and dispersiblity in common organic solvents. Furthermore, PAA based particles have a dual morphology with smaller spheres structure to aggregate to form larger particles. First, the reaction solution was investigated to find the suitable water to ethanol ratio for the largest BET surface area and it is confirmed that for water soluble shell parts, the water to ethanol ratio equals 60:40 (wt.%) is best. PEG based particles were prepared in the water to ethanol mixture with a ratio of 60:40 (wt.%) has the large BET surface area as well.[1–3,13] Then, the ratios of DVB and FN were investigated to find the suitable combination for the biggest BET surface area. It is confirmed that the concentration of nitrogen has influence on the BET surface area and particle size for the FN/St or FN/DVB system and the best ratio of DVB to FN is 4 to 3. HCPN[8] and PEG based particles[1–3,13] also show the same results. Finally, the different core-shell ratios were investigated to find the tendency of different core-shell ratios to the BET surface area. The optimum core-shell ratio was explored by fixing the shell chain length and varying the core size (or fixing the core size and varying the shell chain length). Here, we found that the BET surface area increases with the core size growing. However, when the BET surface area increased reaching a maximum at one point, the BET surface area decreases with the core size further growing compared to PEG based particles which has the same trend, but the core size at which the BET surface reaches a maximum is lower compared to that for the PEG based particles. Moreover, the particles with small shells have a good BET surface area up to 322 m^2 g^{-1} which is a little smaller than the BET surface area of PEG based particle (409 m^2 g^{-1}).

Furthermore, the PAA based particles can also dissolve in different solvent with good separation and last for a long time same as the PEG based particle (Figure 3.20-3.25 in appendix). However, the most of PAA based particles have smaller particle sizes compared to PEG based particles, which is due to the shorter of the shell chain length.

3.5 References

(1) James, A. M.; Derry, M. J.; Train, J. S.; Dawson, R. Dispersible Microporous Diblock Copolymer Nanoparticles via Polymerisation-Induced Self-Assembly. *Polym. Chem.* **2019**, *10* (28), 3879–3886. https://doi.org/10.1039/C9PY00596J.

(2) James, A. M.; Dawson, R. Efficient and Tunable White-Light Emission Using a Dispersible Porous Polymer. *Macromol. Rapid Commun.* **2020**, *41* (12), 2000176. https://doi.org/10.1002/marc.202000176.

(3) Ivko, S. A.; James, A. M.; Derry, M. J.; Dawson, R.; Haynes, A. Heterogenisation of a Carbonylation Catalyst on Dispersible Microporous Polymer Nanoparticles. *Catal. Sci. Technol.* **2022**, *12* (2), 664–673. https://doi.org/10.1039/D1CY01989A.

(4) Ferguson, C. T. J.; Huber, N.; Kuckhoff, T.; Zhang, K. A. I.; Landfester, K. Dispersible Porous Classical Polymer Photocatalysts for Visible Light-Mediated Production of Pharmaceutically Relevant Compounds in Multiple Solvents. *J. Mater. Chem. A* **2020**, *8* (3), 1072–1076. https://doi.org/10.1039/C9TA11242A.

(5) Pangborn, A. B.; Giardello, M. A.; Grubbs, R. H.; Rosen, R. K.; Timmers, F. J. Safe and Convenient Procedure for Solvent Purification. *Organometallics* **1996**, *15* (5), 1518–1520. https://doi.org/10.1021/om9503712.

(6) Skey, J.; K. O'Reilly, R. Facile One Pot Synthesis of a Range of Reversible Addition–Fragmentation Chain Transfer (RAFT) Agents. *Chem. Commun.* **2008**, *0* (35), 4183–4185. https://doi.org/10.1039/B804260H.

(7) Chaduc, I.; Crepet, A.; Boyron, O.; Charleux, B.; D'Agosto, F.; Lansalot, M. Effect of the PH on the RAFT Polymerisation of Acrylic Acid in Water. Application to the Synthesis of Poly(Acrylic Acid)-Stabilized Polystyrene Particles by RAFT Emulsion Polymerisation. *Macromolecules* **2013**, *46* (15), 6013–6023. https://doi.org/10.1021/ma401070k.

(8) Xie, F.; Hu, W.; Ding, L.; Tian, K.; Wu, Z.; Li, L. Synthesis of Microporous Organic Polymers via Radical Polymerisation of Fumaronitrile with Divinylbenzene. *Polym. Chem.* **2017**, *8* (39), 6106–6111. https://doi.org/10.1039/C7PY01240C.

(9) Ham, G. E. Application of an Expanded Copolymerisation Equation to the System Styrene–Fumaronitrile. *J. Polym. Sci.* **1960**, *45* (145), 177–181. https://doi.org/10.1002/pol.1960.1204514517.

(10) Ham, G. E. Tacticity as a Problem in Copolymerisation: Influence of Neighboring Units on Reactivity of Growing Chains. *J. Polym. Sci.* **1962**, *61* (171), 9–17. https://doi.org/10.1002/pol.1962.1206117103.

(11) Barb, W. G. Effect of Nonterminal Monomer Units on the Reactivity of Polymeric Free Radicals. *J. Polym. Sci.* **1953**, *11* (2), 117–126. https://doi.org/10.1002/pol.1953.120110202.

(12) Ham, G. E. Reactivity of Polar Monomers in Copolymerisation. *J. Polym. Sci.* **1954**, *14* (73), 87–93. https://doi.org/10.1002/pol.1954.120147308.

(13) Ferguson, C. T. J.; Huber, N.; Kuckhoff, T.; Zhang, K. A. I.; Landfester, K. Dispersible Porous Classical Polymer Photocatalysts for Visible Light-Mediated Production of Pharmaceutically Relevant Compounds in Multiple Solvents. *J. Mater. Chem. A* **2020**, *8* (3), 1072–1076. https://doi.org/10.1039/C9TA11242A.

3.6 Appendix

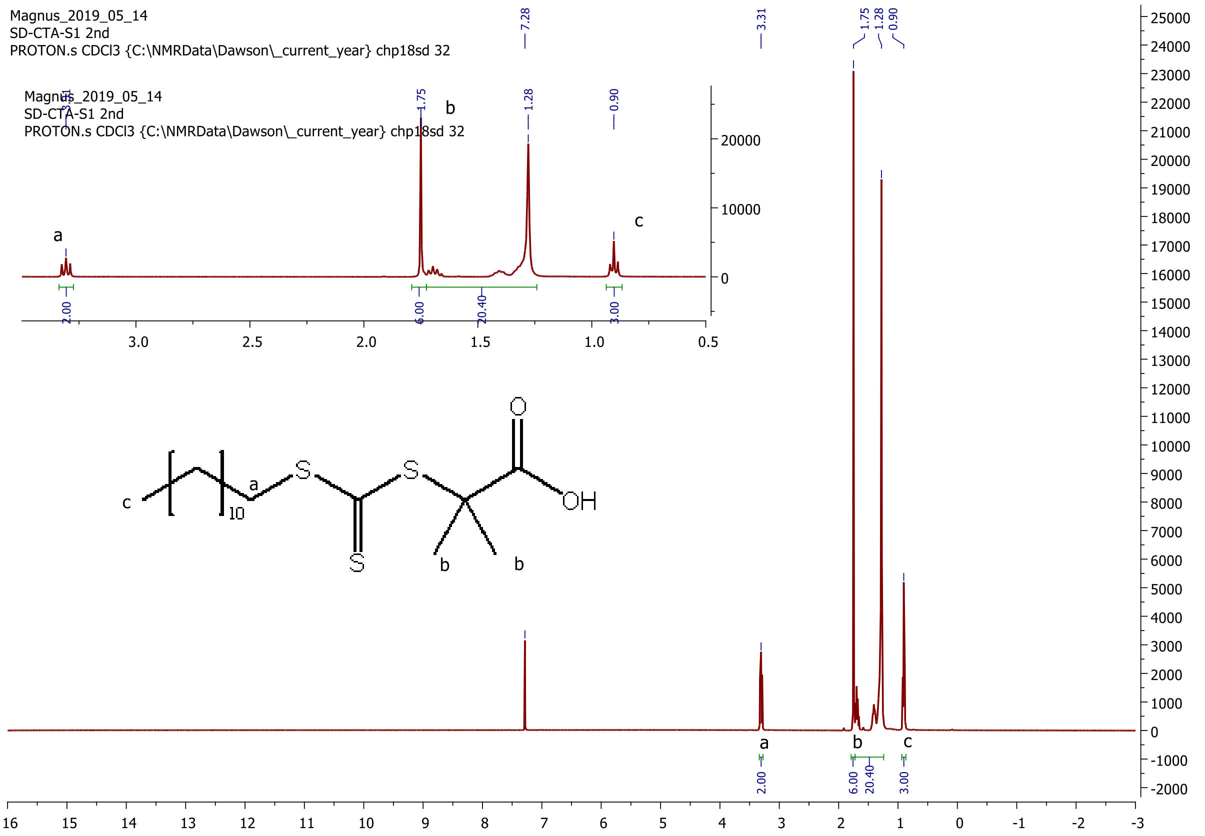
Magnus_2019_05_14
SD-CTA-S1 2nd
PROTON.s CDCl3 {C:\NMRData\Dawson_current_year} chp18sd 32
7.28
3.31
1.75
1.28
0.90
Magnus_2019_05_14
SD-CTA-S1 2nd
PROTON.s CDCl3 {C:\NMRData\Dawson_current_year} chp18sd 32
1.75
1.28
0.90
a
b
c
2.00
6.00
20.40
3.00
20000
10000
0
3.0
2.5
2.0
1.5
1.0
0.5
O
S
S
OH
S
c
a
10
b
b
25000
24000
23000
22000
21000
20000
19000
18000
17000
16000
15000
14000
13000
12000
11000
10000
9000
8000
7000
6000
5000
4000
3000
2000
1000
0
-1000
-2000
a
b
c
2.00
6.00
20.40
3.00
16
15
14
13
12
11
10
9
8
7
6
5
4
3
2
1
0
-1
-2
-3

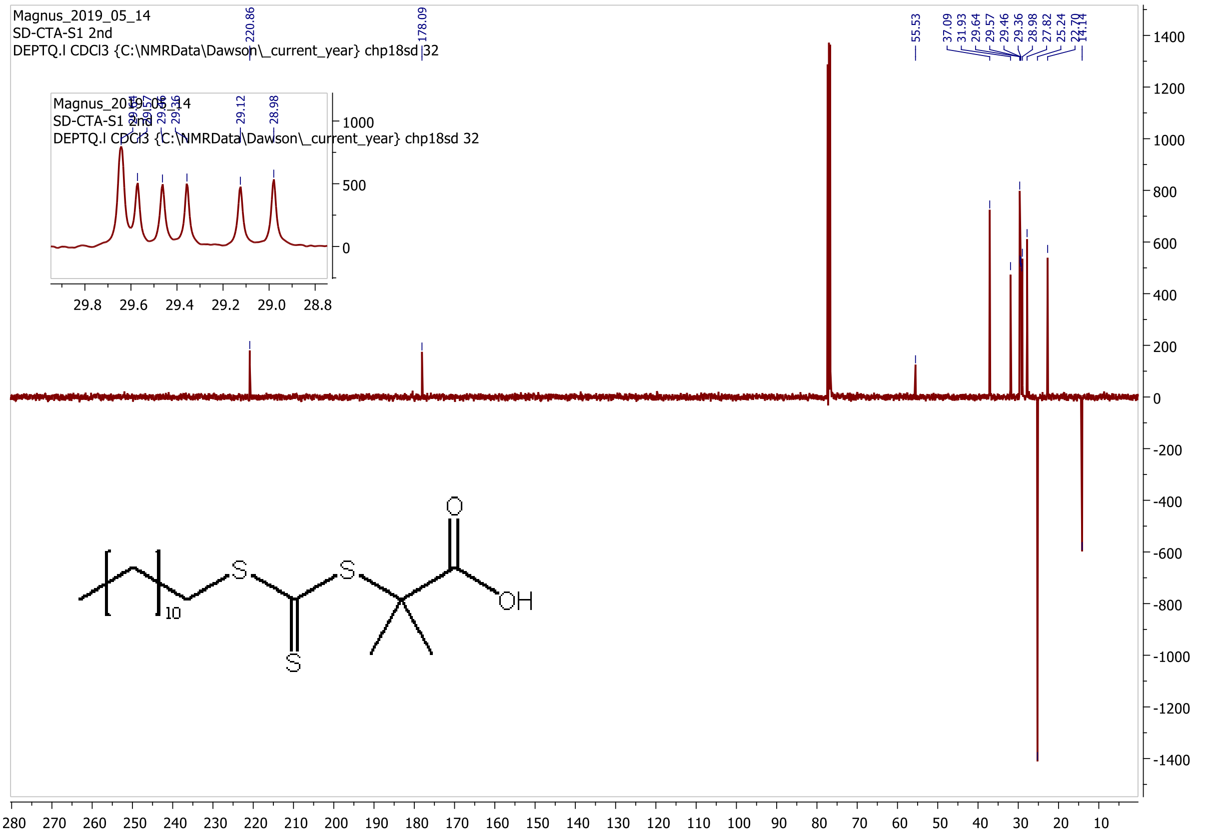
Magnus_2019_05_14
SD-CTA-S1 2nd
DEPTQ.l CDCl3 {C:\NMRData\Dawson_current_year} chp18sd 32
220.86
178.09
55.53
37.09
31.93
29.64
29.57
29.46
29.36
28.98
27.82
25.24
22.70
14.14
Magnus_2019_05_14
SD-CTA-S1 2nd
DEPTQ.l CDCl3 {C:\NMRData\Dawson_current_year} chp18sd 32
29.12
28.98
1000
500
0
29.8
29.6
29.4
29.2
29.0
28.8
O
S
S
OH
S
10
1400
1200
1000
800
600
400
200
0
-200
-400
-600
-800
-1000
-1200
-1400
280
270
260
250
240
230
220
210
200
190
180
170
160
150
140
130
120
110
100
90
80
70
60
50
40
30
20
10

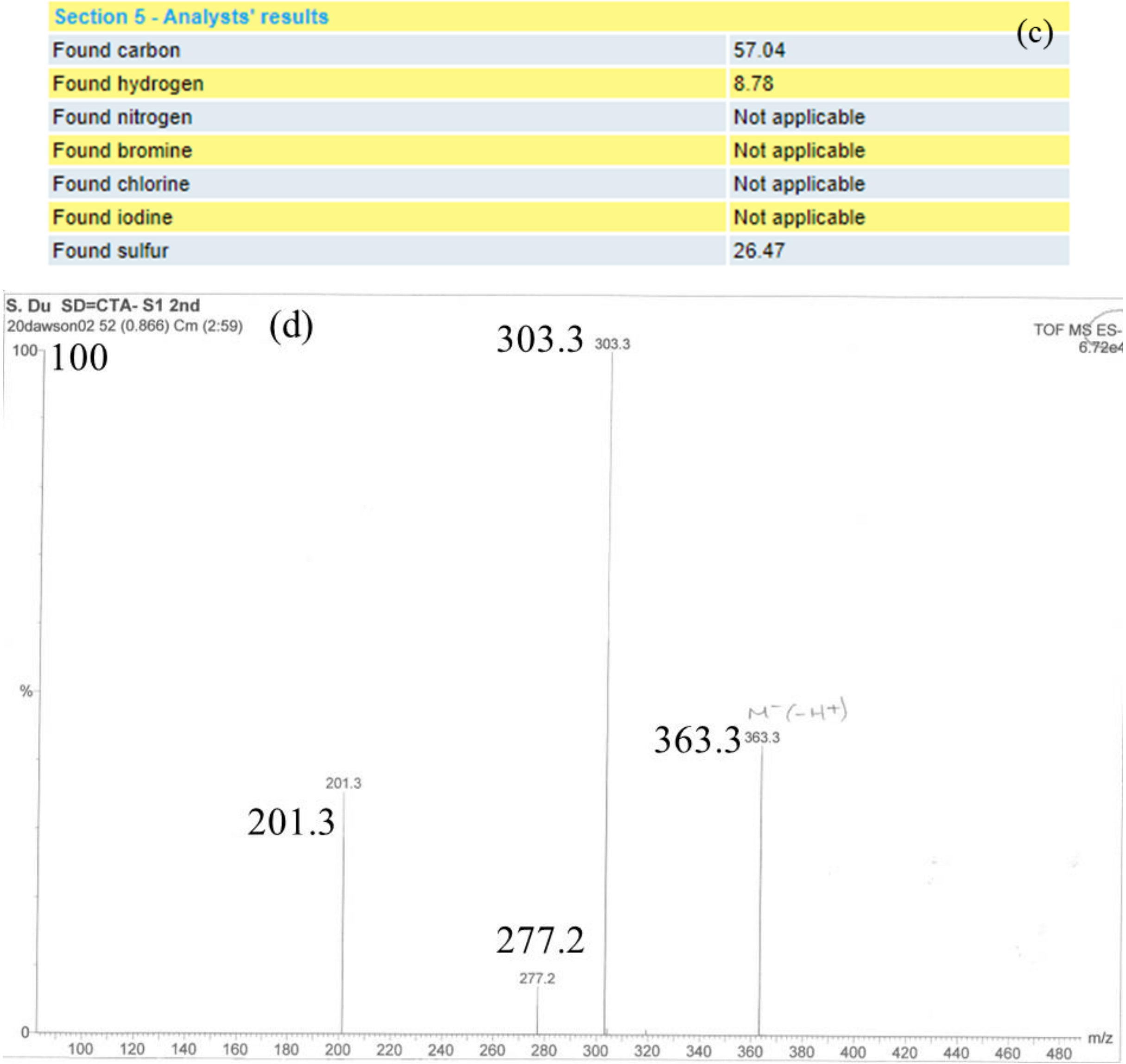

Section 5 - Analysts' results	
Found carbon	57.04
Found hydrogen	8.78
Found nitrogen	Not applicable
Found bromine	Not applicable
Found chlorine	Not applicable
Found iodine	Not applicable
Found sulfur	26.47

Figure 3.1 (a) ^{1}H NMR spectrum of CTA, (b) ^{13}C NMR spectrum, (c) elemental analysis, and (d) mass spectrum

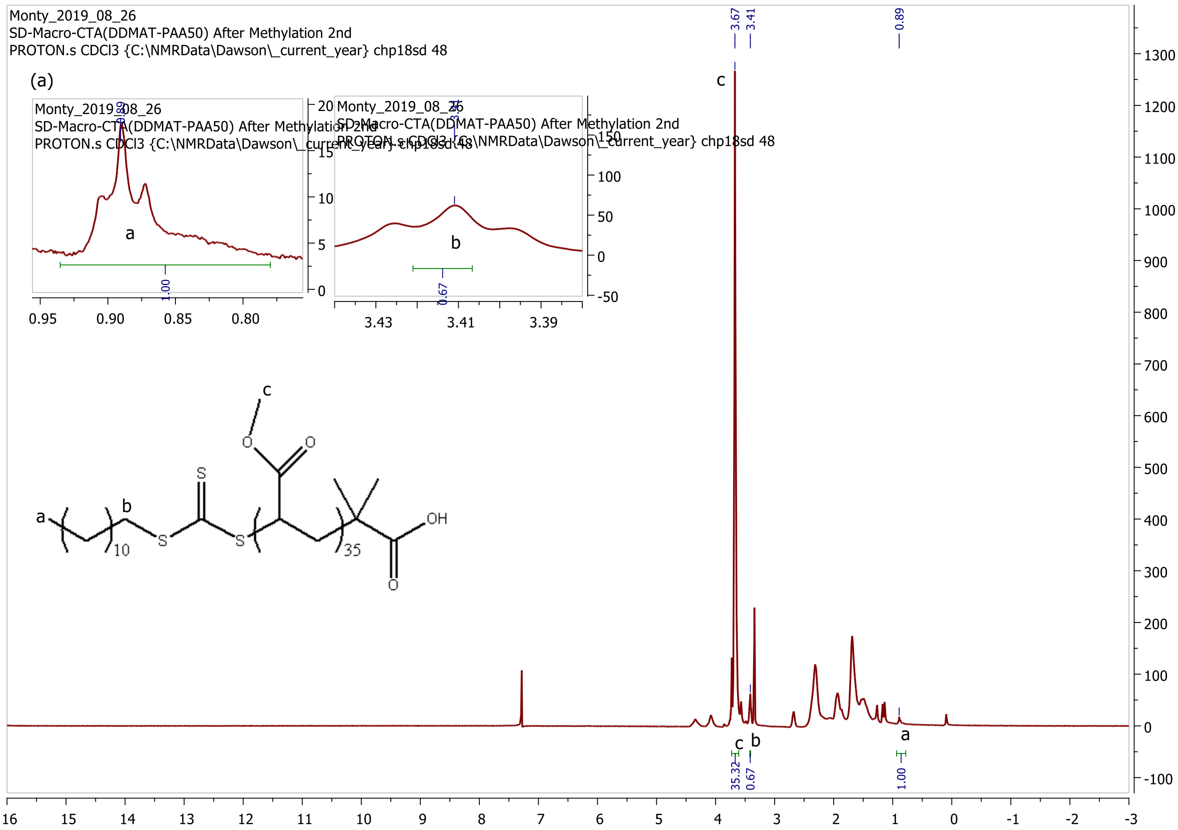
Monty_2019_08_26
SD-Macro-CTA(DDMAT-PAA50) After Methylation 2nd
PROTON.s CDCl3 {C:\NMRData\Dawson_current_year} chp18sd 48
(a)
3.67
3.41
0.89
c
a
b
1.00
0.67
0.95
0.90
0.85
0.80
3.43
3.41
3.39
OH
S
O
10
35
35.32
c b
a
16 15 14 13 12 11 10 9 8 7 6 5 4 3 2 1 0 -1 -2 -3
1300 1200 1100 1000 900 800 700 600 500 400 300 200 100 0 -100

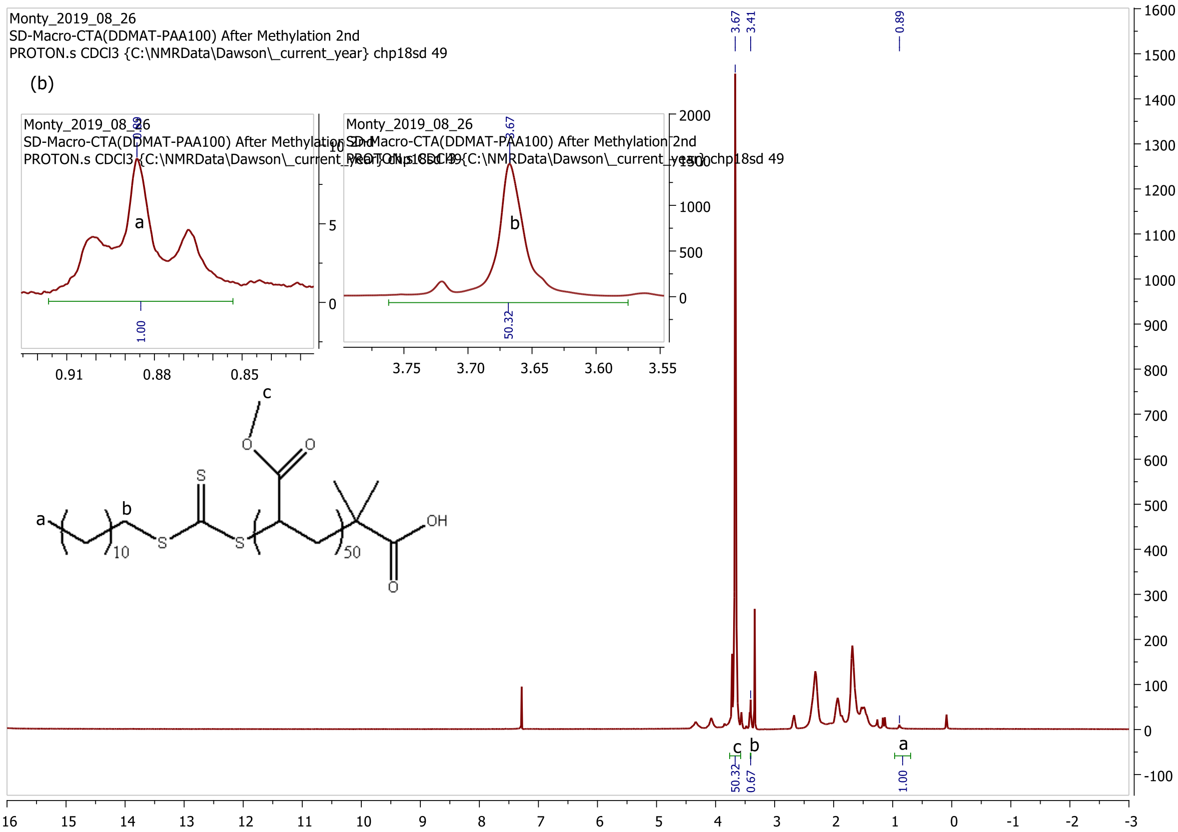
Monty_2019_08_26
SD-Macro-CTA(DDMAT-PAA100) After Methylation 2nd
PROTON.s CDCl3 {C:\NMRData\Dawson_current_year} chp18sd 49
(b)
3.67
3.41
0.89
a
b
c
1.00
50.32
0.91
0.88
0.85
3.75
3.70
3.65
3.60
3.55
OH
S
O
10
50
0.67
c b
a
16 15 14 13 12 11 10 9 8 7 6 5 4 3 2 1 0 -1 -2 -3
1600 1500 1400 1300 1200 1100 1000 900 800 700 600 500 400 300 200 100 0 -100

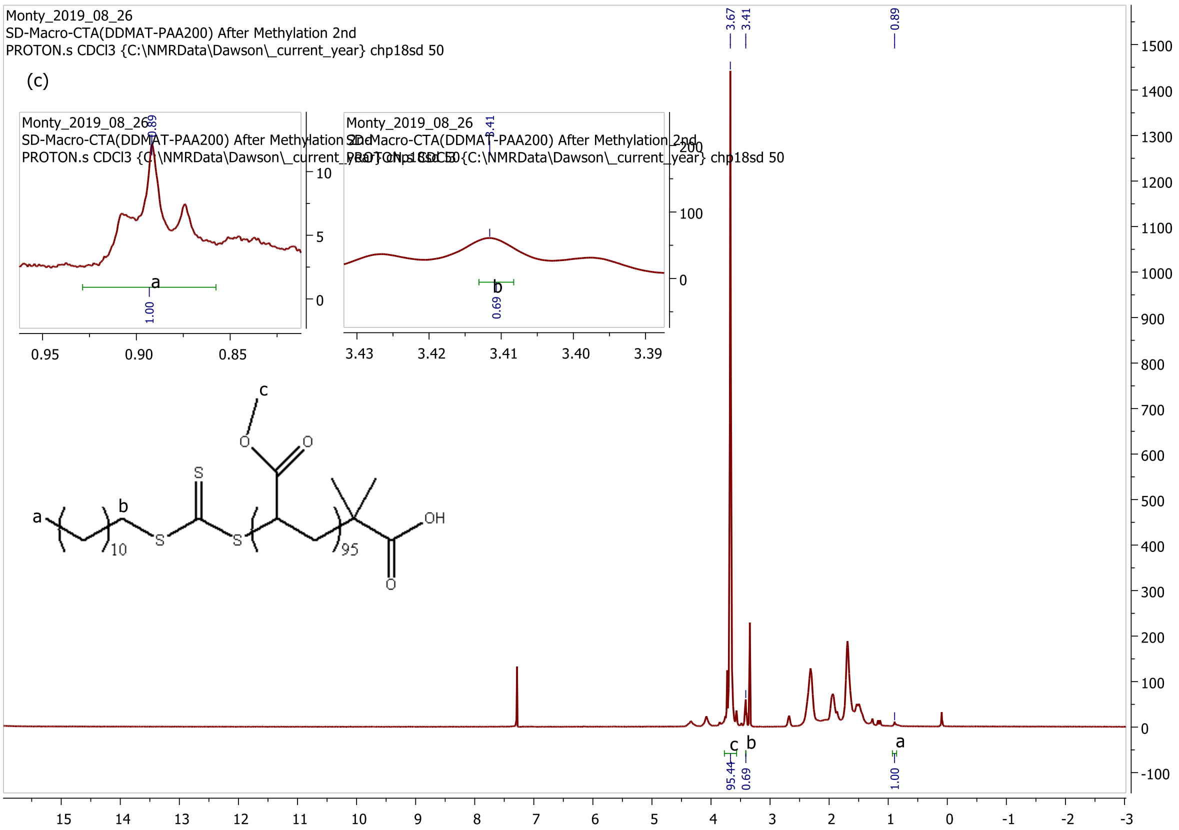

Figure 3.2 The ^{1}H NMR spectrum of PAA$_{35}$ based macro-CTA, PAA$_{50}$ based macro-CTA, and PAA$_{95}$ based macro-CTA after methylation

Table 3. The GPC analysis of PAA$_{35}$ based macro-CTA after methylation

GPC analysis (containing 4 v/v% Acetic acid and 0.025% BHT)

Peak	Mp(g/mol)	Mn(g/mol)	Mw(g/mol)	Mz(g/mol)	Mz+1(g/mol)	Mv(g/mol)	DP
1	4787	3282	4782	6383	7758	6165	1.457

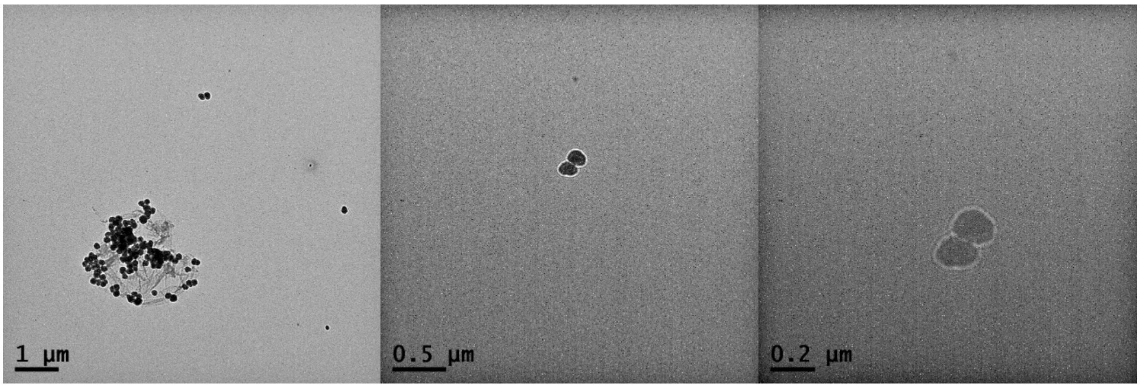

Figure 3.3 The different scales of TEM images of P(AA$_{35}$-DVB$_{210}$FN$_{70}$)

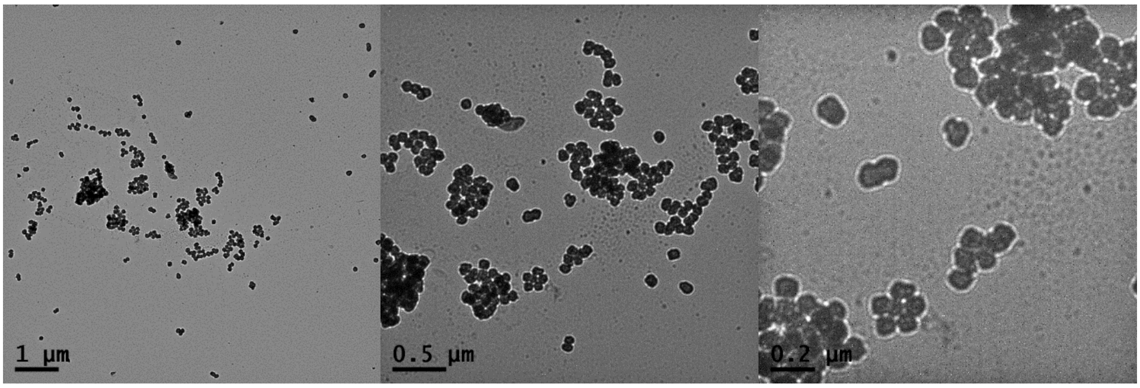

Figure 3.4 The different scales of TEM images of P(AA$_{35}$-DVB$_{140}$FN$_{70}$)

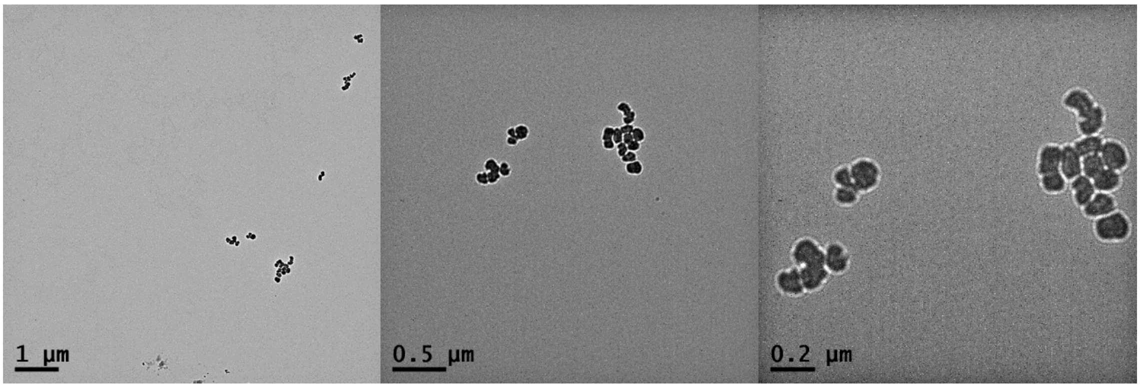

Figure 3.5 The different scales of TEM images of P(AA$_{35}$-DVB$_{105}$FN$_{70}$)

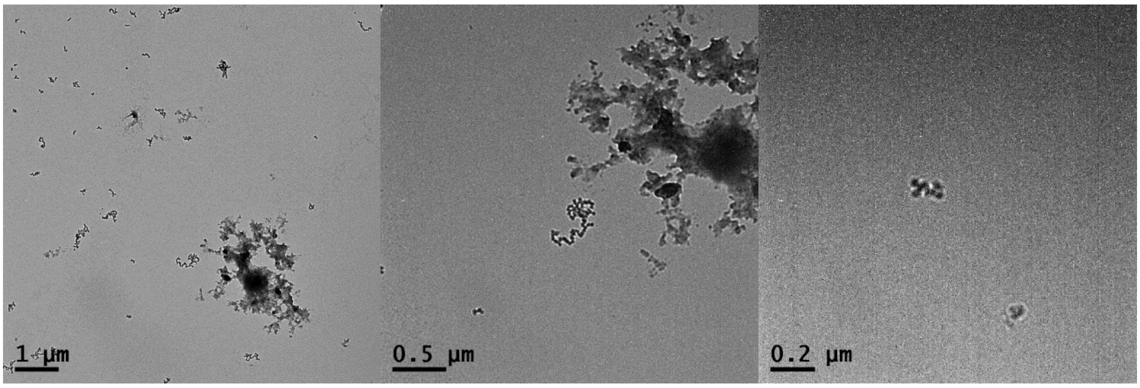

Figure 3.6 The different scales of TEM images of P(AA$_{35}$-DVB$_{70}$FN$_{70}$)

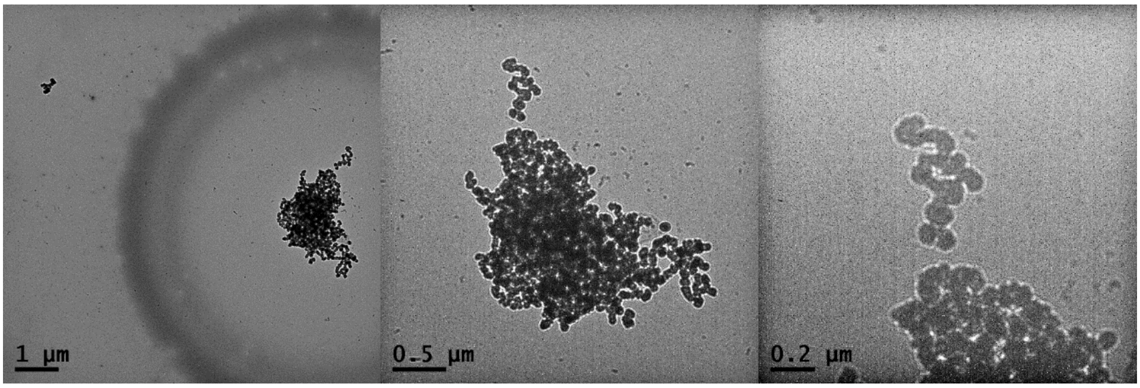

Figure 3.7 The different scales of TEM images of P(AA$_{35}$-DVB$_{70}$FN$_{70}$)

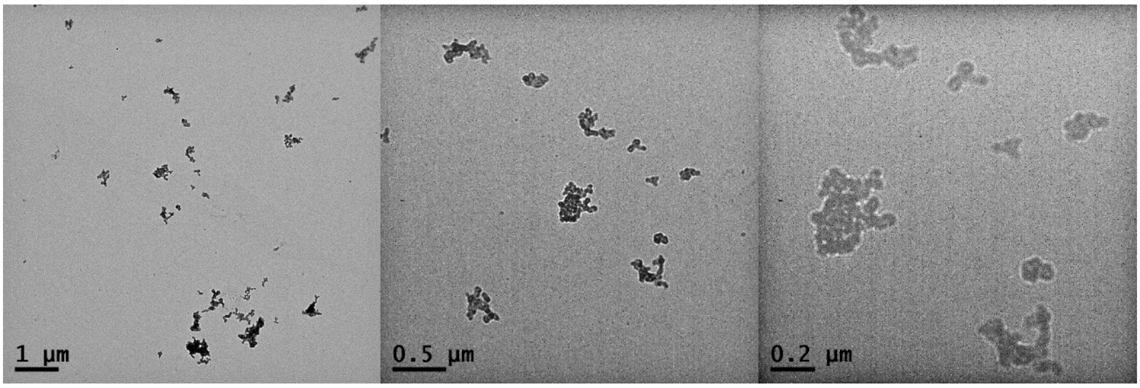

Figure 3.8 The different scales of TEM images of P(AA_{35}-$DVB_{35}FN_{70}$)

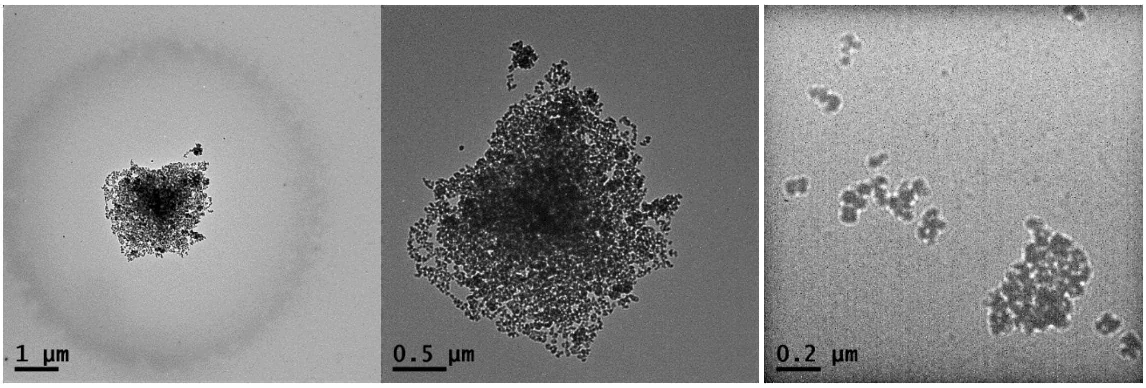

Figure 3.9 The different scales of TEM images of P(AA_{35}-$DVB_{47}FN_{35}$)

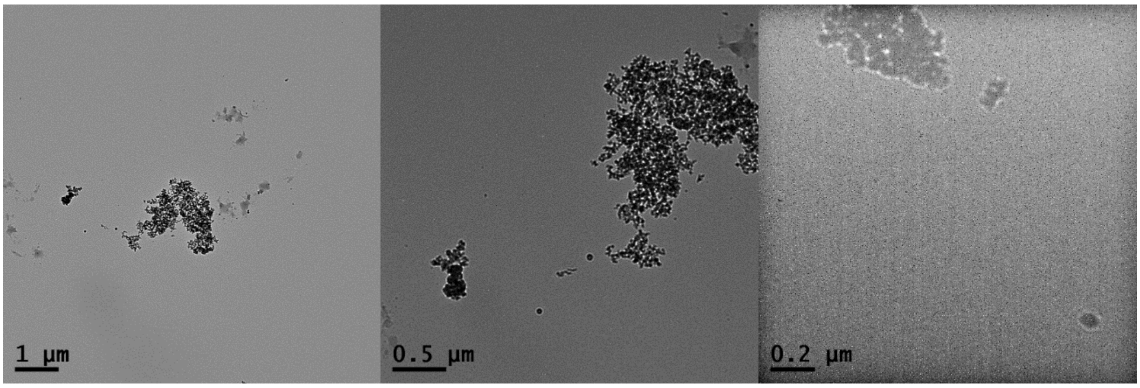

Figure 3.10 The different scales of TEM images of P(AA_{35}-$DVB_{94}FN_{70}$)

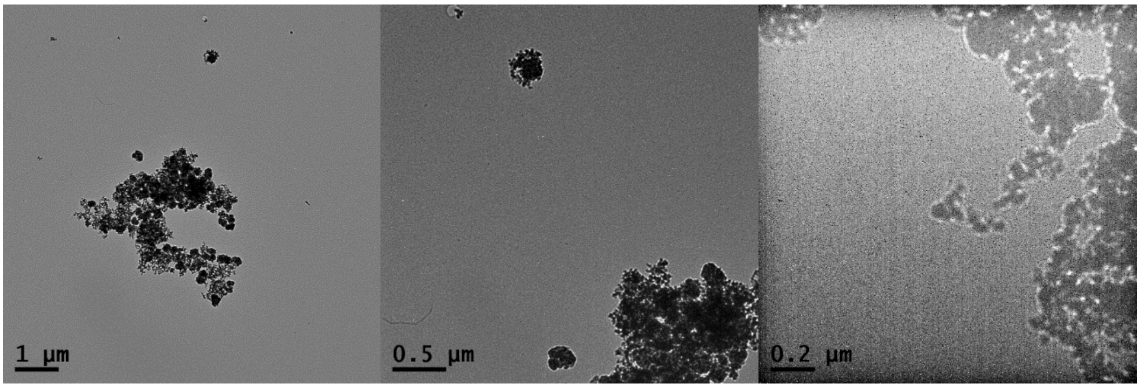

Figure 3.11 The different scales of TEM images of P(AA_{35}-$DVB_{188}FN_{140}$)

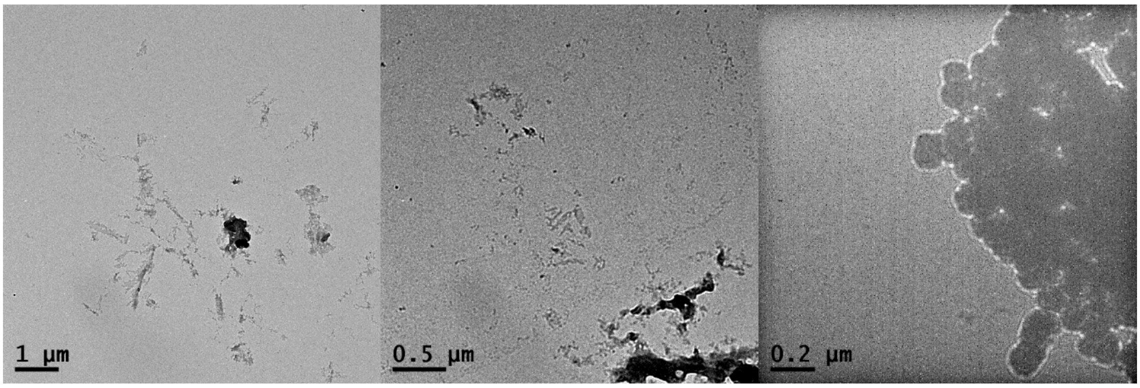

Figure 3.12 The different scales of TEM images of P(AA_{35}-$DVB_{300}FN_{225}$)

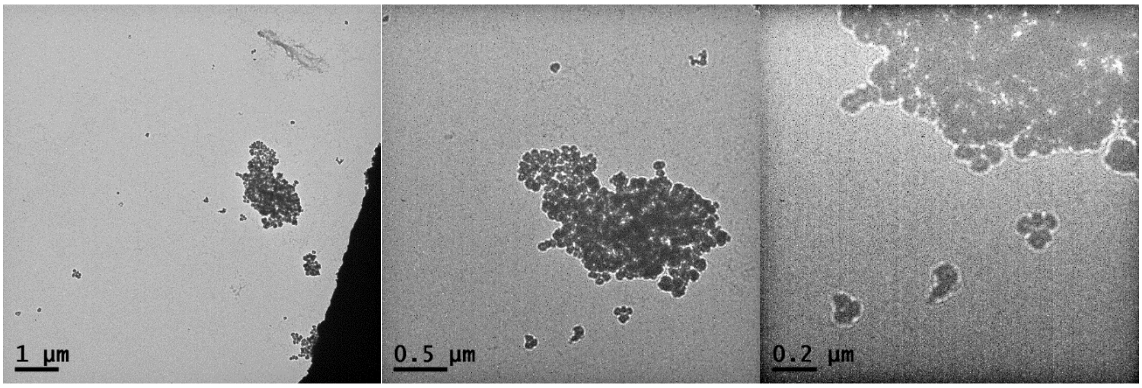

Figure 3.13 The different scales of TEM images of P(AA_{50}-$DVB_{47}FN_{35}$)

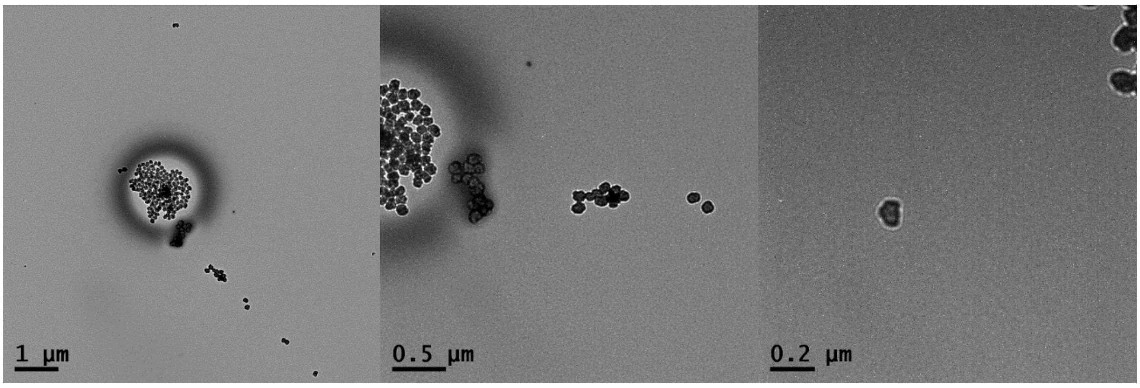

Figure 3.14 The different scales of TEM images of P(AA_{50}-$DVB_{188}FN_{140}$)

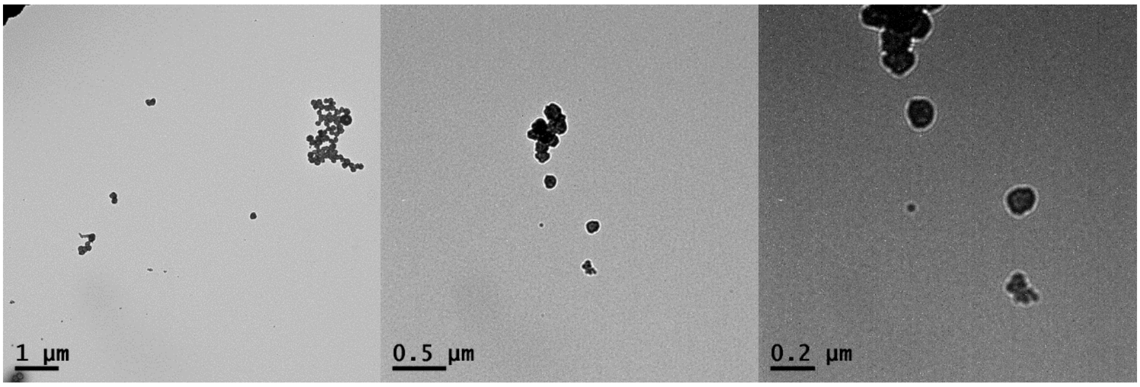

Figure 3.15 The different scales of TEM images of P(AA_{50}-$DVB_{300}FN_{225}$)

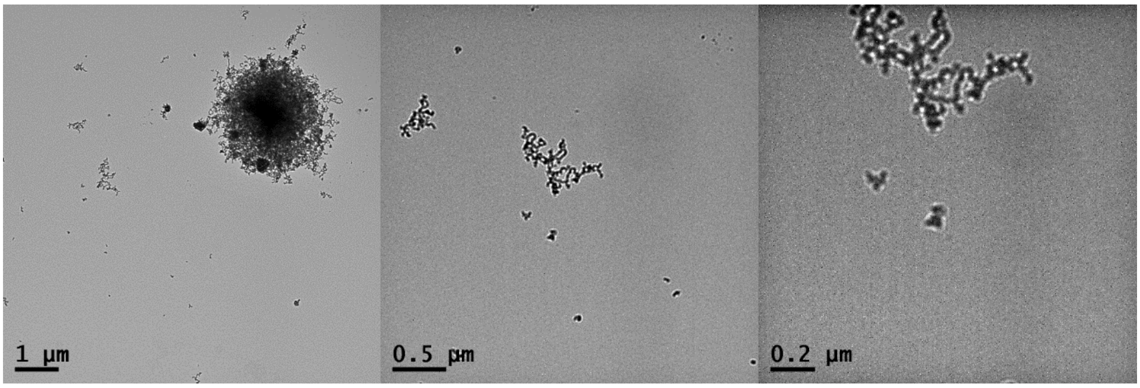

Figure 3.16 The different scales of TEM images of P(AA_{95}-$DVB_{47}FN_{35}$)

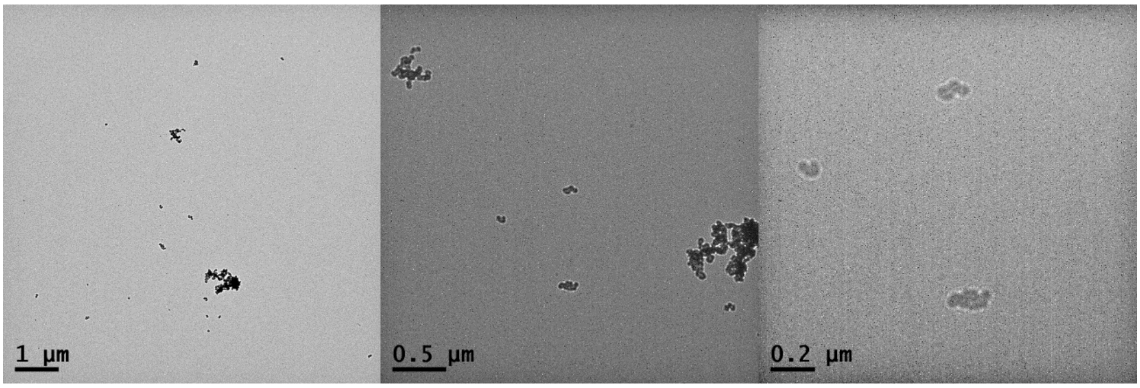

Figure 3.17 The different scales of TEM images of P(AA_{95}-$DVB_{94}FN_{70}$)

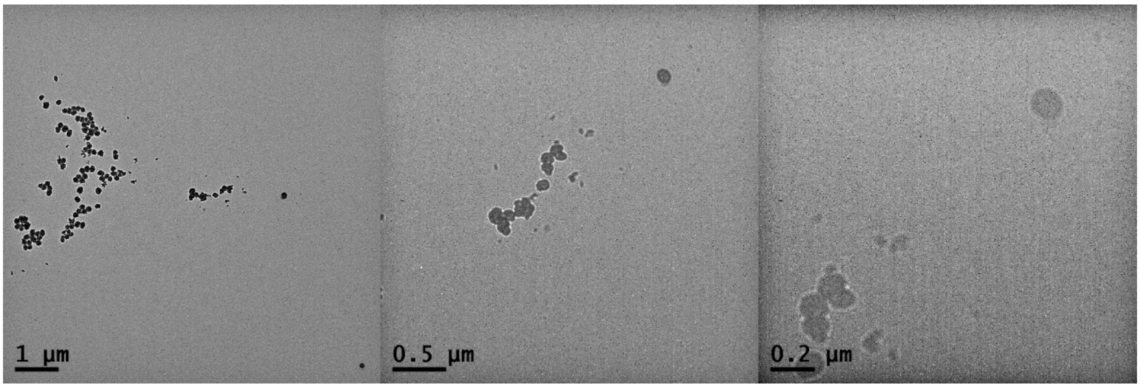

Figure 3.18 The different scales of TEM images of P(AA_{95}-$DVB_{188}FN_{140}$)

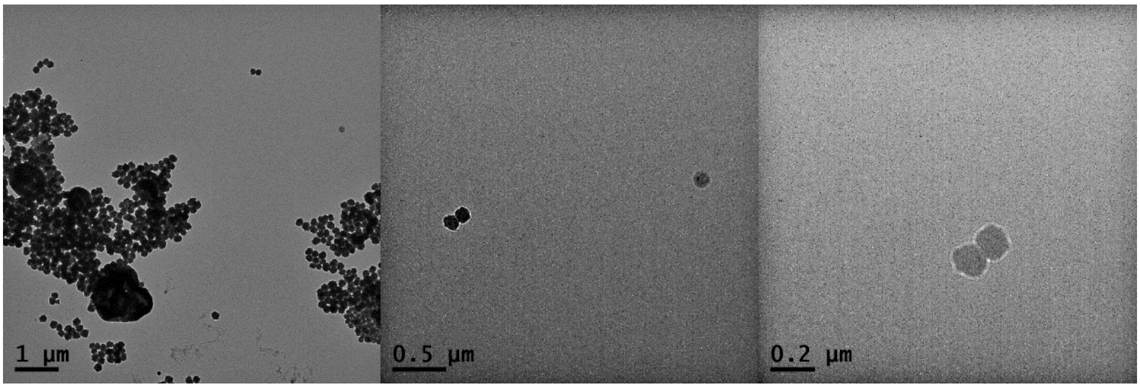

Figure 3.19 The different scales of TEM images of P(AA_{95}-$DVB_{300}FN_{225}$)

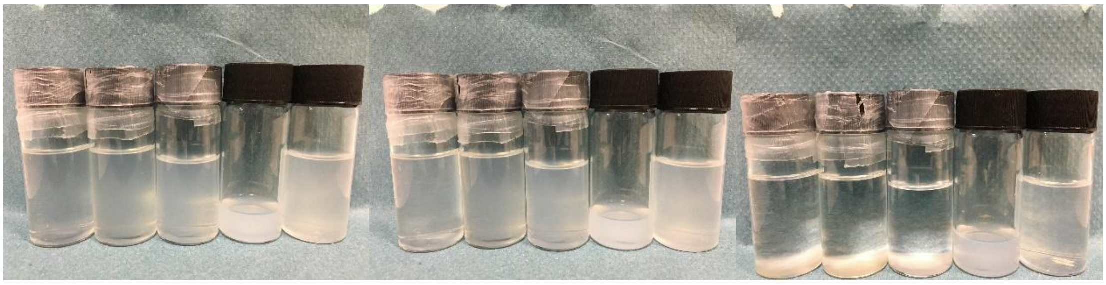

(a) (b) (c)

Figure 3.20 From left to right: PAA_{35}-DVB_{47}/FN_{35}, PAA_{35}-DVB_{94}/FN_{70}, PAA_{35}-DVB_{188}/FN_{140}, PAA_{35}-DVB_{300}/FN_{225}, PAA_{35}-DVB_{600}/FN_{450} in methanol (a) immediately after 30 min sonication, (b) immediately after 3.0 h sonication and (c) after 1 week

(a) (b) (c)

Figure 3.21 From left to right: PAA_{50}-DVB_{47}/FN_{35}, PAA_{50}-DVB_{94}/FN_{70}, PAA_{50}-DVB_{188}/FN_{140}, PAA_{50}-DVB_{300}/FN_{225}, PAA_{50}-DVB_{600}/FN_{450} in methanol (a) immediately after 30 min sonication, (b) immediately after 3.0 h sonication and (c) after 1 week

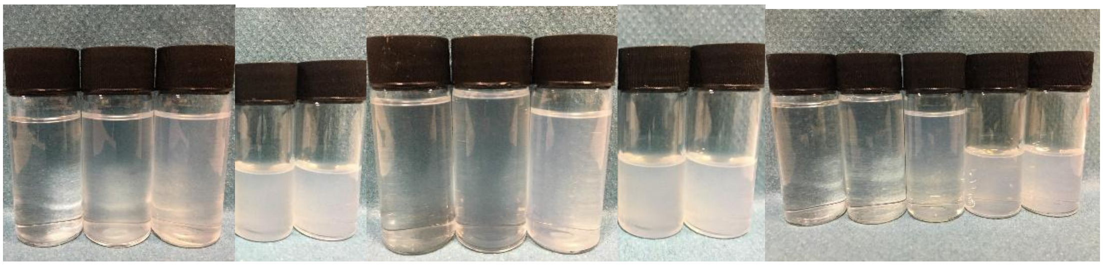

(a) (b) (c)

Figure 3.22 From left to right: PAA_{95}-DVB_{47}/FN_{35}, PAA_{95}-DVB_{94}/FN_{70}, PAA_{95}-DVB_{188}/FN_{140}, PAA_{95}-DVB_{300}/FN_{225}, PAA_{95}-DVB_{600}/FN_{450} in methanol (a) immediately after 30 min sonication, (b) immediately after 3.0 h sonication and (c) after 1 week

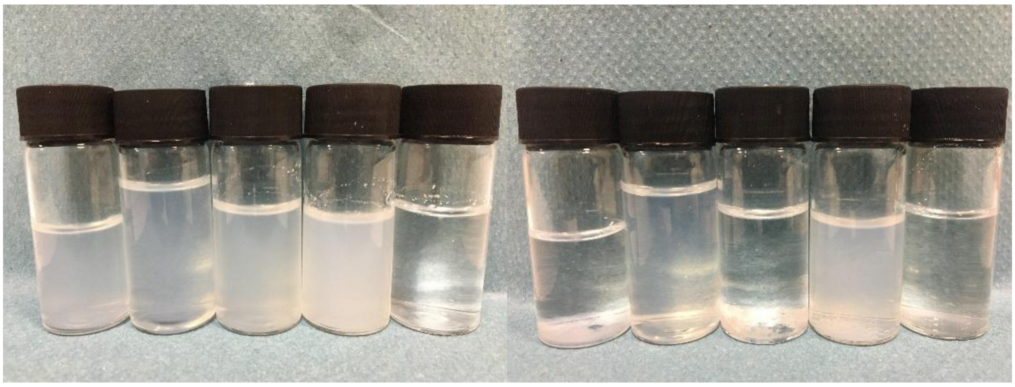

(a) (b)

Figure 3.23 From left to right: PAA$_{35}$-DVB$_{47}$/FN$_{35}$, PAA$_{35}$-DVB$_{94}$/FN$_{70,}$ PAA$_{35}$-DVB$_{188}$/FN$_{140,}$ PAA$_{35}$-DVB$_{300}$/FN$_{225,}$ PAA$_{35}$-DVB$_{600}$/FN$_{450}$ in water (a) immediately after 3.0 h sonication, and (b) after 1 week

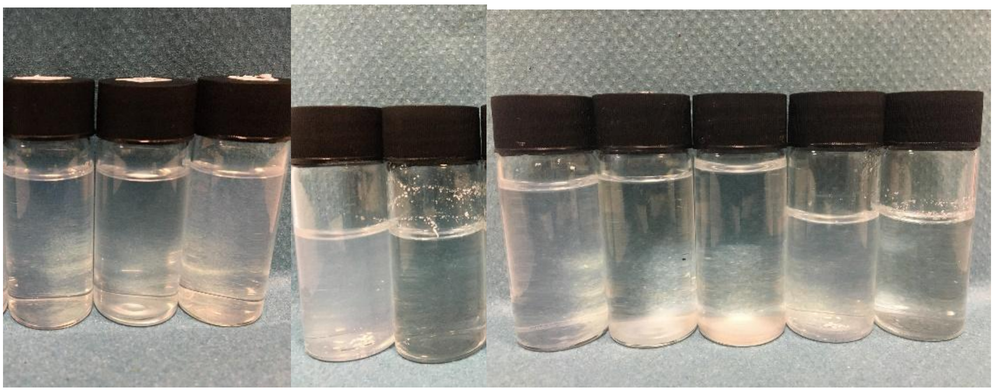

(a) (b)

Figure 3.24 From left to right: PAA$_{50}$-DVB$_{47}$/FN$_{35}$, PAA$_{50}$-DVB$_{94}$/FN$_{70,}$ PAA$_{50}$-DVB$_{188}$/FN$_{140,}$ PAA$_{50}$-DVB$_{300}$/FN$_{225,}$ PAA$_{50}$-DVB$_{600}$/FN$_{450}$ in water (a) immediately after 3.0 h sonication, and (b) after 1 week

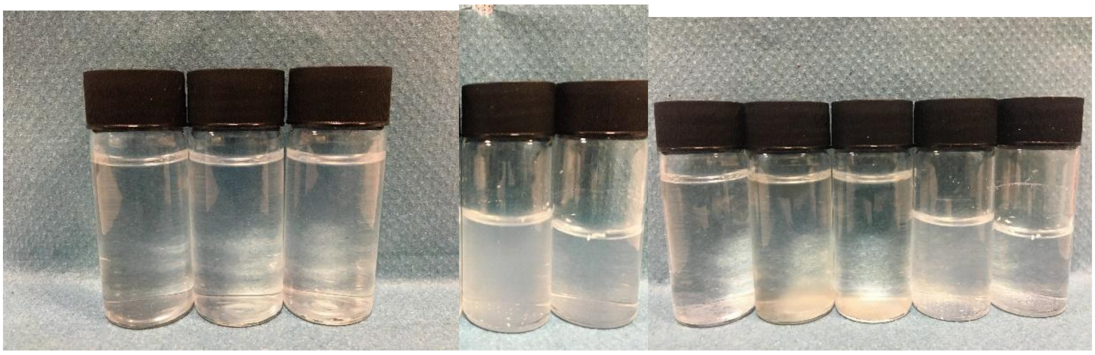

(a) (b)

Figure 3.25 From left to right: PAA$_{95}$-DVB$_{47}$/FN$_{35}$, PAA$_{95}$-DVB$_{94}$/FN$_{70,}$ PAA$_{95}$-DVB$_{188}$/FN$_{140,}$ PAA$_{95}$-DVB$_{300}$/FN$_{225,}$ PAA$_{95}$-DVB$_{600}$/FN$_{450}$ in water (a) immediately after 3.0 h sonication, and (b) after 1 week

Chapter-4 pH-responsive Shell

4.1 Aims

The P(EG$_{113}$-DVB$_x$/FN$_y$) particles which were synthesised by metal-free radical addition fragmentation transfer mediated polymerisation induced self-assembly (RAFT mediated PISA) approach in our group, introduced both porosity and dispersibility. We believe the strategy of using block copolymers to synthesise porous polymers has much promise. However, just the PEG based macro-CTA[1–4] and the PAA based macro-CTA which prepared in the Chapter 3 as the outer shell solubilizing chain have been used toward in all of these materials. Moreover, Mai et al.[5] and Yu et al.[6] used poly(2-dimethylaminoethyl methacrylate) (PDMAEMA) as the outer shell which introduce not only dispersibility, but also pH/temperature dual-responsive to the hairy microporous polymeric nanospheres by gifting shell segments to the microporous polymeric particles through ATRP, and as the same as Wang and co-workers[7] who used poly(diethylaminoethyl methacrylate) (PDEAEMA) as the shell with the pH/temperature dual-responses to modify the mesoporous silica nanomaterials.

Based on the methods and results to determine the reaction conditions, the required ratios of the different components as well as the core-shell ratio, this chapter aims to use the DEAEMA (Figure 4.1 (a)) and 4-vinylpyridine (4-VP) (Figure 4.1 (b)) with pH- responses to investigate the reaction conditions, core-shell ratio, and pH- responses of the particles.

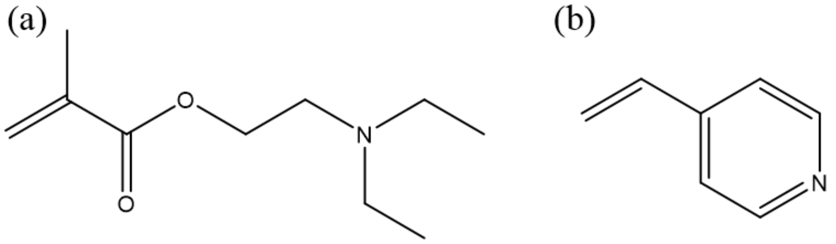

Figure 4.1 Molecular structure of diethylaminoethyl methacrylate (DEAEMA) (a), and 4-vinylpyridine (4-VP) (b)

4.2 Experimental

4.2.1 Materials

2-Bromoisobutyryl bromide, 2-cyano-2-propyl dodecyl trithiocarbonate (CPDTC, 98%), fumaronitrile (FN, 98 %), potassium persulfate (KPS), potassium phosphate tribasic (K_3PO_4) were purchased from Sigma-Aldrich and used as received. Carbon disulfide, 1-dodecanethiol (98%) were purchased from Alfa Aesar and used as received. Dry Tetrahydrofuran (THF) was obtained in a method analogous to the one outlined by Grubbs.[8] Magnesium sulfate (Mg_2SO_4) was purchased from Fischer and used as received. Diethylaminoethyl methacrylate (DEAEMA), divinylbenzene (DVB, technical grade 80 %), 4-vinylpyridine (4-VP, 95%) were passed through an alumina column in order to remove the inhibitor before use. 2,2′-Azobis(2-methylpropionitrile) (AIBN, 98 %) was purified by recrystallization from ethanol at 40 °C. All other chemicals were purchased from Sigma-Aldrich and used without any further purification.

4.2.2 Synthesis (The preparations were used a method adapted from James et al.[1])

4.2.2.1 Synthesis of 2-(dodecylthiocarbonothioylthio)-2-methylpropanoic acid (DDMAT) (chain transfer agent (CTA))

The synthesis of 2-(dodecylthiocarbonothioylthio)-2-methylpropanoic acid (DDMAT) was conducted using a modified method from O’Reilly et al.[9] Initially, dodecane thiol (3.61 mL, 15.07 mmol) was added to a stirred mixture of K_3PO_4 (3.199 g, 15.07 mmol) in acetone (20 ml) and stirred for 30 minutes. The mixture was then treated with CS_2 (3.129 g, 41.10 mmol) and stirred for an additional 60 minutes. Next, 2-bromoisobutyric acid (2.288 g, 13.70 mmol) was added to the reaction mixture, which was stirred overnight at room temperature. The solvent was extracted twice with CH_2Cl_2 (100 mL each) from 1 M HCl (100 mL). The organic extracts were washed with brine (150 mL) and $MgSO_4$ powder, followed by solvent removal using rotary evaporation. The obtained product was purified by precipitation in excess cold n-hexane twice to ensure purity and then dried in a vacuum oven overnight at 40 °C to yield the RAFT CTA (Yield = 49%. Found C: 57.04 %, H: 8.78 %, S: 26.47 %, Expected C: 56.04 %, H: 8.79 %, S: 26.37 %. δH (400 MHz, $CDCl_3$) = 3.31 (2H, t, S-CH_2-$(CH_2)_{10}$-CH_3), 1.75 (6H, s, C-$(CH_3)_2$), 1.76-1.20 (20H, t, S-CH_2-$(CH_2)_{10}$-CH_3), 0.90 (3H, t, SCH_2-$(CH_2)_{10}$-CH_3); δC (400 MHz, $CDCl_3$) = 220.85, 178.08, 55.53, 37.09, 31.93, 29.64, 29.57, 29.46, 29.36, 29.12, 28.98, 27.82, 25.24, 25.23, 22.70, 14.14; m/z (EI) 363.3, 303.3, 277.2, 201.3) (Synthesised in Chapter 3 and see in Figure 3.1 in appendix).

4.2.2.2 Synthesis of Poly(diethylaminoethyl methacrylate) (PDEAEMA) Based Macro-Chain Transfer Agent (CTA) (Macro-CTA (CPDTC-PDEAEMA)) via RAFT

The synthesis of macro-CTA (CPDTC-PDEAEMA$_x$) (x=48, 108, 208) was performed using a modified version of the method described by Wong et al.[10] Specifically, 2-bromoisobutyryl bromide, 2-cyano-2-propyl dodecyl trithiocarbonate (CPDTC), and 1, 3, 5-trioxane were combined in a 2-necked round bottom flask. The flask was subjected to evacuation and nitrogen backfilling procedures three times. Dry THF and diethylaminoethyl methacrylate (DEAEMA) were added to the flask. The solution was bubbled with nitrogen gas to eliminate any residual air and then heated to 75 °C. Polymerisation was initiated by adding 2,2′-azobis(2-methylpropionitrile) (AIBN) with THF (1 mL), and the reaction was allowed to proceed for 24 h at 75 °C. The resulting mixture was purified by precipitation in deionized water, and the sample was subsequently dried in a vacuum oven overnight at 60 °C to yield the RAFT macro-CTA (Table 4.1, Figure 4.1-4.2 in appendix).

Table 4.1 Different components for synthesis of PDEAEMA$_x$ based Macro-CTA

Sample Name	DEAEMA	CTA	Trioxane	AIBN	THF
	mL/mmol	mg/mmol	mg/mmol	mg/mmol	mL
PDEAEMA$_{48}$ based Macro-CTA	2.1/10.00	34.6/0.10	90.0/1.00	1.6/0.01	12.4
PDEAEMA$_{108}$ based Macro-CTA	4.1/20.00	34.6/0.10	180.0/2.00	3.3/0.02	12.4
PDEAEMA$_{208}$ based Macro-CTA	8.2/40.00	34.6/0.10	360.0/4.00	3.3/0.02	12.4

4.2.2.3 Synthesis of Poly(4-vinylpyridine) (P4-VP) Based Macro-Chain Transfer Agent (CTA) (Macro-CTA (DDMAT-P4-VP)) via RAFT

The synthesis of macro-CTA (DDMAT-P4-VP$_x$) (x=45, 82) was performed using a method similar to that described by Liu et al.[11] In this method, 2-(Dodecylthiocarbonothioylthio)-2-methylpropionic acid (DDMAT) and 1, 3, 5-trioxane were combined in a 2-necked round bottom flask, which was evacuated and backfilled with nitrogen three times. Anhydrous 1,4-dioxane and ethanol, along with 4-vinylpyridine (4-VP), were added to the flask. The solution was then bubbled through with nitrogen gas to remove any residual air before being heated to 70 °C. Polymerisation was initiated by adding 2,2′-azobis(2-methylpropionitrile) (AIBN) in 1,4-dioxane (0.2 mL), and the mixture was held at 70 °C for 8.0 h. The product was then purified by precipitation into diethyl ether and dried in a vacuum oven overnight at 60 °C, yielding the RAFT macro-CTA (Table 4.2, Figure 4.3-4.4 in appendix).

Table 4.2 Different components for synthesis of P4-VP$_x$ based Macro-CTA

Sample Name	4-VP	CTA	Trioxane	AIBN	Dioxane	Ethanol
	mL/mmol	mg/mmol	mg/mmol	mg/mmol	mL	mL
P4-VP$_{45}$ based Macro-CTA	5.2/47.56	173.0/0.4756	42.8/0.48	19.5/0.1189	1.2	13.8
P4-VP$_{82}$ based Macro-CTA	10.4/95.12	173.0/0.4756	85.6/0.95	19.5/0.1189	1.2	13.8

4.2.2.4 Synthesis of Poly(diethylaminoethyl methacrylate) (PDEAEMA) Based Particles via RAFT Mediated Polymerisation Induced Self-Assembly in different ratios of water to methanol

The P(DEAEMA$_{108}$DVB$_{288}$FN$_{216}$) was prepared following method by Wong et al.[10]. To a 2-necked round bottom flask, Macro-CTA (CPDTC-PDEAEMA$_{108}$) and FN were added. The flask was then evacuated and backfilled with nitrogen three times. Next, DVB was added to a mixture of methanol and water in a certain ratio (60:40, 50:50, 40:60, 30:70, 20:80, 10:90, 00:100) (wt.%) to create a 1.0 wt. % solution, and the solution was bubbled with nitrogen to remove any air before heating to 70 °C. Polymerisation was initiated by adding AIBN and held at 70 °C for 24 hours. The product was isolated as a gray solid through reprecipitation into diethyl ether before drying in vacuo at 40 °C for 16 h (Table 4.3).

Table 4.3 Different solution components for synthesis of PDEAEMA$_{108}$DVB$_{288}$FN$_{216}$

Monomer Composition				Solution Composition		Ratio of water to methanol
PDEAEMA$_{108}$	DVB	FN	AIBN	Water	Methanol	
mg/mmol	mL/mmol	mg/mmol	mg/mmol	mL	mL	
101.6/0.005	0.20/1.44	84.2/1.08	0.2/0.001	10.0	18.9	60:40
101.6/0.005	0.20/1.44	84.2/1.08	0.2/0.001	18.6	23.6	50:50
101.6/0.005	0.20/1.44	84.2/1.08	0.2/0.001	15.0	28.2	40:60
101.6/0.005	0.20/1.44	84.2/1.08	0.2/0.001	11.2	33.0	30:70
101.6/0.005	0.20/1.44	84.2/1.08	0.2/0.001	7.4	37.6	20:80
101.6/0.005	0.20/1.44	84.2/1.08	0.2/0.001	3.8	42.4	10:90
101.6/0.005	0.20/1.44	84.2/1.08	0.2/0.001	0.0	47.2	00:100

4.2.2.5 Synthesis of Poly(4-vinylpyridine) (P4-VP) Based Particles via RAFT Mediated Polymerisation Induced Self-Assembly in different ratios of water to methanol

Synthesis of P4-VP$_{45}$DVB$_{67}$FN$_{50}$ with ratio of water to methanol equals 60 to 40

The P(4-VP$_{45}$DVB$_{67}$FN$_{50}$) was prepared following the method by Liu and coworkers.[11] To a 2-necked round bottom flask, Macro-CTA (DDMAT-P4-VP$_{45}$) and FN were added. The flask was then evacuated and backfilled with nitrogen three times. Next, DVB was added to a mixture of methanol and water in a certain ratio (60:40, 50:50, 40:60, 30:70, 20:80, 10:90, 00:100) (wt.%) to create a 1.0 wt. % solution, and the solution was bubbled with nitrogen to remove any air before heating to 70 °C. Polymerisation was initiated by adding AIBN and held at 70 °C for 24 hours. There is no precipitate after 24 h reaction. No precipitate was observed after the reaction had been allowed to proceed for 24 hours (Table 4.4).

Table 4.4 Different solution components for synthesis of P4-$VP_{45}DVB_{67}FN_{50}$

Monomer Composition				Solution Composition		Ratio of water to methanol
P4-VP_{45}	DVB	FN	AIBN	Water	Methanol	
mg/mmol	mL/mmol	mg/mmol	mg/mmol	mL	mL	
72.4/0.014	0.13/0.94	54.6/0.70	0.7/0.004	15.0	12.6	60:40
72.4/0.014	0.13/0.94	54.6/0.70	0.7/0.004	12.5	15.8	50:50
72.4/0.014	0.13/0.94	54.6/0.70	0.7/0.004	10.0	18.9	40:60
72.4/0.014	0.13/0.94	54.6/0.70	0.7/0.004	7.5	22.1	30:70
72.4/0.014	0.13/0.94	54.6/0.70	0.7/0.004	5.0	25.2	20:80
72.4/0.014	0.13/0.94	54.6/0.70	0.7/0.004	2.5	28.4	10:90
72.4/0.014	0.13/0.94	54.6/0.70	0.7/0.004	0.0	31.5	00:100

4.2.2.6 Synthesis of Poly(diethylaminoethyl methacrylate) (PDEAEMA) Based Particles via RAFT Mediated Polymerisation Induced Self-Assembly with Different Core-Shell Ratios

Synthesis of $PDEAEMA_{108}DVB_{288}FN_{216}$

The PDEAEMA based particles were prepared following the above method. To a 2-necked round bottom flask, Macro-CTA (CPDTC-$PDEAEMA_x$) (x=48, 108, 208) and FN were added. The flask was then evacuated and backfilled with nitrogen three times. Next, DVB was added to a mixture of methanol and water in a 60:40 (wt.%) ratio to create a 1.0 wt. % solution, and the solution was bubbled with nitrogen to remove any air before heating to 70 °C. Polymerisation was initiated by adding AIBN and held at 70 °C for 24 hours. The product was obtained as a gray solid through reprecipitation into diethyl ether before drying in vacuo at 40 °C for 16 h (Table 4.5).

Table 4.5 Different monomer components for synthesis of different PDEAEMA based particles

Sample Name	Monomer Composition				Solution Composition	
	$PDEAEMA_x$	DVB	FN	AIBN	Water	Methanol
	mg/mmol	mL/mmol	mg/mmol	mg/mmol	mL	mL
$PDEAEMA_{48}DVB_{72}FN_{54}$	276.8/0.03	0.30/2.16	126.4/1.62	1.0/0.006	27.4	51.9
$PDEAEMA_{48}DVB_{144}FN_{108}$	184.5/0.02	0.40/2.88	168.5/2.16	0.7/0.04	29.1	55.2
$PDEAEMA_{48}DVB_{288}FN_{216}$	138.4/0.015	0.60/4.32	252.7/3.24	0.5/0.003	38.1	72.2
$PDEAEMA_{108}DVB_{72}FN_{54}$	406.5/0.02	0.20/1.44	84.2/1.08	0.7/0.004	27.1	51.4
$PDEAEMA_{108}DVB_{144}FN_{108}$	406.5/0.02	0.40/2.88	168.5/2.16	0.7/0.004	38.0	72.0
$PDEAEMA_{108}DVB_{288}FN_{216}$	101.6/0.005	0.20/1.44	84.2/1.08	0.2/0.001	14.9	28.3
$PDEAEMA_{208}DVB_{72}FN_{54}$	582.4/0.015	0.15/1.08	63.2/0.81	0.5/0.003	31.5	59.6
$PDEAEMA_{208}DVB_{144}FN_{108}$	388.3/0.01	0.20/1.44	84.2/1.08	0.3/0.002	26.4	50.0
$PDEAEMA_{208}DVB_{288}FN_{216}$	291.2/0.008	0.30/2.16	126.4/1.62	0.2/0.002	27.9	52.9

4.2.2.7 Synthesis of Poly(4-vinylpyridine) (P4-VP) Based Particles via RAFT Mediated Polymerisation Induced Self-Assembly with Different Core-Shell Ratios

The P4-VP based particles were prepared following the above method. Macro-CTA (DDMAT-P4-VP$_x$) (x=45, 82) and FN were added and the flask was evacuated and backfilled with nitrogen three times. A solution of DVB in water and methanol (40:60 wt%) was added to the flask to yield a 1.0 wt% solution. The mixture was bubbled with nitrogen to remove any air, then heated to 70 °C and AIBN was added to initiate polymerisation. The reaction was maintained at 70 °C for 24 hours. The product was obtained as a yellow solid through reprecipitation into diethyl ether and dried in vacuo at 40 °C for 16 hours (Table 4.6).

Table 4.6 Different monomer components for synthesis of different P4-VP based particles

Sample Name	Monomer Composition				Solution Composition	
	P4-VP$_x$	DVB	FN	AIBN	Water	Methanol
	mg/mmol	mL/mmol	mg/mmol	mg/mmol	mL	mL
P4-VP$_{45}$DVB$_{67}$FN$_{50}$	72.4/0.014	0.13/0.94	54.6/0.70	0.7/0.004	15.0	18.9
P4-VP$_{45}$DVB$_{134}$FN$_{100}$	72.4/0.014	0.26/1.88	109.2/1.40	0.7/0.004	17.8	33.8
P4-VP$_{45}$DVB$_{268}$FN$_{200}$	72.4/0.014	0.52/3.76	218.4/2.80	0.7/0.004	32.0	60.5
P4-VP$_{45}$DVB$_{300}$FN$_{225}$	36.2/0.007	0.41/3.00	175.5/2.25	0.3/0.002	24.8	47.0
P4-VP$_{82}$DVB$_{67}$FN$_{50}$	134.6/0.015	0.14/1.005	58.5/0.75	0.5/0.003	13.0	24.6
P4-VP$_{82}$DVB$_{134}$FN$_{100}$	134.6/0.015	0.28/2.01	117.0/1.50	0.5/0.003	20.5	38.9
P4-VP$_{82}$DVB$_{268}$FN$_{200}$	89.7/0.01	0.37/2.68	156.0/2.00	0.0/0.002	23.8	45.0
P4-VP$_{82}$DVB$_{300}$FN$_{225}$	89.7/0.01	0.559/4.28	250.4/3.21	0.0/0.002	35.9	67.9

4.3 Results and discussion

4.3.1 Investigation of suitable solution composition for PDEAEMA and P4-VP based particles

Both Diethylaminoethyl methacrylate (DEAEMA) and 4-vinylpyridine (4-VP) are well known as pH- responsive polymers and their conjugated acids have a pK_a of 7.3[7,12,13] and a pK_a of 5.1[14,15], respectively. The pendant tertiary amine groups on PDEAEMA chains can be protonated and hence become hydrophilic at $pH < pK_a$, whereas at high pHs (higher than the pK_a), the polymer chains are deprotonated and hydrophobic. The pyridine groups on 4-VP follow the same principle as the tertiary amine of PDEAEMA. Additionally, previous research has been demonstrated that PDEAEMA can be used as pH- responsive chains of mesoporous silica nanospheres.[7] PDEAEMA was therefore chosen to be investigated to form the outer shell of porous polymer particles synthesised by RAFT-PISA. Due to the different solubility of monomers, the reaction conditions vary with the polarity. Our previous research on PEG based particles and PAA based particles were synthesised in water-ethanol mixture with a ratio of 60:40 (wt.%) via RAFT-PISA. The poly(ethylene glycol) (PEG) and poly(acrylic acid) (PAA) block can dissolve in the water, and the addition of ethanol was used to improve the solubility of DVB and FN in the solution. However, PDEAEMA is only slightly soluble in water, and therefore, the ideal reaction conditions may be different from the previous research. Wong et al.[10] reported they used water-methanol mixture to synthesise block structures via RAFT-PISA, therefore, a water-methanol mixture to synthesise PDEAEMA based particles was investigated. PDEAEMA based macro-CTA shells were prepared for the investigation and the degree of polymerisation (DP) of each sample were obtained to be 48 and 108 by ^1H NMR spectroscopy. This was calculated by comparing the ratio of methylene ($-O-CH_2-$) peak on PDEAEMA to methylene ($-S-CH_2-$) peak on CTA which was similar to the PAA based macro-CTA shells, compared to a target DP of 50 and 100 respectively (Figure 4.1, Figure 4.2 in appendix).

A precipitate was obtained only when a water to methanol ratio of 40:60 (wt.%) was used. No was observed using other water/methanol ratio mixtures or water/ethanol mixture which was used to obtain PEG based particles and PAA based particles (Table 4.7). It is therefore clear that the best reaction condition for synthesis of the PDEAEMA based particles is in the water to methanol ratio equals 40:60 (wt.%).

Table 4.7 Solution composition and precipitation of P(DEAEMA$_{108}$-DVB$_{288}$FN$_{216}$) particles

Solution Composition			Precipitate	BET surface area
Water	Methanol	Ethanol		(m^2 g^{-1})
60	-	40	No	-
60	40	-	No	-
50	50	-	No	-
40	60	-	Yes	62
30	70	-	No	-
20	80	-	No	-
10	90	-	No	-
00	100	-	No	-

Due to the fact that 4-VP has a similar polarity to the PDEAEMA based shell as well as being reported previously by Liu et al.[11] who used a water-methanol mixture to synthesise block structures via RAFT-PISA, water-methanol mixture was selected to synthesise P4-VP based particles. Firstly, P4-VP based macro-CTAs were prepared before the investigation with DPs of 45 and 82 compared to the target DP of 50 and 100. These were calculated by ^{1}H NMR spectroscopy with the ratio of the 2 methine (-CH-N=CH- or –CH-C=CH-) peaks on the pyridine ring of P4-VP to methylene (-S-CH$_2$-) peak on CTA, which following the same analysis method as the PAA, PDEAEMA based macro-CTA shells (Figure 4.3, Figure 4.4 in appendix).

Table 4.8 Solution composition and precipitation of P(4-VP$_{35}$-DVB$_{67}$FN$_{50}$) particles

Solution Composition		Precipitate	BET surface area
Water	Methanol		(m^2 g^{-1})
60	40	No	-
50	50	No	-
40	60	Yes	42
30	70	Yes	-
20	80	Yes	36
10	90	Yes	-
00	100	Yes	15

Precipitates of P4-VP based particles were obtained with the ratio of water-methanol mixture from 40:60 (wt.%) to 00:100 (wt.%) (Table 4.3). From the gas sorption analysis, the particles with water-methanol ratios of 40:60 (wt.%), 20:80 (wt.%) and 00:100 (wt.%) are porous, the others were found to be nonporous. Furthermore, the BET surface area decreased with increasing methanol composition (Table 4.8). Consequently, the sample with a water-methanol ratio of 40:60 (wt.%) as selected as the optimal reaction condition since it exhibited the highest

BET surface area among the other samples and showed porosity. Therefore, it was selected as the most suitable sample for further exploration.

4.3.2 Investigation of monomer composition of PDEAEMA and P4-VP based particles with different core-shell ratios

Based on the study of PAA based particles in Chapter 3.3.4 and the original PEG based particles,[1] the BET surface area can be influenced by the core-shell ratios. As previously DVB and FN were used as the core segment as they are known to result in particles with the highest BET surface areas, particularly when the ratio of DVB to FN equals 4:3.[1–4,16] Therefore, the ratios of core to shell were investigated to find the highest BET surface area of PDEAEMA and P4-VP based particles by using the three chain lengths (or DP) of PDEAEMA based macro-CTAs and two chain lengths (or DP) of P4-VP based macro-CTAs, respectively, which obtained in Chapter 4.3.1. BET surface areas were calculated from the nitrogen adsorption isotherms at 77.3 K using the BET equation.

Table 4.9 Monomer composition and BET surface area of PDEAEMA and P4-VP based particles with different ratios of core-shell, respectively

Monomer Composition				BET Surface Area
PDEAEMA	P4-VP	DVB	FN	(m^2 g^{-1})
48		72	54	36
48		144	108	101
48		288	216	79
108		72	54	53
108		144	108	78
108		288	216	62
208		72	54	-
208		144	108	-
208		288	216	-
	45	67	50	42
	45	134	100	134
	45	268	200	126
	45	400	300	1
	82	67	50	2
	82	134	100	4
	82	268	200	40
	82	400	300	0

For PDEAEMA based particles, it was observed that when the PDEAEMA shell DP equaled 208, no precipitate was observed. This result may be attributed to the larger shell has greater steric hindrance which hinders the DVB and FN to form a core. The porosity for P4-VP based particles was found to be similar to those of PDEAEMA based particles, especially for the P4-

VP_{82} based particles, which may be due to the high polarity and large steric bulkiness of the pyridine group hindering the polymerisation (Table 4.9).

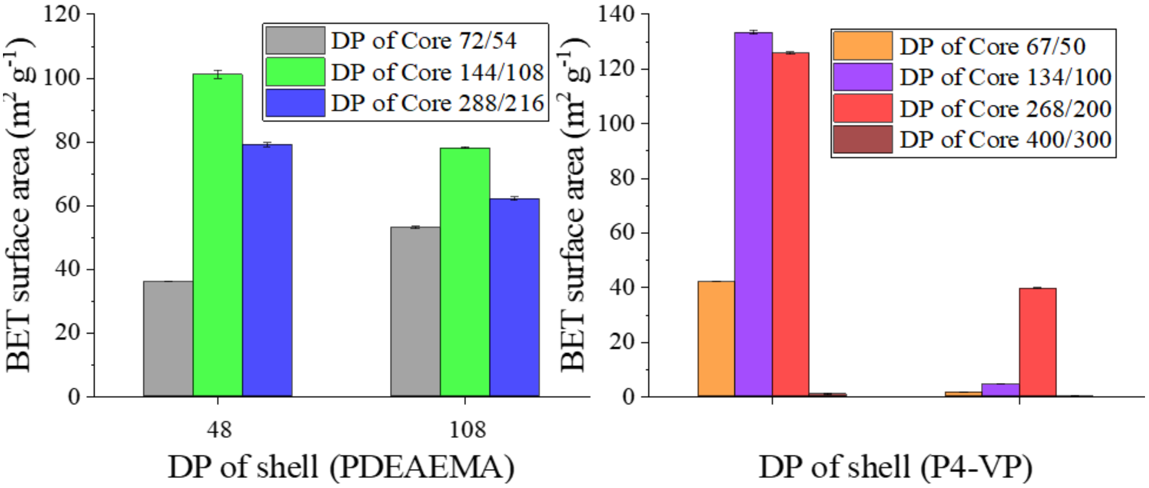

Figure 4.2 BET surface area of (a) PDEAEMA and (b) P4-VP based particles synthesised when using different core-shell ratios

For $PDEAEMA_{48}$ based shell, the BET surface area is the highest when the core size DP of DVB is 144 with surface areas of 101 m^2 g^{-1}. However, the BET surface area decreases with the core size growing to a DVB DP of 288. The $PDEAEMA_{108}$ based shell, reveals the same trend with the maximum BET surface area of 78 m^2 g^{-1} observed with same DP of DVB is 144 compared to the $PDEAEMA_{48}$ based shell (Figure 4.2 a). For P4-VP_{45} based shells, the BET surface area is the highest when the core size DP of DVB is 134 or 268 with surface areas of around 120-130 m^2 g^{-1}. However, when the core is increased to a DVB DP of 400, the resulting particles become non-porous. The P4-VP_{82} based shell, shows the maximum BET surface area is achieved when the DVB DP of 268, although this is much lower than the P4-VP_{48} shell (Figure 4.2 b). In general, the PAA based particles that obtained in Chapter 3.3.4, and the PEG based particles show the same tendency where the BET surface area increases with an increasing core size to reach a maximum but then begins to fall again when the core size becomes very large. For a given core size (same colour), the BET surface trends to decrease with increasing shell chain length. The PAA based particles have the same trend that the BET surface decreases with the growing of the shell chain length. In brief, particles with a smaller shell have larger BET surface areas compared to those with longer shell chains. The particles with the largest BET surface areas, $P(DEAEMA_{48}\text{-}DVB_{144}FN_{108})$, $P(DEAEMA_{108}\text{-}DVB_{144}FN_{108})$, $P(4\text{-}VP_{45}\text{-}DVB_{134}FN_{100})$ and $P(4\text{-}VP_{82}\text{-}DVB_{268}FN_{200})$ particles were selected to do further analysis.

The PDEAEMA and P4-VP based particles are also confirmed that they contain a dual morphology with smaller spheres structure to aggregate to form larger particles compared to the PAA based particles and the PEG based particles (Figure 4.3). Furthermore, SEM images show the same results (Figure 4.14 in appendix).

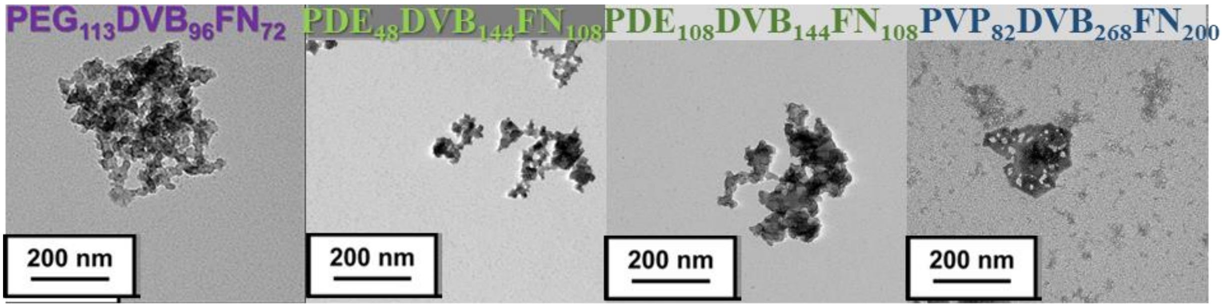

Figure 4.3 TEM images of P(EG$_{113}$-DVB$_{96}$FN$_{72}$)[1], P(DEAEMA$_{48}$-DVB$_{144}$FN$_{108}$), P(DEAEMA$_{108}$-DVB$_{144}$FN$_{108}$) and P(4-VP$_{82}$-DVB$_{268}$FN$_{200}$) particles in the water solution

The nitrogen adsorption isotherms exhibit only a slight increase for P(DEAEMA$_{48}$-DVB$_{144}$FN$_{108}$) and P(DEAEMA$_{108}$-DVB$_{144}$FN$_{108}$) particles at a very low pressure ($P/P_0 < 0.1$) corresponding to samples have limited microporosity. This contrasts with the PEG based particles synthesised using DVB and FN cores, which demonstrate more microporous structures.[1–4] The substantial increase in the gas uptake at a high pressure ($P/P_0 > 0.9$), which corresponds to nitrogen condensation in large pores (Figure 4.4 a). As previously observed in the PEG based particles this is attributed to condensation between the smaller particles in the larger particle agglomeration. In comparison to other microporous polymer nanospheres, the nitrogen isotherms display both similarities and differences. The large increase in gas uptake at very low pressure and limited nitrogen uptake at high pressure observed in the studies of Mai et al.[5] and Yu et al.[6] are due to the pre-prepared microporous cores. Therefore, micropores primarily contribute to the BET surface area compared to the interstitial voids formed by the aggregating of the nanospheres in the RAFT-PISA particles described here. However, a small nitrogen uptake at low pressure and large increase in the relative pressure region of ($0.2 < P/P_0 < 0.6$) and high pressure are observed in the study conducted by Wang and co-worker,[7] which is attributable to the initial porous silica cores that had a media size of particle. The isotherms also reveal a larger increase at low pressure for the P(4-VP$_{45}$-DVB$_{134}$FN$_{100}$) particles compared to the P(4-VP$_{82}$-DVB$_{268}$FN$_{200}$) particles, indicating that shorter shell particles are expected to have more microporous structures than longer shell particles. They also exhibit a substantial increase of gas uptake at a high pressure, same to other particles synthesised by RAFT-PISA (Figure 4.4 d).

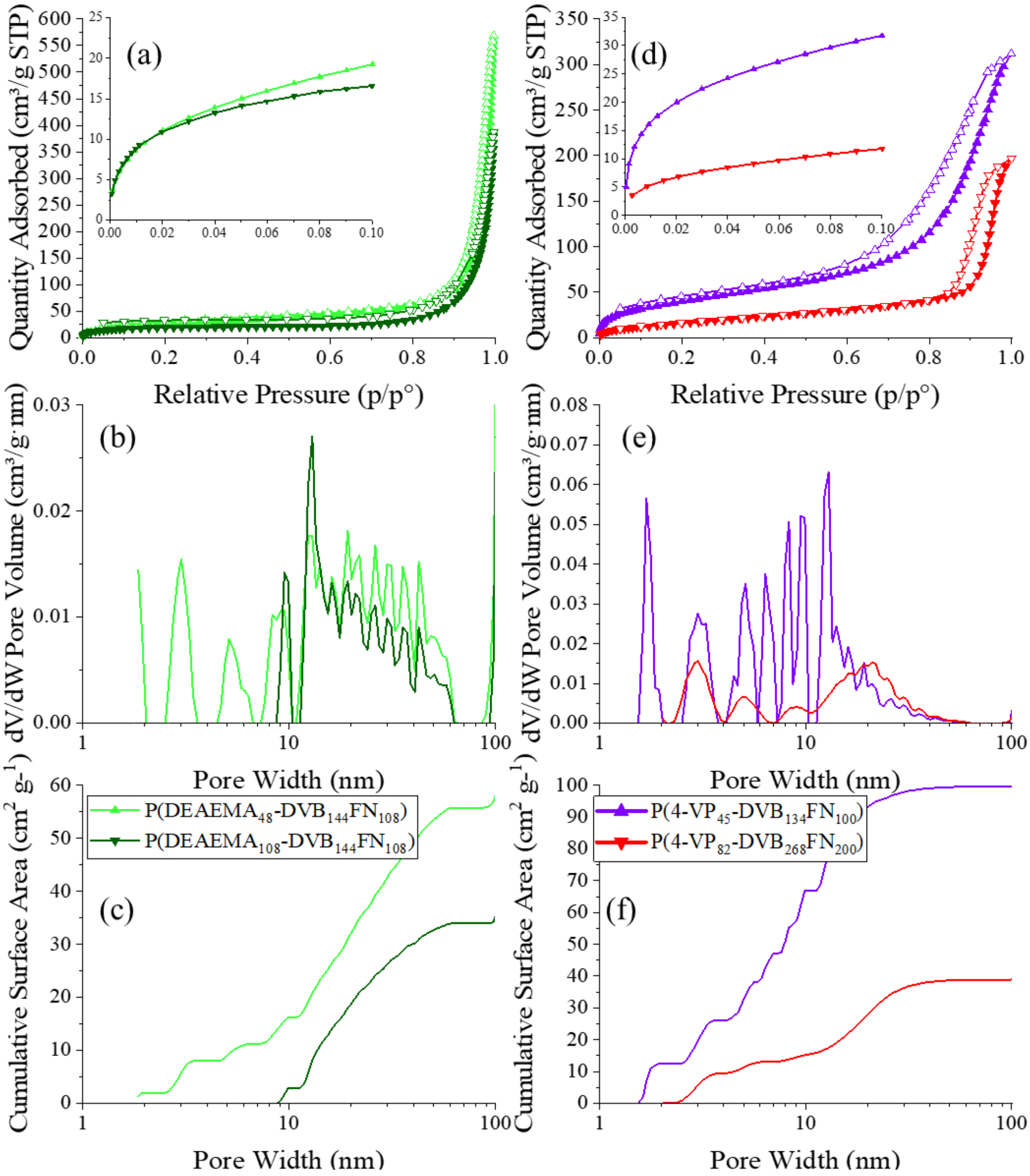

Figure 4.4 Nitrogen adsorption isotherms of (a) PDEAEMA and (d) P4-VP based particles with different combination of DVB and FN at 77.3 K; Pore size distributions calculated using NLDFT method (slit pore models, differential pore volume vs pore width) of (b) PDEAEMA (e) P4-VP based particles, and Cumulative surface areas of (c) PDEAEMA (f) P4-VP based particles

The pore size distributions (PSDs) were calculated by nonlocal density functional theory (NLDFT) show the pore sizes of P(DEAEMA$_{48}$-DVB$_{144}$FN$_{108}$), P(DEAEMA$_{108}$-DVB$_{144}$FN$_{108}$), P(4-VP$_{45}$-DVB$_{134}$FN$_{100}$) and P(4-VP$_{82}$-DVB$_{268}$FN$_{200}$) particles, respectively. The P(DEAEMA$_{48}$-DVB$_{144}$FN$_{108}$) particles display peaks at pore widths of around 3.0 nm, 5.1 nm, 8.0 nm, and along with further larger pores and voids, which are formed due to the aggregation of small sphere particles. The particles are also expected to have micropores. In contrast, P(DEAEMA$_{108}$-DVB$_{144}$FN$_{108}$) particles reveal a main peak at pore width about 9.1 nm and along with further larger pores and voids (Figure 4.4.b). The P(4-VP_{45}-$DVB_{134}FN_{100}$) particles exhibit multiple large peaks at pore widths of around 1.8 nm, 3.1 nm, 5.0 nm, 6.5 nm, 8.0 nm, 9.0 nm, and along with further larger pores and voids compared to the P(4-VP_{82}-$DVB_{268}FN_{200}$) particles which have a pore size of 3.1 nm, 5.1 nm and larger pore sizes from 10 nm to 60 nm (Figure 4.4.e). The cumulative surface area plots also indicate that majority of the pore volume is present in the meso- and macroporous regions. This means that these materials with long shell are all non-microporous unlike the PEG based particles, except for short shell particles, P(4-VP_{45}-$DVB_{134}FN_{100}$) and P($DEAEMA_{48}$-$DVB_{144}FN_{108}$) particles. This may be due to the longer shell of PDEAEMA and P4-VP with a large steric structure than the PEG based particles, which cover the core segment and decrease the microporosity (Figure 4.4 c, and f).

4.3.3 Investigation of pH- responsive of PDEAEMA and P4-VP based particles

Particles of PDEAEMA and P4-VP exhibits swelling, resulting in changes in size in either high or low pH solutions. P($DEAEMA_{48}$-$DVB_{144}FN_{108}$) particles with BET surface area 101 m^2 g^{-1} and P($DEAEMA_{108}$-$DVB_{144}FN_{108}$) with BET surface area 79 m^2 g^{-1}, which were obtained in Chapter 4.3.2 and were selected as they have the highest BET surface area in different PDEAEMA based chain lengths. Moreover, P(4-$VP_{45}DVB_{134}FN_{100}$) and P(4-VP_{82}-$DVB_{268}FN_{200}$) particles with BET surface area 134 m^2 g^{-1} and 40 m^2 g^{-1}, respectively, were selected with the same reason as they have the highest BET surface areas for the two different chain lengths (DP=45 and DP=82). In order to measure the size of the particles, dynamic light scattering (DLS) was carried out. The P($DEAEMA_{48}$-$DVB_{144}FN_{108}$) particles were prepared in 0.1 mg mL^{-1} of 9 different pH solutions from low to high by adding HCl or NaOH. Each sample was sonicated for 3 hours before analysis. At low pH ($0 \leq pH \leq 1.3$), P($DEAEMA_{48}$-$DVB_{144}FN_{108}$) particles had diameters of around 600 nm. The particle size began to increase at the pH increased from around neutral (pH = 7.5) to a final particle diameter of around 900 nm at high pH ($13.4 \leq pH \leq 14$) (Figure 4.5 a). This confirmed that the particles were indeed pH-responsive.

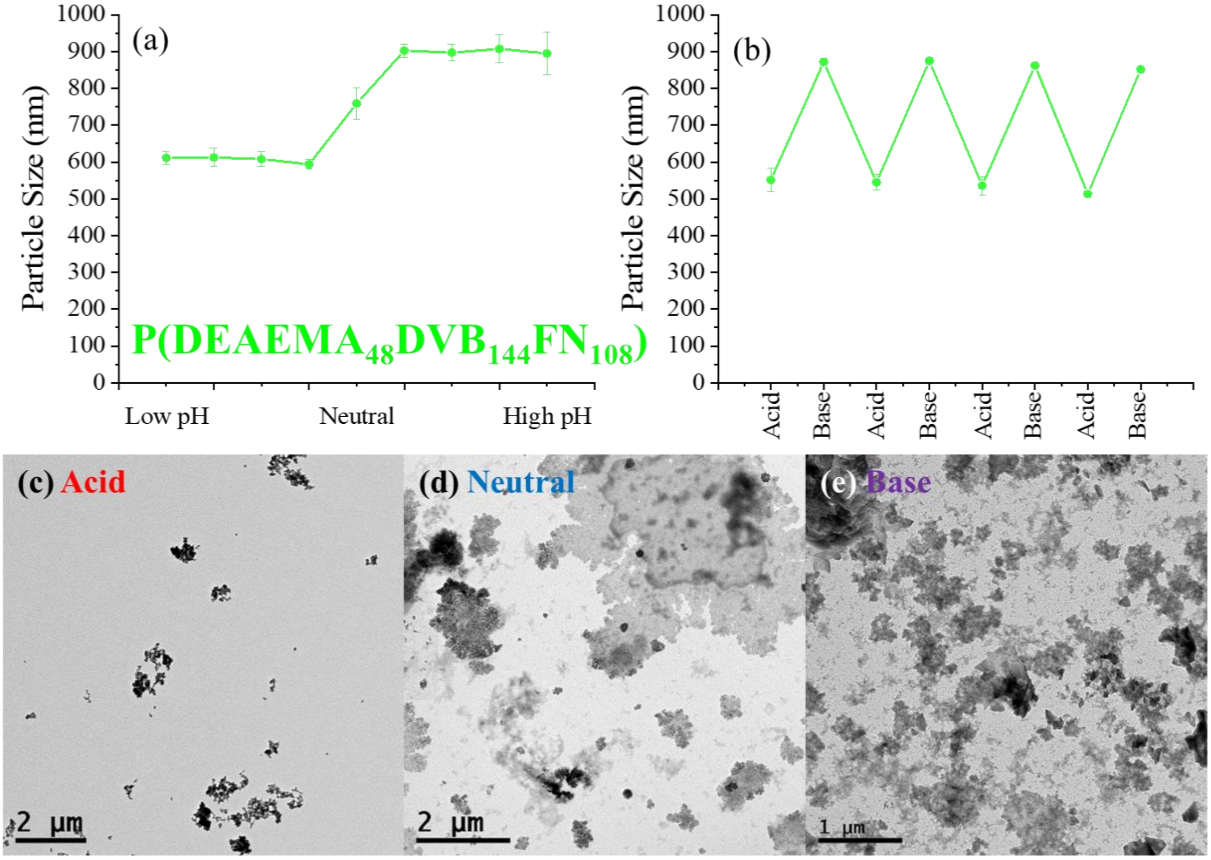

Figure 4.5 Particle size of (a) P(DEAEMA$_{48}$-DVB$_{144}$FN$_{108}$) particles in different pH solution from low to high; (b) Particle size of (b) P(DEAEMA$_{48}$-DVB$_{144}$FN$_{108}$) particles in acid and base switchable; TEM images in (c) acid, (d) neutral and (e) base solutions

The above experiment only demonstrates that dispersing the particles at a certain pH gives different sizes, however it is also important to know whether or not the particles can dynamically change size once in solution. Therefore, a sample of P(DEAEMA$_{48}$-DVB$_{144}$FN$_{108}$) particles was prepared in 0.1 mg mL^{-1} of 0.5 M HCl solution (pH = 0.3) after which the sample was switched to high pH (pH = 13.7) by the addition of NaOH followed by switching to acid conditions and back again a number of times. The sample was sonicated for 3 hours before the first analysis, and then the sample was sonicated for 0.5 hours after the addition of the acid or base. The particles can dynamically change size alternately in acid and base and the particle sizes are matched to the particle sizes at acid or base in above experiment (Figure 4.5 b). The TEM images illustrate the same trend that matches the particle size which is measured by DLS trends (Figure 4.5 c, d, and e). In addition, the SEM images also match the P(DEAEMA$_{48}$-DVB$_{144}$FN$_{108}$) particle size which is measured by DLS trends (Figure 4.14 a in appendix).

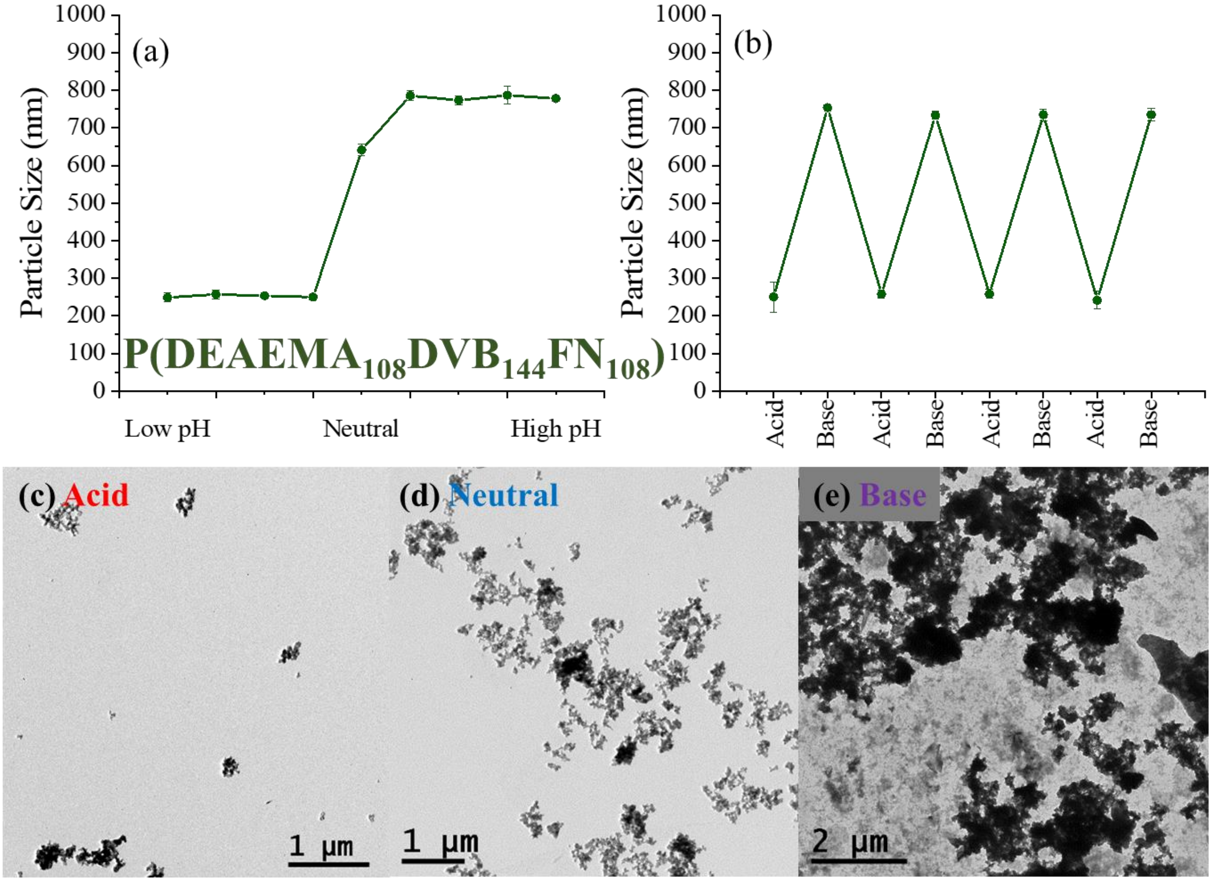

Figure 4.6 Particle size of (a) P(DEAEMA$_{108}$-DVB$_{144}$FN$_{108}$) particles in different pH solution from low to high; Particle size of (b) P(DEAEMA$_{108}$-DVB$_{144}$FN$_{108}$) particles in acid and base switchable; TEM images in (c) acid, (d) neutral and (e) base solutions

For P(DEAEMA$_{108}$-DVB$_{144}$FN$_{108}$) particles, the particle size is about 250 nm in acid condition ($0 \leq pH \leq 1.3$), while it is about 800 nm in base condition ($13.4 \leq pH \leq 14$) (Figure 4.6 a). The longer shell resulted in smaller particle size in acid conditions. This may be due to the long chains have more chargers and being more hydrophilic resulted a larger electrostatic repulsion to separate particles compared to the short chains that may still aggregate, making separation difficult. Zhou and co-workers[17], who reported the similar results that the PDMAEMA-PHFBA polymer micelles with short chains had a slightly lower critical micelle concentration (CMC) than the long chains. The particles can also dynamically change size alternately in acid (pH = 0.3) and base (pH = 13.7) and the particle sizes are matched to the particle sizes at acid (pH = 0.3) or base (pH = 13.7) in above experiment (Figure 4.6 b). The TEM images also reveal the same trend that matches the particle size which is measured by DLS trends (Figure 4.6 c, d, and e). Furthermore, the SEM images also match the P(DEAEMA$_{108}$-DVB$_{144}$FN$_{108}$) particle size which is measured by DLS trends (Figure 4.14 b in appendix).

The $P(4\text{-}VP_{82}\text{-}DVB_{268}FN_{200})$ particles display a particle diameter of around 200 nm at low pH (pH = 0.3), at higher pH (pH = 13.7) the particle diameter increases to over 600 nm, however this do not appear to plateau as is observed for PDEAEMA particles. Instead, the particle diameter gradually increases to over 800 nm at the highest pHs ($13.8 \leq pH \leq 14$). However, $P(4\text{-}VP_{45}\text{-}DVB_{134}FN_{100})$ particles do not demonstrate a size response with change in pH. This may be due to very short shell chain lengths not being long enough and the particles aggregate together which hinder the size of the particle changes. $P(4\text{-}VP_{82}\text{-}DVB_{268}FN_{200})$ particles on the other hand have a long enough chain length to stabilize the particles and keep them from aggregating in solution and allowing pH- responses to be observed (Figure 4.7 a). In addition, the particle size can be repeatable when it switches in acid (pH = 0.3) and base (pH = 13.7) (Figure 4.7 b). The TEM images illustrate the same trend that matches the particle size which is measured by DLS trends (Figure 4.7 c, d, and e).

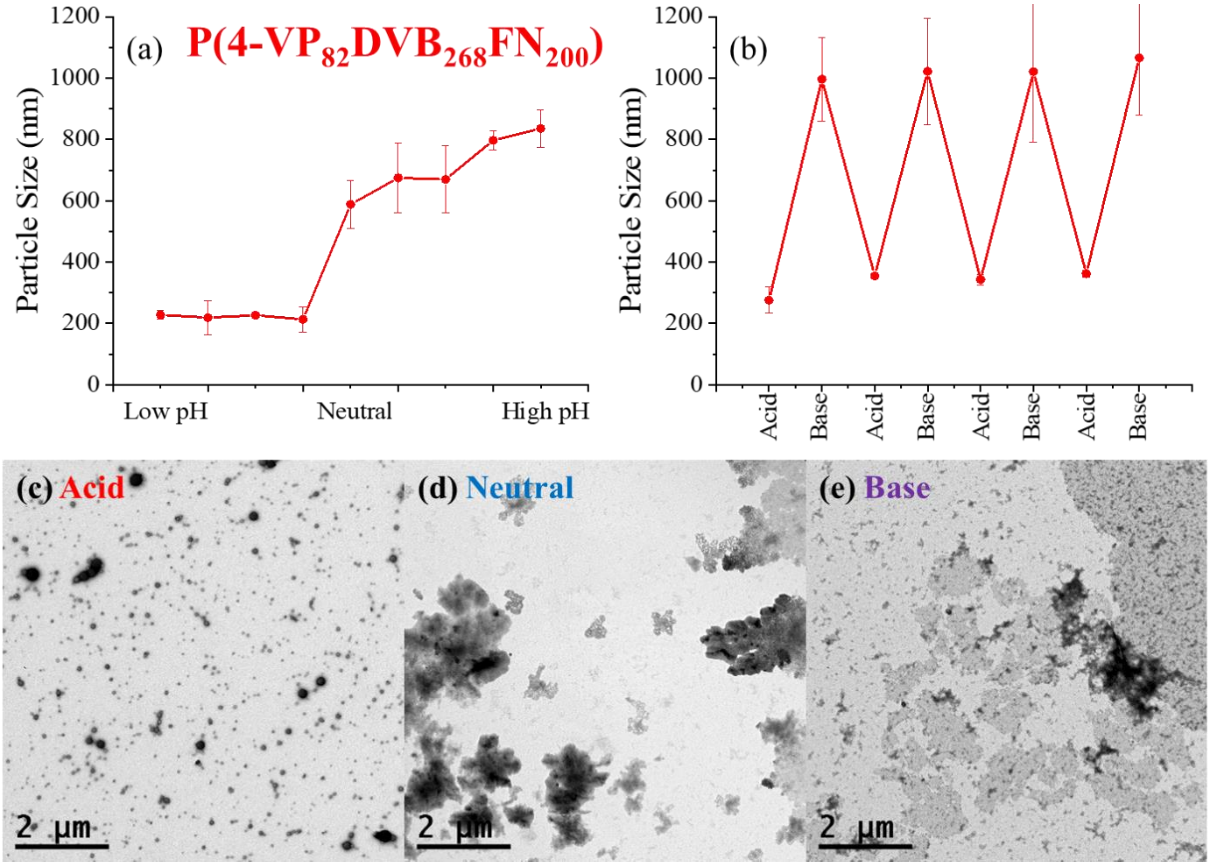

Figure 4.7 Particle size of (a) $P(4\text{-}VP_{82}\text{-}DVB_{268}FN_{200})$ particles in different pH solution from low to high; (b) Particle size of (b) $P(4\text{-}VP_{82}\text{-}DVB_{268}FN_{200})$ particles in acid and base switchable; TEM images in (c) acid, (d) neutral and (e) base solutions

For normal pH- responsive basic polymers which contain amine group (such as PDEAEMA[12,13,18]) or pyridine group (such as PVP[14,15]) can be used to form an amphiphilic block copolymer. Generally, the hydrogel or micelle is formed with a hydrophobic core part and hydrophilic shell parts.[19] The particle is normally large in the acidic condition and small in basic condition, which is attributed to the basic polymers with amine group or pyridine group are full protonated and the transformed into cationic polyelectrolytes under acidic condition.[20–22] Due to the inter-chain electrostatic repulsion and high water affinity, the polymer chains extend and the hydrogel or micelle swells. Conversely, when it is in basic condition, the basic polymer chains are deprotonated and become less hydrophilic. The inter-chain interactions become dominate and stronger than chain-solvent interactions. Therefore, the polymer chains contract, and the hydrogel or micelle is collapsed (Figure 4.8).

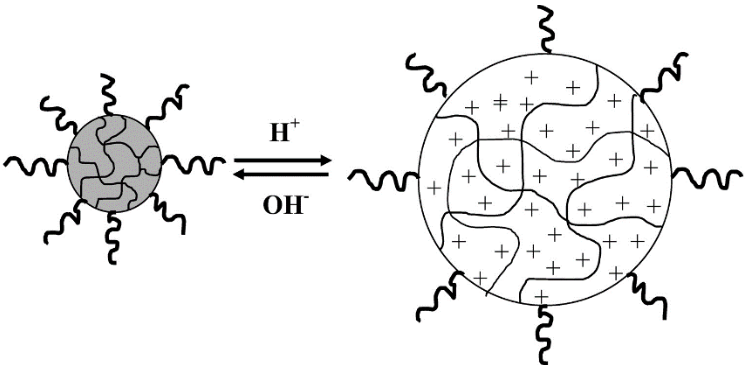

Figure 4.8 Schematic representation of the latex-to-microgel swelling transition

For the microporous polymer nanospheres, Mai et al.[5] and Yu et al.[6] who pre-prepared microporous cores and then gifted pH- responsive shells, showed a similar trend. The particles were large at low pH, a small and small at high pH, due to the hydrophobic parts are full crosslinked by rigid monomers with benzene rings which cannot swell or compress, resulting in the hydrophilic parts dominate the particle size. The P(DEAEMA$_{48}$-DVB$_{144}$FN$_{108}$), P(DEAEMA$_{108}$-DVB$_{144}$FN$_{108}$) and P(4-VP$_{82}$-DVB$_{268}$FN$_{200}$) particles clearly demonstrate a pH- response with small particle sizes at low pH solution ($0 \leq pH \leq 1.3$) and larger sizes at high pH solution ($13.4 \leq pH \leq 14$) (Figure 4.6 a, and Figure 4.7 a, and Figure 4.8 a). At first thought, this may not be the expected result, which the PDEAEMA and P4-VP particles were expected to have a large particle size at low pH, conversely, it is expected to be small at high pH. The results show the opposite of this behavior. This may be explained as follows: at low pH, the amino groups (pyridine groups) on the shell chains are protonated and charged each particle is well solvated and separated from the other particles in solution due to electrostatic repulsion. At high pH, the amino groups (pyridine groups) on the shell chains are deprotonated, however rather than contracting the chains are no longer able to stabilize the large cores and begin to aggregate together resulting in a larger particle being observed (Figure 4.9). Furthermore, for

PDEAEMA based particles, the pK_a of PDEAEMA polymer chains are about 7.3, which is mentioned in chapter 4.3.1. The particle sizes are small and particles separate & disperse at low pH solution, and when the particles begin to aggregate at neutral (pH = 7.5) which is close to its pK_a value. With the pH further increasing ($13.4 \leq pH \leq 14$), the particles form small lumps and precipitate (Figure 4.5 and Figure 4.6). However, for P4-VP based particles, the pK_a of P4-VP polymer chains are about 5.1, which is mentioned in chapter 4.3.1. Following the similar reason as PDEAEMA based particles, the particle sizes are small at low pH solution. While when at neutral condition (pH = 7.5), the particles have already aggregated as its pK_a value is lower than 7.5. With the pH further increasing ($13.4 \leq pH \leq 14$), the particle sizes do not change a lot (Figure 4.7).

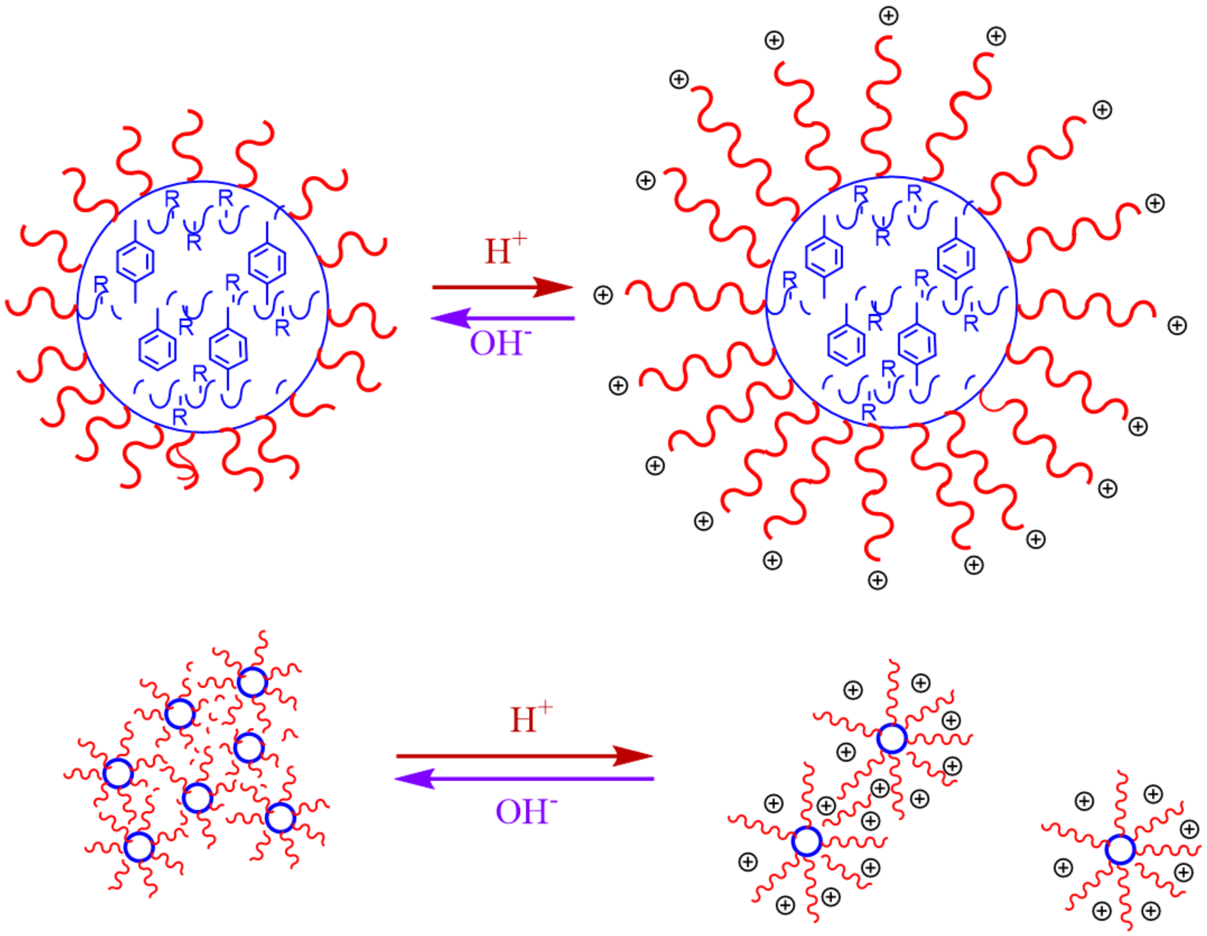

Figure 4.8 Schematic representation of the microporous polymeric nanospheres swelling transition

4.3.4 Investigation of the application of pH-responsive particles

Due to the combined properties of porosity and pH- responsivity, it is envisaged that these materials can capture small molecules in basic conditions and release them in acidic conditions, and therefore could potentially be used for drug or dye capture and release. A simple experiment was conducted to confirm this application using methylene blue as a model molecule due to its small molecular weight and visible color. In the experiment, 0.5 mg of P(DEAEMA$_{108}$-DVB$_{144}$FN$_{108}$) particles were dissolved in 5 mL methylene blue 2.5 ppm MB solution in a water-methanol mixture (Figure 4.10 a, and the blue line in Figure 4.10 d). The solvent was changed to acidic conditions (0.5 M HCl) by adding 12 M HCl, which caused the shell to swell and open. The mixture was sonicated for 1 hour and stirred for another 2 hours. Then, 3 M NaOH solution was added to make the mixture basic (0.5 M NaOH) and stirring under room temperature for 3 hours to close the shell. This caused the particles to switch to an aggregated form and precipitated. The precipitate was washed and collected by centrifuge and the remained solution which obtained first time was nearly clean (the red line in Figure 4.10 c). The precipitate was then re-dissolved in 5 mL of 0.5 M HCl water-methanol mixture solution and stirred at room temperature for 3 hours. Finally, the mixture was separated by centrifugation. The remaining solution was blue indicating that methylene blue had been released from the particles (Figure 4.10 b, and the black line in Figure 4.10 d). Furthermore, the particles released 18.1% MB in the remaining calculated through calibration curve (Figure 4.15 in appendix).

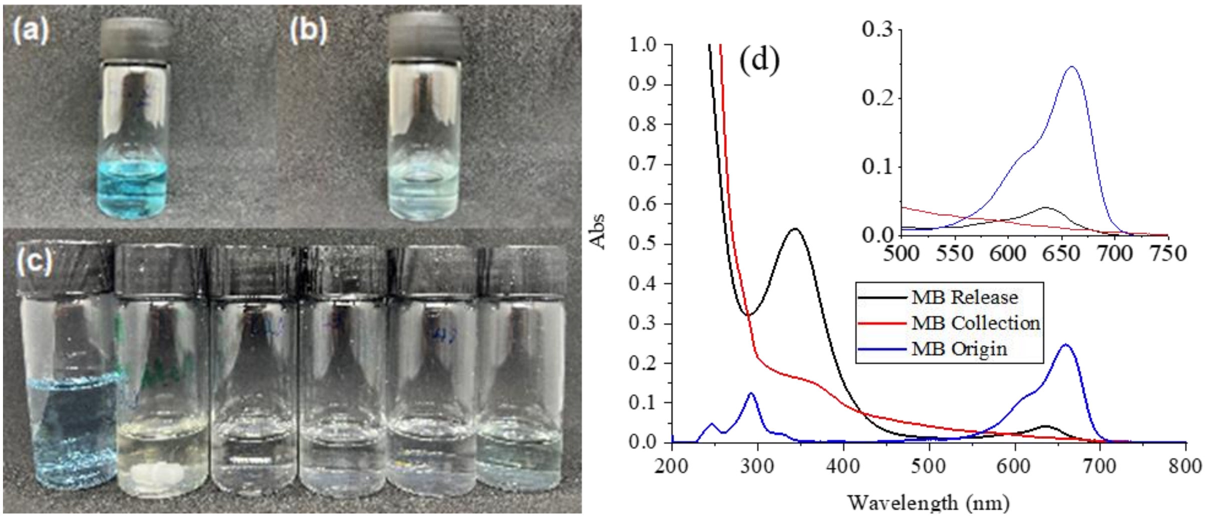

Figure 4.10 The experiment of dye capture and release. (a) is the mixture in MB solution. (b) is the MB released in a new acid solution. (c) is MB solution, solution after centrifuge, 1st wash after centrifuge, 2nd wash after centrifuge, 3rd wash after centrifuge, solution after dye release (from left to right); and (d) UV spectrum of MB peak before collection (blue) and after release (black)

4.4 Conclusion

Solvent-dispersible porous polymers with pH- responsive properties synthesised by reversible addition fragmentation chain transfer polymerisation induced self-assembly (RAFT-PISA) approach were successfully obtained. 2-cyano-2-propyl dodecyl trithiocarbonate (CPDTC) and 2-(dodecylthiocarbonothioylthio)-2-methylpropanoic acid (DDMAT) were used as CTAs for PDEAEMA and P4-VP, respectively and were synthesised via one pot step, firstly. The reaction kinetics were investigated in the previous chapter, and the same approach was followed in this study. For PDEAEMA shells, the DPs of 48, 108 and 208 were obtained, for P4-VP shells, the DPs of 45 and 82 were obtained were obtained.

Poly(diethylaminoethyl methacrylate-divinylbenzene/fumaronitrile) (PDEAEMA-DVB/FN), and poly(4vinlypyridine-divinylbenzene/fumaronitrile) (P4-VP-DVB/FN) were successfully synthesised via RAFT mediated polymerisation induced self-assembly. First, the suitable reaction solution with the water to methanol ratio of 40:60 (wt.%) was confirmed for the particles with the highest BET surface area. Then, the best core-shell ratios with the largest BET surface area were confirmed. However, there were no precipitate for the $PDEAEMA_{208}$ based particles, which maybe to the larger shell, resulting in greater steric hindrance that hinders the formation of the core of DVB and FN. The BET surface areas were much lower than those PEG and the PAA based particles, which can be attributed to the polar and large steric structure of the PDEAEMA, and PVP shells. Furthermore, the PDEAEMA, and P4-VP based particles have a dual morphology with smaller spheres structure to aggregate to form larger particles compared to the PAA, and PEG based particles from the SEM images and TEM images. At last, the PDEAEMA, and P4-VP based particles were confirmed with the pH-responsive properties in which the particle size is small at low pH, and it easily form the aggregates with the big size at high pH. Most strikingly, the particle size changes are repeatable and can switch among pH. Due to the properties, the methylene blue capture and release application confirmed that the dye can be captured when the solution changes from acid to base, and the dye releases from the particles when the solution changes from base to acid.

4.5 References

(1) James, A. M.; Derry, M. J.; Train, J. S.; Dawson, R. Dispersible Microporous Diblock Copolymer Nanoparticles via Polymerisation-Induced Self-Assembly. *Polym. Chem.* **2019**, *10* (28), 3879–3886. https://doi.org/10.1039/C9PY00596J.

(2) James, A. M.; Dawson, R. Efficient and Tunable White-Light Emission Using a Dispersible Porous Polymer. *Macromol. Rapid Commun.* **2020**, *41* (12), 2000176. https://doi.org/10.1002/marc.202000176.

(3) Ivko, S. A.; James, A. M.; Derry, M. J.; Dawson, R.; Haynes, A. Heterogenisation of a Carbonylation Catalyst on Dispersible Microporous Polymer Nanoparticles. *Catal. Sci. Technol.* **2022**, *12* (2), 664–673. https://doi.org/10.1039/D1CY01989A.

(4) Ferguson, C. T. J.; Huber, N.; Kuckhoff, T.; Zhang, K. A. I.; Landfester, K. Dispersible Porous Classical Polymer Photocatalysts for Visible Light-Mediated Production of Pharmaceutically Relevant Compounds in Multiple Solvents. *J. Mater. Chem. A* **2020**, *8* (3), 1072–1076. https://doi.org/10.1039/C9TA11242A.

(5) Mai, W.; Sun, B.; Chen, L.; Xu, F.; Liu, H.; Liang, Y.; Fu, R.; Wu, D.; Matyjaszewski, K. Water-Dispersible, Responsive, and Carbonizable Hairy Microporous Polymeric Nanospheres. *J. Am. Chem. Soc.* **2015**, *137* (41), 13256–13259. https://doi.org/10.1021/jacs.5b08978.

(6) Yu, H.; Wang, Z.; Wu, R.; Chen, X.; Chan, T.-W. D. Water-Dispersible PH/Thermo Dual-Responsive Microporous Polymeric Microspheres as Adsorbent for Dispersive Solid-Phase Extraction of Fluoroquinolones from Environmental Water Samples and Food Samples. *J. Chromatogr. A* **2019**, *1601*, 27–34. https://doi.org/10.1016/j.chroma.2019.05.004.

(7) Wang, J.; Yang, H.; Meng, Z.; Xie, B.; Yu, X.; Su, G.; Wang, L. Epoxy Coating with Excellent Anticorrosion and PH-Responsive Performances Based on DEAEMA Modified Mesoporous Silica Nanomaterials. *Colloids Surf. Physicochem. Eng. Asp.* **2022**, *634*, 127951. https://doi.org/10.1016/j.colsurfa.2021.127951.

(8) Pangborn, A. B.; Giardello, M. A.; Grubbs, R. H.; Rosen, R. K.; Timmers, F. J. Safe and Convenient Procedure for Solvent Purification. *Organometallics* **1996**, *15* (5), 1518–1520. https://doi.org/10.1021/om9503712.

(9) Skey, J.; K. O'Reilly, R. Facile One Pot Synthesis of a Range of Reversible Addition–Fragmentation Chain Transfer (RAFT) Agents. *Chem. Commun.* **2008**, *0* (35), 4183–4185. https://doi.org/10.1039/B804260H.

(10) Wong, A. S. M.; Mann, S. K.; Czuba, E.; Sahut, A.; Liu, H.; Suekama, T. C.; Bickerton, T.; R. Johnston, A. P.; K. Such, G. Self-Assembling Dual Component Nanoparticles with Endosomal Escape Capability. *Soft Matter* **2015**, *11* (15), 2993–3002. https://doi.org/10.1039/C5SM00082C.

(11) Liu, R.; Rong, Z.; Han, G.; Yang, X.; Zhang, W. Synthesis and Self-Assembly of Star Multiple Block Copolymer of Poly(4-Vinylpyridine)-Block-Polystyrene. *Polymer* **2021**, *215*, 123431. https://doi.org/10.1016/j.polymer.2021.123431.

(12) Thavanesan, T.; Herbert, C.; Plamper, F. A. Insight in the Phase Separation Peculiarities of Poly(Dialkylaminoethyl Methacrylate)s. *Langmuir* **2014**, *30* (19), 5609–5619. https://doi.org/10.1021/la5007583.

(13) Wang, X.; Liu, Z.; Huang, L. PH and Thermo Dual-Responsive Starch-g-P(DEAEMA-Co-PEGMA): Synthesis via SET-LRP, Self-Assembly and Drug Release Behaviors. *React. Funct. Polym.* **2019**, *141*, 165–171. https://doi.org/10.1016/j.reactfunctpolym.2019.05.011.

(14) Kennemur, J. G. Poly(Vinylpyridine) Segments in Block Copolymers: Synthesis, Self-Assembly, and Versatility. *Macromolecules* **2019**, *52* (4), 1354–1370. https://doi.org/10.1021/acs.macromol.8b01661.

(15) Satoh, M.; Yoda, E.; Hayashi, T.; Komiyama, J. Potentiometric Titration of Poly(Vinylpyridines) and Hydrophobic Interaction in the Counterion Binding. *Macromolecules* **1989**, *22* (4), 1808–1812. https://doi.org/10.1021/ma00194a051.

(16) Xie, F.; Hu, W.; Ding, L.; Tian, K.; Wu, Z.; Li, L. Synthesis of Microporous Organic Polymers via Radical Polymerisation of Fumaronitrile with Divinylbenzene. *Polym. Chem.* **2017**, *8* (39), 6106–6111. https://doi.org/10.1039/C7PY01240C.

(17) Zhou, J.; Wang, L.; Zha, X.; Wang, H. Synthesis of PH-Responsive Block Copolymer Micelles via RAFT Polymerisation Induced Self-Assembly and Its Application in Emulsifier-Free Emulsion Polymerisation. *Phosphorus Sulfur Silicon Relat. Elem.* **2020**, *195* (2), 131–141. https://doi.org/10.1080/10426507.2019.1655419.

(18) Schmalz, A.; Hanisch, M.; Schmalz, H.; Müller, A. H. E. Double Stimuli-Responsive Behavior of Linear and Star-Shaped Poly(N,N-Diethylaminoethyl Methacrylate) in Aqueous Solution. *Polymer* **2010**, *51* (6), 1213–1217. https://doi.org/10.1016/j.polymer.2009.11.023.

(19) Kocak, G.; Tuncer, C.; Bütün, V. PH-Responsive Polymers. *Polym. Chem.* **2017**, *8* (1), 144–176. https://doi.org/10.1039/C6PY01872F.

(20) Dai, S.; Ravi, P.; Chiu Tam, K. PH-Responsive Polymers : Synthesis, Properties and Applications. *Soft Matter* **2008**, *4* (3), 435–449. https://doi.org/10.1039/B714741D.

(21) Palioura, D.; Armes, S. P.; Anastasiadis, S. H.; Vamvakaki, M. Metal Nanocrystals Incorporated within PH-Responsive Microgel Particles. *Langmuir* **2007**, *23* (10), 5761–5768. https://doi.org/10.1021/la063359v.

(22) Dupin, D.; Rosselgong, J.; Armes, S. P.; Routh, A. F. Swelling Kinetics for a PH-Induced Latex-to-Microgel Transition. *Langmuir* **2007**, *23* (7), 4035–4041. https://doi.org/10.1021/la063278z.

4.6 Appendix

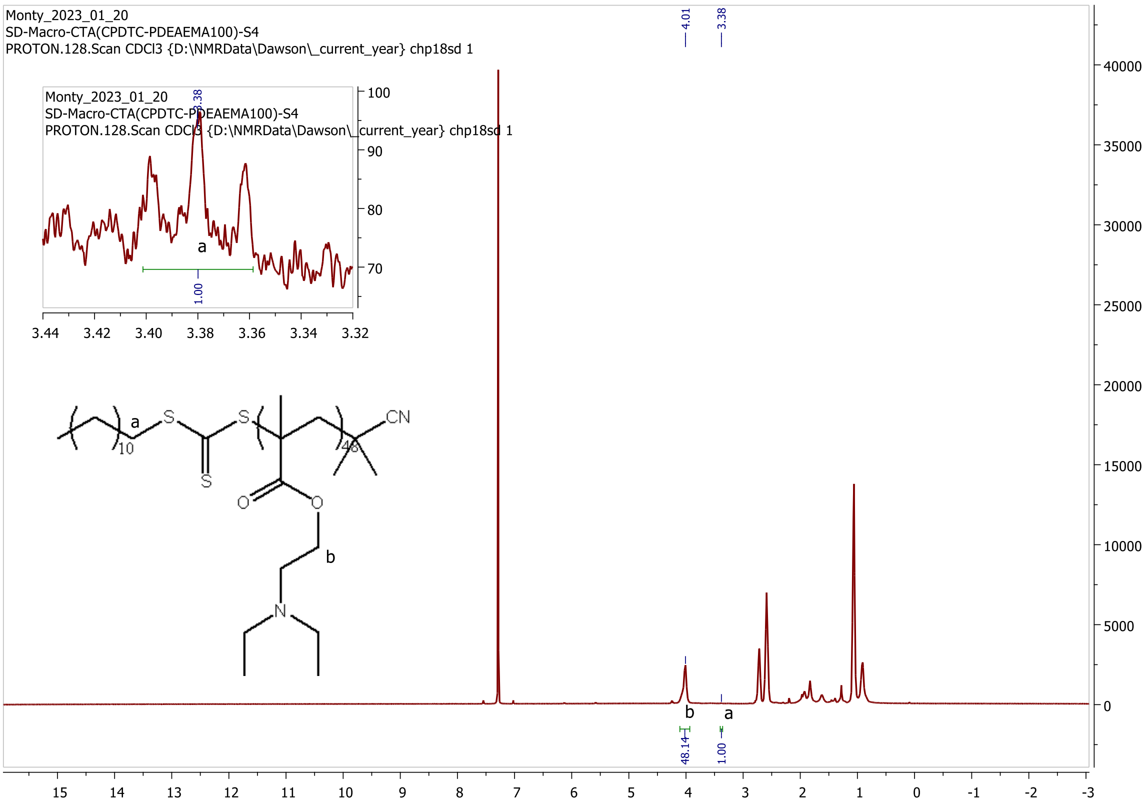

Figure 4.1 The ^{1}H NMR spectrum of Macro-CTA(CPDTC-PDEAEMA$_{48}$)

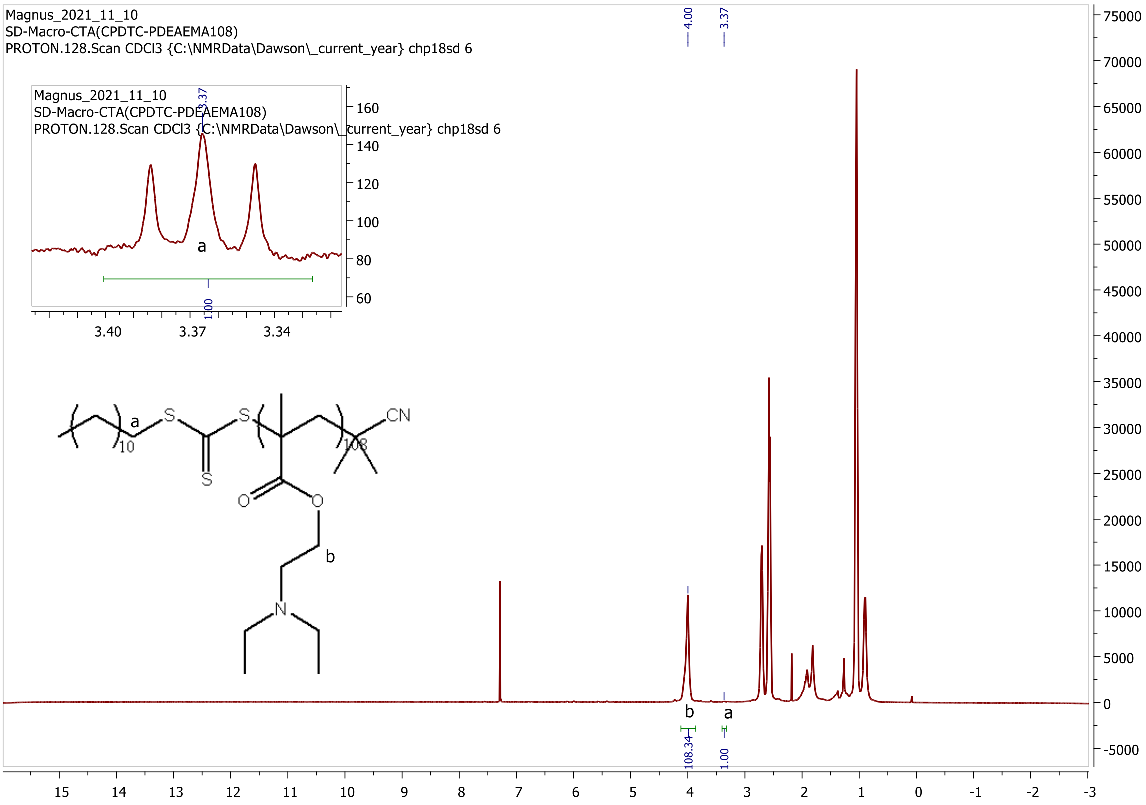

Figure 4.2 The ^{1}H NMR spectrum of Macro-CTA(CPDTC-PDEAEMA$_{108}$)

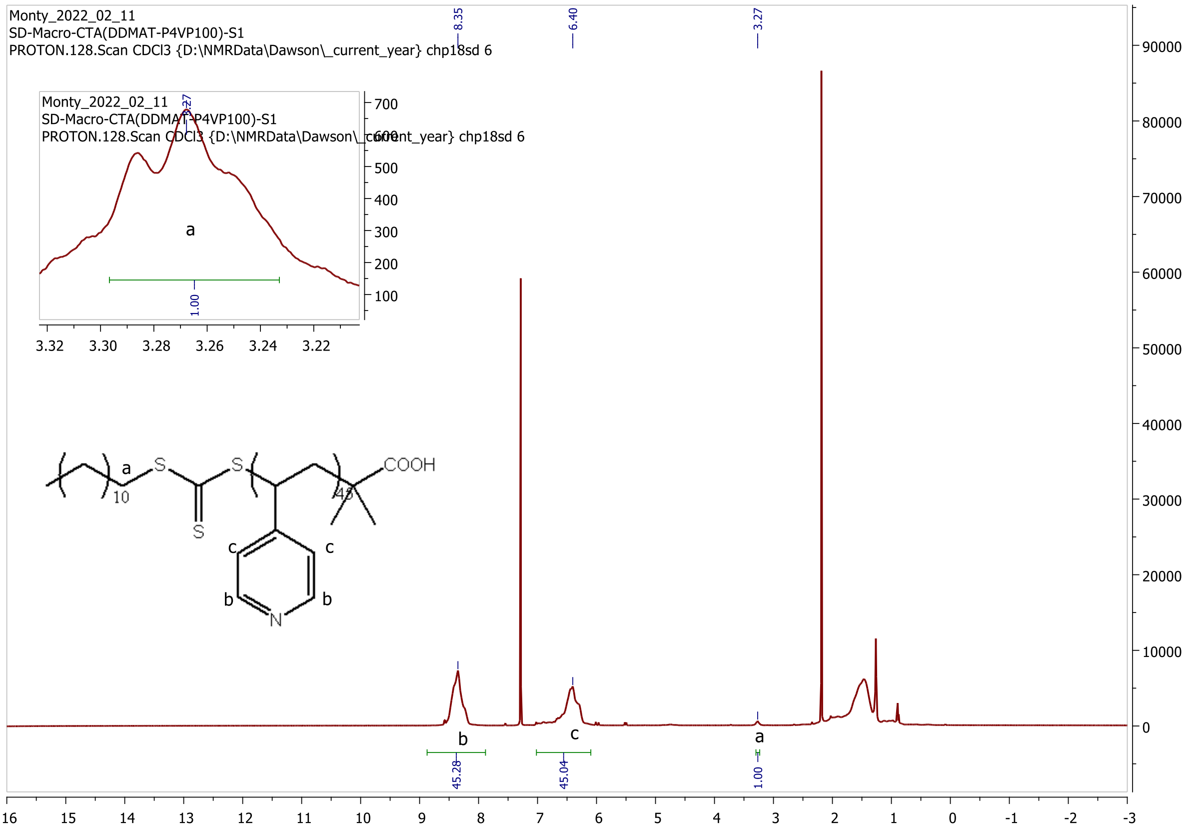

Figure 4.3 The ^{1}H NMR spectrum of Macro-CTA(DDMAT-P4-VP$_{45}$)

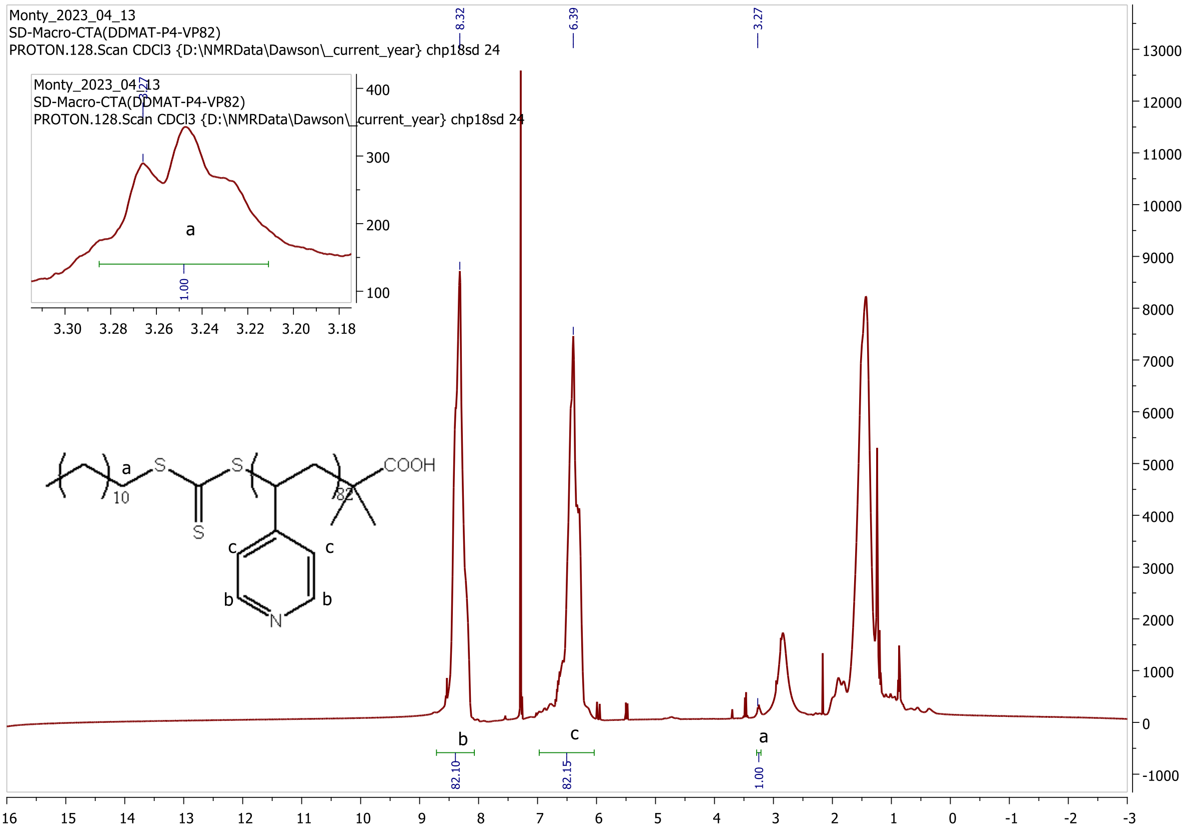

Figure 4.4 The ^{1}H NMR spectrum of Macro-CTA(DDMAT-P4-VP$_{82}$)

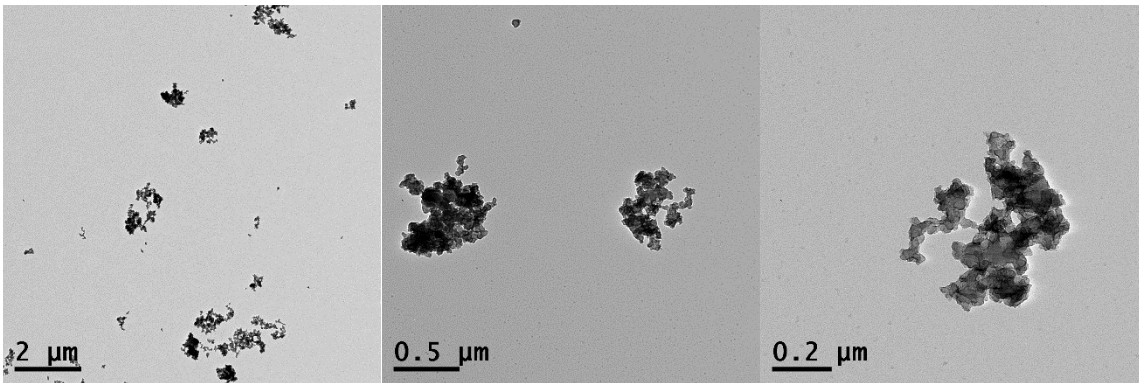

Figure 4.5 The different scales of TEM images of P(DEA$_{48}$-DVB$_{144}$FN$_{108}$) in acid

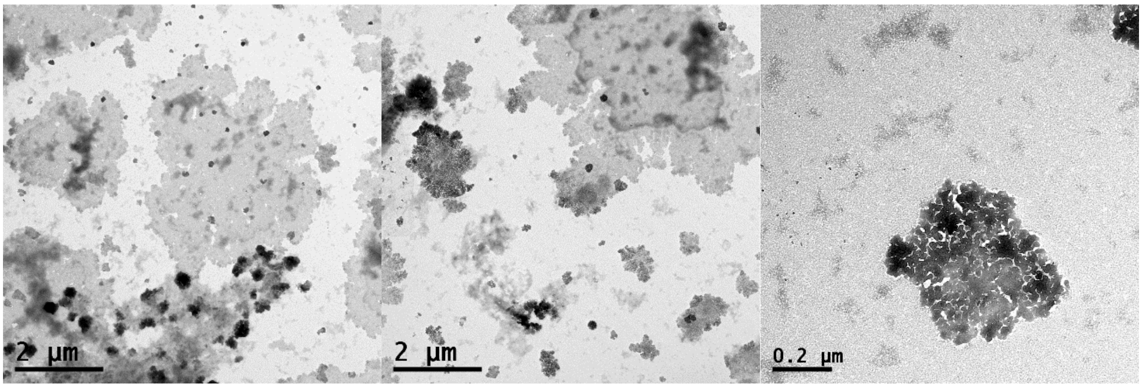

Figure 4.6 The different scales of TEM images of P(DEA$_{48}$-DVB$_{144}$FN$_{108}$) in neutral

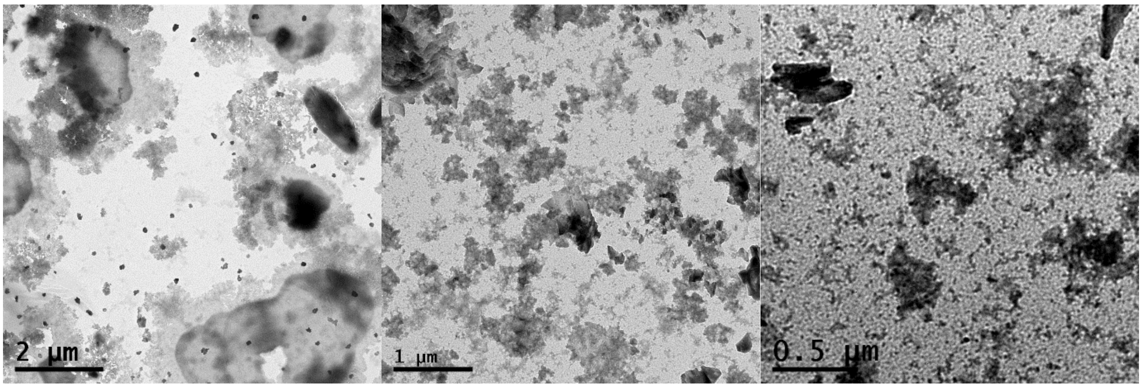

Figure 4.7 The different scales of TEM images of P(DEA$_{48}$-DVB$_{144}$FN$_{108}$) in base

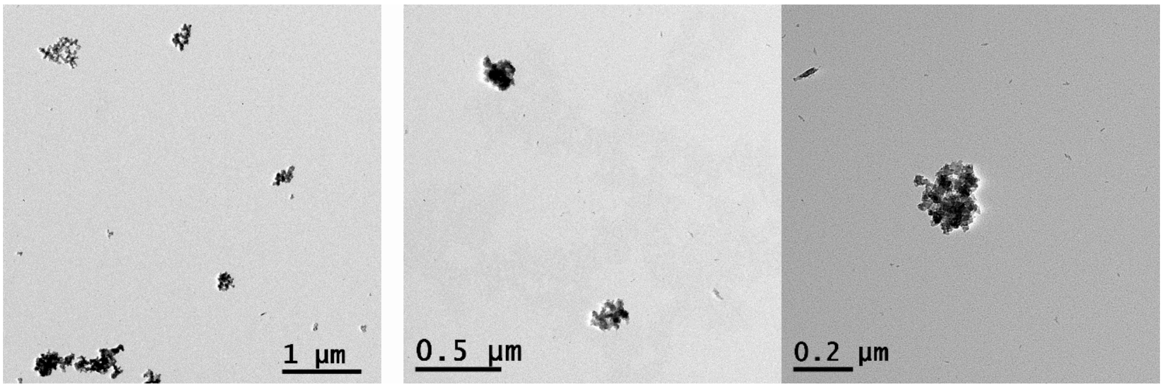

Figure 4.8 The different scales of TEM images of P(DEA$_{108}$-DVB$_{144}$FN$_{108}$) in acid

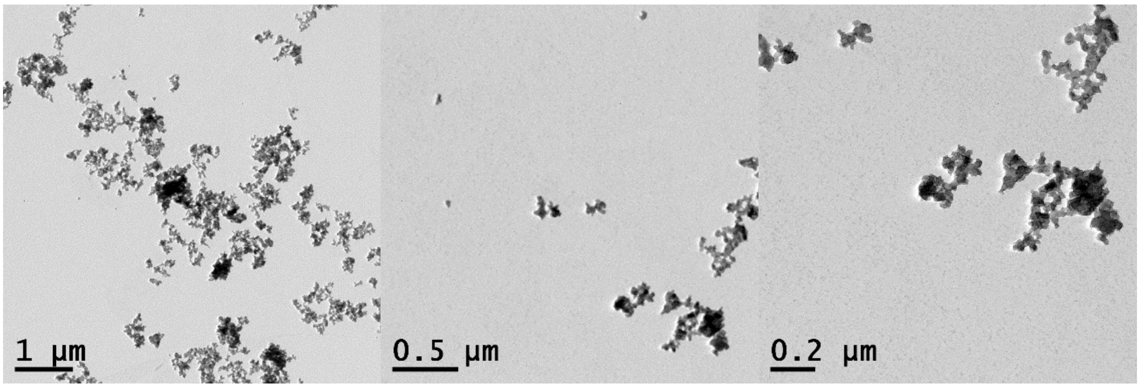

Figure 4.9 The different scales of TEM images of P(DEA$_{108}$-DVB$_{144}$FN$_{108}$) in neutral

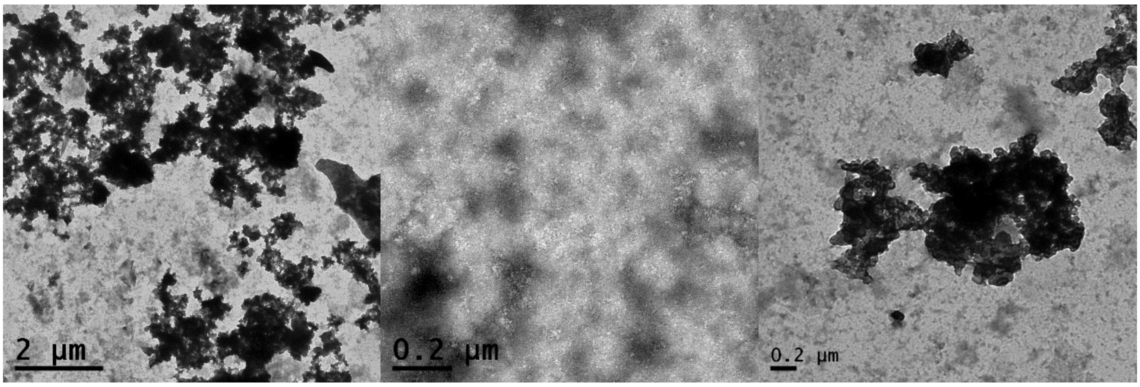

Figure 4.10 The different scales of TEM images of P(DEA$_{108}$-DVB$_{144}$FN$_{108}$) in base

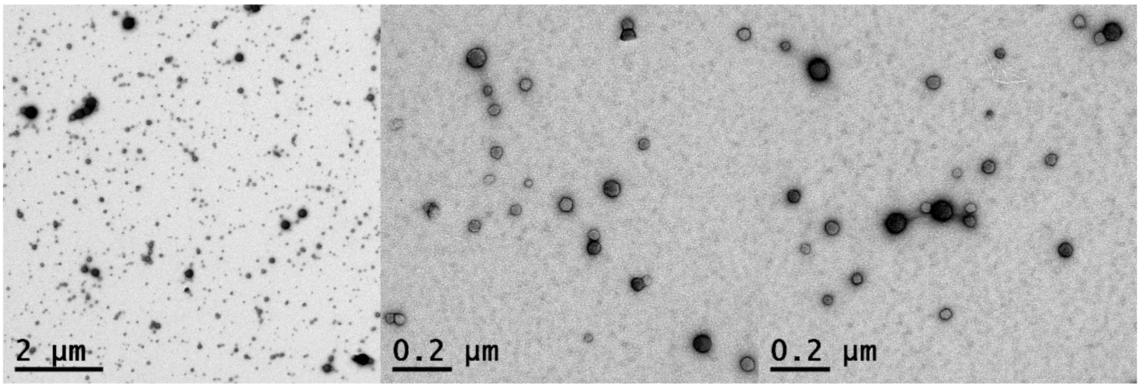

Figure 4.11 The different scales of TEM images of P(4-VP$_{82}$-DVB$_{268}$FN$_{200}$) acid

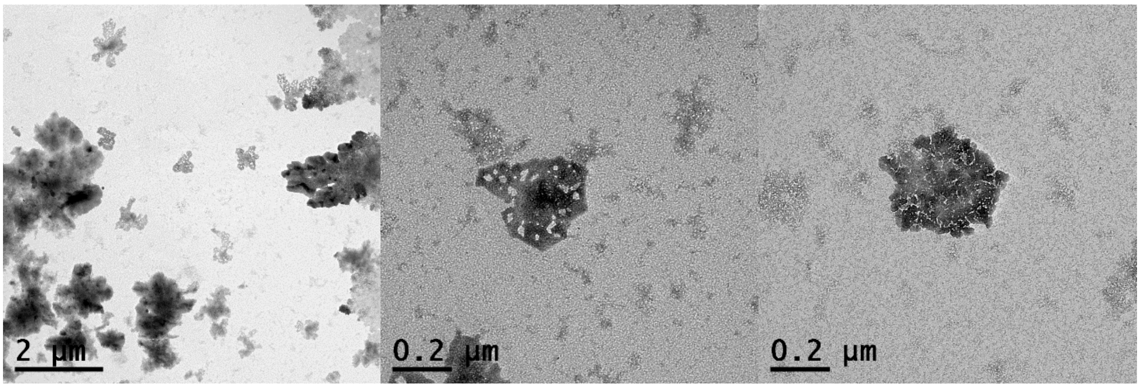

Figure 4.12 The different scales of TEM images of P(4-VP$_{82}$-DVB$_{268}$FN$_{200}$) in neutral

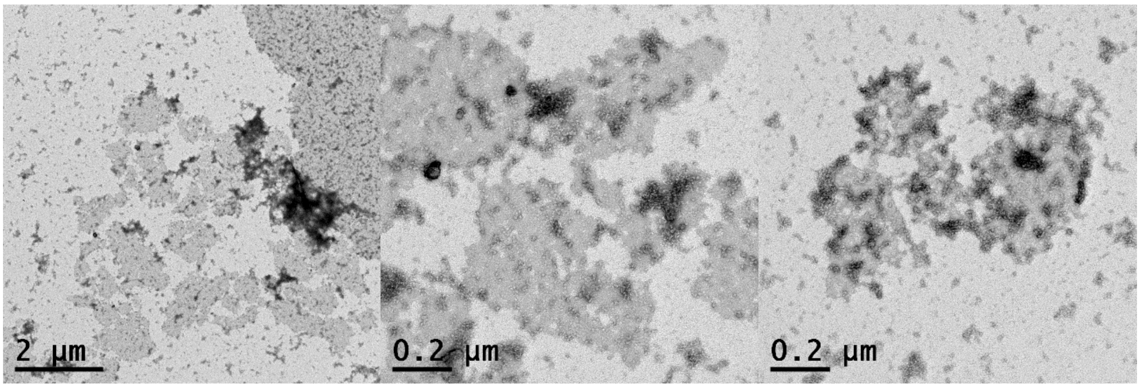

Figure 4.13 The different scales of TEM images of P(4-VP_{82}-$DVB_{268}FN_{200}$) in base

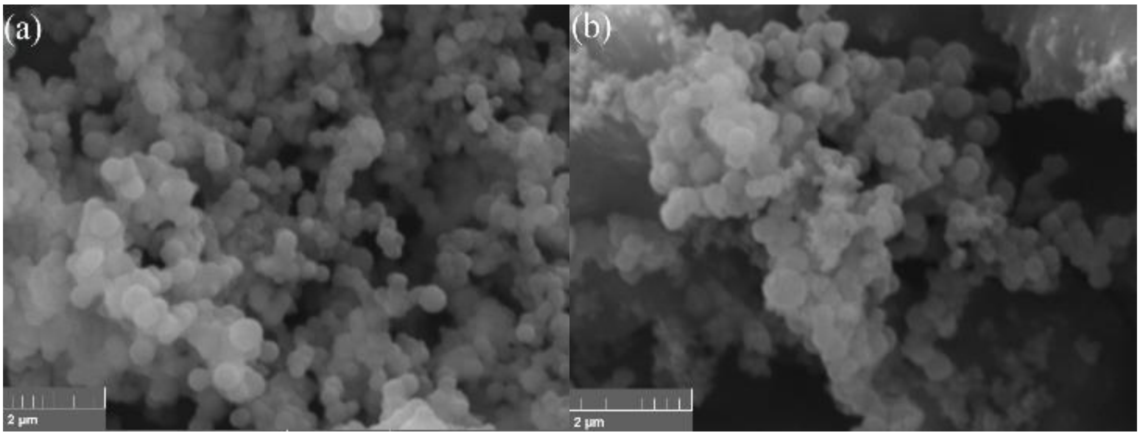

Figure 4.14 SEM images of PDEAEMA based particles (a) P($DEAEMA_{48}$-$DVB_{144}FN_{108}$) and (b) P($DEAEMA_{108}$-$DVB_{144}FN_{108}$)

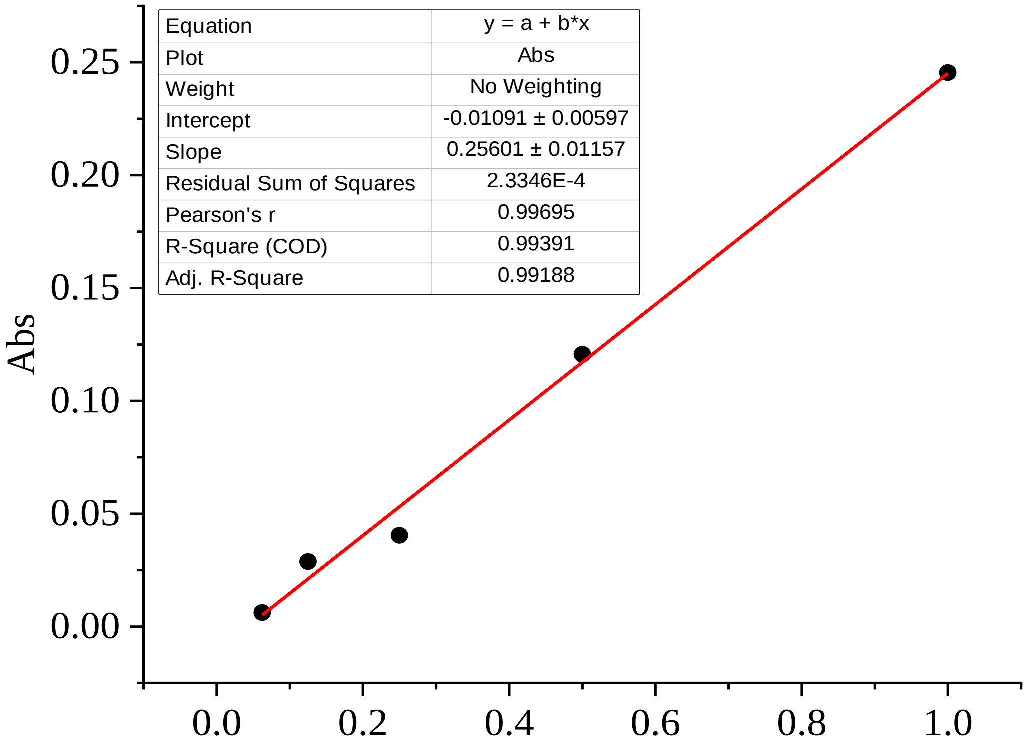

Figure 4.15 Calibration curve of MB at different concentrations

Chapter-5 Thermo-Responsive Shell

5.1 Aims

Following on from Chapter 4, where pH- responsive outer shells were used to switch the size of the particles by changing the pH, this chapter aims to investigate thermo- responsive porous polymer particles using DEAEMA (Figure 5.1 a), 4-VP (Figure 5.1 b), and N-isopropylacrylamide (NIPAm) (Figure 5.1 c), outer polymer chains. The thermo- responses will be investigated by changing the reaction conditions, core-shell ratio, and thermo-responses of the particles.

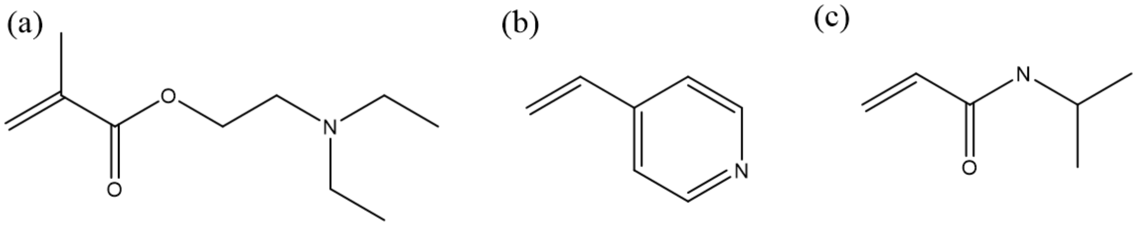

Figure 4.1 Molecular structure of DEAEMA (a), 4-VP (b), and NIPAm (c)

5.2 Experimental

5.2.1 Materials

2-Bromoisobutyryl bromide, cyanomethyl me-thyl(phenyl) carbamodithioate (CPDTC, 98%), fumaronitrile (FN, 98 %), potassium persulfate (KPS), potassium phosphate tribasic (K_3PO_4) were purchased from Sigma-Aldrich and used as received. Carbon disulfide, 1-dodecanethiol (98%) were purchased from Alfa Aesar and used as received. Dry 1,4-Dioxane and Tetrahydrofuran (THF) was obtained in a method analogous to the one outlined by Grubbs.[1] Magnesium sulfate (Mg_2SO_4) was purchased from Fischer and used as received. Diethylaminoethyl methacrylate (DEAEMA), divinylbenzene (DVB, technical grade 80 %), 4-vinylpyridine (4-VP, 95%) were passed through an alumina column in order to remove the inhibitor before use. 2,2′-Azobis(2-methylpropionitrile) (AIBN, 98 %) was purified by recrystallization from ethanol at 40 °C. N-Isopropylacrylamide (NIPAm, 97%) was recrystallized from benzene/hexane before use. All other chemicals were purchased from Sigma-Aldrich and used without any further purification.

5.2.2 Synthesis (The synthesis methods was adapted from James et al.[6])

5.2.2.1 Synthesis of 2-(dodecylthiocarbonothioylthio)-2-methylpropanoic acid (DDMAT) (chain transfer agent (CTA))

The synthesis of 2-(dodecylthiocarbonothioylthio)-2-methylpropanoic acid (DDMAT) was conducted using a modified method from O’Reilly et al.[2] Initially, dodecane thiol (3.61 mL, 15.07 mmol) was added to a stirred mixture of K_3PO_4 (3.199 g, 15.07 mmol) in acetone (20 ml) and stirred for 30 minutes. The mixture was then treated with CS_2 (3.129 g, 41.10 mmol) and stirred for an additional 60 minutes. Next, 2-bromoisobutyric acid (2.288 g, 13.70 mmol) was added to the reaction mixture, which was stirred overnight at room temperature. The solvent was extracted twice with CH_2Cl_2 (100 mL each) from 1 M HCl (100 mL). The organic extracts were washed with brine (150 mL) and $MgSO_4$ powder, followed by solvent removal using rotary evaporation. The obtained product was purified by precipitation in excess cold n-hexane twice to ensure purity and then dried in a vacuum oven overnight at 40 °C to yield the RAFT CTA (Yield = 49%. Found C: 57.04 %, H: 8.78 %, S: 26.47 %, Expected C: 56.04 %, H: 8.79 %, S: 26.37 %. δH (400 MHz, $CDCl_3$) = 3.31 (2H, t, S-CH_2-$(CH_2)_{10}$-CH_3), 1.75 (6H, s, C-$(CH_3)_2$), 1.76-1.20 (20H, t, S-CH_2-$(CH_2)_{10}$-CH_3), 0.90 (3H, t, SCH_2-$(CH_2)_{10}$-CH_3); δC (400 MHz, $CDCl_3$) = 220.85, 178.08, 55.53, 37.09, 31.93, 29.64, 29.57, 29.46, 29.36, 29.12, 28.98, 27.82, 25.24, 25.23, 22.70, 14.14; m/z (EI) 363.3, 303.3, 277.2, 201.3) (Synthesised in Chapter 3 and see in Figure 3.1 in appendix).

5.2.2.2 Synthesis of Poly (diethylaminoethyl methacrylate) (PDEAEMA) Based Macro-Chain Transfer Agent (CTA) (Macro-CTA (CPDTC-PDEAEMA)) via RAFT

The synthesis of macro-CTA (CPDTC-PDEAEMA$_x$) (x=48, 108) was performed using a modified version of the method described by Wong et al.[10] Specifically, 2-bromoisobutyryl bromide, 2-cyano-2-propyl dodecyl trithiocarbonate (CPDTC), and 1, 3, 5-trioxane were combined in a 2-necked round bottom flask. The flask was subjected to evacuation and nitrogen backfilling procedures three times. Dry THF and diethylaminoethyl methacrylate (DEAEMA) were added to the flask. The solution was bubbled with nitrogen gas to eliminate any residual air and then heated to 75 °C. Polymerisation was initiated by adding 2,2′-azobis(2-methylpropionitrile) (AIBN) with THF (1 mL), and the reaction was allowed to proceed for 24 h at 75 °C. The resulting mixture was purified by precipitation in deionized water, and the sample was subsequently dried in a vacuum oven overnight at 60 °C to yield the RAFT macro-CTA (Table 5.1, Figure 4.1-4.2 in appendix).

Table 5.1 Different components for synthesis of PDEAEMA$_x$ based Macro-CTA

Sample Name	DEAEMA	CTA	Trioxane	AIBN	THF
	mL/mmol	mg/mmol	mg/mmol	mg/mmol	mL
PDEAEMA$_{48}$ based Macro-CTA	2.1/10.00	90.0/1.00	90.0/1.00	1.6/0.01	12.4
PDEAEMA$_{108}$ based Macro-CTA	4.1/20.00	180.0/2.00	180.0/2.00	3.3/0.02	12.4

5.2.2.3 Synthesis of Poly (4-vinylpyridine) (P4-VP) Based Macro-Chain Transfer Agent (CTA) (Macro-CTA (DDMAT-P4-VP)) via RAFT

The synthesis of macro-CTA (DDMAT-P4-VP$_x$) (x-45, 82) was performed using a method similar to that described by Liu et al.[11] In this method, 2-(Dodecylthiocarbonothioylthio)-2-methylpropionic acid (DDMAT) and 1, 3, 5-trioxane were combined in a 2-necked round bottom flask, which was evacuated and backfilled with nitrogen three times. Anhydrous 1,4-dioxane and ethanol, along with 4-vinylpyridine (4-VP), were added to the flask. The solution was then bubbled through with nitrogen gas to remove any residual air before being heated to 70 °C. Polymerisation was initiated by adding 2,2′-azobis(2-methylpropionitrile) (AIBN) in 1,4-dioxane (0.2 mL), and the mixture was held at 70 °C for 8.0 h. The product was then purified by precipitation into diethyl ether and dried in a vacuum oven overnight at 60 °C, yielding the RAFT macro-CTA (Table 5.2, Figure 4.3-4.4 in appendix).

Table 5.2 Different components for synthesis of P4-VP$_x$ based Macro-CTA

Sample Name	4-VP	CTA	Trioxane	AIBN	Dioxane	Ethanol
	mL/mmol	mg/mmol	mg/mmol	mg/mmol	mL	mL
P4-VP$_{45}$ based Macro-CTA	5.2/47.56	173.0/0.4756	42.8/0.48	19.5/0.1189	1.2	13.8
P4-VP$_{82}$ based Macro-CTA	10.4/95.12	173.0/0.4756	85.6/0.95	19.5/0.1189	1.2	13.8

5.2.2.4 Synthesis of Poly (N-isopropylacrylamide) (PNIPAm) Based Macro-Chain Transfer Agent (CTA) (Macro-CTA (DDMAT-PNIPAm)) via RAFT

Synthesis of Macro-CTA (DDMAT-PNIPAm$_{100}$)

The macro-CTA (DDMAT-PNIPAm$_{100}$) prepared followed Li and coworker.[5] 2-(Dodecylthiocarbonothioylthio)-2-methylpropionic acid (DDMAT, 145.6 mg, 0.40 mmol) and N-isopropylacrylamide (PNIPAm, 454 mg, 4.00 mmol) were added to a 2-necked round bottom flask, which was evacuated and back-filled with nitrogen three times. Then, anhydrous 1,4-dioxane (2.09 mL) was added and the solution was purged with nitrogen gas to remove any air before heating to 80 °C. Polymerisation was initiated by adding 2,2′-azobis(2-methylpropionitrile) (AIBN, 32.8 mg, 0.20 mmol) with 1,4-dioxane (0.1 mL) and the reaction was held at 80 °C for 8.0 h. After the reaction, the mixture was diluted with a small amount of acetone and purified by precipitation into a large amount of cold n-hexane. The resulting product was dried overnight at 40 °C in a vacuum oven, yielding the RAFT macro-CTA (Figure 5.1 in appendix).

5.2.2.5 Synthesis of Poly (diethylaminoethyl methacrylate) (PDEAEMA) Based Particles via RAFT Mediated Polymerisation Induced Self-Assembly with Different Core-Shell Ratios

The PDEAEMA based particles were prepared in the same way. To a 2-necked round bottom flask, Macro-CTA (CPDTC-PDEAEMA$_x$) (x=48, 108) and FN were added. The flask was then evacuated and backfilled with nitrogen three times. Next, DVB was added to a mixture of methanol and water in a 60:40 (wt.%) ratio to create a 1.0 wt. % solution, and the solution was bubbled with nitrogen to remove any air before heating to 70 °C. Polymerisation was initiated by adding AIBN and held at 70 °C for 24 hours. The product was obtained as a gray solid through reprecipitation into diethyl ether before drying in vacuo at 40 °C for 16 h (Table 5.3).

Table 5.3 Different monomer components for synthesis of different PDEAEMA based particles

Sample Name	Monomer Composition				Solution Composition	
	PDEAEMA$_x$	DVB	FN	AIBN	Water	Methanol
	mg/mmol	mL/mmol	mg/mmol	mg/mmol	mL	mL
PDEAEMA$_{48}$DVB$_{144}$FN$_{108}$	184.5/0.02	0.40/2.88	168.5/2.16	0.7/0.04	29.1	55.2
PDEAEMA$_{108}$DVB$_{144}$FN$_{108}$	406.5/0.02	0.40/2.88	168.5/2.16	0.7/0.004	38.0	72.0

5.2.2.6 Synthesis of Poly (4-vinylpyridine) (P4-VP) Based Particles via RAFT Mediated Polymerisation Induced Self-Assembly with Different Core-Shell Ratios

The P4-VP based particles were prepared in the same way. Macro-CTA (DDMAT-P4-VP$_x$) (x=45, 82) and FN were added and the flask was evacuated and backfilled with nitrogen three times. A solution of DVB (0.26 ml, 1.88 mmol) in water and methanol (40:60 wt%) was added to the flask to yield a 1.0 wt% solution. The mixture was bubbled with nitrogen to remove any air, then heated to 70 °C and AIBN was added to initiate polymerisation. The reaction was maintained at 70 °C for 24 hours. The product was obtained as a yellow solid through reprecipitation into diethyl ether and dried in vacuo at 40 °C for 16 hours (Table 5.4).

Table 5.4 Different monomer components for synthesis of different P4-VP based particles

Sample Name	Monomer Composition				Solution Composition	
	P4-VP$_x$	DVB	FN	AIBN	Water	Methanol
	mg/mmol	mL/mmol	mg/mmol	mg/mmol	mL	mL
P4-VP$_{45}$DVB$_{134}$FN$_{100}$	72.4/0.014	0.26/1.88	109.2/1.40	0.7/0.004	17.8	33.8
P4-VP$_{82}$DVB$_{268}$FN$_{200}$	89.7/0.01	0.37/2.68	156.0/2.00	0.0/0.002	23.8	45.0

5.2.2.7 Synthesis of Poly (N-Isopropylacrylamide) (PNIPAm) Based Particles via RAFT Mediated Polymerisation Induced Self-Assembly with Different Core-Shell Ratios

The PNIPAm based particles were performed using a method adapted from James et al.[6]. Firstly, a PNIPAm based macro-CTA (Macro-CTA (DDMAT-PNIPAm$_{100}$) and FN were introduced into a 2-necked round bottom flask. The flask was then subjected to evacuation and backfilling with nitrogen gas three times. Next, DVB was added to a mixture of water and ethanol in a 60:40 (wt.%) ratio to create a 1.0 wt. % solution. The solution was bubbled with nitrogen to remove any air before heating to 70 °C. Polymerisation was initiated by adding KPS and the reaction mixture was held at 70 °C for 24 hours. The product was obtained as a grey solid through reprecipitation into diethyl ether before drying in vacuo at 40 °C for 16 h (Table 5.5).

Table 5.5 Different monomer components for synthesis of different PNIPAm based particles

Sample Name	Monomer Composition				Solution Composition	
	PNIPAm$_{100}$	DVB	FN	KPS	Water	Methanol
	mg/mmol	mL/mmol	mg/mmol	mg/mmol	mL	mL
PNIPAm$_{100}$DVB$_{50}$FN$_{37.5}$	233.3/0.02	0.14/1.00	58.5/0.75	1.1/0.004	25.4	21.4
PNIPAm$_{100}$DVB$_{100}$FN$_{75}$	116.6/0.01	0.14/1.00	58.5/0.75	0.5/0.002	18.3	15.5
PNIPAm$_{100}$DVB$_{300}$FN$_{225}$	58.3/0.005	0.21/1.50	87.8/1.125	0.3/0.001	20.5	17.3

5.3 Results and discussion

5.3.1 Synthesis of PNIPAm based particles

PNIPAm is a water-soluble polymer, and hence it was predicted that it can be used the same reaction conditions as for the PEG, and PAA based particles in a water-ethanol mixture with the ratio of 60:40 (wt.%). Prior research has indicated that the BET surface area of particles may be influenced by different ratios of core to shell. Here, various sizes of core were investigated to determine the highest BET surface area of PNIPAm based particles. The PNIPAm based macro-CTA shells were prepared following the mothod from Li et al.'s method[5] with a DP=100 and confirmed by ^{1}H NMR spectroscopy with the ratio of methine group (-NH-CH-) peak on PNIPAm to methylene group ($-S-CH_2-$) peak on CTA which is similar to the PAA based macro-CTA shell. As previously DVB and FN were used as the core segment with a ratio of DVB to FN of 4:3.[6–10] The BET surface area was calculated from the nitrogen adsorption isotherms at 77.3 K using the BET equation.

Table 5.6 Monomer composition and BET surface area of PNIPAm based particles using a water to ethanol mix of 60:40 (wt.%)

Monomer Composition			BET Surface Area
PNIPAm	DVB	FN	(m^2 g^{-1})
100	50	37.5	0
100	100	75	62
100	300	225	193

The two larger particles were found to be porous with surface areas of 62 m^2 g^{-1} and 193 m^2 g^{-1}, however the smallest core size of $P(NIP_{100}\text{-}DVB_{50}FN_{37.5})$, found a nonporous structure which may be due to the core size being too small to form a porous structure (Table 5.6).

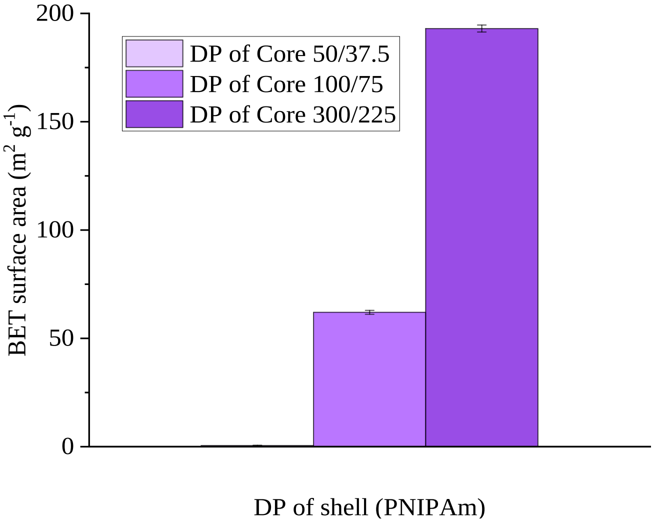

Figure 5.2 BET surface area of particles synthesised when using different core-shell ratios

The increase in BET surface area observed when using larger cores is similar to the PEG based particles which the BET surface area increased before reaching a maximum followed by a decrease in BET surface area (Figure 5.2). This is due to the larger core size will decrease the number of microporous structures. The core size at which the BET surface reaches a maximum is higher compared to that for the PAA, PDEAEMA and P4-VP based particles. The particles with the largest BET surface areas, $P(NIPAm_{100}\text{-}DVB_{300}FN_{225})$ particles were selected to do the further analysis.

In addition, the particle morphology of PNIPAm based particles was observed to exhibit a dual structure, consisting of smaller spheres that aggregate to form larger particles, which is consistent with the behavior observed in PAA, PDEAEMA, P4-VP, and PEG based particles (Figure 5.3).

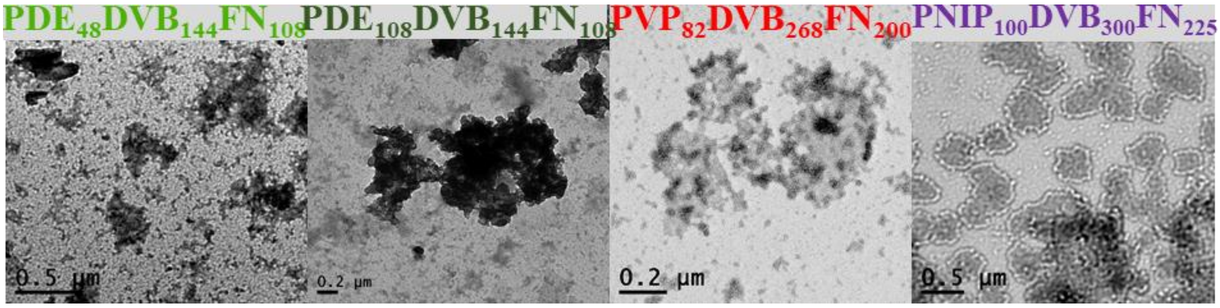

Figure 5.3 TEM images of $P(DEAEMA_{48}\text{-}DVB_{144}FN_{108})$, $P(DEAEMA_{108}\text{-}DVB_{144}FN_{108})$, $P(4\text{-}VP_{82}\text{-}DVB_{268}FN_{200})$ and $P(NIPAm_{100}\text{-}DVB_{300}FN_{225})$ particles in the water solution

The nitrogen adsorption isotherms (Figure 5.4 a) of $P(NIPAm_{100}\text{-}DVB_{300}FN_{225})$ particles exhibit a large increase uptake of nitrogen at low pressure, indicating the presence of microporous structure. At a high pressure ($P/P_0 > 0.9$), a significant increase in the gas uptake is observed, which is again attributed to the condensation of nitrogen between the smaller particles in the larger particle aggregates (inter-particulate condensation). The pore size distributions (PSDs) calculated by nonlocal density functional theory (NLDFT) (Figure 5.4 b) show major peaks at pore widths around 1.8 nm, 3.0 nm, 5.1 nm, 6.5 nm, 8.1 nm and along with further larger pores and voids, which made up by the aggregation of the small sphere particles. The cumulative surface area plots (Figure 5.4 c) also show that most of the pore volume is the larger meso- and macropore region with only a few microporous structures present.

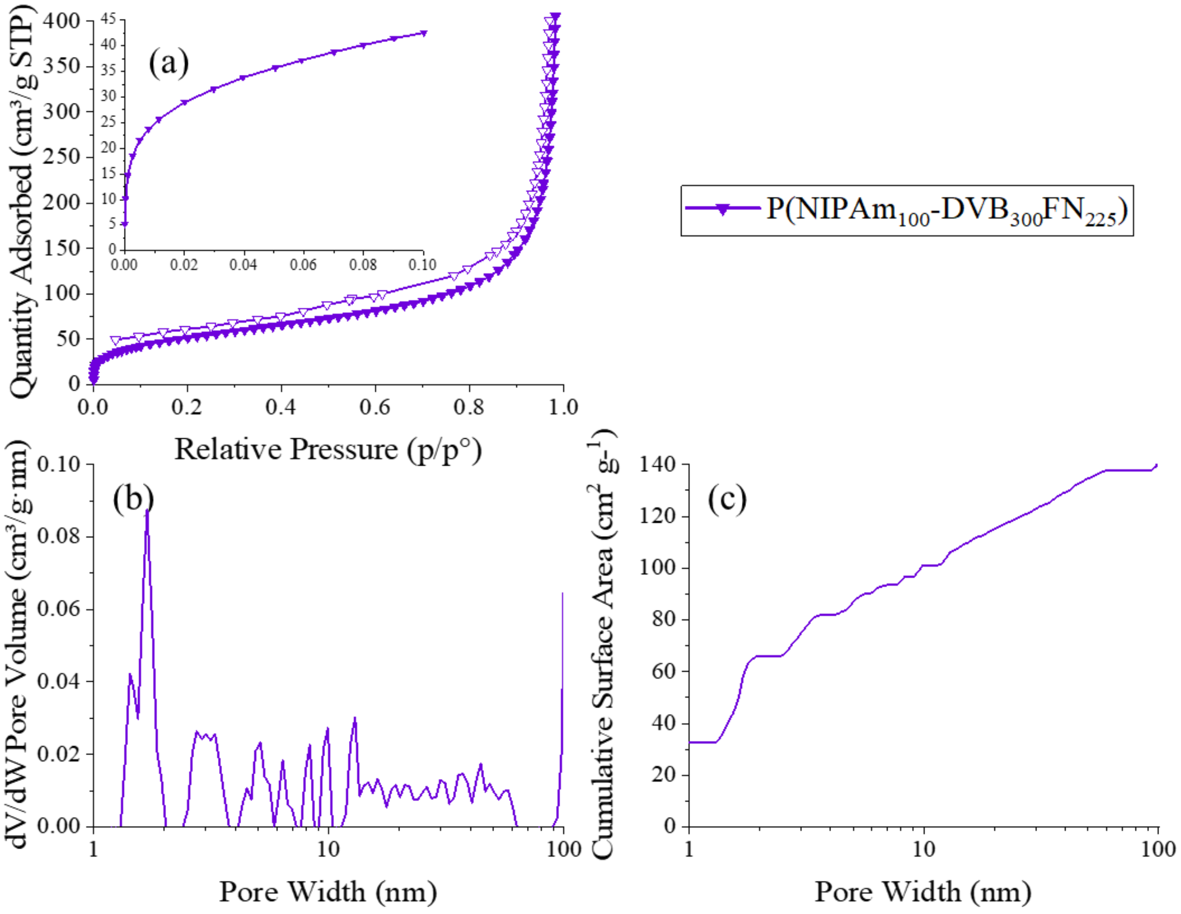

Figure 5.4 (a) Nitrogen adsorption isotherms of PNIPAm based particles with different combination of DVB and FN at 77.3 K; (b) Pore size distributions calculated using NLDFT method (slit pore models, differential pore volume vs pore width); and (c) Cumulative surface areas

5.3.2 Investigation of thermo-responsive of PDEAEMA, P4-VP and PNIPAm based particles

Poly(N-isopropylacrylamide) (PNIPAm) is well known as a thermo- responsive polymer and is one of the most researched temperature responsive polymers with LCST of 32 °C, which is close to body temperature; it has therefore been widely investigated for drug delivery. It undergoes a phase transition from hydrophobic (dewatering) state to hydrophilic (swollen) state when the temperature is decreased down to the LCST, leading to the realignment of water molecules around hydrophobic and hydrophilic groups in the polymer chains. This results in swelling of hydrogel networks and water adsorbtion.[11–13] The carboxyl group on the PDEAEMA follows a similar response mechanism to the amide group on the PNIPAm.[14,15] Although, P4-VP is normally known as a pH- responsive polymer, a few papers have also reported it has thermo- response which is attributed to the inner arrangement of P4-VP molecules.[16]

P($DEAEMA_{48}$-$DVB_{144}FN_{108}$) particles with a BET surface area of 101 m^2 g^{-1} and P($DEAEMA_{108}$-$DVB_{144}FN_{108}$) particles with a BET surface area of 79 m^2 g^{-1}, which were obtained in Chapter 4.3.2 and selected due to having the highest BET surface areas of the different PDEAEMA based chain length particles. P(4-$VP_{45}DVB_{134}FN_{100}$) particles with a BET surface area of 134 m^2 g^{-1} and P(4-VP_{82}-$DVB_{268}FN_{200}$) particles with a BET surface area of 40 m^2 g^{-1}, were also selected for the same reason as they have the highest BET surface areas for the two different chain lengths (DP=45 and DP=82). Furthermore, P($NIPAm_{100}$-$DVB_{300}FN_{225}$) with a BET surface area 214 m^2 g^{-1} was selected as it has the largest BET surface area among the same shell based particles. In order to measure the size of the particles, dynamic light scattering (DLS) was carried out in aqueous solution. The P($DEAEMA_{48}$-$DVB_{144}FN_{108}$) particle solutions were prepared at a concentration of 0.1 mg mL^{-1} under three different pHs by adding HCl or NaOH. Each sample was sonicated for 3 hours before analysis and then the particle sizes were measured by switching the temperature between 20 °C and 60 °C. At 20 °C, P($DEAEMA_{48}$-$DVB_{144}FN_{108}$) particles have diameters of around 600 nm, 750 nm, and 850 nm under acidic, neutral and basic conditions, respectively. At 60 °C, the particle diameters are around 250 nm at all pHs (Figure 5.5 a, b, and c). The TEM images illustrate the same trend that matches the particle size, which is measured by DLS trends (Figure 5.5 d, and e).

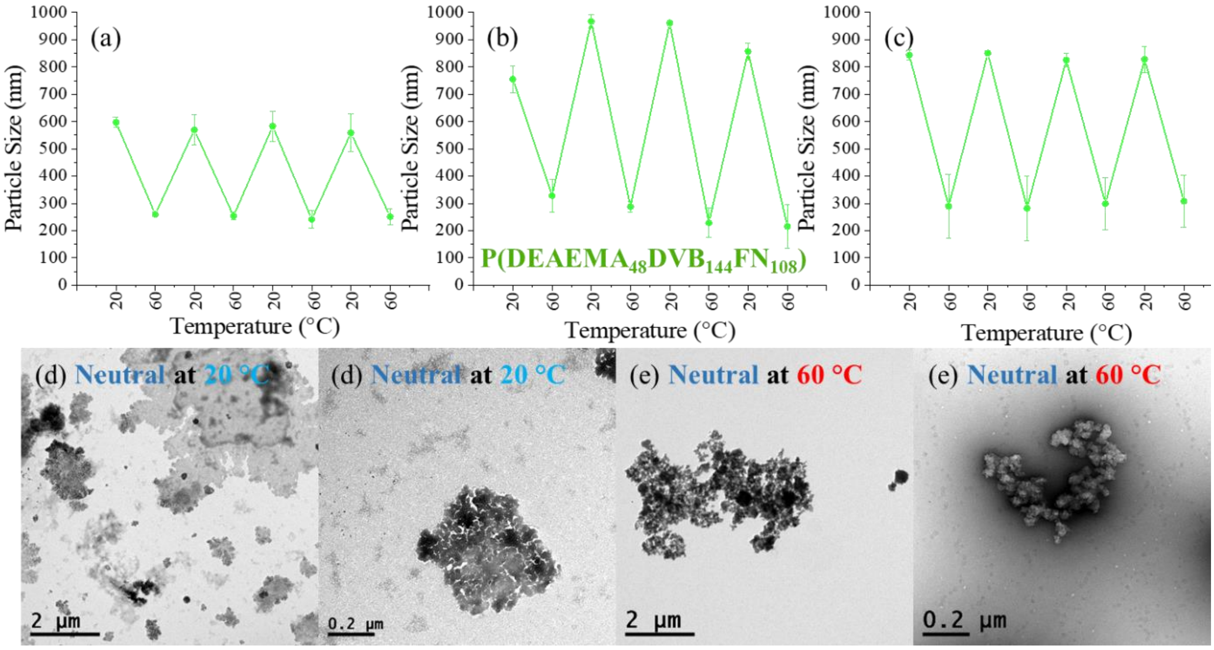

Figure 5.5 Particle size of P($DEAEMA_{48}$-$DVB_{144}FN_{108}$) in (a) the acid condition, (b) the neutral, and (c) the base; TEM images of P($DEAEMA_{48}$-$DVB_{144}FN_{108}$) particles at (d) 20 °C and (e) 60 °C

For P($DEAEMA_{108}$-$DVB_{144}FN_{108}$) particles, the particle size is about 250 nm, 650 nm, and 850 nm in acid, neutral and base at 20 °C, respectively, while it is consistently around 250 nm in acid, neutral and base at 60 °C (Figure 5.6 a, b and c). Interestingly, the particles did not show thermo- responsive in the acidic condition (Figure 5.6 a), this is likely due to the fact that the abundance of hydrogen ions led to the transformation of almost all amine groups to protonated quaternary amine groups, which hindered thermal transitions. The presence protonated PDEAEMA shell may hinder the thermal transitions.[16] For the longer shell chains containing more amino groups, resulted in a greater number of charges and when the temperature increasing, the repulsion of charges among the polymer chains overcame packing of the polymer chains. Therefore, the particle size did not change. In contrast, the short shell chains, the packing of the polymer chains which is due to the expulsion of the water from the polymer chains overcame the repulsion of charges among the polymer chains and dominated the changing of the polymer chains (Figure 5.5 a). The TEM images also display the same trend that matches the particle size, which is measured by DLS trends (Figure 5.6 d, and e)

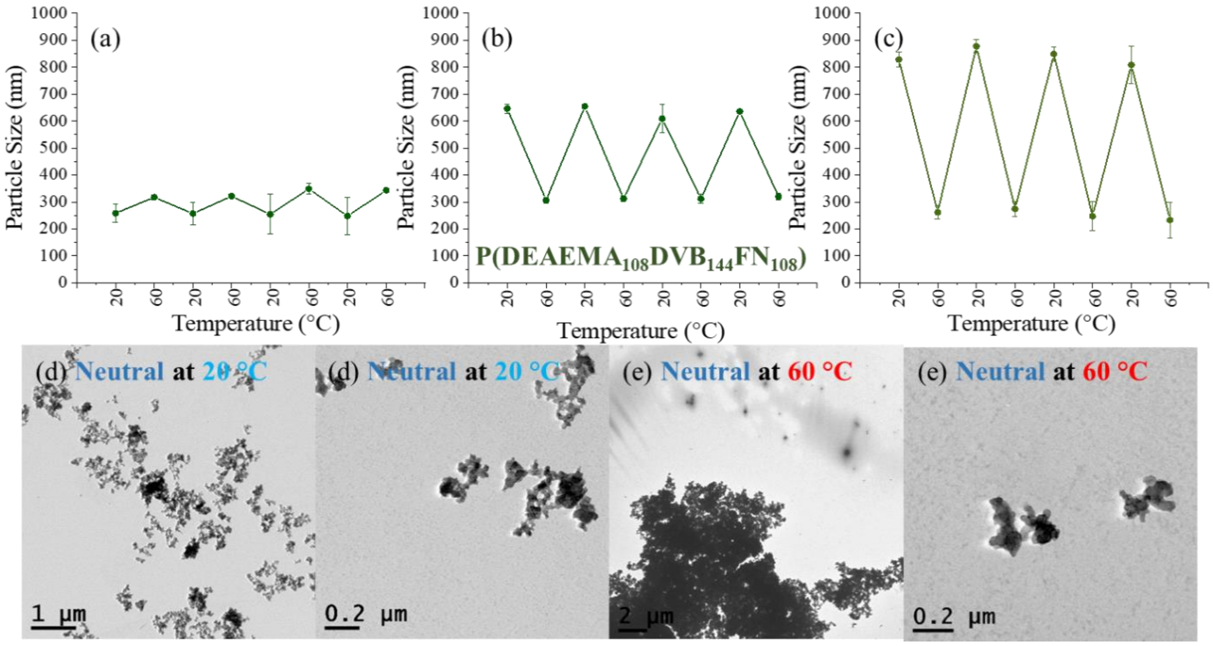

Figure 5.6 Particle size of P(DEAEMA$_{108}$-DVB$_{144}$FN$_{108}$) in (a) the acid condition, (b) the neutral, and (c) the base; TEM images of P(DEAEMA$_{108}$-DVB$_{144}$FN$_{108}$) particles at (d) 20 °C and (e) 60 °C

The P4-VP based particles reveal the same trend as the PDEAEMA based particles, at 20 °C, P(4-VP$_{45}$-DVB$_{134}$FN$_{100}$) particles have a diameter of around 1200 nm in acidic, neutral and basic solutions, while the particle size is around 300 nm at 60 °C (Figure 5.7 a, b, and c).

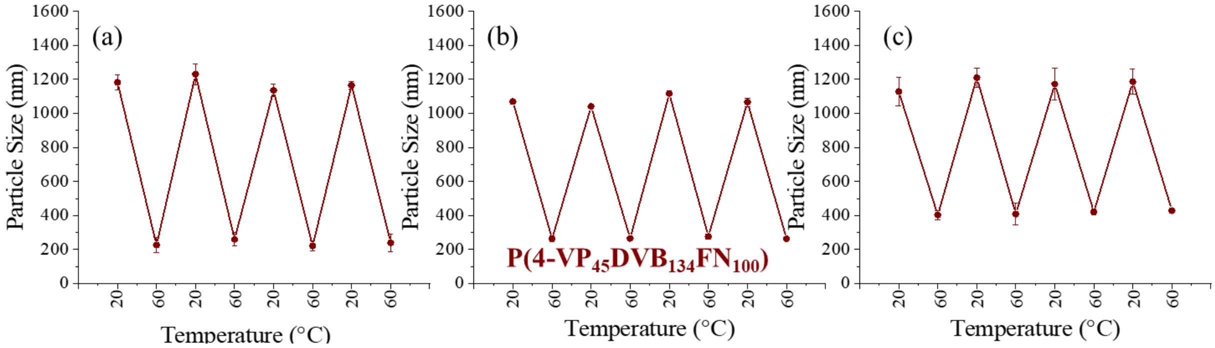

Figure 5.7 Particle size of P(4-VP$_{45}$-DVB$_{134}$FN$_{100}$) in (a) the acid condition, (b) the neutral, and (c) the base

For P(4-VP$_{82}$-DVB$_{268}$FN$_{200}$) particles, the particle size is about 200 nm, 600 nm, and 850 nm in acid, neutral and base at 20 °C, respectively, and it is around 150 nm in acid and 300 nm in neutral and base at 60 °C (Figure 5.8 a, b and c). Similar to the PDEAEMA-based particles, the P4-VP particles are also less thermo-responsive under acidic conditions, particularly for the longer chain P(4-VP$_{82}$-DVB$_{268}$FN$_{200}$) particles, which is attributed to the presence of additional protons in the acidic condition hindering the deprotonation of the pyridine group of the particles, following the same mechanism as that of the PDEAEMA-based particles. The TEM images also show the same trend that corresponds to the particle size measured by DLS trends (Figure 5.8 d, and e).

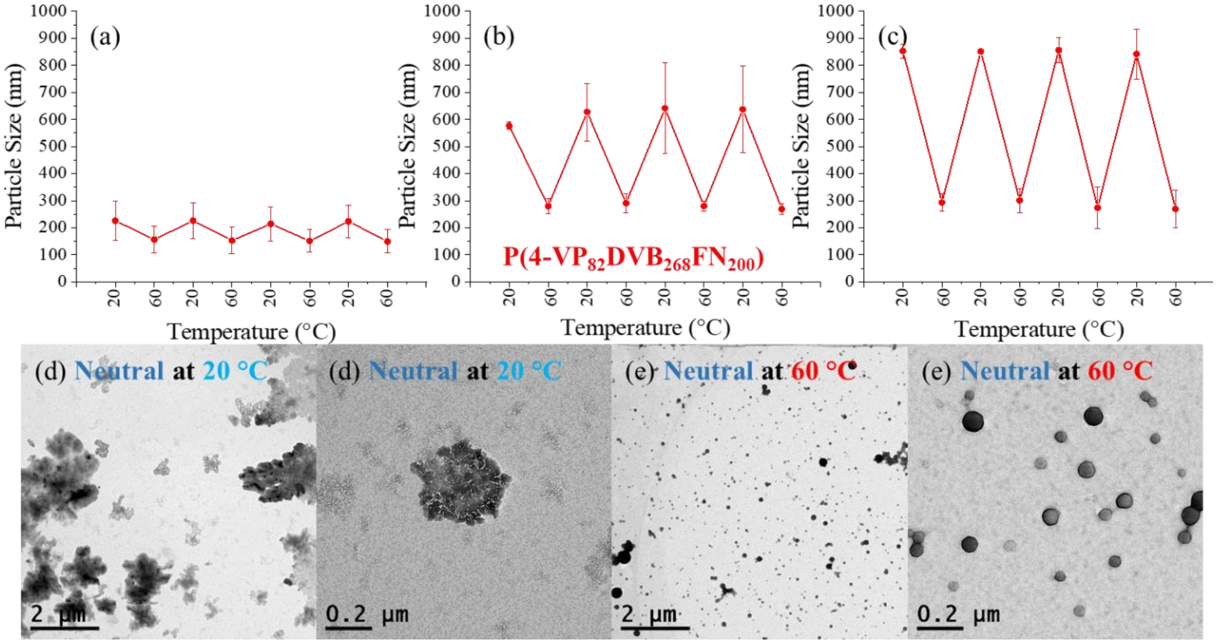

Figure 5.8 Particle size of P(4-VP$_{82}$-DVB$_{268}$FN$_{200}$) in (a) the acid condition, (b) the neutral, and (c) the base; TEM images of P(4-VP$_{82}$-DVB$_{268}$FN$_{200}$) particles at (d) 20 °C and (e) 60 °C

P(NIPAm$_{100}$-DVB$_{300}$FN$_{225}$) particles demonstrate a similar behaviour to those PDEAEMA, and P4-VP based particles. At 20 °C, the particle sizes are about 1400 nm, 900 nm, and 1200 nm in acidic, neutral and basic conditions, respectively. Conversely, the particle diameter are around 700 nm, 400 nm, and 200 nm acidic, neutral and basic conditions at 60 °C, respectively (Figure 5.9 a, b and c). The TEM images reveal the same trend that corresponds to the particle size as determined by DLS analysis as well (Figure 5.9 d, and e).

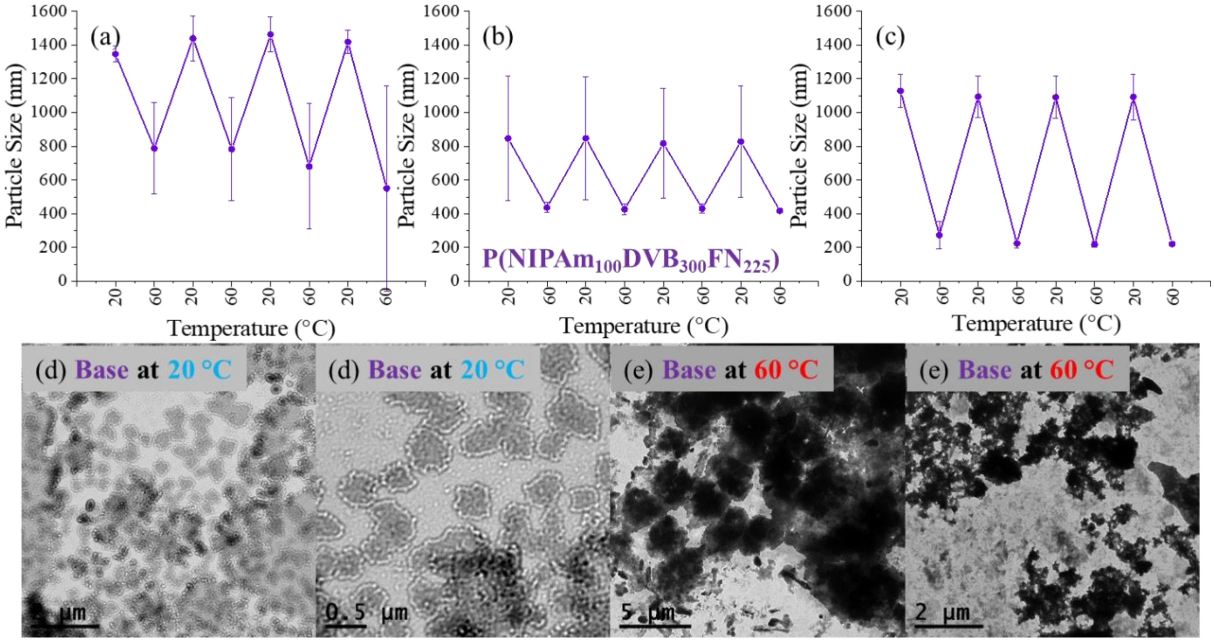

Figure 5.9 Particle size of P(NIPAm$_{100}$-DVB$_{300}$FN$_{225}$) in (a) the acid condition, (b) the neutral, and (c) the base; TEM images of P(NIPAm$_{100}$-DVB$_{300}$FN$_{225}$) particles at (d) 20 °C and (e) 60 °C

Similar to the pH-responsive polymers, polymers with an LCST like PDMAEMA[14,15] P4-VP[16] and PNIPAm[11–13] exhibit a clear temperature response, which is phase separation at high temperature (higher than LCST) and has single-phase at low temperature (lower than LCST).[17,18] For normal LCST thermo- responsive polymers, such as hydrogels[19] and cross-linked micelles with di-block structures[20], which show swollen network at low temperature, and are collapsed at high temperature, which is due to the hydrophobic effect (Figure 5.10). When a polymer is dissolved in water, there are three different types of interactions: intermolecular forces, the forces between the polymer and water, and the interaction between water molecules. For LCST polymers, increasing the temperature results in phases separation and also results a negative free energy of the system (ΔG) which decreases the force between the polymer and water and increases the other two interactions. This negative free energy (ΔG) is attributed to a higher increase the entropy term (ΔS) rather than an increase of the enthalpy term (ΔH) based on the Gibbs equation $\Delta G = \Delta H - T\Delta S$. The main driving force is the entropy of the water, so that when the polymer is not in solution the water is less ordered and has a higher entropy. This will result in the polymer chains collapsing and showing less hydrophilicity and this phenomenon is the so-called hydrophobic effect.[17,21]

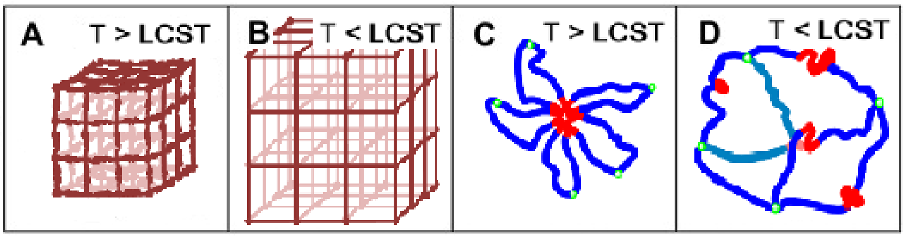

Figure 5.10 Schematic representation of the hydrogel at high temperature (A) and low temperature (B) and cross-linked micelle at high temperature (C) and low temperature (D)[17]

The P($DEAEMA_{48}$-$DVB_{144}FN_{108}$), P($DEAEMA_{108}$-$DVB_{144}FN_{108}$), P(4-VP_{45}-$DVB_{134}FN_{100}$), P(4-VP_{82}-$DVB_{268}FN_{200}$), and P($NIPAm_{100}$-$DVB_{300}FN_{225}$) particles clearly demonstrate a thermo- response with larger particle sizes at low temperature and smaller sizes at high temperature not only at neutral pH but also in different pH solutions (Figure 5.5 a, b, c; Figure 5.6 a, b, c; Figure 5.7 a, b, c; Figure 5.8 a, b, c; and Figure 5.9 a, b, c). Although, they show the same trend as the normal LCST thermo- responsive polymers, which are expected to have a large particle size at low temperature, conversely, and it is expected to be small at high temperature, the reason for their behaviour may differ. This may be explained as follows: for PDEAEMA and PNIPAm based particles, at low temperature, the carboxyl group (amide group) on the shell chains are separated and hydrophilic, while the particles disperse in the solution. Conversely, when it was at high temperature, the polymer chains become hydrophobic and were collapsed to form large aggregates which are then easily precipitated out, while a few numbers of small particles still disperse in the solvent. Meanwhile, for P4-VP based particles, the pyridine groups are protonated and re-arranged at low temperature, and it is deprotonated with particles aggregating together at high temperature. For other microporous polymer nanospheres such as Mai et al.[22] and Yu et al.[23], who obtained a kind of pre-crosslinker microporous core with temperature responsive shells display the same phenomenon as well (Figure 5.11), which is due to the fact that, the hydrophobic parts are full crosslinked by rigid monomers with benzene rings which cannot swell or collapse. Therefore, the hydrophilic parts dominate the particle size with the same principle as the normal LCST thermo- responsive polymers.

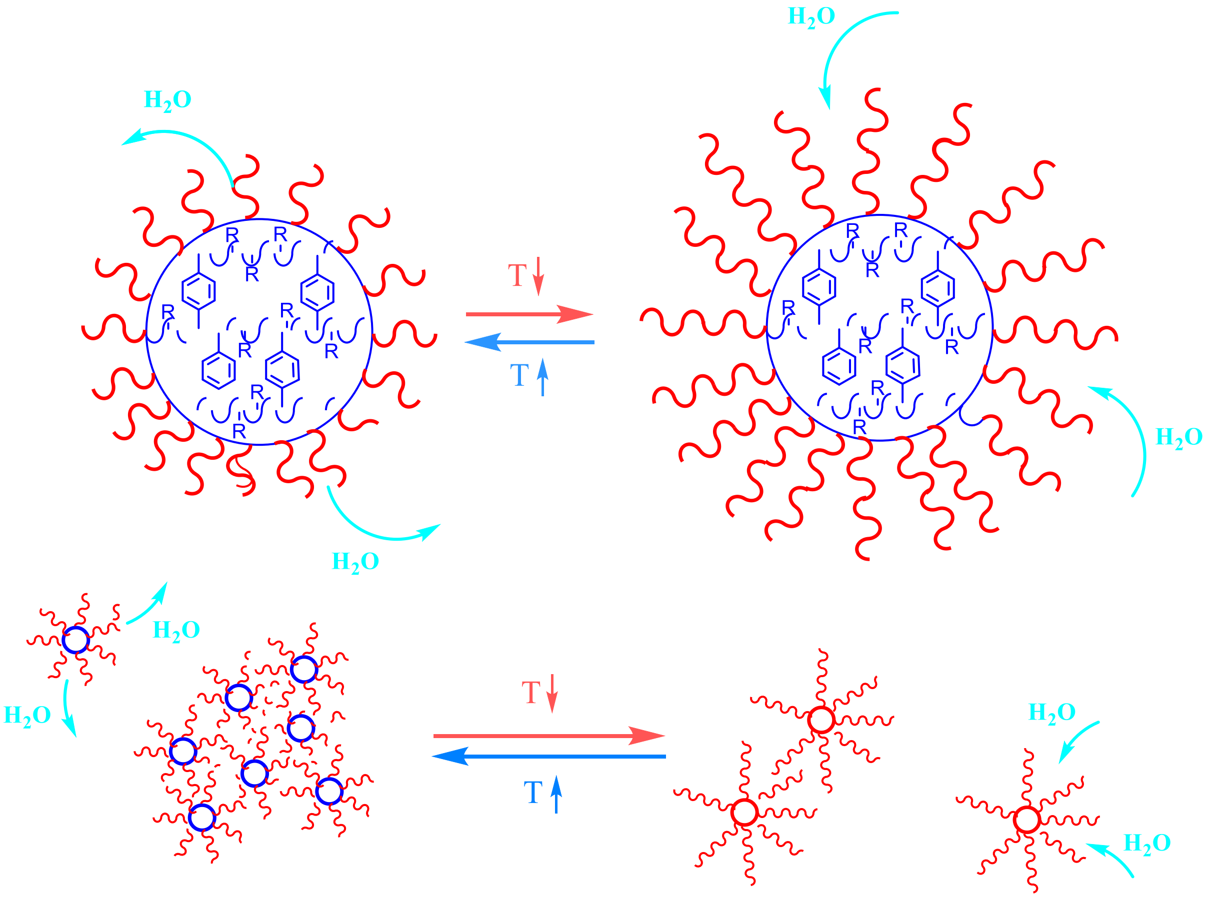

Figure 5.11 Schematic representation of the microporous polymeric nanospheres swelling transition

5.4 Conclusion

Solvent-dispersible porous polymers with thermo- responsive properties synthesised by reversible addition fragmentation chain transfer polymerisation induced self-assembly (RAFT-PISA) approach were successfully obtained. 2-(dodecylthiocarbonothioylthio)-2-methylpropanoic acid (DDMAT) were used as a CTA and was synthesised via one pot step, firstly. The reaction kinetics were studied in the previous chapter. Thus, this time, the same method was followed. For PNIPAm shells, the DP of 100 was obtained.

Poly(diethylaminoethyl methacrylate-divinylbenzene/fumaronitrile) (PDEAEMA-DVB/FN), poly(4-vinylpyridine-divinylbenzene/fumaronitrile) (P4-VP-DVB/FN), and poly(N-isopropylacrylamide-divinylbenzene/fumaronitrile) (PNIPAm-DVB/FN) were synthesised via RAFT mediated polymerisation induced self-assembly. The suitable reactions and best core-shell ratio for PDEAEMA, and P4-VP based particles were determined in Chapter 4.3.2 and 4.3.3, respectively. PNIPAm based particles were synthesised using the same water to ethanol ratio (60:40) as for the synthesis of PEG and PAA-based particles. The best core-shell ratio for PNIPAm based particles was identified and the P(NIPAm$_{100}$-DVB$_{300}$FN$_{225}$) particles exhibited the highest BET surface area of 214 m^2 g^{-1} compared to other core-shell ratios for PNIPAm-based particles. Additionally, the PNIPAm based particles contain a dual morphology with smaller spheres structure to aggregate to form larger particles, in contrast to other particles synthesised by RAFT-PISA approach. Finally, the thermo- response was observed and confirmed for PDEAEMA, P4-VP, and PNIPAm based particles with larger particle sizes at low temperature and smaller sizes at high temperature. This is attributed to the shell chains are separated and hydrophilic at low temperature, while the particles disperse in the solution. Conversely, when it was at high temperature, the polymer chains become hydrophobic and were collapsed to form large aggregates which are then easily precipitated out.

5.5 References

(1) Pangborn, A. B.; Giardello, M. A.; Grubbs, R. H.; Rosen, R. K.; Timmers, F. J. Safe and Convenient Procedure for Solvent Purification. *Organometallics* **1996**, *15* (5), 1518–1520. https://doi.org/10.1021/om9503712.
(2) Skey, J.; K. O'Reilly, R. Facile One Pot Synthesis of a Range of Reversible Addition–Fragmentation Chain Transfer (RAFT) Agents. *Chem. Commun.* **2008**, *0* (35), 4183–4185. https://doi.org/10.1039/B804260H.
(3) Wong, A. S. M.; Mann, S. K.; Czuba, E.; Sahut, A.; Liu, H.; Suekama, T. C.; Bickerton, T.; Johnston, A. P. R.; Such, G. K. Self-Assembling Dual Component Nanoparticles with Endosomal Escape Capability. *Soft Matter* **2015**, *11* (15), 2993–3002. https://doi.org/10.1039/C5SM00082C.
(4) Liu, R.; Rong, Z.; Han, G.; Yang, X.; Zhang, W. Synthesis and Self-Assembly of Star Multiple Block Copolymer of Poly(4-Vinylpyridine)-Block-Polystyrene. *Polymer* **2021**, *215*, 123431. https://doi.org/10.1016/j.polymer.2021.123431.
(5) Li, C.; Wang, C.; Ji, Z.; Jiang, N.; Lin, W.; Li, D. Synthesis of Thiol-Terminated Thermoresponsive Polymers and Their Enhancement Effect on Optical Limiting Property of Gold Nanoparticles. *Eur. Polym. J.* **2019**, *113*, 404–410. https://doi.org/10.1016/j.eurpolymj.2019.02.009.
(6) James, A. M.; Derry, M. J.; Train, J. S.; Dawson, R. Dispersible Microporous Diblock Copolymer Nanoparticles via Polymerisation-Induced Self-Assembly. *Polym. Chem.* **2019**, *10* (28), 3879–3886. https://doi.org/10.1039/C9PY00596J.
(7) Xie, F.; Hu, W.; Ding, L.; Tian, K.; Wu, Z.; Li, L. Synthesis of Microporous Organic Polymers via Radical Polymerisation of Fumaronitrile with Divinylbenzene. *Polym. Chem.* **2017**, *8* (39), 6106–6111. https://doi.org/10.1039/C7PY01240C.
(8) James, A. M.; Dawson, R. Efficient and Tunable White-Light Emission Using a Dispersible Porous Polymer. *Macromol. Rapid Commun.* **2020**, *41* (12), 2000176. https://doi.org/10.1002/marc.202000176.
(9) Ferguson, C. T. J.; Huber, N.; Kuckhoff, T.; Zhang, K. A. I.; Landfester, K. Dispersible Porous Classical Polymer Photocatalysts for Visible Light-Mediated Production of Pharmaceutically Relevant Compounds in Multiple Solvents. *J. Mater. Chem. A* **2020**, *8* (3), 1072–1076. https://doi.org/10.1039/C9TA11242A.
(10) Ivko, S. A.; James, A. M.; Derry, M. J.; Dawson, R.; Haynes, A. Heterogenisation of a Carbonylation Catalyst on Dispersible Microporous Polymer Nanoparticles. *Catal. Sci. Technol.* **2022**, *12* (2), 664–673. https://doi.org/10.1039/D1CY01989A.
(11) Zhang, K.; Li, F.; Wu, Y.; Feng, L.; Zhang, L. Construction of Ionic Thermo-Responsive PNIPAM/γ-PGA/PEG Hydrogel as a Draw Agent for Enhanced Forward-Osmosis Desalination. *Desalination* **2020**, *495*, 114667. https://doi.org/10.1016/j.desal.2020.114667.
(12) Yu, Y.-L.; Zhang, M.-J.; Xie, R.; Ju, X.-J.; Wang, J.-Y.; Pi, S.-W.; Chu, L.-Y. Thermo-Responsive Monodisperse Core–Shell Microspheres with PNIPAM Core and Biocompatible Porous Ethyl Cellulose Shell Embedded with PNIPAM Gates. *J. Colloid Interface Sci.* **2012**, *376* (1), 97–106. https://doi.org/10.1016/j.jcis.2012.03.028.
(13) Slemming-Adamsen, P.; Song, J.; Dong, M.; Besenbacher, F.; Chen, M. In Situ Cross-Linked PNIPAM/Gelatin Nanofibers for Thermo-Responsive Drug Release. *Macromol. Mater. Eng.* **2015**, *300* (12), 1226–1231. https://doi.org/10.1002/mame.201500160.
(14) Wang, J.; Yang, H.; Meng, Z.; Xie, B.; Yu, X.; Su, G.; Wang, L. Epoxy Coating with Excellent Anticorrosion and PH-Responsive Performances Based on DEAEMA

Modified Mesoporous Silica Nanomaterials. *Colloids Surf. Physicochem. Eng. Asp.* **2022**, *634*, 127951. https://doi.org/10.1016/j.colsurfa.2021.127951.

(15) Wang, X.; Liu, Z.; Huang, L. PH and Thermo Dual-Responsive Starch-g-P(DEAEMA-Co-PEGMA): Synthesis via SET-LRP, Self-Assembly and Drug Release Behaviors. *React. Funct. Polym.* **2019**, *141*, 165–171. https://doi.org/10.1016/j.reactfunctpolym.2019.05.011.

(16) Raczkowska, J.; Stetsyshyn, Y.; Awsiuk, K.; Zemła, J.; Kostruba, A.; Harhay, K.; Marzec, M.; Bernasik, A.; Lishchynskyi, O.; Ohar, H.; Budkowski, A. Temperature-Responsive Properties of Poly(4-Vinylpyridine) Coatings: Influence of Temperature on the Wettability, Morphology, and Protein Adsorption. *RSC Adv.* **2016**, *6* (90), 87469–87477. https://doi.org/10.1039/C6RA07223B.

(17) Ward, M. A.; Georgiou, T. K. Thermoresponsive Polymers for Biomedical Applications. *Polymers* **2011**, *3* (3), 1215–1242. https://doi.org/10.3390/polym3031215.

(18) Kim, Y.-J.; T. Matsunaga, Y. Thermo-Responsive Polymers and Their Application as Smart Biomaterials. *J. Mater. Chem. B* **2017**, *5* (23), 4307–4321. https://doi.org/10.1039/C7TB00157F.

(19) Coughlan, D. C.; Corrigan, O. I. Release Kinetics of Benzoic Acid and Its Sodium Salt From a Series of Poly(N-Isopropylacrylamide) Matrices with Various Percentage Crosslinking. *J. Pharm. Sci.* **2008**, *97* (1), 318–330. https://doi.org/10.1002/jps.21095.

(20) Cohn, D.; Sagiv, H.; Benyamin, A.; Lando, G. Engineering Thermoresponsive Polymeric Nanoshells. *Biomaterials* **2009**, *30* (19), 3289–3296. https://doi.org/10.1016/j.biomaterials.2009.02.026.

(21) Klouda, L.; Mikos, A. G. Thermoresponsive Hydrogels in Biomedical Applications. *Eur. J. Pharm. Biopharm.* **2008**, *68* (1), 34–45. https://doi.org/10.1016/j.ejpb.2007.02.025.

(22) Mai, W.; Sun, B.; Chen, L.; Xu, F.; Liu, H.; Liang, Y.; Fu, R.; Wu, D.; Matyjaszewski, K. Water-Dispersible, Responsive, and Carbonizable Hairy Microporous Polymeric Nanospheres. *J. Am. Chem. Soc.* **2015**, *137* (41), 13256–13259. https://doi.org/10.1021/jacs.5b08978.

(23) Yu, H.; Wang, Z.; Wu, R.; Chen, X.; Chan, T.-W. D. Water-Dispersible PH/Thermo Dual-Responsive Microporous Polymeric Microspheres as Adsorbent for Dispersive Solid-Phase Extraction of Fluoroquinolones from Environmental Water Samples and Food Samples. *J. Chromatogr. A* **2019**, *1601*, 27–34. https://doi.org/10.1016/j.chroma.2019.05.004.

5.6 Appendix

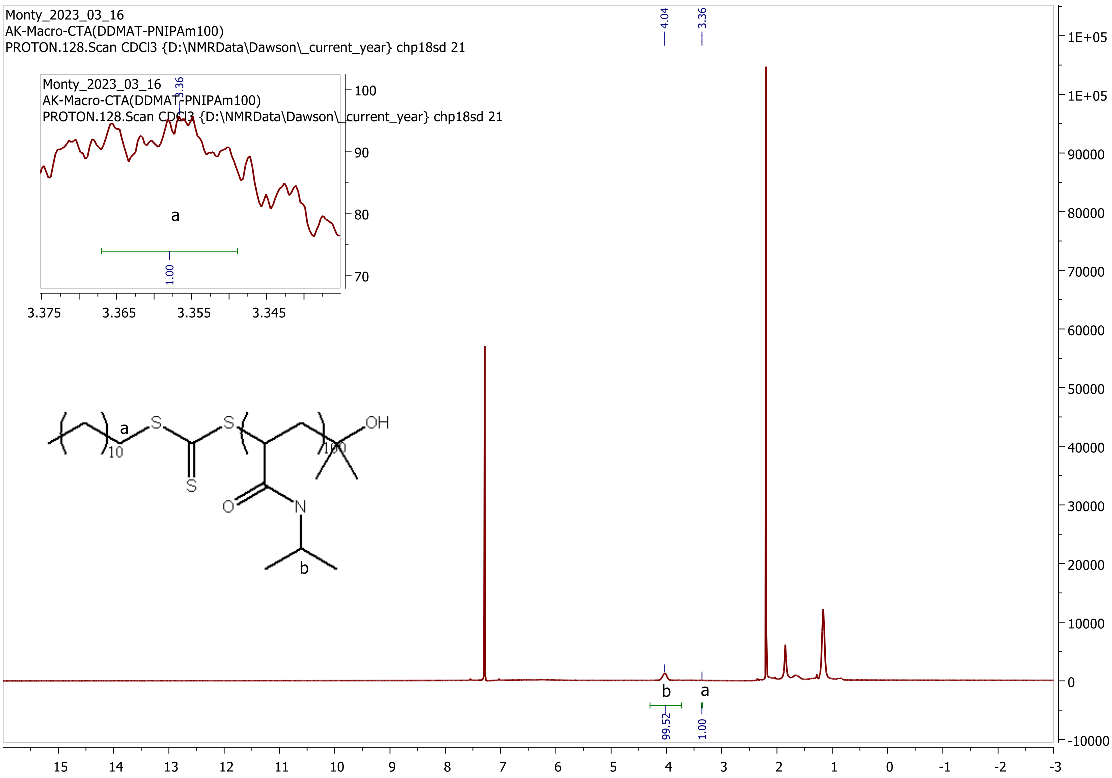

Figure 5.1 The ^{1}H NMR spectrum of Macro-CTA(DDMAT-PNIPAm$_{100}$)

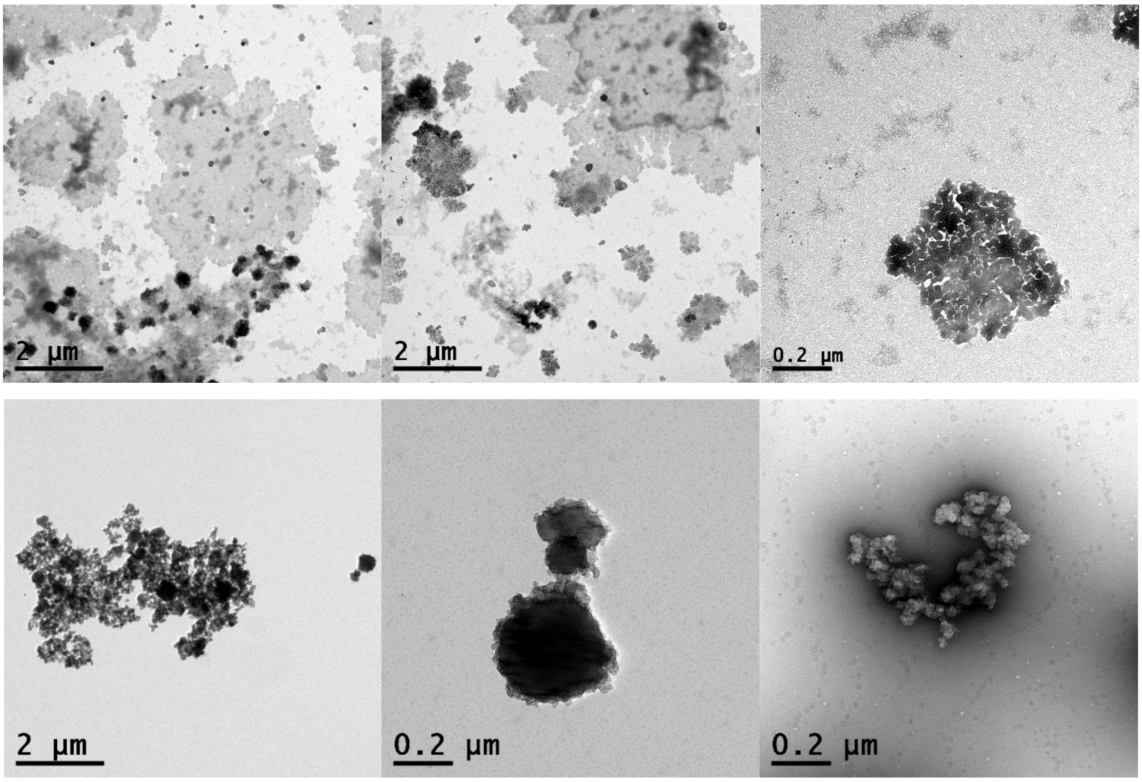

Figure 5.2 The different scales of TEM images of P(DEAEMA$_{48}$-DVB$_{144}$FN$_{108}$) in neutral at 20 °C (up) and 60 °C (down)

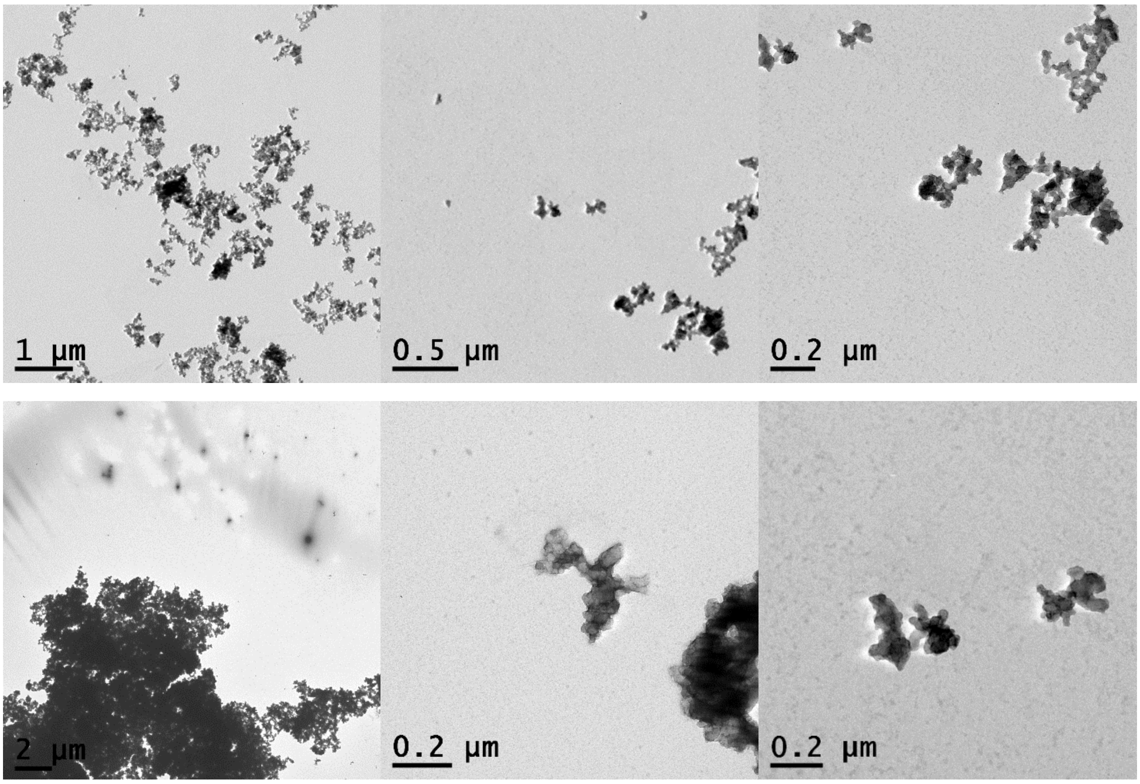

Figure 5.3 The different scales of TEM images of P(DEAEMA$_{108}$-DVB$_{144}$FN$_{108}$) in neutral at 20 °C (up) and 60 °C (down)

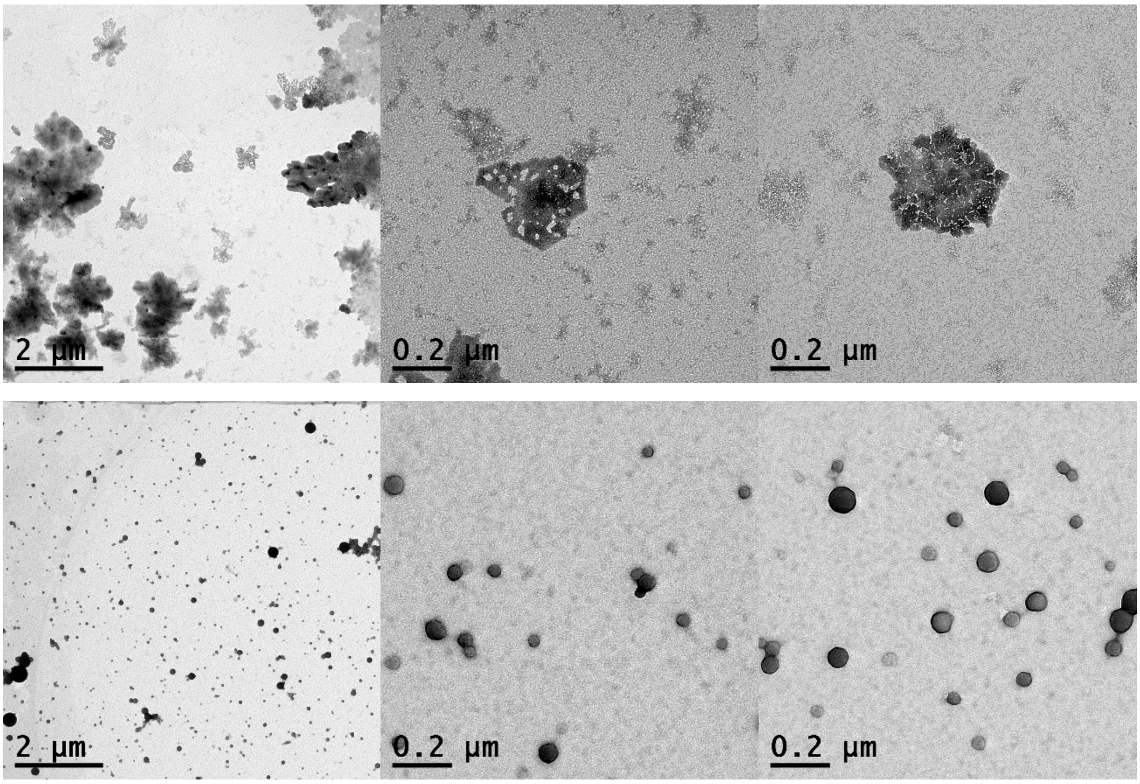

Figure 5.4 The different scales of TEM images of P(4-VP$_{82}$-b-DVB$_{268}$FN$_{200}$) in neutral at 20 °C (up) and 60 °C (down)

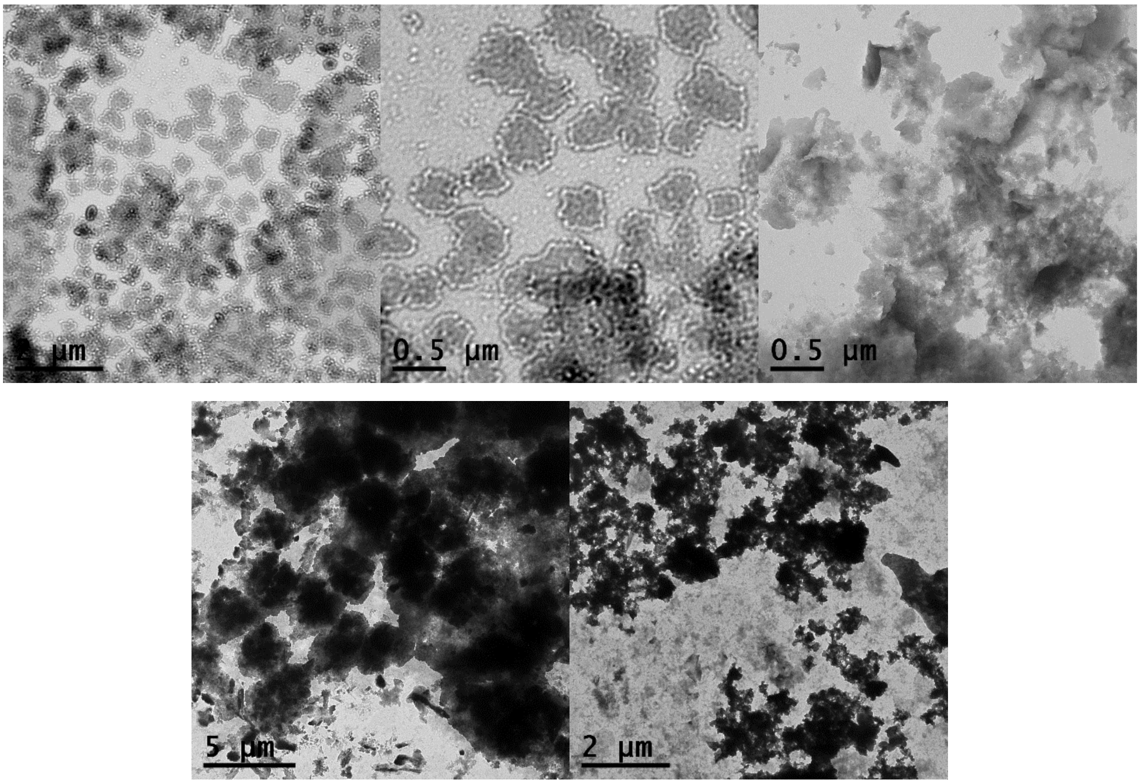

Figure 5.5 The different scales of TEM images of P(NIPAm$_{100}$-DVB$_{300}$FN$_{225}$) in base at 20 °C (up) and 60 °C (down)

Chapter-6 Increasing the BET surface area

6.1 Aims

Although the different outer shells in Chapters 3, 4 and 5 give rise to dispersible porous polymer particles (d-PPPs) as well as interesting properties such as pH- and thermo-responsivity, the particles show very low BET surface areas. Other studies on (non-porous) polymer particles such as Williams and coworkers.[1] reported that the strong lateral repulsion between the highly cationic poly(2-aminoethyl methacrylate hydrochloride) (PAMA) stabiliser chains prevents the hydrophobic core parts growing bigger. However, the core part is able to grow larger when another non-ionic block poly(glycerol monomethacrylate) (PGMA) was added. They theorised that these additional blocks acted as effective steric stabilisation during the synthesis. Penfold et al.[2] used the non-ionic block poly(ethylene oxide) (PEO_{113}) and a cationic block poly([2-methacryloyloxy)ethyl] trimethylammonium chloride) ($PQDMA_{125}$) to synthesise linear cationic diblock copolymer nanoparticles with worm copolymer morphology by RAFT polymerisation. The ratio of the non-ionic component and cationic component was 9 to 1 in the polymerisation.

Building upon previous research findings, it has been observed that pH-responsive and thermo-responsive particles, such as $PDEAEMA_{108}$ and P4-VP_{82} based particles, exhibit relatively low BET surface areas. This limitation is primarily attributed to their elongated shell chains may cover the small particles with the absence of microporous structures. This chapter aims to improve the BET surface areas especially for increasing the microporous structures of the particles using the anionic shell (PAA_{35} based shell), and non-ionic shell (PEG_{113} based shell) to investigate the addition of extra types of shells have influent to the BET surface area, pH-responses and thermo- responses.

6.2 Experimental

6.2.1 Materials

2-Bromoisobutyryl bromide, cyanomethyl me-thyl(phenyl) carbamodithioate (CPDTC, 98%), fumaronitrile (FN, 98 %), potassium persulfate (KPS), potassium phosphate tribasic (K_3PO_4) were purchased from Sigma-Aldrich and used as received. Carbon disulfide, 1-dodecanethiol (98%) were purchased from Alfa Aesar and used as received. Dry 1,4-Dioxane and Tetrahydrofuran (THF) was obtained in a method analogous to the one outlined by Grubbs.[3] Magnesium sulfate (Mg_2SO_4) was purchased from Fischer and used as received. Diethylaminoethyl methacrylate (DEAEMA), divinylbenzene (DVB, technical grade 80 %), 4-vinylpyridine (4-VP, 95%) were passed through an alumina column in order to remove the inhibitor before use. 2,2′-Azobis(2-methylpropionitrile) (AIBN, 98 %) was purified by recrystallization from ethanol at 40 °C. N-Isopropylacrylamide (NIPAm, 97%) was recrystallized from benzene/hexane before use. PEG_{113} based macro-CTA was synthesise from my group member. All other chemicals were purchased from Sigma-Aldrich and used without any further purification.

6.2.2 Synthesis (The preparations were used a method adapted from James et al.[9])

6.2.2.1 Synthesis of 2-(dodecylthiocarbonothioylthio)-2-methylpropanoic acid (DDMAT) (chain transfer agent (CTA))

The synthesis of 2-(dodecylthiocarbonothioylthio)-2-methylpropanoic acid (DDMAT) was conducted using a modified method from O’Reilly et al.[4] Initially, dodecane thiol (3.61 mL, 15.07 mmol) was added to a stirred mixture of K_3PO_4 (3.199 g, 15.07 mmol) in acetone (20 ml) and stirred for 30 minutes. The mixture was then treated with CS_2 (3.129 g, 41.10 mmol) and stirred for an additional 60 minutes. Next, 2-bromoisobutyric acid (2.288 g, 13.70 mmol) was added to the reaction mixture, which was stirred overnight at room temperature. The solvent was extracted twice with CH_2Cl_2 (100 mL each) from 1 M HCl (100 mL). The organic extracts were washed with brine (150 mL) and $MgSO_4$ powder, followed by solvent removal using rotary evaporation. The obtained product was purified by precipitation in excess cold n-hexane twice to ensure purity and then dried in a vacuum oven overnight at 40 °C to yield the RAFT CTA (Yield = 49%. Found C: 57.04 %, H: 8.78 %, S: 26.47 %, Expected C: 56.04 %, H: 8.79 %, S: 26.37 %. δH (400 MHz, $CDCl_3$) = 3.31 (2H, t, S-CH_2-$(CH_2)_{10}$-CH_3), 1.75 (6H, s, C-$(CH_3)_2$), 1.76-1.20 (20H, t, S-CH_2-$(CH_2)_{10}$-CH_3), 0.90 (3H, t, SCH_2-$(CH_2)_{10}$-CH_3); δC (400 MHz, $CDCl_3$) = 220.85, 178.08, 55.53, 37.09, 31.93, 29.64, 29.57, 29.46, 29.36, 29.12, 28.98, 27.82, 25.24, 25.23, 22.70, 14.14; m/z (EI) 363.3, 303.3, 277.2, 201.3) (Synthesised in Chapter 3 and see in Figure 3.1 in appendix).

6.2.2.2 Synthesis of Macro-Chain Transfer Agent (Macro-CTA) via RAFT

Synthesis of Macro-CTA (DDMAT-PAA$_{35}$)

The macro-CTA (DDMAT-PAA$_{35}$) was prepared in a method similar to that reported by Chaduc and coworkers.[5] In brief, 2-(dodecylthiocarbonothioylthio)-2-methylpropanoic acid (DDMAT, 364.0 mg, 1.00 mmol) and 1, 3, 5-trioxane (656.3 mg, 7.29 mmol) were combined in a 2-necked round bottom flask, which was then subjected to evacuation and nitrogen backfilling procedures three times. A solution of dry THF (30 mL) and acrylic acid (AA, 3.5 mL, 51.00 mmol) was added to the flask, followed by bubbling with nitrogen gas to remove any residual air. The mixture was then heated to 75 °C, and polymerisation was initiated by adding 2,2′-azobis(2- methylpropionitrile) (AIBN, 16.5 mg, 0.10 mmol) with THF (1 mL), which was allowed to react for 3.5 h at 75 °C. The resulting product was purified by recrystallisation with cold n-hexane and THF for three cycles, and subsequently dried overnight in a vacuum oven at 60 °C to yield the desired product (Which was synthesised in Chapter-3).

Synthesis of Macro-CTA (DDMAT-PAA$_{95}$)

The macro-CTA(DDMAT-PAA$_{95}$) was synthesised following a similar procedure. In brief, 2-(dodecylthiocarbonothioylthio)-2-methylpropanoic acid (DDMAT, 91.3 mg, 0.25 mmol) and 1, 3, 5-trioxane (171.3 mg, 1.90 mmol) were combined in a 2-necked round bottom flask, which was then subjected to evacuation and nitrogen backfilling procedures three times. A solution of dry THF (30 mL) and acrylic acid (AA, 3.5 mL, 51.00 mmol) was added to the flask, followed by bubbling with nitrogen gas to remove any residual air. The mixture was then heated to 75 °C, and polymerisation was initiated by adding 2,2′-azobis(2- methylpropionitrile) (AIBN, 4.2 mg, 0.025 mmol) with THF (1 mL), which was allowed to react for 3.5 h at 75 °C. The resulting product was purified by recrystallisation with cold n-hexane and THF for three cycles, and subsequently dried overnight in a vacuum oven at 60 °C to yield the desired product (Which was synthesised in Chapter-3).

Synthesis of PDEAEMA based Macro-CTA (CPDTC-PDEAEMA$_{108}$)

The macro-CTA (CPDTC-PDEAEMA$_{108}$) was synthesised by the method adapted from the paper published by Wong and co-workers.[6] 2-bromoisobutyryl bromide, 2-cyano-2-propyl dodecyl trithiocarbonate (CPDTC, 34.6 mg, 0.10 mmol), and 1, 3, 5-trioxane (180 mg) were combined in a 2-necked round bottom flask. The flask was subjected to evacuation and nitrogen backfilling procedures three times. Dry THF (11.4 mL) and diethylaminoethyl methacrylate (DEAEMA, 4.1 mL, 20.0 mmol) were added to the flask. The solution was bubbled with nitrogen gas to eliminate any residual air and then heated to 75 °C. Polymerisation was initiated by adding 2,2′-azobis(2- methylpropionitrile) (AIBN, 3.28 mg, 0.02 mmol) with THF (1 mL), and the reaction was allowed to proceed for 24 h at 75 °C. The resulting mixture was purified by precipitation in deionized water, and the sample was subsequently dried in a vacuum oven overnight at 60 °C to yield the RAFT macro-CTA (Which was synthesised in Chapter-4).

Synthesis of P4-VP based Macro-CTA (DDMAT-P4-VP$_{82}$)

The macro-CTA (DDMAT-P4-VP$_{82}$) prepared in a method similar to that reported by Liu and coworkers.[7] 2-(Dodecylthiocarbonothioylthio)-2-methylpropionic acid (DDMAT, 173.0 mg, 0.4756 mmol) and 1, 3, 5-trioxane (85.6 mg) were combined in a 2-necked round bottom flask, which was evacuated and backfilled with nitrogen three times. Anhydrous 1,4-dioxane (1.0 mL) and ethanol (13.8 mL), along with 4-vinylpyridine (4-VP, 10.4 mL, 95.12 mmol), were added to the flask. The solution was then bubbled through with nitrogen gas to remove any residual air before being heated to 70 °C. Polymerisation was initiated by adding 2,2′-azobis(2-methylpropionitrile) (AIBN, 19.5 mg, 0.1189 mmol) in 1,4-dioxane (0.2 mL), and the mixture was held at 70 °C for 8.0 h. The product was then purified by precipitation into diethyl ether and dried in a vacuum oven overnight at 60 °C, yielding the RAFT macro-CTA (Which was synthesised in Chapter-4).

Synthesis of PNIPAm based Macro-CTA (DDMAT-PNIPAm$_{100}$)

The macro-CTA (DDMAT-PNIPAm$_{100}$) prepared followed Li and coworker.[8] 2-(Dodecylthiocarbonothioylthio)-2-methylpropionic acid (DDMAT, 145.6 mg, 0.40 mmol) and N-isopropylacrylamide (PNIPAm, 454 mg, 4.00 mmol) were added to a 2-necked round bottom flask, which was evacuated and back-filled with nitrogen three times. Then, anhydrous 1,4-dioxane (2.09 mL) was added and the solution was purged with nitrogen gas to remove any air before heating to 80 °C. Polymerisation was initiated by adding 2,2′-azobis(2-methylpropionitrile) (AIBN, 32.8 mg, 0.20 mmol) with 1,4-dioxane (0.1 mL) and the reaction was held at 80 °C for 8.0 h. After the reaction, the mixture was diluted with a small amount of acetone and purified by precipitation into a large amount of cold n-hexane. The resulting product was dried overnight at 40 °C in a vacuum oven, yielding the RAFT macro-CTA (Which was synthesised in Chapter-4).

6.2.2.3 Synthesis of Mixed Shell Based Particles via RAFT Mediated Polymerisation Induced Self-Assembly

Synthesis of $PAA_{35}AA_{95}DVB_{47}FN_{35}$ with a ratio of water to ethanol equals 60 to 40

The $P(AA_{35}AA_{95}DVB_{47}FN_{35})$ was prepared using a method adapted from James et al.[9] In a 2-necked round bottom flask, Macro-CTA (DDMAT-PAA_{35}) (51.9 mg, 0.018 mmol), Macro-CTA (DDMAT-PAA_{95}) (14.4 mg, 0.002 mmol), and FN (54.6 mg, 0.700 mmol) were combined and subjected to three rounds of evacuation and nitrogen backfilling. Subsequently, a 1.0 wt. % solution was prepared by adding DVB (0.13 ml, 0.940 mmol) to a mixture of water and ethanol in a 60:40 (wt.%) ratio, which was then bubbled with nitrogen gas to eliminate air. The reaction mixture was heated to 70°C and polymerisation was initiated by adding KPS (1.1 mg, 0.004 mmol), followed by incubation for 24 h. The resulting product was obtained as a white solid via reprecipitation into diethyl ether and dried under vacuum at 40°C for 16 h.

Synthesis of $PAA_{35}4\text{-}VP_{82}DVB_{268}FN_{200}$ with a ratio of water to ethanol equals 60 to 40

The $P(AA_{35}4\text{-}VP_{82}DVB_{268}FN_{200})$ was prepared using a similar way. In a 2-necked round bottom flask, Macro-CTA (DDMAT-PAA_{35}) (26.0 mg, 0.009 mmol), Macro-CTA (DDMAT-P4-VP_{82}) (9.0 mg, 0.001 mmol), and FN (54.6 mg, 0.700 mmol) were combined and subjected to three rounds of evacuation and nitrogen backfilling. Subsequently, a 1.0 wt. % solution was prepared by adding DVB (0.37 ml, 2.680 mmol) to a mixture of water and ethanol in a 60:40 (wt.%) ratio, which was then bubbled with nitrogen gas to eliminate air. The reaction mixture was heated to 70°C and polymerisation was initiated by adding KPS (0.5 mg, 0.002 mmol), followed by incubation for 24 h. The resulting product was obtained as a white solid via reprecipitation into diethyl ether and dried under vacuum at 40°C for 16 h.

Synthesis of $PAA_{35}4\text{-}VP_{82}DVB_{268}FN_{200}$ with a ratio of water to methanol equals 40 to 60

The $P(AA_{35}4\text{-}VP_{82}DVB_{268}FN_{200})$ was prepared using a similar way. In a 2-necked round bottom flask, Macro-CTA (DDMAT-PAA_{35}) (26.0 mg, 0.009 mmol), Macro-CTA (DDMAT-P4-VP_{82}) (9.0 mg, 0.001 mmol), and FN (54.6 mg, 0.700 mmol) were combined and subjected to three rounds of evacuation and nitrogen backfilling. Subsequently, a 1.0 wt. % solution was prepared by adding DVB (0.37 ml, 2.680 mmol) to a mixture of methanol and water in a 60:40 (wt.%) ratio, which was then bubbled with nitrogen gas to eliminate air. The reaction mixture was heated to 70°C and polymerisation was initiated by adding AIBN (0.3 mg, 0.002 mmol), followed by incubation for 24 h. The resulting product was obtained as a white solid via reprecipitation into diethyl ether and dried under vacuum at 40°C for 16 h.

Synthesis of $PEG_{113}4\text{-}VP_{82}DVB_{452}FN_{339}$ with a ratio of water to ethanol equals 60 to 40

The P(EG_{113}4-$VP_{82}DVB_{452}FN_{339}$) was prepared using a similar way. In a 2-necked round bottom flask, PEG based macro-CTA (48.2 mg, 0.009 mmol), Macro-CTA (DDMAT-P4-VP_{82}) (9.0 mg, 0.001 mmol), and FN (264.4 mg, 3.390 mmol) were combined and subjected to three rounds of evacuation and nitrogen backfilling. Subsequently, a 1.0 wt. % solution was prepared by adding DVB (0.63 ml, 4.520 mmol) to a mixture of water and ethanol in a 60:40 (wt.%) ratio, which was then bubbled with nitrogen gas to eliminate air. The reaction mixture was heated to 70°C and polymerisation was initiated by adding KPS (0.5 mg, 0.002 mmol), followed by incubation for 24 h. The resulting product was obtained as a white solid via reprecipitation into diethyl ether and dried under vacuum at 40°C for 16 h.

Synthesis of $PEG_{113}4\text{-}VP_{82}DVB_{452}FN_{339}$ with a ratio of water to methanol equals 40 to 60

The P(EG_{113}4-$VP_{82}DVB_{452}FN_{339}$) was prepared using a similar way. In a 2-necked round bottom flask, PEG based macro-CTA (48.2 mg, 0.009 mmol), Macro-CTA (DDMAT-P4-VP_{82}) (9.0 mg, 0.001 mmol), and FN (264.4 mg, 3.390 mmol) were combined and subjected to three rounds of evacuation and nitrogen backfilling. Subsequently, a 1.0 wt. % solution was prepared by adding DVB (0.63 ml, 4.520 mmol) to a mixture of methanol and water in a 60:40 (wt.%) ratio, which was then bubbled with nitrogen gas to eliminate air. The reaction mixture was heated to 70°C and polymerisation was initiated by adding AIBN (0.3 mg, 0.002 mmol), followed by incubation for 24 h. The resulting product was obtained as a white solid via reprecipitation into diethyl ether and dried under vacuum at 40°C for 16 h.

Synthesis of $PEG_{113}DEAEMA_{108}DVB_{452}FN_{339}$ with a ratio of water to ethanol equals 60 to 40

The P($EG_{113}DEAEMA_{108}DVB_{452}FN_{339}$) was prepared using a similar way. In a 2-necked round bottom flask, PEG based macro-CTA (48.2 mg, 0.009 mmol), Macro-CTA (CPDTC-$PDEAEMA_{108}$) (20.3 mg, 0.001 mmol), and FN (264.4 mg, 3.390 mmol) were combined and subjected to three rounds of evacuation and nitrogen backfilling. Subsequently, a 1.0 wt. % solution was prepared by adding DVB (0.63 ml, 4.520 mmol) to a mixture of water and ethanol in a 60:40 (wt.%) ratio, which was then bubbled with nitrogen gas to eliminate air. The reaction mixture was heated to 70°C and polymerisation was initiated by adding KPS (0.5 mg, 0.002 mmol), followed by incubation for 24 h. The resulting product was obtained as a yellow solid via reprecipitation into diethyl ether and dried under vacuum at 40°C for 16 h.

Synthesis of $PEG_{113}DEAEMA_{108}DVB_{452}FN_{339}$ with a ratio of water to methanol equals 40 to 60

The P($EG_{113}DEAEMA_{108}DVB_{452}FN_{339}$) was prepared using a similar way. In a 2-necked round bottom flask, PEG based macro-CTA (48.2 mg, 0.009 mmol), Macro-CTA (CPDTC-$PDEAEMA_{108}$) (20.3 mg, 0.001 mmol), and FN (264.4 mg, 3.390 mmol) were combined and subjected to three rounds of evacuation and nitrogen backfilling. Subsequently, a 1.0 wt. % solution was prepared by adding DVB (0.63 ml, 4.520 mmol) to a mixture of methanol and water in a 60:40 (wt.%) ratio, which was then bubbled with nitrogen gas to eliminate air. The reaction mixture was heated to 70°C and polymerisation was initiated by adding AIBN (0.3 mg, 0.002 mmol), followed by incubation for 24 h. The resulting product was obtained as a gray solid via reprecipitation into diethyl ether and dried under vacuum at 40°C for 16 h.

Synthesis of $PEG_{113}NIPAm_{100}DVB_{452}FN_{339}$ *with a ratio of water to ethanol equals 60 to 40*

The P($EG_{113}NIPAm_{100}DVB_{452}FN_{339}$) was prepared in the same way. In a 2-necked round bottom flask, PEG based macro-CTA (48.2 mg, 0.009 mmol), Macro-CTA (CPDTC-$PNIPAm_{100}$) (10.3 mg, 0.001 mmol), and FN (264.4 mg, 3.390 mmol) were combined and subjected to three rounds of evacuation and nitrogen backfilling. Subsequently, a 1.0 wt. % solution was prepared by adding DVB (0.63 ml, 4.520 mmol) to a mixture of water and ethanol in a 60:40 (wt.%) ratio, which was then bubbled with nitrogen gas to eliminate air. The reaction mixture was heated to 70°C and polymerisation was initiated by adding KPS (0.5 mg, 0.002 mmol), followed by incubation for 24 h. The resulting product was obtained as a white solid via reprecipitation into diethyl ether and dried under vacuum at 40°C for 16 h.

6.3 Results and discussion

6.3.1 Same shell mixing

The BET surface areas of dispersible porous polymer particles (d-PPPs) synthesised by RAFT-PISA are low in comparison to other porous polymers for example CMPs[10] typically have surface areas > 500 m^2 g^{-1} while PAFs[11] can have surface areas over 5000 m^2 g^{-1}, In comparison the porous polymers in Chapters 4-5 have surface areas of ~150 m^2 g^{-1} or lower. In particular the particles with pH and temperature dual responsive shells (such as the PDEAEMA and P4-VP based particles) have very low surface areas and to take advantage of their responsivity, higher surface areas would be desirable. It was therefore decided to investigate the effect of adding another hydrophilic shell to particles (such as the PEG$_{113}$ and PAA$_{35}$ based shell which have higher BET surface areas) to investigate the effect this has on the BET surface area and microporous structure.

Of those particles synthesised with PAA (see Chapter 3), P(AA$_{35}$-DVB$_{47}$FN$_{35}$) particles have the highest BET surface area while shells of PAA$_{95}$ such as the P(AA$_{95}$-DVB$_{47}$FN$_{35}$) particles have a lower BET surface area. In addition, the P(AA$_{35}$-DVB$_{47}$FN$_{35}$) particles have much morr microporous structure compared to P(AA$_{95}$-DVB$_{47}$FN$_{35}$) particles. P(AA$_{35}$AA$_{95}$-DVB$_{47}$FN$_{35}$) mixed-shell particles were therefore targeted, successfully synthesised and used to compare to their single-shell-based particle counterparts. The BET surface area was first found to increases by about 40% when the PAA$_{35}$ shell is added (Table 6.1) and it is clearly to the increasing from the Figure 6.1.

Table 6.1 Monomer composition and BET surface area of different shell particles

Monomer Composition				BET Surface Area (m^2 g^{-1})
Shell		Core		
PAA$_{35}$	PAA$_{95}$	DVB	FN	
0	1	47	35	186
0.9	0.1	47	35	258
1	0	47	35	322

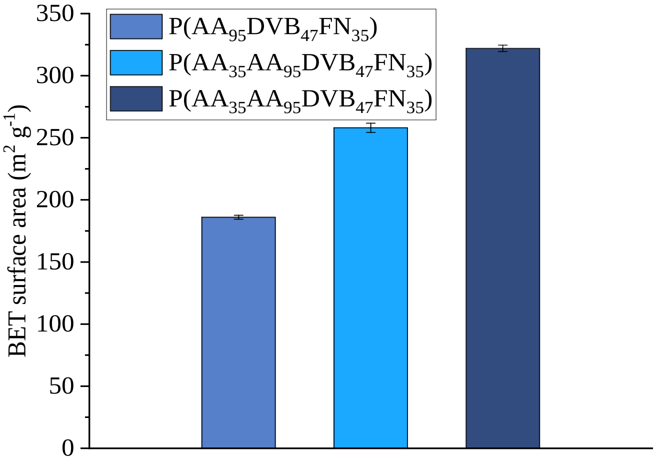

Figure 6.1 BET surface area of particles synthesised with different shells

The nitrogen adsorption isotherms (Figure 6.2 a) exhibit a little increase for both particles at a very low pressure indicating a lack of micropores. This is different to the PEG based particles[9,12–14] which were synthesised by DVB and FN shows microporous structures. There is a large uptake at high pressure as seen for all the other particles. The $P(AA_{35}AA_{95}$-$DVB_{47}FN_{35})$ mixed-shell particles exhibit large peaks in the pore size distributions (Figure 6.2 b) at a pore width about 1.8 nm, 3.1 nm, 5.1 nm and further larger pores and voids, which made up by the aggregation of the small sphere particles compared to the $P(AA_{95}$-$DVB_{47}FN_{35})$ single-shell particles which have more mesopores (Figure 6.2 b). The cumulative surface area plots (Figure 6.2 c) also show that most of the pore volume is the larger mesoporous region. The addition of PAA_{35} based shells help the original PAA_{95} based shells increasing the microporous region. The results demonstrate that the $P(AA_{35}AA_{95}$-$DVB_{47}FN_{35})$ mixed-shell particles have an extra 22 m^2 g^{-1} and 34 m^2 g^{-1} BET surface area contributed by microporous region and mesoporous region respectively compared to $P(AA_{35}$-$DVB_{47}FN_{35})$ single-shell particles.

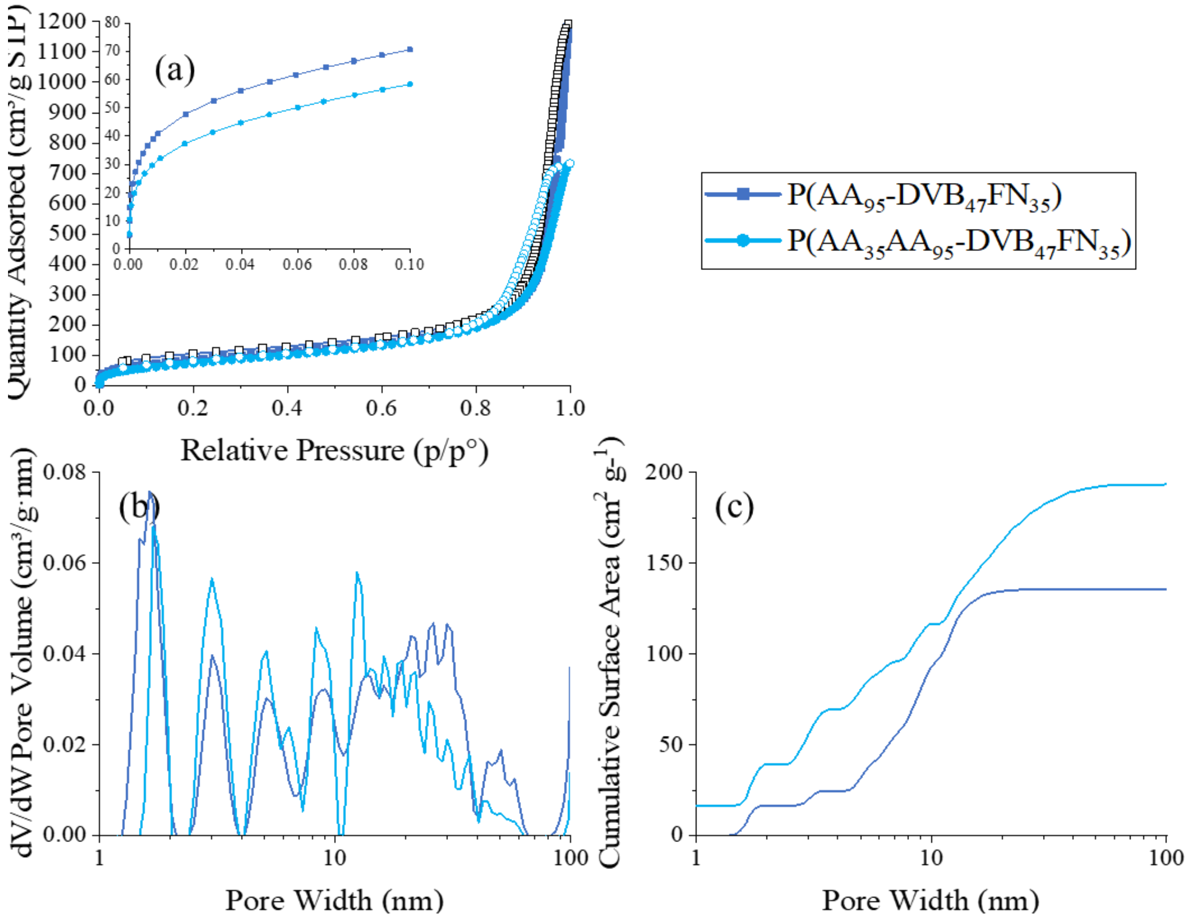

Figure 6.2 (a) Nitrogen adsorption isotherms of PAA$_{95}$ based particles with addition of the PAA$_{35}$ based shell at 77.3 K; (b) Pore size distributions calculated using NLDFT method (slit pore models, differential pore volume vs pore width); and (c) Cumulative surface areas

6.3.2 Incorporation of anionic shells

P4-VP based shells can be either neutral or cationic when in acidic solution, whereas the PAA$_{35}$ based shells are acidic and can be anionic when deprotonated, due to the carboxyl groups on the polymer chains. Mixing these two polymers together should result in a transfer of the acidic proton of PAA to the P4-VP. This could aid the core to grow larger which may increase the BET surface area.

P(4-VP$_{82}$-DVB$_{268}$FN$_{200}$) particles were selected as they have the largest BET surface area among the same shell chain length-based particles, the synthesis of the PAA$_{35}$ and P4-VP$_{82}$ based macro-CTA required different solution compositions according to previous study. Which the PAA based particles were synthesised in the water-ethanol mixture solution with a ratio of 60:40 (wt.%), while the P4-VP based particles were synthesised in a methanol-water mixture solution with a ratio of 60:40 (wt.%). These 2 solution compositions were selected to do the comparisons. Following the procedure in Chapter 6.2.2.3, P(AA$_{35}$4-VP$_{82}$-DVB$_{452}$FN$_{339}$)

particles were successfully synthesised in both water-ethanol and methanol-water mixture solutions as follows.

Table 6.2 Monomer composition and BET surface area

Monomer Composition				Solution Composition (wt.%)			BET Surface Area (m^2 g^{-1})
Shell		Core					
PAA_{35}	$P4\text{-}VP_{82}$	DVB	FN	Water	Ethanol	Methanol	
0	1	268	200	40	-	60	40
0.9	0.1	268	200	60	40	-	124
0.9	0.1	268	200	40	-	60	58
1	0	300	225	60	40	-	150

For $P(AA_{35}4\text{-}VP_{82}\text{-}DVB_{268}FN_{200})$ particles synthesised in a water-ethanol mixture solution reaction system, the BET surface area increased about 3 times when the anionic PAA_{35} based shell was added. In addition, for $P(AA_{35}4\text{-}VP_{82}\text{-}DVB_{268}FN_{200})$ particles synthesised in a methanol-water mixture solution reaction system, the BET surface area increased about 45% when the addition PAA_{35} based shell was added (Table 6.2). This may be due to that the PAA_{35} based macro-CTAs have more activity during the reaction in the water-ethanol mixture solution, and less active for P4-VP based macro-CTAs, which means more PAA_{35} shells formed a particle compared to the $P4\text{-}VP_{82}$ shells. In contrast, the $P4\text{-}VP_{82}$ based macro-CTAs have more activity in the methanol-water mixture solution compared to the PAA_{35} based macro-CTAs, which are less active. Therefore, more $P4\text{-}VP_{82}$ shells formed a particle compared to the PAA_{35} shells. In addition, it is clearly to the large increasing of particles with mixed shell from the Figure 6.3.

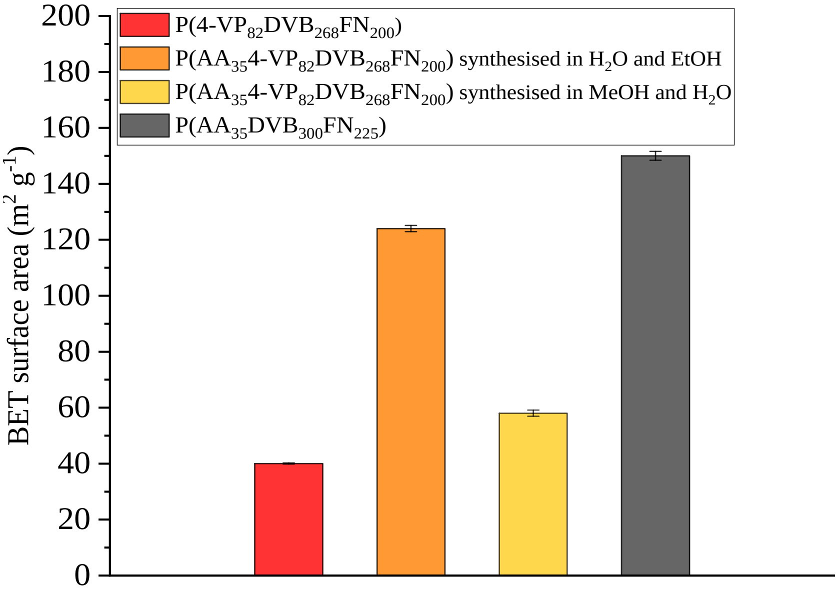

Figure 6.3 BET surface area of particles synthesised with different shells

The nitrogen adsorption isotherms (Figure 6.4 a) exhibit a large increase at low pressure for the $P(AA_{35}4\text{-}VP_{82}\text{-}DVB_{268}FN_{200})$ particles synthesised in the water-ethanol mixture solution compared to the $P(4\text{-}VP_{82}\text{-}DVB_{268}FN_{200})$ and $P(AA_{35}4\text{-}VP_{82}\text{-}DVB_{268}FN_{200})$ particles synthesised in the methanol-water mixture solution, which means the mixed-shell particles synthesised in the water-ethanol mixture solution are expected to have more small pores than others. There is a large uptake as seen for all the other particles. The $P(4\text{-}VP_{82}\text{-}DVB_{268}FN_{200})$ particles have already in Chapter 4.3.2, which have a pore size of 3.1 nm, 5.1 nm and larger pore sizes from 10 nm to 60 nm in the pore size distributions (Figure 6.4 b). Both mixed-shell $P(AA_{35}4\text{-}VP_{82}\text{-}DVB_{268}FN_{200})$ particles synthesised in water-ethanol and methanol-water mixture solution exhibit the large peaks at a pore width of around 1.7 nm, 3.1 nm, 5.1 nm, 8.1 nm and mesoporous structure or small voids among the small particles of the aggregates.

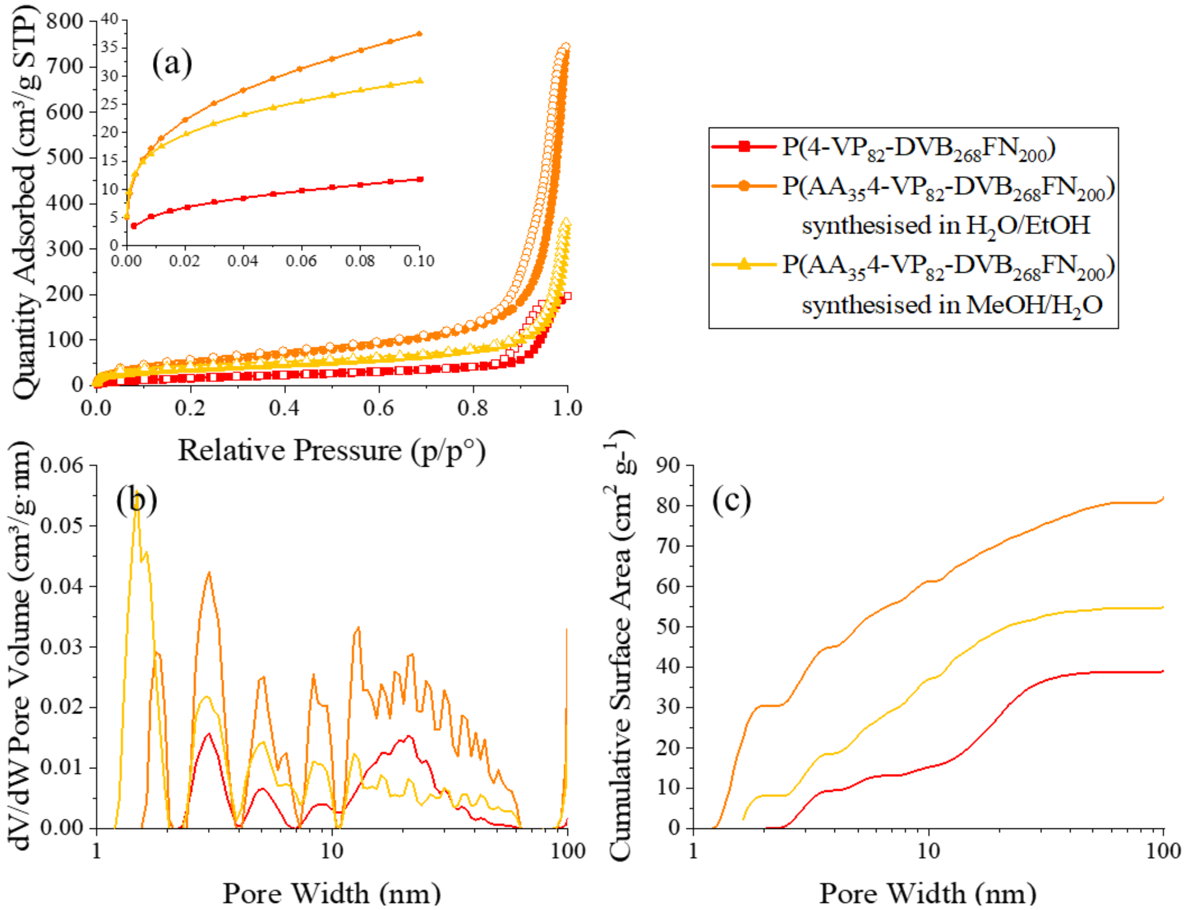

Figure 6.4 (a) Nitrogen adsorption isotherms of $P4\text{-}VP_{82}$ based particles with addition of the PAA_{35} based shell at 77.3 K; (b) Pore size distributions calculated using NLDFT method (slit pore models, differential pore volume vs pore width); and (c) Cumulative surface areas

The cumulative surface area plots (Figure 6.4 c) also show that most of the pore volume is the larger meso- and macropore region. The addition of PAA based shell to the P4-VP based particles will introduce the microporous structure. The experimental results clearly shown that the both of the mixed-shell particles have an extra 30 m^2 g^{-1} and 8 m^2 g^{-1} BET surface area contributed by microporous region and 50 m^2 g^{-1} and 46 m^2 g^{-1} BET surface area contributed by mesoporous region respectively compared to P(4-VP$_{82}$-DVB$_{268}$FN$_{200}$) single-shell particles.

6.3.3 Investigation increasing of BET surface area by adding non-ionic shells

According to the research of Williams et al. and Penfold et al., the non-ionic PEG based shell can decrease the repulsion between the fully charged cationic polymer chains. Therefore, the addition of the PEG$_{113}$ based shell will help the synthesis of P4-VP, PDEAEMA, and PNIPAm based particles with bigger core parts and the prevent the long shell chains cover the core parts, which may increase the BET surface area and the microporous structure on the small particles. The core size of DVB$_{452}$FN$_{339}$ is selected as the PEG based particles have the largest BET surface are among the same PEG$_{113}$ based particles. However, the PEG based macro-CTA and the P4-VP$_{82}$ (or PDEAEMA$_{108}$) based macro-CTA are in the different solution composition according to previous study, the ratios of water to ethanol with 60:40 (wt.%) and methanol to water with 60:40 (wt.%) are selected to do the comparisons. The PNIPAm based macro-CTA is water soluble compared to the PEG based particles, which they can use the same solution composition with the ratio of water to ethanol with 60:40 (wt.%).

Table 6.3 Monomer composition, solution composition and BET surface area of P4-VP and PDEAEMA based particles with addition of PEG$_{113}$ based shell

Monomer Composition					Solution Composition (wt.%)			BET Surface Area (m^2 g^{-1})
Shell			Core					
PEG$_{113}$	P4-VP$_{82}$	PDEAEMA$_{108}$	DVB	FN	Water	Ethanol	Methanol	
0	1	-	268	200	40	-	60	40
0.9	0.1	-	452	339	60	40	-	241
0.9	0.1	-	452	339	40	-	60	200
0	-	1	268	200	40	-	60	78
0.9	-	0.1	452	339	60	40	-	1
0.9	-	0.1	452	339	40	-	60	137

For P4-VP$_{82}$ and PEG$_{113}$ mixed shell particles. With the addition of non-ionic PEG based shell, the BET surface area increased a lot, which is about 6 times large for P(EG$_{113}$4-VP$_{82}$-DVB$_{452}$FN$_{339}$) particles synthesised in a water-ethanol solution (wt.%) and 5 times large for P(EG$_{113}$4-VP$_{82}$-DVB$_{452}$FN$_{339}$) particles synthesised in a methanol-water solution compared to the P4-VP single-shell particles (Table 6.3). This may be due to similar reason compared to the P(AA$_{35}$4-VP$_{82}$-DVB$_{268}$FN$_{200}$) mixed-shell particles which discussed in Chapter 6.3.2. In the water-ethanol solution reaction system, the PEG$_{113}$ based macro-CTAs are more active than the $P4-VP_{82}$ based macro-CTAs, leading more PEG_{113} based macro-CTAs into the particles. In contrast, the $P4-VP_{82}$ based macro-CTAs are more active in methanol-water solution reaction system compared to the PEG_{113} based macro-CTAs, leading more $P4-VP_{82}$ based macro-CTAs into the particles.

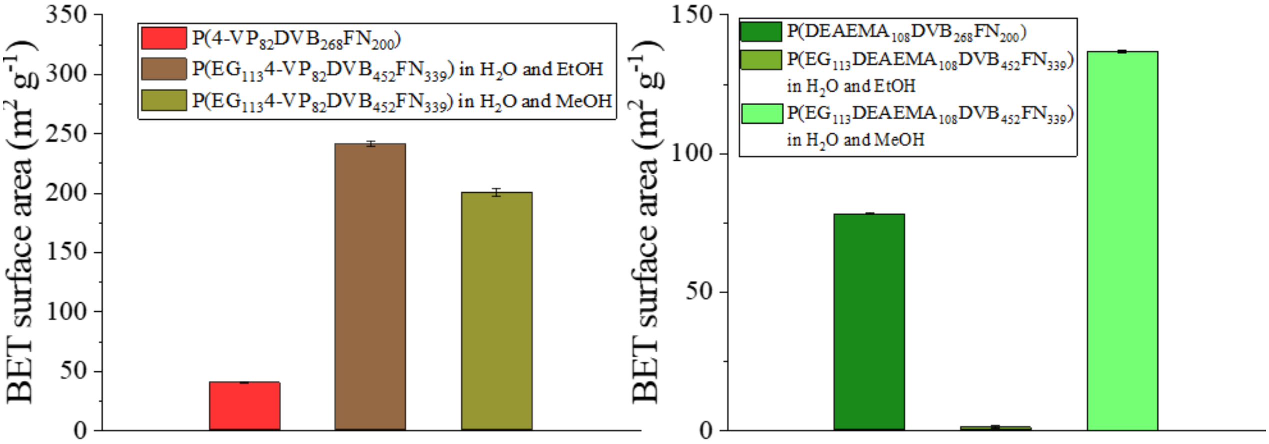

Figure 6.5 BET surface area of (a) $P4-VP_{82}$ and (b) $PDEAEMA_{108}$ based particles with PEG_{113} based shell and synthesised in different solution composition

For $PDEAEMA_{108}$ and PEG_{113} mixed shell particles. The $P(EG_{113}DEAEMA_{108}-DVB_{452}FN_{339})$ synthesised in a water-ethanol mixture solution, was nonporous when the addition of PEG based shell was added (Table 6.3). This may be due to the fact that the PDEAEMA is more hydrophobic than the P-4VP, and in this reaction, the PDEAEMA based macro-CTA prevents the particles from coming out. However, for $P(EG_{113}DEAEMA_{108}-DVB_{452}FN_{339})$ particles synthesised in a methanol-water mixture solution, the BET surface increased nearly 2 times when the addition of PEG based shell was added.

Table 6.4 Monomer composition, and BET surface area of PNIPAm based particles with addition of PEG_{113} based shell

Monomer Composition				BET Surface Area (m^2 g^{-1})
Shell		Core		
PEG_{113}	$PNIPAm_{100}$	DVB	FN	
0	1	300	225	193
0.9	0.1	452	339	159

For $PNIPAm_{100}$ and PEG_{113} mixed shell particles, $P(EG_{113}NIPAm_{100}-DVB_{452}FN_{339})$, which has the same reaction system as the $PNIPAm_{100}$ or PEG_{113} single-shell particles with the water-ethanol mixture solution (Table 6.4). However, the mixed-shell particles have a less porous structure than the PEG_{113} single-shell particles, which may be due to the $P(EG_{113}NIPAm_{100}-DVB_{452}FN_{339})$ particles were synthesised in the neutral condition, the amino groups are not charged at this pH. Therefore, the incorporation of PEG_{113}-based shell chains not only fails to provide effective steric stabilization but also hinders the growth of the core particles.

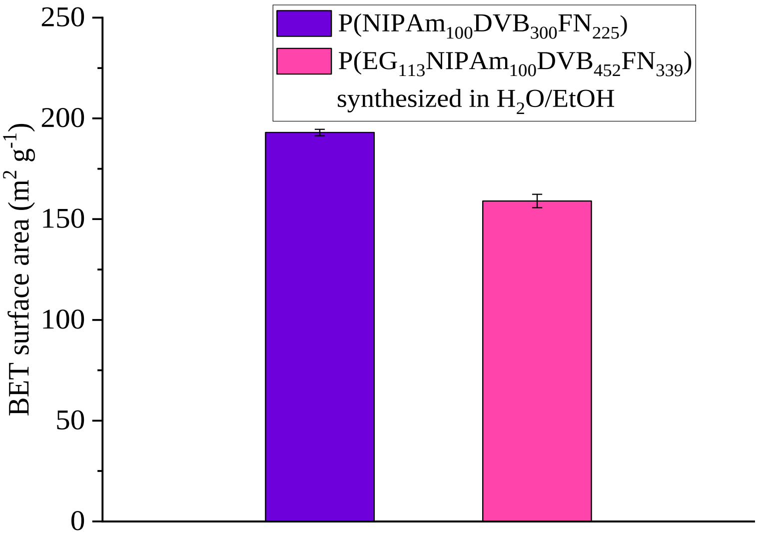

Figure 6.6 BET surface area of PNIPAm based particles synthesised with PEG_{113} based shell

The mixed-shell particles of P4-VP, PDEAEMA, and PNIPAm based particles are also confirmed to contain a dual morphology with smaller spheres structure to aggregate to form larger particles compared to the single-shell particles of P4-VP, PDEAEMA, PNIPAm, PAA and PEG based particles (Figure 6.7).

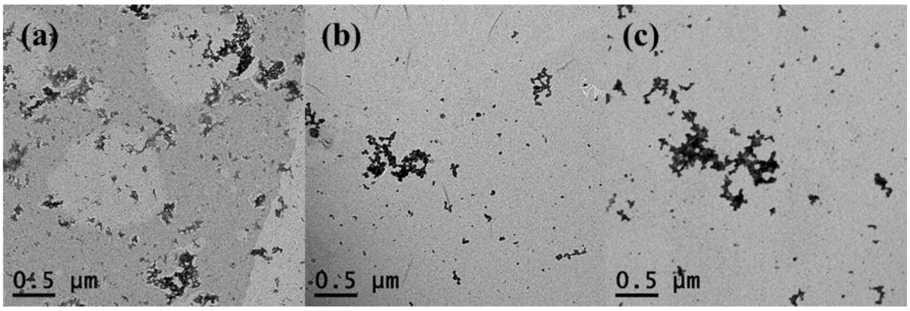

Figure 6.7 TEM images of (a) P4-VP, (b) PDEAEMA, and (c) PNIPAm based particles with additional PEG based shell in the acidic condition

The nitrogen adsorption isotherms of $P4\text{-}VP_{82}$ based particles with addition of the PEG_{113} based shell (Figure 6.8 a) show a large increase at low pressure compared to the $P4\text{-}VP_{82}$ single-shell particles, which means the mixed shell particles as expected to have more micropores than the single-shell based particles. $P(EG_{113}4\text{-}VP_{82}\text{-}DVB_{452}FN_{339})$ particles synthesised in the water-ethanol and methanol-water mixture solution both exhibit the large peaks at a pore width of around 1.8 nm, 3.0 nm, 5.1 nm, 7.0 nm and further larger pores and voids from the pore size distributions (Figure 6.8 b). However, the $P(4\text{-}VP_{82}\text{-}DVB_{268}FN_{200})$ single-shell particles, only has a small number of pore size of 3.0 nm, 5.1 nm, 9.0 nm, and some larger pores with the pore with from 10 nm to 60 nm. Both P(EG$_{113}$4-VP$_{82}$-DVB$_{452}$FN$_{339}$) mixed-shell particles have microporous compared to P(4-VP$_{82}$-DVB$_{268}$FN$_{200}$) single-shell particles which have limited micropores in the cumulative surface area plots due to the larger meso- and macropore region (Figure 6.8 c). It is clearly shown that the both of the mixed-shell particles have an extra 112 m^2 g^{-1} and 90 m^2 g^{-1} BET surface area contributed by microporous and mesoporous regions respectively compared to P(4-VP$_{82}$-DVB$_{268}$FN$_{200}$) single-shell particles.

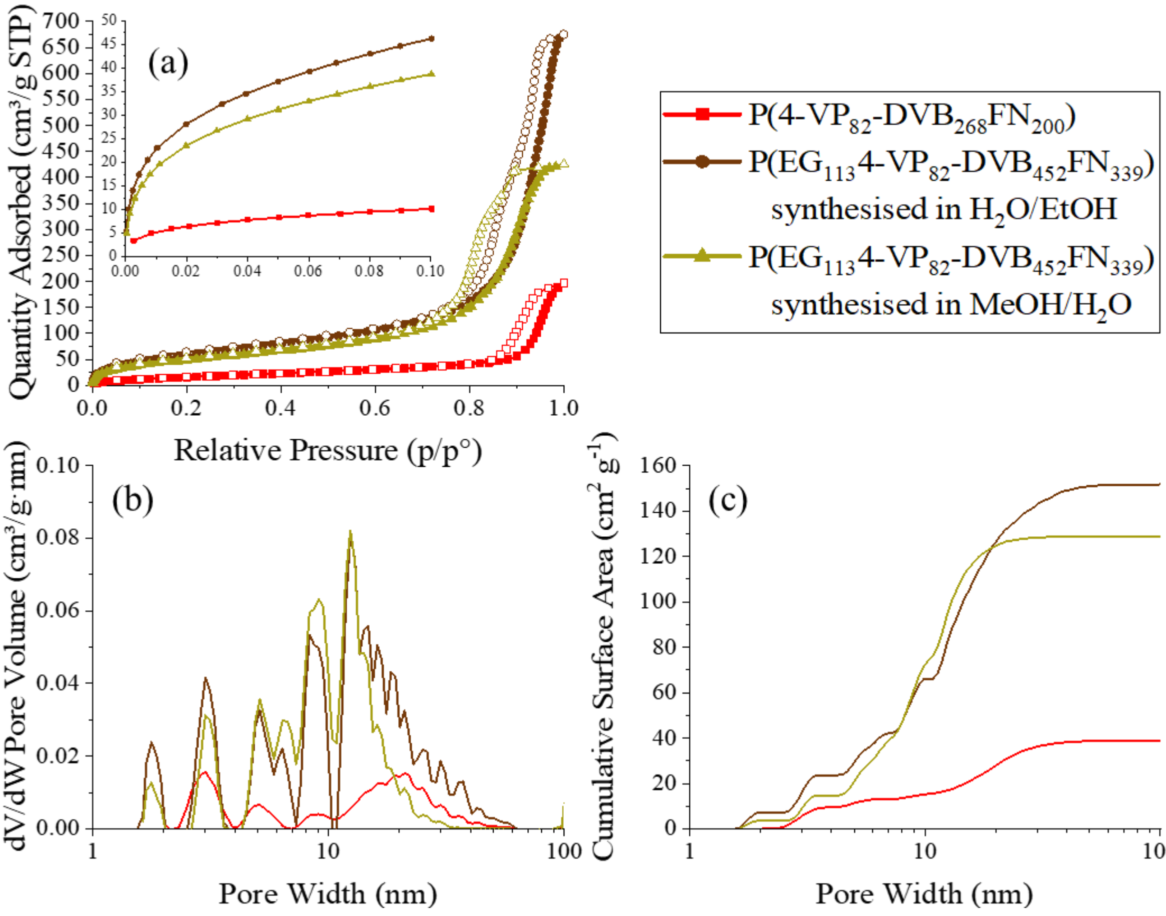

Figure 6.8 (a) Nitrogen adsorption isotherms of P4-VP$_{82}$ based particles with addition of the PEG$_{113}$ based shell at 77.3 K; (b) Pore size distributions calculated using NLDFT method (slit pore models, differential pore volume vs pore width); and (c) Cumulative surface areas

There is a similar nitrogen uptake (Figure 6.9 a) to the P4-VP$_{82}$ based particles and with addition of the PEG$_{113}$ based shell, which means the P(EG$_{113}$DEAEMA$_{108}$-DVB$_{452}$FN$_{339}$) mixed-shell particles synthesised in the methanol-water mixture solution expected to have more small porous structure compared to the single-shell particles. It is different from P(EG$_{113}$4-VP$_{82}$-DVB$_{452}$FN$_{339}$) particles, although the addition of PEG$_{113}$ based shell are added, the different solution components may influence the porous structures. The pore size distributions (Figure 6.9 b) show the mixed-shell particles which have the large peaks at a pore width of around 3.0 nm, 5.1 nm, 7.1 nm, 8.1 nm and further larger pores and voids, whereas the P(DEAEMA$_{108}$-DVB$_{144}$FN$_{108}$) single particles only have the main peak at pore width about 9.1 nm and further larger pores and voids. Unfortunately, these materials are non-microporous in the cumulative surface area plots (Figure 6.9 c). The results clearly demonstrate that the mixed-shell particles have an extra 33 m^2 g^{-1} BET surface area contributed by microporous and mesoporous regions compared to P(DEAEMA$_{108}$-DVB$_{452}$FN$_{339}$) single-shell particles.

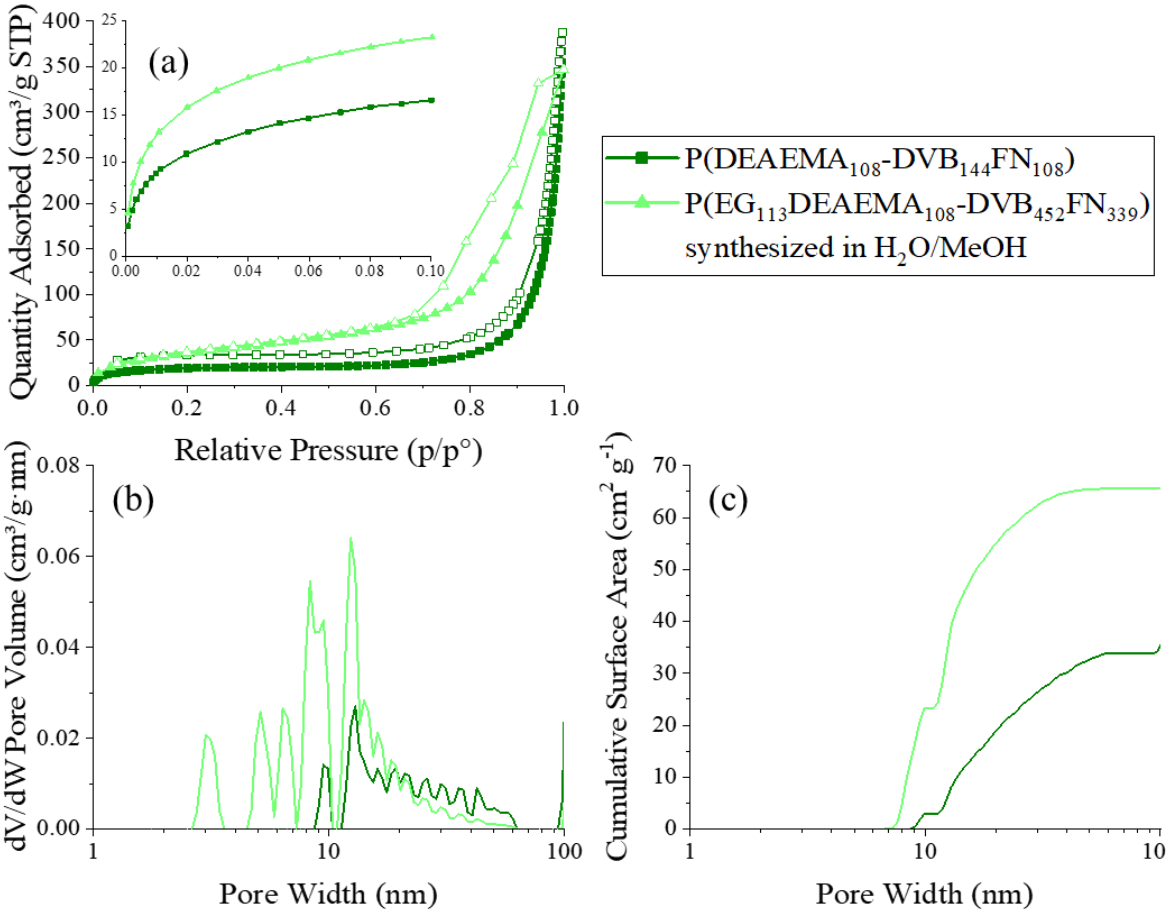

Figure 6.9 (a) Nitrogen adsorption isotherms of PDEAEMA$_{108}$ based particles with addition of the PEG$_{113}$ based shell at 77.3 K; (b) Pore size distributions calculated using NLDFT method (slit pore models, differential pore volume vs pore width); and (c) Cumulative surface areas

There is a same nitrogen uptake (Figure 6.10 a) as seen for all the other particles. Both exhibit a very low pressure corresponding to samples with little micropores. Both PNIPAm$_{100}$ based particles reveal a large peak in the pore size distributions (Figure 6.10 b) at a pore width about 1.8 nm, 3.0 nm, 5.1 nm, 6.5 nm, 8.1 nm and further larger pores and voids. The cumulative surface area plots (Figure 6.10 c) also show that most of the pore volume is the larger meso- and macropore region, which resulted microporous structure for P(NIPAm$_{100}$-DVB$_{300}$FN$_{225}$)

single-shell particles, and nearly non-microporous structure for $P(EG_{113}NIPAm_{100}-DVB_{452}FN_{339})$ mixed-shell particles. The results clearly demonstrate that the mixed-shell particles have a reduced BET surface area of 56 m^2 g^{-1} of microporous structure compared to $P(NIPAm_{100}-DVB_{300}FN_{225})$ single-shell particles.

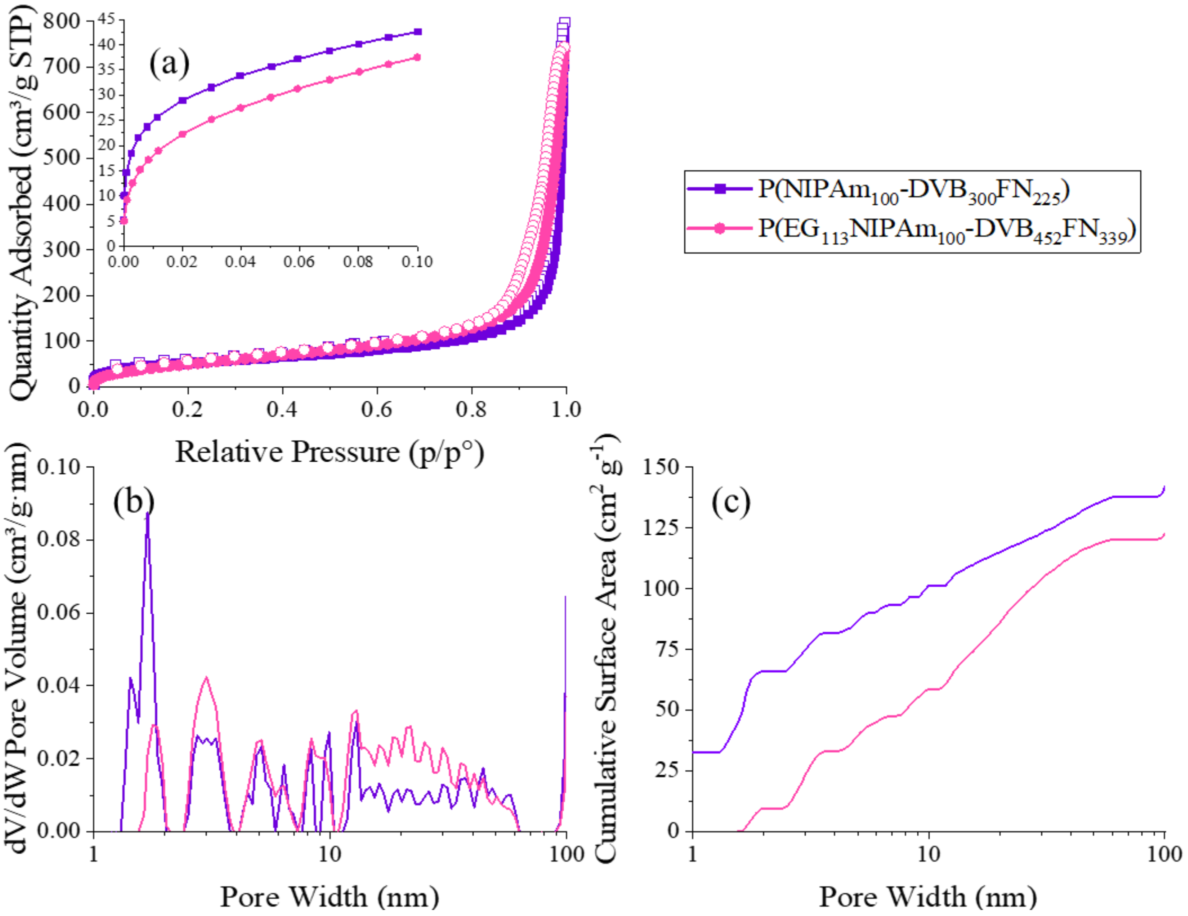

Figure 6.10 (a) Nitrogen adsorption isotherms of $PNIPAm_{100}$ based particles with addition of the PEG_{113} based shell at 77.3 K; (b) Pore size distributions calculated using NLDFT method (slit pore models, differential pore volume vs pore width); and (c) Cumulative surface areas

6.3.4 Investigation of pH-responses of particles with non-ionic shells

While the mixing of the polymer shells was able to increase the surface areas of the particles and as well as the small pore size structures, the reduction in the amount of responsive polymer chains may affect the response itself. It is important to ascertain the effect of adding these non-responsive polymer chains on the response of the particles. Therefore, the size of the mixed-shell particles was measured under different pHs using dynamic light scattering (DLS).

The $P(EG_{113}4-VP_{82}-DVB_{452}FN_{339})$ particles were prepared in 0.1 mg mL^{-1} of 9 different pH solutions from low to high by adding either HCl ($0 \leq pH \leq 1.3$) or NaOH ($13.4 \leq pH \leq 14$).

Each sample was sonicated for 3 hours before analysis. To measure the switch-ability of the particle size, a sample was prepared in 0.1 mg mL^{-1} of acid condition (pH = 0.3) and was switched to based condition (pH = 13.7) with several repeat tests. Each sample was sonicated for 3 hours before the first analysis, then the sample was sonicated for 0.5 hours between each switching. P($EG_{113}DEAEMA_{108}$-$DVB_{144}FN_{108}$) particle samples were prepared in a similar way.

Both of the mixed-shell-based particles which are synthesised in the methanol-water mixture solution are pH-responsive and they are also switchable when the pH changes compared to those synthesised in the water-ethanol mixture solution, which show limited pH- responsive. This may be due to the PEG based macro-CTAs have the similar solubility compared to the PAA based macro-CTAs, which can easily dissolve in the water. The PDEAEMA and P4-VP based macro-CTAs are slightly soluble in the water, which makes them less active in this solution component. Therefore, very less the P4-VP or PDEAEMA based shells join in the reaction which may decrease the concentration of the P4-VP or PDEAEMA based shell to form the particles. Due to the less pH- responsive polymer formed the particle, the particles do less responses to the pH changing. In contrast, there are higher concentration of the P4-VP or PDEAEMA based shell to form the particles in the methanol-water mixture solution. Therefore, the particles do better responses to the pH changing. Moreover, the particle size of each mixed-shell-based particle is larger than the particle size of the single-shell based particle. This is due to the addition of non-ionic PEG_{113} based shell will help the synthesis of P4-VP based particles or PDEAEMA based particles with bigger core parts. The difference of particle size changes in different pH, may be due to the long PEG shell chains hinder the particles separate easily. The P(EG_{113}4-VP_{82}-$DVB_{268}FN_{200}$) particle size is about 650 nm at acid condition, and it is about 1000 nm at base condition (Figure 6.11 a and b). And the P($EG_{113}DEAEMA_{108}$-$DVB_{452}FN_{339}$) particle size is about 580 nm at acid condition ($0 \leq pH \leq 1.3$), and it is about 970 nm at base condition ($13.4 \leq pH \leq 14$) (Figure 6.11 f and g). The TEM images show the same trends (Figure 6.11 c, d, e, h, i and j).

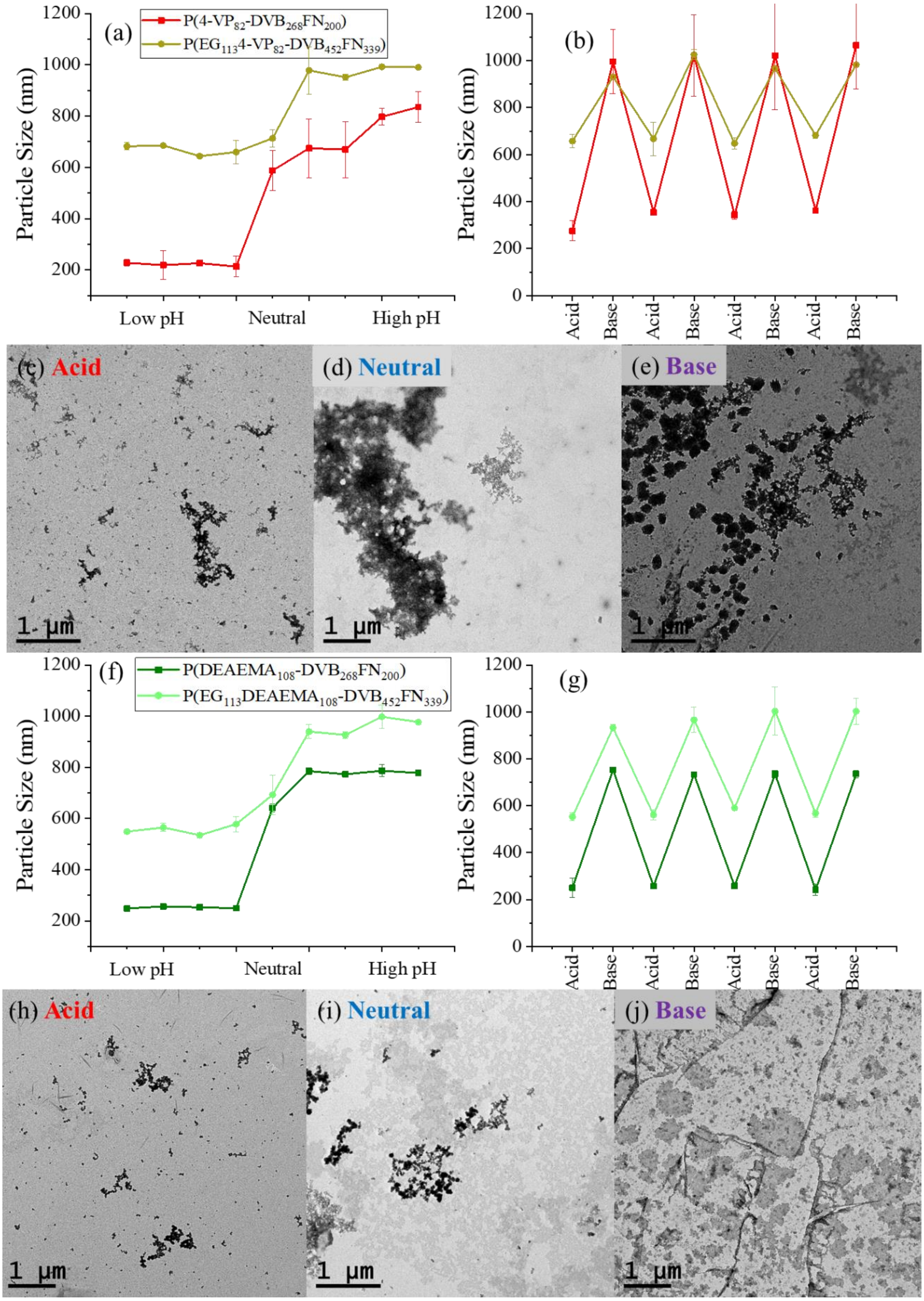

Figure 6.11 Particle size of (a) P(4-VP$_{82}$-DVB$_{268}$FN$_{200}$) particle and P(EG$_{113}$4-VP$_{82}$-DVB$_{452}$FN$_{339}$) particle in different pH- solution from low to high and (b) in acid and base switchable; Particle size of (f) P(DEAEMA$_{108}$-DVB$_{144}$FN$_{108}$) particle and P(EG$_{113}$DEAEMA$_{108}$-DVB$_{452}$FN$_{339}$) particle in different pH- solution from low to high and (g) in acid and base switchable; and TEM images of P(EG$_{113}$4-

VP_{82}-$DVB_{452}FN_{339}$)particles in (c) the acid, (d) the neutral, (e) the base; and P($EG_{113}DEAEMA_{108}$-$DVB_{452}FN_{339}$) particle in (h) the acid, (i) the neutral, (j) the base

6.3.7 Investigation of thermo-responses of particles with non-ionic shells

The mixed-shell thermo- responsive particles were measured, using dynamic light scattering (DLS) to ascertain their size and thermo- response. The of P(4-VP_{82}-$DVB_{268}FN_{200}$) particle were prepared in 0.1 mg/mL of neutral water solvent at 20 °C and the sample was sonicated for 3 hours before analysis. Then, the sample was repeated between 20 °C and 60 °C compared to the single-shell based particles. Moreover, the P($EG_{113}DEAEMA_{108}$-$DVB_{452}FN_{339}$) particles and the P($NIPAm_{100}$-$DVB_{300}FN_{225}$) particles were prepared in the same way.

Both of the mixed-shell-based particles (PDEAEMA and P4-VP based particles) which are synthesised in the water-ethanol mixture solution exhibit limited thermo- responsive as well, which following the same reason as explained in Chapter 6.3.6. For the P4-VP and PDEAEMA based particles. The mixed-shell-based particles which synthesised in the water-methanol mixture solution are thermo-responsive and they can also switch when the temperature changes as the single-shell-based particles (Figure 6.12 b, c, k and l). The TEM images (Figure 6.12 d, e, f, g, h, I, m, n, o, p, q and r) can show the same trend. Moreover, the adding the non-ionic shell can help the thermos-responsive particles more easily to responsive to the temperature. The P(4-VP_{82}-$DVB_{268}FN_{200}$) particles and the P($DEAEMA_{108}$-$DVB_{144}FN_{108}$) particles exhibit the limited responsive in the acid condition in the Chapter 4.3.3; In contrast, the P(EG_{113}4-VP_{82}-$DVB_{452}FN_{339}$) particles and the P($EG_{113}DEAEMA_{108}$-$DVB_{452}FN_{339}$) particles are responsive to the temperature in the acid condition (Figure 6.12 a and j). For PNIPAm based particles, it is different from above mixed-shell-particles. When the PEG based shell is added, the particle size doesn't change so much or a little bit smaller than the particle size of a single-shell-based particle, P($NIPAm_{100}$-$DVB_{300}FN_{225}$) (Figure 6.12 s, t and u). This may be due to the fact that P($EG_{113}NIPAm_{100}$-$DVB_{452}FN_{339}$) particles were synthesised in neutral condition, the amino groups are therefore not charged at this pH. Therefore, the addition of PEG_{113} based shell chains not only won't do the effective steric stabilisation but also prevent the core part growing larger. The particle size is quite smaller than the P($NIPAm_{100}$-$DVB_{300}FN_{225}$). The TEM images show the same trend (Figure 6.12 v, w, x and y).

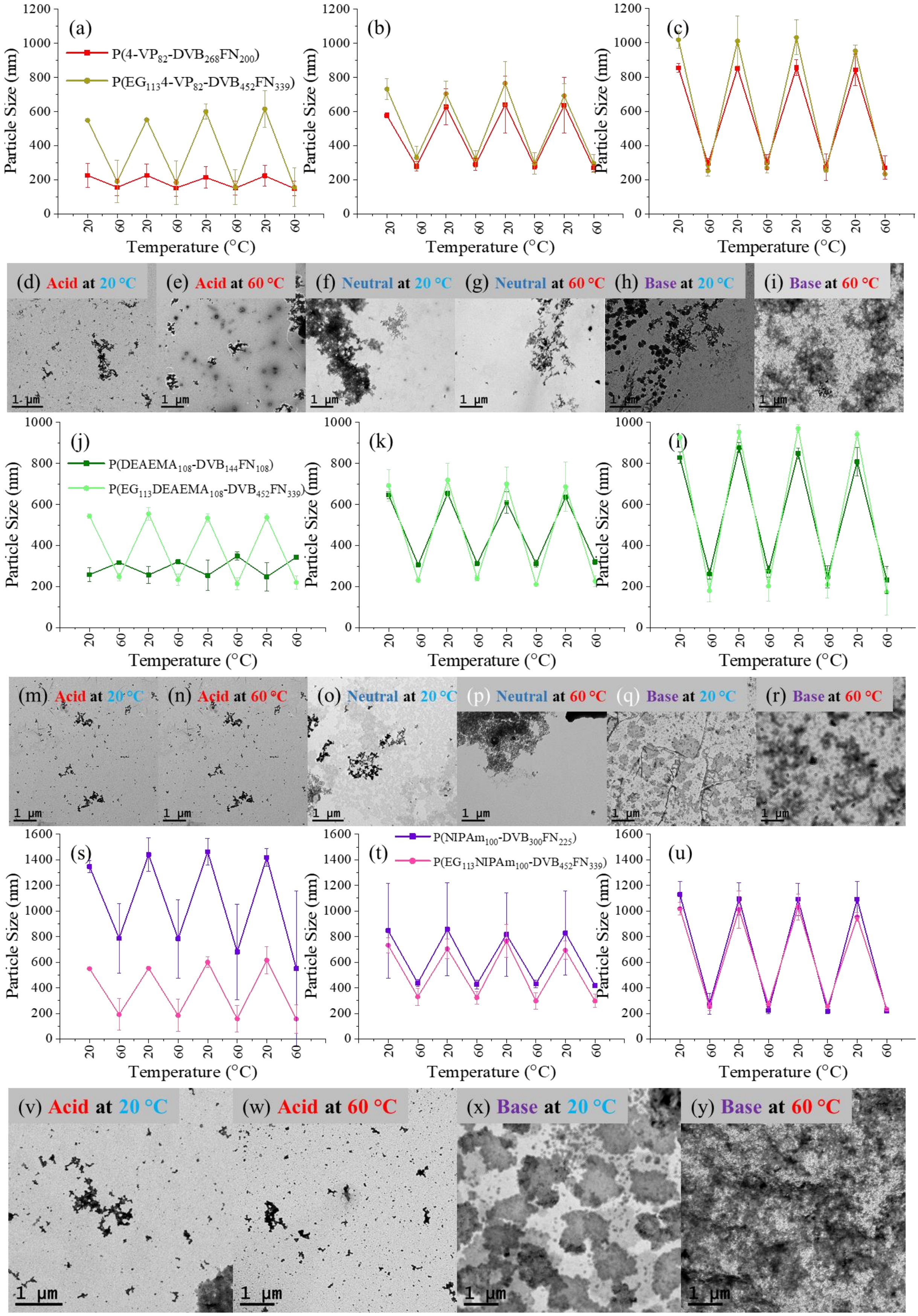
(a)
(b)
(c)
$P(4\text{-}VP_{82}\text{-}DVB_{268}FN_{200})$
$P(EG_{113}4\text{-}VP_{82}\text{-}DVB_{452}FN_{339})$
Particle Size (nm)
Temperature (°C)
(d) Acid at 20 °C
(e) Acid at 60 °C
(f) Neutral at 20 °C
(g) Neutral at 60 °C
(h) Base at 20 °C
(i) Base at 60 °C
(j)
(k)
(l)
$P(DEAEMA_{108}\text{-}DVB_{144}FN_{108})$
$P(EG_{113}DEAEMA_{108}\text{-}DVB_{452}FN_{339})$
(m) Acid at 20 °C
(n) Acid at 60 °C
(o) Neutral at 20 °C
(p) Neutral at 60 °C
(q) Base at 20 °C
(r) Base at 60 °C
(s)
(t)
(u)
$P(NIPAm_{100}\text{-}DVB_{300}FN_{225})$
$P(EG_{113}NIPAm_{100}\text{-}DVB_{452}FN_{339})$
(v) Acid at 20 °C
(w) Acid at 60 °C
(x) Base at 20 °C
(y) Base at 60 °C
1 µm

Figure 6.12 Particle size of the P(EG$_{113}$4-VP$_{82}$-DVB$_{452}$FN$_{339}$) in (a) the acid, (b) the neutral, (c) the base condition switchable between 20 °C and 60 °C switchable; Particle size of the P(EG$_{113}$DEAEMA$_{108}$-DVB$_{452}$FN$_{339}$) in (j) the acid, (k) the neutral, (l) the base condition; Particle size of P(EG$_{113}$NIPAm$_{100}$-DVB$_{452}$FN$_{339}$) particle in (s) the acid, (t) the neutral, (u) the base; and TEM images of P(EG$_{113}$4-VP$_{82}$-DVB$_{452}$FN$_{339}$) particles in the acid with (d) 20 °C and (e) 60 °C, in the neutral with (f) 20 °C and (g) 60 °C, in the base with (h) 20 °C and (i) 60 °C; P(EG$_{113}$DEAEMA$_{108}$-DVB$_{452}$FN$_{339}$) in the acid with (m) 20 °C and (n) 60 °C, in the neutral with (o) 20 °C and (p) 60 °C, in the base with (q) 20 °C and (r) 60 °C; P(EG$_{113}$NIPAm$_{100}$-DVB$_{452}$FN$_{339}$) particle in the acid with (v) 20 °C and (w) 60 °C, in the base with (x) 20 °C and (y) 60 °C

6.4 Conclusion

In conclusion, we have reported 3 methods to increase the BET surface. The $P(AA_{95}$-$DVB_{47}FN_{35})$ particles with the addition of the same shell, PAA_{35} based shell, the BET surface area of $P(AA_{35}AA_{95}$-$DVB_{47}FN_{35})$ increase from 186 m^2 g^{-1} to 258 m^2 g^{-1}. Moreover, it has an extra 22 m^2 g^{-1} and 34 m^2 g^{-1} BET surface area contributed by microporous region and mesoporous region respectively. The addition of anionic shell, PAA_{35} based shell chains, the BET surface area increases from 40 m^2 g^{-1} ($P(4$-VP_{82}-$DVB_{268}FN_{200})$ particles) up to 124 m^2 g^{-1} ($P(AA_{35}4$-VP_{82}-$DVB_{268}FN_{200})$ particles). Moreover, it has an extra 112 m^2 g^{-1} and 90 m^2 g^{-1} BET surface area contributed by microporous and mesoporous regions respectively. This is due to anionic PAA_{35} based shell chains are added to the cationic P4-VP based shells which the neutralization of charges may decrease the repulsion between the highly cationic polymer chains. This will make core parts grow larger which may increase the BET surface area.

The $P(4$-VP_{82}-$DVB_{268}FN_{200})$, $P(DEAEMA_{108}$-$DVB_{47}FN_{35})$, with non-ionic PEG_{113} based shell chains were added, the BET surface area of $P(EG_{113}4$-VP_{82}-$DVB_{452}FN_{339})$, $P(EG_{113}DEAEMA_{108}$-$DVB_{452}FN_{339})$, increase from 40 m^2 g^{-1} up to 241 m^2 g^{-1} and from 78 m^2 g^{-1} up to 137 m^2 g^{-1}, respectively. In addition, they have an extra 112 m^2 g^{-1} & 90 m^2 g^{-1} BET surface area contributed by microporous and mesoporous regions respectively and an extra 33 m^2 g^{-1} BET surface area contributed by microporous and mesoporous regions for $P(4$-VP_{82}-$DVB_{268}FN_{200})$ synthesised in water/ethanol solution & methanol/water solution and $P(DEAEMA_{108}$-$DVB_{47}FN_{35})$ particles respectively. This is due to the addition of non-ionic PEG_{113} based shell will help the synthesis of P4-VP based particles or PDEAEMA based particles with bigger core parts which may increase the BET surface area. The particle sizes of both mixed shell based particles are a little bit larger than the particle sizes of single-shell based particles. This may be due to the PEG based shell chains having a larger volume.

However, for $P(EG_{113}NIPAm_{100}$-$DVB_{452}FN_{339})$ based particles. The addition of PEG_{113} based shell chains made the BET surface area of $P(NIPAm_{100}$-$DVB_{452}FN_{339})$ particles decreased from 214 m^2 g^{-1} to 159 m^2 g^{-1}. Furthermore, it has a reduced BET surface area of 56 m^2 g^{-1} of microporous structure. This may be due to the $P(EG_{113}NIPAm_{100}$-$DVB_{452}FN_{339})$ particles were synthesised in the neutral condition, the amino groups are not charged at this pH. Therefore, the addition of PEG_{113} based shell chains not only won’t do the effective steric stabilisation but also prevent the core part growing larger. Due to this reason, the particle size of mixed shell-based particles is similar or a little bit smaller than the particle size of single-shell based particles.

Moreover, the additional non-ionic PEG_{113} based shells synthesised in methanol-water mixture for PDEAEMA and P4-VP based particles; and synthesised in water-ethanol mixture for PNIPAm based particles, not only doesn’t influence the particles with pH or temperature responses, but also stable the particle size.

6.5 References

(1) Williams, M.; W. Penfold, N. J.; P. Armes, S. Cationic and Reactive Primary Amine-Stabilised Nanoparticles via RAFT Aqueous Dispersion Polymerisation. *Polym. Chem.* **2016**, *7* (2), 384–393. https://doi.org/10.1039/C5PY01577D.

(2) Penfold, N. J. W.; Ning, Y.; Verstraete, P.; Smets, J.; Armes, S. P. Cross-Linked Cationic Diblock Copolymer Worms Are Superflocculants for Micrometer-Sized Silica Particles. *Chem. Sci.* **2016**, *7* (12), 6894–6904. https://doi.org/10.1039/C6SC03732A.

(3) Pangborn, A. B.; Giardello, M. A.; Grubbs, R. H.; Rosen, R. K.; Timmers, F. J. Safe and Convenient Procedure for Solvent Purification. *Organometallics* **1996**, *15* (5), 1518–1520. https://doi.org/10.1021/om9503712.

(4) Skey, J.; K. O'Reilly, R. Facile One Pot Synthesis of a Range of Reversible Addition–Fragmentation Chain Transfer (RAFT) Agents. *Chem. Commun.* **2008**, *0* (35), 4183–4185. https://doi.org/10.1039/B804260H.

(5) Chaduc, I.; Crepet, A.; Boyron, O.; Charleux, B.; D'Agosto, F.; Lansalot, M. Effect of the PH on the RAFT Polymerisation of Acrylic Acid in Water. Application to the Synthesis of Poly(Acrylic Acid)-Stabilized Polystyrene Particles by RAFT Emulsion Polymerisation. *Macromolecules* **2013**, *46* (15), 6013–6023. https://doi.org/10.1021/ma401070k.

(6) Wong, A. S. M.; Mann, S. K.; Czuba, E.; Sahut, A.; Liu, H.; Suekama, T. C.; Bickerton, T.; Johnston, A. P. R.; Such, G. K. Self-Assembling Dual Component Nanoparticles with Endosomal Escape Capability. *Soft Matter* **2015**, *11* (15), 2993–3002. https://doi.org/10.1039/C5SM00082C.

(7) Liu, R.; Rong, Z.; Han, G.; Yang, X.; Zhang, W. Synthesis and Self-Assembly of Star Multiple Block Copolymer of Poly(4-Vinylpyridine)-Block-Polystyrene. *Polymer* **2021**, *215*, 123431. https://doi.org/10.1016/j.polymer.2021.123431.

(8) Li, C.; Wang, C.; Ji, Z.; Jiang, N.; Lin, W.; Li, D. Synthesis of Thiol-Terminated Thermoresponsive Polymers and Their Enhancement Effect on Optical Limiting Property of Gold Nanoparticles. *Eur. Polym. J.* **2019**, *113*, 404–410. https://doi.org/10.1016/j.eurpolymj.2019.02.009.

(9) James, A. M.; Derry, M. J.; Train, J. S.; Dawson, R. Dispersible Microporous Diblock Copolymer Nanoparticles via Polymerisation-Induced Self-Assembly. *Polym. Chem.* **2019**, *10* (28), 3879–3886. https://doi.org/10.1039/C9PY00596J.

(10) Xu, Y.; Jin, S.; Xu, H.; Nagai, A.; Jiang, D. Conjugated Microporous Polymers : Design, Synthesis and Application. *Chem. Soc. Rev.* **2013**, *42* (20), 8012–8031. https://doi.org/10.1039/C3CS60160A.

(11) Tian, Y.; Zhu, G. Porous Aromatic Frameworks (PAFs). *Chem. Rev.* **2020**, *120* (16), 8934–8986. https://doi.org/10.1021/acs.chemrev.9b00687.

(12) James, A. M.; Dawson, R. Efficient and Tunable White-Light Emission Using a Dispersible Porous Polymer. *Macromol. Rapid Commun.* **2020**, *41* (12), 2000176. https://doi.org/10.1002/marc.202000176.

(13) Ferguson, C. T. J.; Huber, N.; Kuckhoff, T.; Zhang, K. A. I.; Landfester, K. Dispersible Porous Classical Polymer Photocatalysts for Visible Light-Mediated Production of Pharmaceutically Relevant Compounds in Multiple Solvents. *J. Mater. Chem. A* **2020**, *8* (3), 1072–1076. https://doi.org/10.1039/C9TA11242A.

(14) Ivko, S. A.; James, A. M.; Derry, M. J.; Dawson, R.; Haynes, A. Heterogenisation of a Carbonylation Catalyst on Dispersible Microporous Polymer Nanoparticles. *Catal. Sci. Technol.* **2022**, *12* (2), 664–673. https://doi.org/10.1039/D1CY01989A.

(15) Mai, W.; Sun, B.; Chen, L.; Xu, F.; Liu, H.; Liang, Y.; Fu, R.; Wu, D.; Matyjaszewski, K. Water-Dispersible, Responsive, and Carbonizable Hairy Microporous Polymeric Nanospheres. *J. Am. Chem. Soc.* **2015**, *137* (41), 13256–13259. https://doi.org/10.1021/jacs.5b08978.

(16) Yu, H.; Wang, Z.; Wu, R.; Chen, X.; Chan, T.-W. D. Water-Dispersible PH/Thermo Dual-Responsive Microporous Polymeric Microspheres as Adsorbent for Dispersive Solid-Phase Extraction of Fluoroquinolones from Environmental Water Samples and Food Samples. *J. Chromatogr. A* **2019**, *1601*, 27–34. https://doi.org/10.1016/j.chroma.2019.05.004.

6.6 Appendix

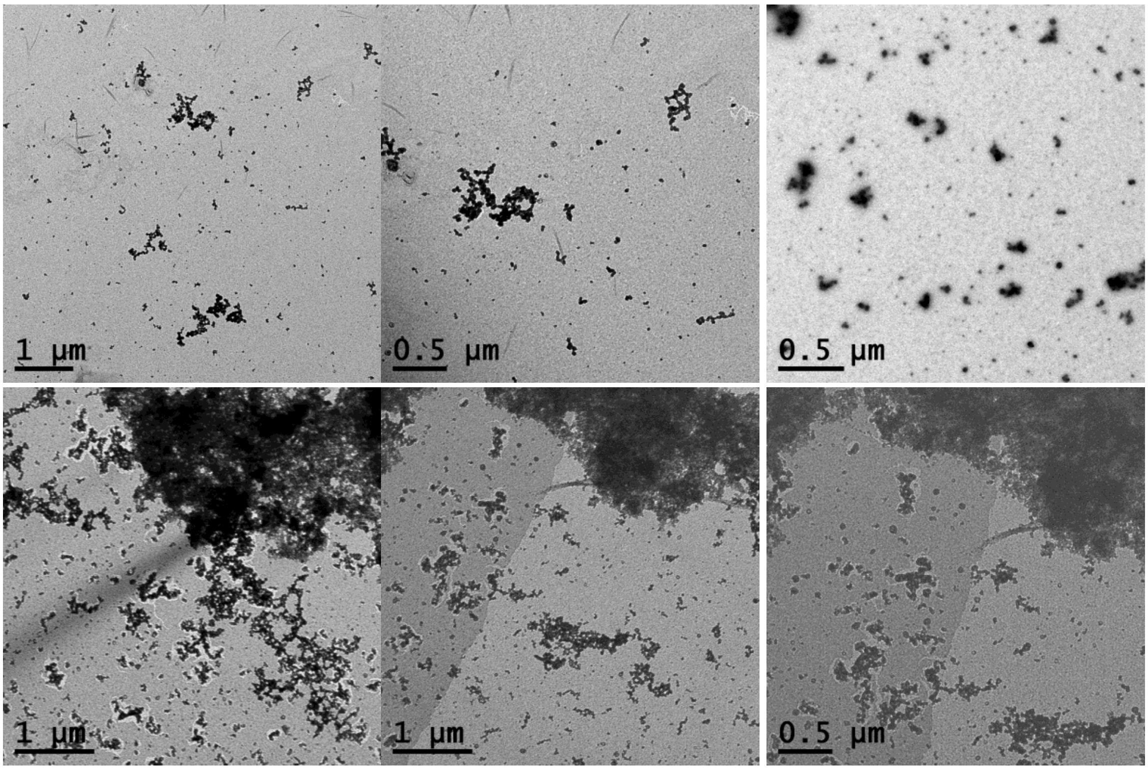

Figure 6.1 The different scales of TEM images of P($EG_{113}DEAEMA_{108}$-$DVB_{452}FN_{339}$) particles in the acid condition at 20 °C (up) and 60 °C (down)

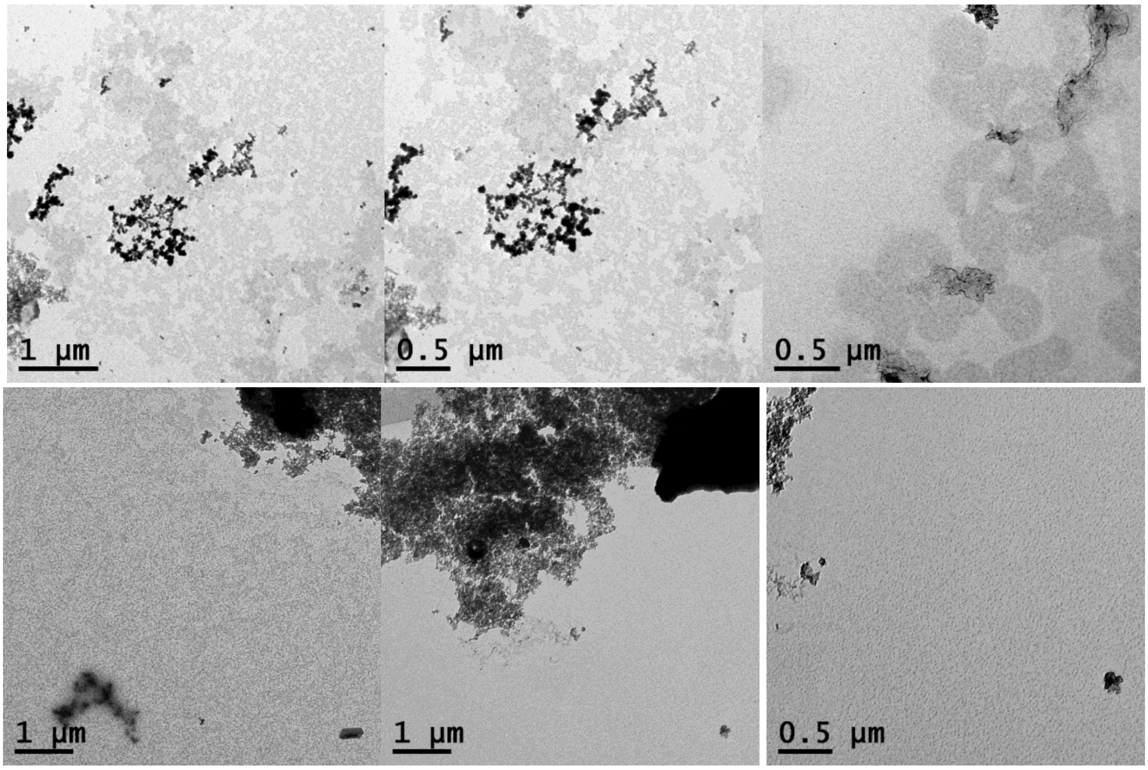

Figure 6.2 The different scales of TEM images of P($EG_{113}DEAEMA_{108}$-$DVB_{452}FN_{339}$) particles in the neutral condition at 20 °C (up) and 60 °C (down)

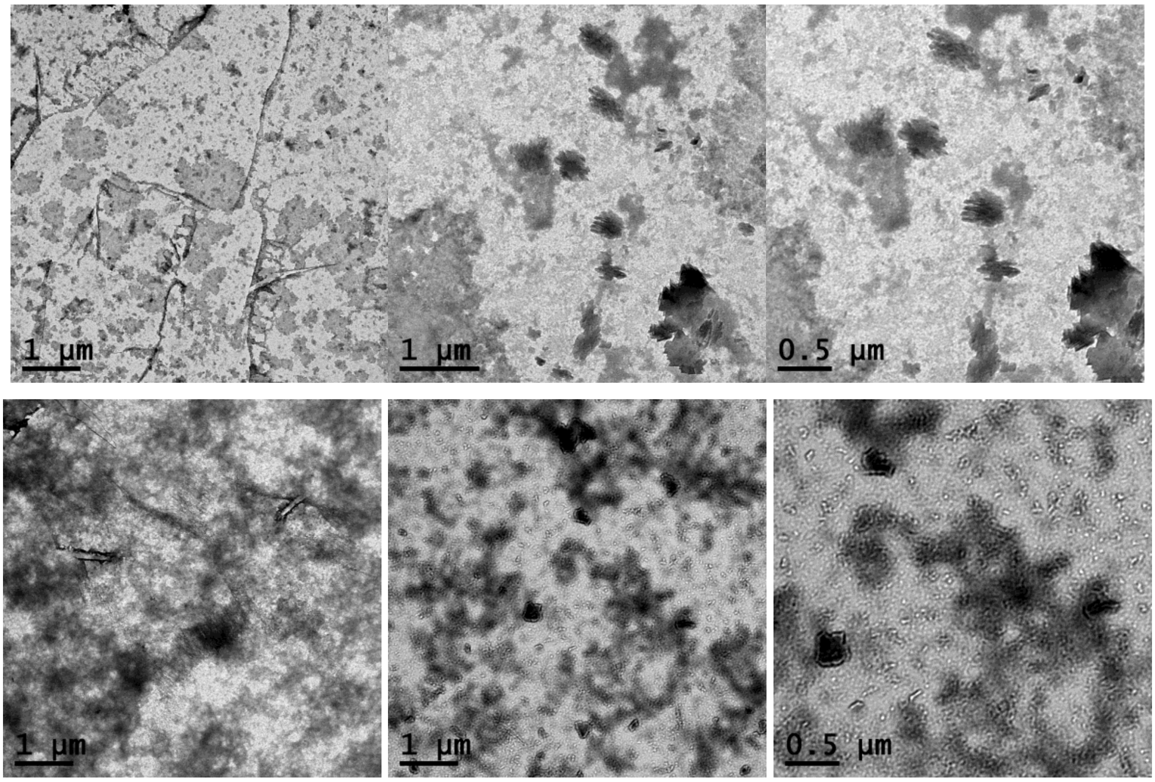

Figure 6.3 The different scales of TEM images of P(EG$_{113}$DEAEMA$_{108}$-DVB$_{452}$FN$_{339}$) particles in the base condition at 20 °C (up) and 60 °C (down)

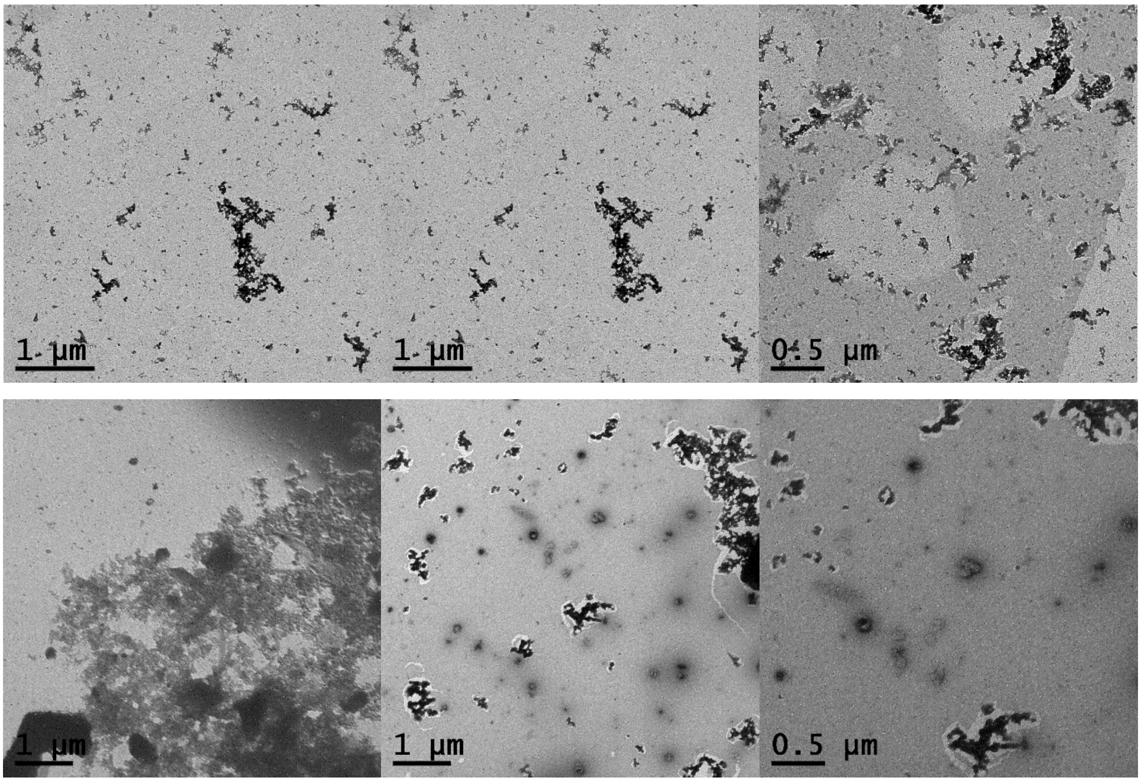

Figure 6.4 The different scales of TEM images of P(EG$_{113}$4-VP$_{82}$-DVB$_{452}$FN$_{339}$) particles in the acid condition at 20 °C (up) and 60 °C (down)

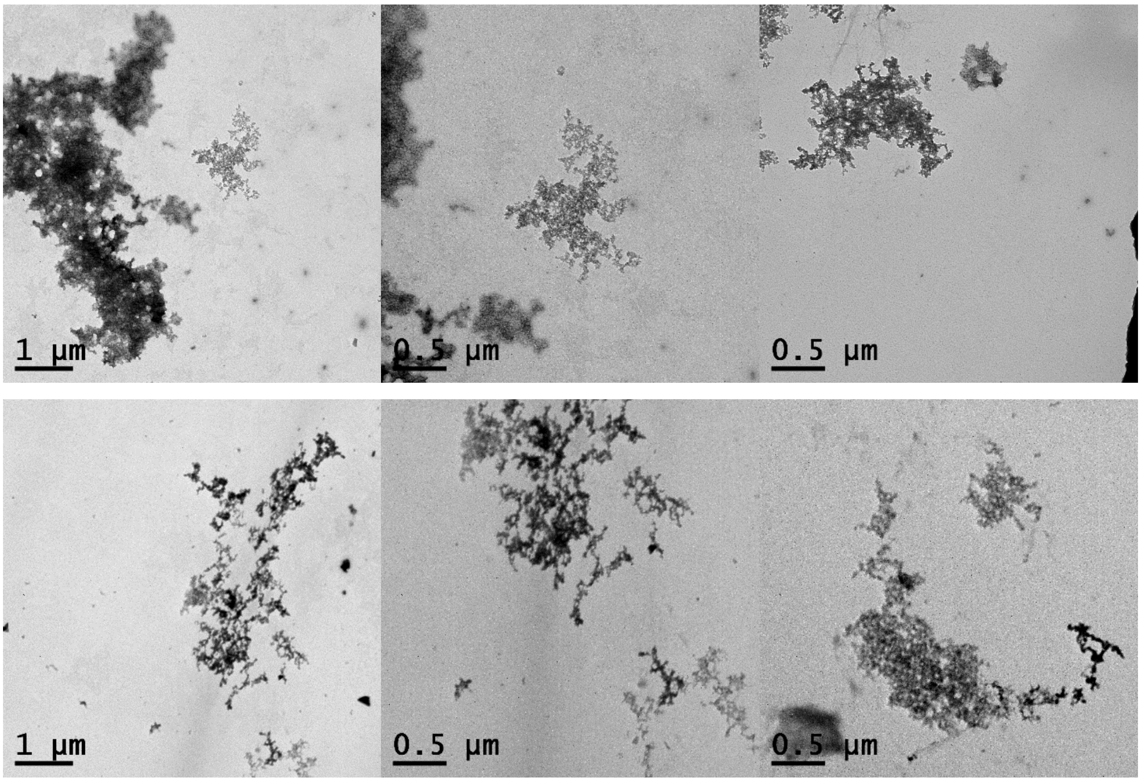

Figure 6.5 The different scales of TEM images of P(EG_{113}4-VP_{82}-$DVB_{452}FN_{339}$) particles in the neutral condition at 20 °C (up) and 60 °C (down)

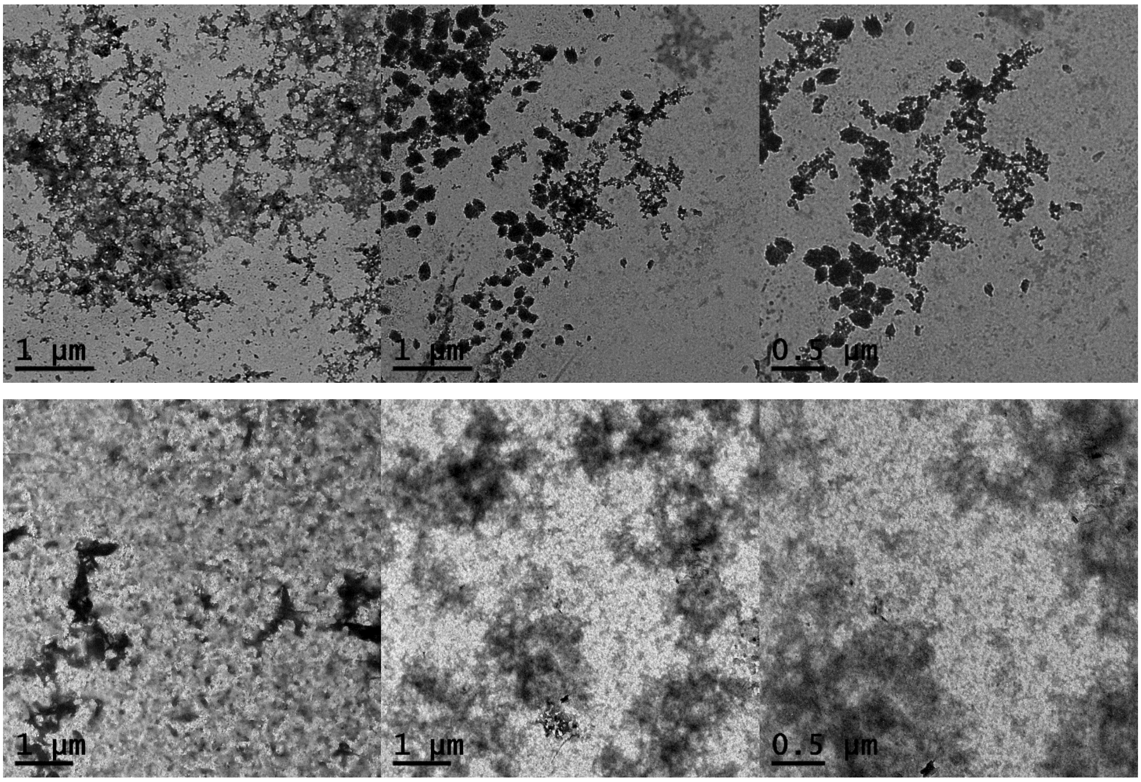

Figure 6.6 The different scales of TEM images of P(EG_{113}4-VP_{82}-$DVB_{452}FN_{339}$) particles in the base condition at 20 °C (up) and 60 °C (down)

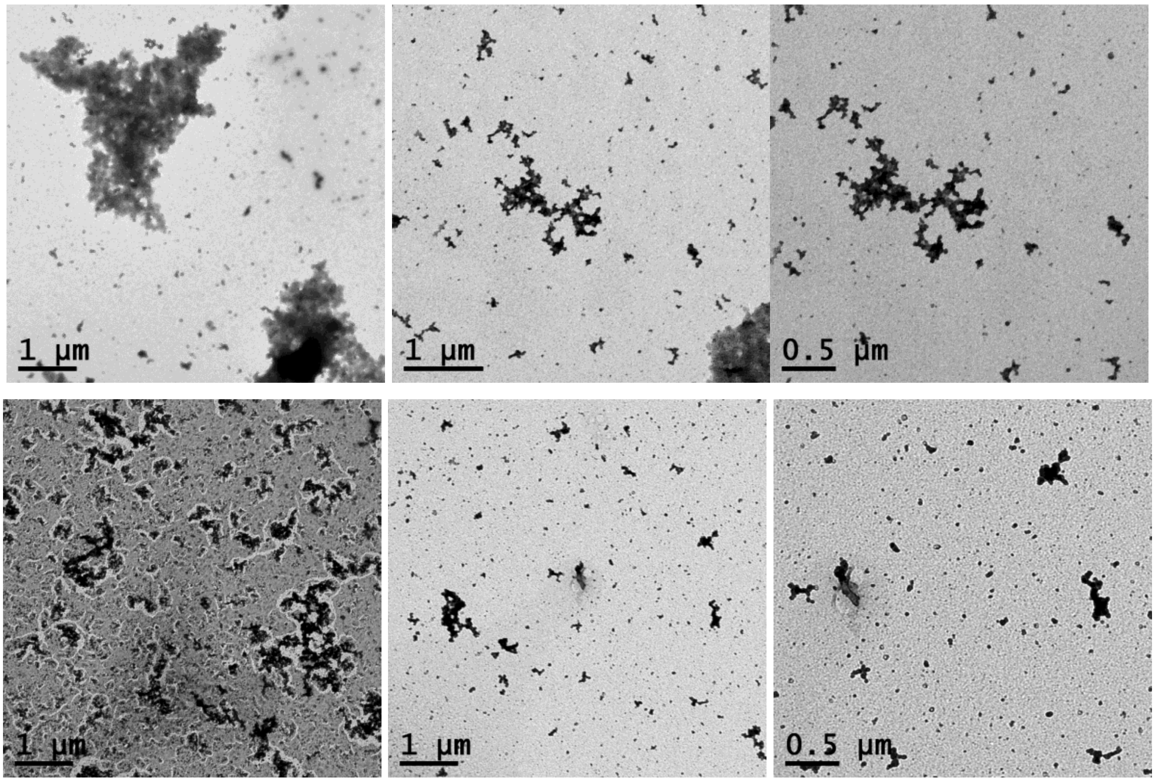

Figure 6.7 The different scales of TEM images of P($EG_{113}NIPAm_{100}$-$DVB_{452}FN_{339}$) particles in the acid condition at 20 °C (up) and 60 °C (down)

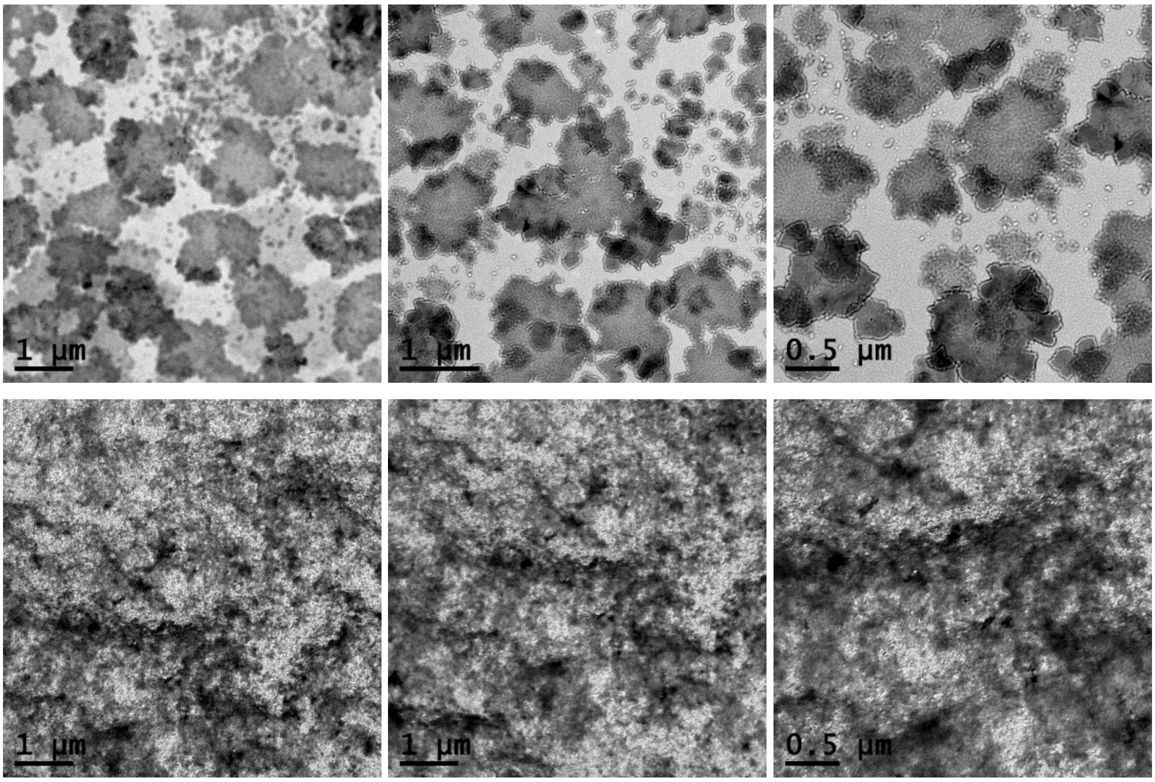

Figure 6.8 The different scales of TEM images of P($EG_{113}NIPAm_{100}$-$DVB_{452}FN_{339}$) particles in the base condition at 20 °C (up) and 60 °C (down)

Chapter-7 Conclusions and Future Work

7.1 Conclusions

Previous research of our group[1] produced a novel and versatile synthesis strategy towards dispersible porous polymer particles (d-PPPs) using RAFT-PISA. That work used a PEG-based macro-CTA to disperse a porous core of divinylbenzene and fumaronitrile. This thesis builds upon these findings and describes the use of the new solubilising polymer chains, poly(acrylic acid) (PAA), poly(diethylaminoethyl methacrylate) (PDEAEMA), poly(4-vinylpyridine) (P4- VP) and poly(N-isopropylacrylamide) (PNIPAm).

Chapter 3 investigates the use of a PAA shell. The best reaction conditions were determined by using PAA chain length of 35, a water to ethanol ratio of 60:40 with a core ratio of divinylbenzene (DVB) to fumaronitrile (FN) of 4:3, and a (DP 47:35) as previously found for the PEG-based particles. The particles are stable in common organic solvents with particle sizes of around 150 nm similar to the PEG-based system. However, in comparison to the PEG based system, the highest BET surface area was only 322 m^2 g^{-1} compared to 407 m^2 g^{-1} and the pore size distribution shows that the surface area is mostly comprised of external porosity rather than in internal microporous structure.

Chapter 4 introduces outer polymer chains with pH- responsivity by incorporating the following pH- responsive monomers diethylaminoethyl methacrylate (DEAEMA), and 4-vinlypyridine (4-VP). In initial investigation into the reaction conditions is conduced to yield particles with the BET surface areas up to 101 m^2 g^{-1}. While these surface areas are even lower than those from Chapter 3, they were nevertheless tested to ascertain whether or not they were indeed pH responsive. DLS and TEM measurements confirmed that the particles change in size from around 200 nm at low pH to around 800 nm at high pH. This is in contrast to what would be expected: at low pH the particles should be protonated and be more soluble due to the charge on the chains resulting in repulsion between the chains and hence larger particle sizes. In reality, the particles sizes are small at low pH and larger at high pH due to the aggregation of the now less soluble chains.

The temperature responsive of PDEAEMA, P4-VP and new particles synthesised from PNIPAm are investigated in Chapter 5. The PNIPAm based particles were found to have relatively low surface areas of up to 193 m^2 g^{-1}, however all particles demonstrated thermo-responsive properties at different pHs. Interestingly, the particle sizes are large at low temperature when the particles are hydrated but at high temperature, they begin to aggregate and precipitate as the water molecules are expelled. In both chapters 4 and 5, these responses can be seen to be easily reversible which may of interest for future applications of these particles if the surface areas can be increased.

Chapter 6 therefore looks at methods to try to increase the BET surface areas. The different strategies used include same shell mixing (mixing PAA_{35} based shells with PAA_{95} based shells); incorporation of anionic shells (PAA_{35} based shell with $P4\text{-}VP_{82}$ based shell); and adding non-ionic shells (PEG_{113} based shells with $P4\text{-}VP_{82}$, $PDEAEMA_{108}$, $PNIPAm_{100}$ based shells). The results show that the shell surface areas can be improved by up to 5 times in the case of P4-VP, furthermore despite the inclusion of a large percentage of non-responsive PEG shells the particles are still able to undergo responsive switching by pH or temperature.

7.2 Future Work

This thesis has therefore demonstrated that a range of outer solubilising shells can be used including responsive shells, this opens up the field for the investigation of many more monomers in the hope that they could lead to increased surface areas and the potential the incorporation of shells with further interesting properties.

To date, we have only investigated the use of DVB and FN as core forming monomers, there are many more different commercially available crosslinkers as well as many more which could be envisioned. The spacer unit could also be changed to incorporate interesting properties into the core such as for catalysts as has previously been demonstrated. Combining both the properties of the switchable outer polymer chains with catalytically active cores could lead to processes where the particles can easily be recovered between catalytic cycles using a simple pH or temperature change therefore possessing both the benefits of homogeneous catalysts (good interaction between catalysts and solvents/substates) and heterogeneous catalysts (ease of reuse).

The wide range of monomers available as well as the many variables used in their synthesis (solvent composition, core: shell ratios, crosslinker ratios etc.) lends these materials to their investigation by robotic chemistry particularly as these materials are able to be made and collected from solution (something not common for porous materials).

I believe dispersible porous polymer particles have many interesting properties some of which I have touched upon in this thesis. The field is now wide open for further investigation using the wide range of commercially available vinyl monomers for both the shell and core which can be polymerised using RAFT-PISA chemistry.

7.3 References

(1) James, A. M.; Derry, M. J.; Train, J. S.; Dawson, R. Dispersible Microporous Diblock Copolymer Nanoparticles via Polymerisation-Induced Self-Assembly. *Polym. Chem.* **2019**, *10* (28), 3879–3886. https://doi.org/10.1039/C9PY00596J.